NORTHWESTERN UNIVERSITY

Experimental Validation of First Principles Simulations and Observation of Diffuse Ion Profiles at Solid/Water Interfaces

A DISSERTATION

SUBMITED TO THE GRADUATE SCHOOL

IN PARTIAL FULFILLMENT OF THE REQUIREMENTS

for the degree

DOCTOR OF PHILOSOPHY

Field of Applied Physics

By

Katherine Jean Harmon

EVANSTON, ILLINOIS

March 2021

Abstract

Experimental Validation of First Principles Simulations and Observation of Diffuse Ion Profiles at Solid/Water Interfaces

Katherine Harmon

Physiochemical phenomena in aqueous systems, such as corrosion, catalysis, and energy storage, are driven by the molecular-scale interactions of ionic species with charged solid surfaces. In particular, an electrical double layer (EDL) of ions forms within nanometers of a charged surface. The properties of the EDL have been explored from both a theoretical perspective and an experimental perspective for over a century, but a precise description of its structure remains elusive. For example, classical theories of the EDL developed over a century ago consider interactions between charged species in solution and a charged interface but neglect solvation effects. Furthermore, we now understand that interfacial phenomena deviate significantly from their bulk counterparts—though the precise nature of these differences depends on the ions, the solvent, and the solid surface itself. This presents a significant barrier to obtaining a comprehensive picture of interfacial phenomena. Complementary efforts from theory and experiment are needed to tackle this challenge, which demands high accuracy from both directions.

X-ray reflectivity provides an exceptionally sensitive probe of interfacial structures and has been used to measure interfacial water and adsorbed ion structures at mineral/water interfaces with atomic resolution. Several recent studies have also used X-ray reflectivity as a validation tool to evaluate the accuracy of simulated structures of solid/water interfaces at different levels of theory. As a natural extension, this thesis uses X-ray reflectivity to explore in detail several

different theoretical and numerical approximations required to carry out first principles molecular dynamics calculations with a focus on the alumina(001)/water interface. The sensitivity of X-ray reflectivity to atomic and electronic displacements provides a direct pathway to assess the strengths and weaknesses of different approximations and identify areas to further improve the accuracy of these simulations.

In addition, this thesis uses X-ray reflectivity with and without element specificity to probe the water and EDL structures at a graphene electrode surface with potentiostatic control. The hydrophobic nature of graphene leads to a confinement-induced ordering of water at the solid surface that may affect ion adsorption. I then use resonant X-ray reflectivity to directly probe the EDL structure. I compare the observe resonance spectra to the ion distribution models derived from Gouy-Chapman theory and find a significant deviation from the classical theory under the experimental conditions employed. The discrepancy between the observed ion structure and classical models can be explained by incorporating the effects of the interfacial water. The results also suggest that the properties of the electrode play a role in establishing the double layer, which is not considered in the classical theories.

Acknowledgement

I thank my advisors, Professor Michael Bedzyk and Dr. Paul Fenter, for providing a unique opportunity to carry out my PhD research at Argonne National Lab and for making my PhD an unforgettable experience. Thank you both for your support and encouragement over the past five years. I especially want to thank Paul for being one of the best teachers I have ever had. Thank you for always welcoming questions and being ready with pen and paper (or marker and white board) and for fostering a welcoming lab environment where students, postdocs, and staff are treated as equals. Your mentorship has been instrumental in helping me grow into the scientist I am today.

I would like to thank Professor Monica Olvera de la Cruz for serving on my committee, for her collaboration on our graphene project, and for her mentorship throughout my PhD. It has been a privilege to interact with you and your group. I thank my theory collaborators without whom my PhD would not have been possible: Dr. Felipe Jiménez-Ángeles of the Olvera group; Dr. Eric Bylaska at Pacific Northwest National Lab; Prof. John Weare at the University of California San Diego; Drs. Kendra Letchworth-Weaver and Maria Chan at Argonne; and Drs. Federico Giberti and Alex Gaiduk and Prof. Giulia Galli at the University of Chicago.

Thanks to my colleagues in the Fenter Lab at Argonne National Lab: first and foremost, Dr. Sang Soo Lee with whom I shared an office, who was instrumental in helping me learn how to run experiments at the APS on my own, and who always gave me guidance on CTR and RAXR data analysis when I asked. I would like to thank former postdocs, Drs. Jonnathan Medina Ramos and Dr. Jacqueline Bracco, for teaching me how to run electrochemistry and AFM measurements

and for their friendship. Finally, I would like to thank Dr. Tim Fister for his help during beamtimes, especially for his assistance in setting up to run electrochemistry measurements at the beamline.

I am grateful to all the Bedzyk group members who welcomed me into the group and helped me feel at home: Dr. Gavin Campbell, Dr. Hypo Chen, Dr. Xiao Chen, Dr. Changrui Gau, Dr. Kurinji Krishnamoorthy, Dr. Stephanie Moffit, Dr. Liane Moreau, Janak Thapa, Dr. Li Zeng, and Dr. Sumit Kewalramani. I want to give a special thanks to Liane for her mentorship and encouragement from the very start, Gavin Campbell for discussion and insights on CTR analysis and graphene, and Stephanie, Hypo, and Kurinji for their enduring friendship. Thanks also to past Bedzyk group members who graduated before my time for their help throughout my PhD: Dr. Jon Emery, master of all things graphene; and Dr. Zhan Zhang, beamline scientist at sector 33-ID-D at the APS. Finally, I would like to thank Dr. D. Kurt Gaskill of the Naval Research Lab for providing quality graphene samples.

I am grateful to my family for all their unwavering support. Thanks to my parents, John and Elizabeth, for instilling in me a curiosity for science and the world and to my brother, Michael, for his enduring friendship. I thank my husband, Nathan for all his love and support over the past seven years, for always encouraging me and helping me through the hard times, and for inspiring me to keep trekking. I would not have made it this far without you by my side. I also thank our cats, Tycho and Frankie, for their companionship and for the pure joy they bring to our lives.

I acknowledge the financial support of the U.S. Department of Defense and the Office of Naval Research through the National Defense Science and Engineering Graduate Fellowship and the support of the Northwestern International Institute for Nanotechnology through the Ryan Fellowship.

List of Abbreviations

2D	Two-Dimensional
AFM	Atomic Force Microscopy
CMD	Classical Molecular Dynamics
CTR	Crystal Truncation Rod
CV	Cyclic Voltammetry
DFT	Density Functional Theory
DIW	Deionized Water
DW	Debye-Waller
EDL	Electrical Double Layer
EDLC	Electrical Double Layer Capacitor
EG	Epitaxial Graphene
FF	Form Factor
FPMD	First Principles Molecular Dynamics
FWHM	Full Width at Half Maximum
GC	Gouy-Chapman
GCS	Gouy-Chapman-Stern
HB	Hydrogen Bond
IS	Inner Sphere
PB	Poisson-Boltzmann
PP	Pseudopotential
OCP	Open Circuit Potential

OS	Outer Sphere
RAXR	Resonant Anomalous X-ray Reflectivity
rms	Root Mean Square
SFG	Sum-Frequency Generation
vdW	van der Waals
UHV	Ultra-High Vacuum
XANES	X-ray Absorption Near Edge Structure
XR	X-ray Reflectivity

Table of Contents

List of Figures

List of Tables

Chapter 1: Introduction

Solid/water interfaces are primary sites for a wide range of physiochemical phenomena in natural and technological systems. These include corrosion [1-4], catalysis [5-9], biomolecule conjugation [10, 11], mineral reactivity and metal ion uptake [12-16], and energy conversion [9, 17-19]. The driving forces behind these processes involve a complex interplay of interactions between the solid surface, ionic species in solution, and solvent molecules. As a result, interfacial phenomena can be difficult to study and interpret but also present a rich opportunity for exploring fundamental science and for the development of novel materials and technologies for use in aqueous environments. A complete picture of the molecular-scale structure of ions at charged surfaces is a prerequisite to understanding how such processes occur.

A fundamental feature of all solid surfaces in contact with an ionic solution is the adsorption of ions into a so-called electrical double layer (EDL). Solid morphology [20-23], surface functional groups [24-29], and the presence of pores and their sizes [30-34] can all influence the EDL structure either directly (i.e., via electrostatic interactions between charges) or indirectly (i.e., through steric effects due to ion size or energetic costs to desolvate the ions). These properties of the solid also influence its hydrophilicity or hydrophobicity, which contributes to the interfacial hydration structure [25, 35-40] and the associated hydrogen bond (HB) network [28, 41-43] and can alter the interfacial water properties (e.g., the dielectric response) [44-47]. Ion adsorption is then predicated on the disruption of interfacial HBs and the displacement of water molecules. The inverse is also true—interfacial hydration and ion adsorption can alter the solid surface via surface relaxations or morphological changes [27, 48-51] and affect its functionality [29, 52]. Clearly, ion adsorption at solid/water interfaces is the result of many competing and complementary mechanisms.

Many experimental techniques have been applied to the study solid/water interfaces over the last several decades. For planar surfaces, these include non-linear vibrational spectroscopies, surface force probes (i.e., based on atomic force microscopy, AFM), and X-ray reflectivity (XR). Each of these has its own strengths and weaknesses. For example, vibrational sum frequency generation (SFG) is sensitive to the average arrangement and dynamics of polar molecules and HB networks at interfaces [53, 54], but the molecular origins of spectral signatures often overlap, leading to ambiguity in the interpretations of experimental results in the absence of robust theoretical insights [28, 54, 55]; AFM techniques are useful for probing static nanoscale structures [46, 56-61] but are inherently perturbative, and deconvolving the effects of the probe tip from the measured structure can be challenging [62, 63]; XR is a theoretically non-perturbative, surface sensitive probe with nanoscale to atomic scale resolution [26, 40, 64-67] but provides only indirect evidence of the interfacial HB network due to the relative insensitivity of X-rays to hydrogen atoms. Together, these probes have contributed significant insights to the molecular scale structure of water and ion adsorption on solid surfaces. Yet, many of the intricacies of interfacial phenomena remain poorly understood.

Among the outstanding mysteries of solid/liquid interfaces is the structure of the EDL and how it depends on electrolyte conditions (e.g., ion charge, size, and concentration). Over a century ago, Gouy [68] and Chapman [69] proposed a simple theory of the EDL based on Boltzmann statistics that describes a diffuse cloud of ions adsorbing near charged surfaces in what has come to be known as the Gouy-Chapman (GC) model. Soon thereafter, Stern combined the GC theory with that of Helmholtz [70] to describe a layer of specifically adsorbed ions immediately adjacent to the charged surface followed by a diffuse layer [71], leading to the Gouy-Chapman-Stern (GCS) model.

EDL theories have grown more complex over the years as the limitations of the GC and GCS theories under certain conditions (e.g., high salt concentrations) became apparent [72-81]. However, the GC model still provides a useful point of reference either to interpret experimental observations that are consistent with the classical theory or to gain insights into the mechanisms contributing to disagreements with GC/GCS [60, 82-85]. Even so, the detailed molecular structure of the diffuse double layer has remained elusive with only one experiment to date that has directly observed an ion distribution consistent with the diffuse profile of GC theory [86].

Elucidation of the EDL structure is important not only to advance our fundamental understanding of solid/liquid interfaces but also to address practical challenges, such as the growing energy needs of society. Electrical double layer capacitors (EDLCs) provide some of the most promising avenues for high power energy storage devices [87]. As the name implies, EDLCs store charge in a capacitive layer via ion adsorption as opposed to storage via chemical bonds as in batteries. Because EDLCs do not require Faradaic charge-transfer (breaking of bonds) to harvest the stored energy, they display superior charging and discharging rates [88] and are known to have lifetimes orders of magnitude longer than batteries. However, the mechanism of charge storage leads EDLCs to have lower energy density than batteries. Significant effort has been made toward improving the design of EDLC electrodes to increase their surface area, thereby providing more adsorption sites and increased capacity [89-93]. Additional efforts have focused on the use of non-aqueous electrolytes, namely room-temperature ionic liquids [94], which have a larger voltage stability window and lead to higher energy storage—the energy stored in a capacitor is proportional to the square of the voltage. While these are worthwhile pursuits, an ongoing scientific challenge remains to resolve the interfacial electrolyte structure in EDLCs in order to understand how it correlates with device performance and guide the development of novel, superior devices.

Computational approaches including classical molecular dynamics (CMD) and first principles MD (FPMD) can offer additional insights to atomistic structures at solid/liquid interfaces. CMD simulations use empirical force fields to describe interatomic interactions by solving the classical equations of motion. Consequently, CMD simulations are scalable both in terms of the number of atoms that can be simulated and in time (dynamics on the order of ns can be predicted). However, CMD cannot directly predict chemical reaction mechanisms and dynamics such as bond breaking or charge transfer between molecules and across interfaces. Conversely, FPMD treats electrons explicitly at the quantum mechanical level and, therefore, includes information about chemical reactions. However, quantum mechanical calculations of many-body systems present a significant computational challenge even for modern supercomputers, and FPMD simulations suffer from scalability issues—dynamics are limited to the ps regime and the number of atoms included in the system is severely constrained compared to CMD. Several numerical and theoretical approximations are required to carry out FP calculations, which means balancing practicality with a desire for predictive accuracy [95-100]. In principle, FPMD can provide a fully self-contained approach to understanding surface reactivity, free of empirical insights. However, the predictive power is predicated on obtaining highly accurate simulations, which is particularly challenging at interface due to the inherent symmetry breaking. Validation of FP approaches via comparison with experimental results has often focused on bulk phases of materials [97, 101-107], but in recent years significant attention has turned to interfaces owing to their ubiquity in both natural and technological systems [24, 43, 51, 67, 108-113]. With its high surface sensitivity, XR is especially well-suited to meeting the validation task.

In this thesis, I present two distinct yet related efforts to advance our understanding of solid/water interfaces. I use XR as the primary experimental tool due to its unparallel ability to illuminate buried surfaces with atomic-scale resolution. In the first aim, I focus on the validation of FP calculations of solid/water interfaces via direct comparison with XR data and gain insights to how different approximations contribute to accurate (or inaccurate) predictions of interfacial structures (Chapter 4). This study establishes a protocol for the future validation of other solid/liquid interfaces and using additional FP methodologies not explored in this work. In the second aim, I investigate the EDL structure adsorbed on a planar graphene electrode by pairing electrochemical probes with XR measurements (Chapter 5). I begin with a study of water adsorption on graphene in the absence of ions and then adapt established resonant XR methods to probe the GC diffuse double layer. I end by discussing possible reasons for the significant discrepancy between the observed EDL structure and the expectation from the electrochemical measurements.

Chapter 2: Aqueous Solutions at Interfaces

2.1: Interfacial Water Structure

Molecular-scale density oscillations of liquids at solid/liquid interfaces were first predicted by Monte Carlo [114] and molecular dynamics (MD) [115] simulations in the 1980s with simulations of water between rigid walls and next to a general hydrophobic surface, respectively. In the following decades, MD simulations of water adjacent to planar Pt [116] and quartz [117] and on TiO_2 nanoparticles [118], among others, all showed similar water density oscillations. The first experimental observations of interfacial liquid density oscillations occurred in the mid-1990s with measurements of interfacial water on gold [119], liquid mercury/vapor [120], liquid gallium/molybdenum [121], and liquid Ga/diamond [122], all using X-ray reflectivity (XR). These were soon followed in the early-to-mid 2000s by XR measurements of water layering on peptide thin films [123], muscovite mica [65, 124], and other geochemically relevant oxide surfaces [125]; neutron diffraction measurements of water layering on clay [126]; and electron diffraction observations of water layering on silicon [127]. Thus, density oscillations are well-established as a general phenomenon of interfacial liquids at the boundary with a material of a different phase (i.e., solid or vapor), and XR in particular is a versatile probe for exploring these structures.

Water layering at surfaces is related to the surface reactivity. For example, a first hydration layer closer to a solid surface indicates a stronger interaction with water that may be driven by an intrinsic surface charge and cavity sites [65] (Figure 2.1a) or under-coordinated ionic species on the substrate and an ability to form hydrogen bonds (HBs) with the surface [27, 108] (Figure 2.1c,d). Conversely, a hydration layer farther from the substrate leads to a low-density space between the

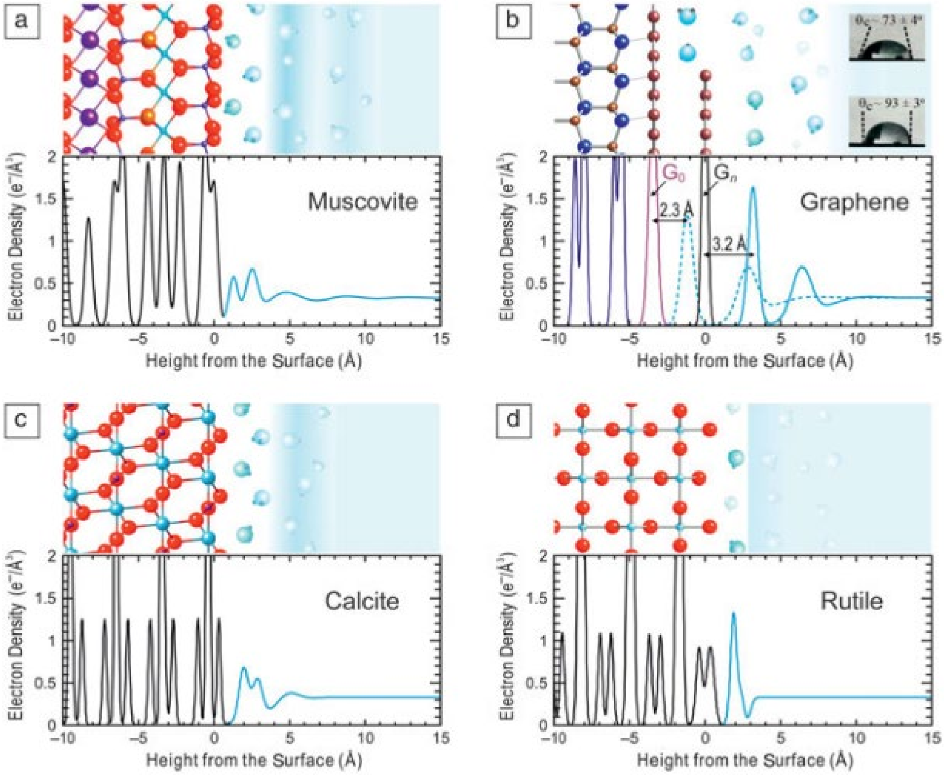

Figure 2.1. Solid/water interface schematics and electron density distributions derived from X-ray reflectivity experiments showing molecular layering of water at the (A) muscovite mica (001) [65], (B) graphene with water contact angle measurements inset [67], (C) calcite (104) [101], and (D) TiO_2 (110) [27] interfaces. Reprinted from Ref. [40].

solid and water, termed the "hydrophobic gap" [25, 37-39, 128] (Figure 2.1b). These structural variations are associated with differences in wettability on the macroscopic scale, as demonstrated for the case of the technologically relevant and hydrophobic two-dimensional (2D) material graphene [45] using water contact angle measurements (Figure 2.1b inset) [67]—the angle a water droplet forms with the graphene surface increases for thicker, more hydrophobic graphene samples. In general, the water contact angle is smaller for a hydrophilic surface than for a hydrophobic surface (Figure 2.2).

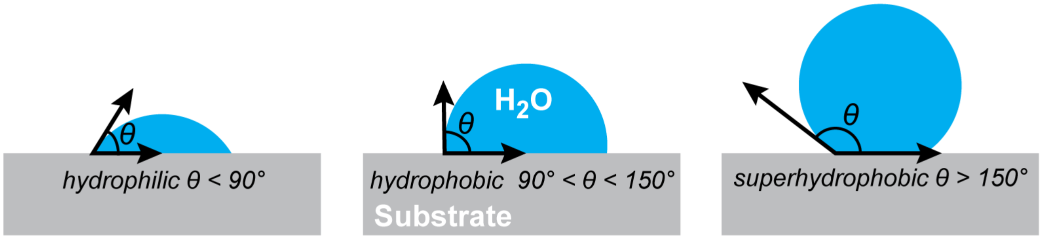

Figure 2.2. Hydrophobicity illustrated by water contact angle.

From the measured interfacial structures, we can see that the HB network of bulk water must be disrupted at an interface, which gives rise to the well-defined density oscillations. We can also see that this disruption can extend several molecular layers from an interface (i.e., ~10 Å where the size of a water molecule is approximately ~2 Å), with a dependence on the nature of the solid surface (Figure 2.1 [40]). Vibrational sum frequency generation (SFG) has shown that the presence of an interface can lead to dangling OH groups and a high surface energy [129]. It is reasonable to expect that water molecules would then reorient to reduce the free energy of the system, leading to a suppression of the random dipole fluctuations that are seen in bulk water. This suppression of dipolar fluctuations has been predicted by MD simulations [44, 117, 130-132] and can be inferred from SFG [43, 53, 133] and other spectroscopic measurements [134, 135]. The change in the HB network at the interface is directly related to the interfacial dielectric permittivity via the water dipole as [136]

$$\frac{\epsilon}{\epsilon_0} = \frac{\mathbf{P}}{\epsilon_0 \mathbf{E}} + 1 \qquad 2.1$$

where $\epsilon_0 = 8.85\times10^{-12}$ F/m is the permittivity of free space, $\mathbf{P} = \langle \mathbf{p} \rangle$ is the polarization field due to the average dipole moment of all water molecules within a small volume near the interface, $\mathbf{E}$ is the local electric field, and the quantity ϵ/ϵ_0 is usually denoted simply as the dielectric "constant" by ϵ. Specifically, the presence of an interface has been shown to reduce the dielectric constant along the direction of the surface normal up to several molecular layers from a surface This dielectric decrement appears to be a universal phenomenon that has been observed by experiments and simulations with a magnitude that depends on the nature of the surface (i.e., hydrophobic [44, 46] versus hydrophilic [117, 134, 137]). Given that the dielectric permittivity is a measure of a medium's ability to transmit an electric field (see Eq. 2.1), this can directly reduce Coulombic interactions between charges near surfaces (i.e., $F = q_1q_2/(4\pi\epsilon\epsilon_0r^2)$ is the force between two ions where $q_1$and q_2 separated by a distance r) and reduce the interfacial capacitance in an electrochemical system [131]. In the case of an ideal parallel plate capacitor with surface area, A, and separation between parallel plates, d, the capacitance is directly related to the dielectric permittivity as

$$C = \frac{\epsilon\epsilon_0A}{d}. \qquad 2.2$$

To complicate this interfacial picture, the presence of ions have been found to change the dielectric decrement, with a dependence on the ion type [137, 138]. It is clear that a robust characterization of water structuring and HB networks at charged surfaces is essential to understand ion adsorption and electrochemical charge storage.

2.2: Electrical Double Layer Theory

2.2.1: Mean Field Poisson-Boltzmann Theory

The charge distribution $\vec{\rho}$ in a dielectric medium with permittivity ϵ is related to the second derivative of the scalar potential field V felt by the charge according to the Poisson equation,

$$\vec{\nabla}^2 V = -\frac{\vec{\rho}}{\epsilon\epsilon_0}. \qquad 2.3$$

For a planar charged surface (e.g., an electrode) in contact with an aqueous solution, we assume that the potential varies only along the surface normal direction (i.e., $\hat{z}$) and is uniform in the lateral direction (i.e., $\hat{x}$ and $\hat{y}$) such that the Eq. 2.3 can be simplified to the one-dimensional case,

$$\nabla_z^2 V(z) = -\frac{\rho(z)}{\epsilon\epsilon_0}. \qquad 2.4$$

The simplest theory for the double layer charge distribution is that of a specifically adsorbed layer of ions adjacent to the surface as described by Helmholtz [70]. This model describes an ideal parallel plate capacitor in which the surface charge is compensated fully by the adsorbed ions. However, the Helmholtz model neglects thermal fluctuations of ions, which are essential to the description of any system at finite temperature. To account for such effects, the charge distribution in the electrolyte may be defined according to Boltzmann statistics, which treats the charges (e.g., ions) as non-interacting point particles. Thus, the concentration gradient of cations and anions are independent from one another and can be defined, respectively, as

$$c^+(z) = c_0^+ \exp\left(-\frac{W^+(z)}{k_B T}\right) \qquad 2.5a$$

$$c^-(z) = c_0^- \exp\left(-\frac{W^-(z)}{k_B T}\right) \qquad 2.5b$$

where a superscript '+' indicates the cation and a superscript '−' indicates the anion, $c_0^{+,-}$ is the bulk ion concentration, $W^{+,-}$ is the work required to move the ion to position z from infinity, $k_B = 1.38 \times 10^{-23}\ \mathrm{m^2kg/s^2K}$ is the Boltzmann constant, and T is the temperature; a useful point of comparison is that at room temperature ($T \sim 300$ K), $k_B T \approx 25.8$ meV. If we assume that ion adsorption near a charged surface is driven only by electrostatic interactions due to that surface, then $W(z) = qV(z)$ where q is the charge on the ion equal to $\mp ve$ (i.e., the valence, v, multiplied by the elementary charge, $e = -1.6022 \times 10^{-19}$ C). For a symmetric salt (e.g., RbCl), the bulk concentrations of anion and cation are equal, $c_0^+ = c_0^- = c_0$, and the charges are equal and opposite, $q^+ = v|e|$ and $q^- = -v|e|$. The net charge density in the interfacial double layer is

$$\begin{aligned} \rho(z) &= v|e|\left(c^+(z) - c^-(z)\right) \\ &= c_0 v|e|\left[\exp\left(-\frac{v|e|V(z)}{k_B T}\right) - \exp\left(\frac{v|e|V(z)}{k_B T}\right)\right] \end{aligned} \qquad 2.6$$

Combining Eq. 2.6 with Eq. 2.4 yields the Poisson-Boltzmann (PB) equation relating the double layer charge density distribution in a dielectric medium to the potential:

$$\nabla_z^2 V(z) = \frac{2c_0 v|e|}{\epsilon\epsilon_0}\sinh\left(\frac{v|e|V(z)}{k_B T}\right). \qquad 2.7$$

From here, we can determine the total charge in the double layer based on the bulk ion concentration and the potential of the charged surface V_0 (either due to an intrinsic charge or an applied potential). We enforce charge neutrality so that the total charge in the double layer equals the charge on the planar surface. From Gauss' law, we know that the surface charge is related to the electric field by $\int \vec{E} \cdot d\vec{a} = q/\epsilon\epsilon_0$, where $d\vec{a}$ is the differential area of an enclosed surface through which the electric field passes. For a charged, infinite plane (e.g., a uniform graphene electrode), the integration is straightforward, giving $EA = q/\epsilon\epsilon_0$ where A is the area of the charged plane, and the surface charge density is then $\sigma = E\epsilon\epsilon_0$. Recalling now that $E = -\nabla V$, we can relate the surface charge density to the adsorbed ion density distribution via Eq. 2.7 as outlined by Grahame [139]. Using the identity

$$\frac{\partial^2 V}{\partial z^2} = \frac{1}{2}\frac{\partial}{\partial V}\left(\frac{\partial V}{\partial z}\right)^2, \qquad 2.8$$

we equate the right-hand sides of Eqs. 2.7 and 2.8 and integrate over $V(z)$ with appropriate boundary conditions, namely $V(0) = V_0$ at the charged solid surface and $V(\infty) = 0$ in the bulk electrolyte, to arrive at

$$\nabla V = \frac{\partial V}{\partial z} = \sqrt{\frac{4c_0 k_B T}{\epsilon\epsilon_0}\left[\cosh\left(\frac{v|e|V_0}{k_B T}\right) - 1\right]}. \tag{2.9}$$

Then recognizing that $\cosh(2x) = \sinh^2 x + \cosh^2 x$ and $\cosh^2 x - \sinh^2 x = 1$ and combining with the surface charge from Gauss' law, we arrive at the Grahame equation:

$$\sigma = -\sqrt{8c_0\epsilon\epsilon_0 k_B T}\,\sinh\left(\frac{v|e|V_0}{2k_B T}\right) \tag{2.10}$$

where the minus sign indicates the equal but opposite charges on the charged surface and in the double layer.

As a final step, we can further simplify Eqs. 2.6, 2.7, and 2.10 by taking the limiting case of small potentials. The Taylor expansion of the exponential term in Eq. 2.6 (i.e., $e^x \approx 1 + x$) yields the linearized PB equation proposed by Gouy and Chapman [68, 69]

$$\nabla_z^2 V(z) = \frac{2c_0 v^2 e^2}{\epsilon\epsilon_0 k_B T} V(z) \tag{2.11}$$

wherein $V(z)$ can be solved for by the selection of an appropriate function that yields a second derivative equal to itself times a constant and which satisfies the aforementioned boundary conditions ($V(0) = V_0$; $V(\infty) = 0$). The result is that the potential decays exponentially from the charged surface into the bulk electrolyte as

$$\mathrm{V}(z) = \mathrm{V}_0 \exp\left[-\sqrt{\frac{2c_0 v^2 e^2}{\epsilon\epsilon_0 k_B T}}\, z\right]. \tag{2.12}$$

Substituting Eq. 2.12 into Eq. 2.11 and setting it equal to Eq. 2.4, we derive the charge density distribution of the *diffuse* ion profile at the interface,

$$\begin{aligned}\rho(z) &= -\frac{2c_0 v^2 e^2 \mathrm{V}_0}{k_B T} \exp\left[-\sqrt{\frac{2c_0 v^2 e^2}{\epsilon\epsilon_0 k_B T}}\, z\right] \\ &= \rho_0 e^{-z/\Lambda}\end{aligned} \qquad 2.13$$

where ρ_0 is the net ion density adjacent to the charged surface, dependent upon the surface potential, and Λ is the Debye length, i.e., the distance from the interface at which the electron density decreases to ρ_0/e, or roughly one third of its initial value,

$$\Lambda = \sqrt{\frac{\epsilon\epsilon_0 k_B T}{2c_0 v^2 e^2}}. \qquad 2.14$$

Similarly, Eq. 2.10 becomes

$$\sigma = -\frac{\epsilon\epsilon_0 V_0}{\Lambda} \qquad 2.15$$

The Debye length may be written in terms of the Bjerrum length, λ_B, which describes the distance between two charges at which they are effectively screened from each other—that is, the Coulombic interaction between the charges is balanced by the thermal energy:

$$\Lambda = \frac{1}{\sqrt{8\pi c_0 v^2 \lambda_B}} \qquad 2.16a$$

and

$$\lambda_B = \frac{e^2}{4\pi\epsilon\epsilon_0 k_B T}. \qquad 2.16b$$

For bulk water at room temperature ($\epsilon \approx 80$), $\lambda_B \approx 7$ Å. Notice that in the GC theory, the shape of the ion profile, defined by the decay length Λ, is a function only of the ionic strength of the solution, $I = \sum_i c_{0,i}(v_i e)^2/2$ where the sum is taken over all i ionic species. GC theory represents the simplest realistic model of the double layer (i.e., excluding the Helmholtz model) and, thus, serves as the point of reference for the analyses in this thesis. Nevertheless, it is important to understand its limitations.

To summarize, the assumptions made in the above derivation are the following:

1) Ions are non-interacting point particles. This requires a *dilute* electrolyte such that the electric field from each ion is sufficiently screened by the solvent molecules and, thereby, has no effect on other ions. It also implies that excluded volume effects (e.g., due to the solvation shell of each ion) are negligible. Consequently, ions can approach infinitely close to a charged surface.
2) The only force acting on the ions is that due to a nearby charged surface (e.g., an electrode). This is partly justified because we have assumed in (1) above that Coulombic interactions between ions are screened.
3) The dielectric medium (the solvent) has a spatially uniform permittivity ϵ—that is, a dielectric *constant*.
4) Ions do not specifically adsorb to the charged surface.
5) The charged surface is an idealized plane, i.e., with a uniform lateral charge density.

2.2.2: Beyond Poisson-Boltzmann

One can easily identify cases where the above assumptions fail. First, bare ions have finite radii that depend on their atomic number (e.g., $r[\mathrm{Rb}^+] > r[\mathrm{K}^+] > r[\mathrm{Na}^+]$), valence and sign (e.g., $r[\mathrm{Rb}^+] > r[\mathrm{Sr}^{2+}] > r[\mathrm{Y}^{3+}]$ and $r[\mathrm{Cl}^-] > r[\mathrm{Rb}^+]$), and molecular make-up (e.g., CO_3^{2-}, SO_4^{2-}) [140, 141]. This radius represents the distance of closest approach of an ion to the surface. Ions in the double layer are surrounded by a solvation shell (specifically a hydration shell in water), which increases the effective size to $r_{\text{ion}} + 2r_{\text{solvent}}$. Then an ion may adsorb with or without its solvation shell in outer sphere (OS) and inner sphere (IS) complexes, respectively. In the latter case, the system must overcome a free energy cost of ion desolvation where the hydration energy depends strongly on the ion [142] and scales as the square of the valence of the radius, ν^2/r [143]. This leads to ion-specific effects, which are also neglected in the GC derivation. Stern modified the GC model to allow for specific adsorption of ions, i.e., the Gouy-Chapman-Stern (GCS) model [71] (Figure 2.3), which may be modeled by a well-defined Gaussian ion distribution followed by the diffuse layer [144]. In the GCS model, the EDL is modeled as two discrete regions where the Stern layer (i.e., the specifically adsorbed layer) is treated as a simple parallel plate capacitor according

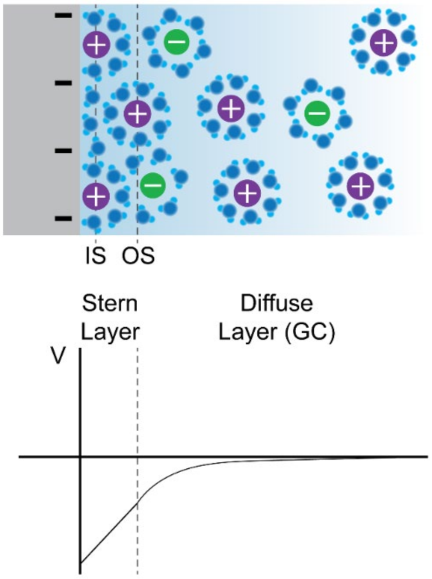

Figure 2.3. Top: electrical double layer schematic next to a negatively charged electrode, including specifically adsorbed (i.e., inner sphere, IS) and outer sphere (OS) adsorbed counterions (cations; purple) and co-ions (anions; green). Ions are shown with their hydration shells (water molecules in blue). Bottom: qualitative voltage profile from the electrode surface to the bulk liquid.

to Eq. 2.2 in series with the GC layer capacitance. Still, further modifications to the theory are required in order to accommodate hydration forces [81].

Second, the transition point from dilute to concentrated electrolyte is not well defined, but it is reasonable to expect that for some concentration the assumption of non-interacting ions (e.g., the assumption of Boltzmann statistics) breaks down. Both crowding due to the finite size of ions and electrostatic interactions between ions would become relevant, and the energy term, W, in Eq. 2.5 should include a free energy contribution from nearby charges in addition to that from the charged surface). Surface force probe measurements [60] suggest that for a simple monovalent salt, the limit of a dilute solution (based on divergence of the decay length Λ from the ideal GC case) is $\sim$1 M. For larger ionic liquids, the transition from the ideal GC model occurs for concentrations of $\sim$0.2 – 0.7 M [60]. Various modifications to the energy term in PB theory have been proposed to account for excluded volume effects [78, 80, 145] and ion polarizability effects [146]. In addition, the presence of asymmetric ions (i.e., anions and cations of vastly different radii or different valence) alters the EDL structure [147-149] with implications for charge storage capabilities. However, the relative contributions from entropic and electrostatic effects [145] is difficult to determine experimentally.

Third, as discussed in Chapter 2.1, the dielectric permittivity adjacent to the charged solid surface is reduced compared to the bulk value [41, 44, 46, 117, 137, 150]. MD simulations suggest that the dielectric permittivity is reduced along the electrode surface normal direction (i.e., $\epsilon_{\perp}$) but enhanced parallel to the surface [44, 131, 132], and the exact form of the dielectric tensor (i.e., the directional variation from interface to bulk) is still unknown. For water $\epsilon \sim 80$ in the bulk, but values as small as $\epsilon_{\perp} \approx 2$ have been reported within a few molecular layers of a charged graphene surface [46].

For purposes of this thesis, I assume that the surface charge density is uniform across the electrode surface. Heterogeneous surface charges are expected to influence the double layer structure through the generation of local displacement fields on the sample surface [151-153]. Epitaxial graphene grown on SiC, used as the electrode for these studies (see Chapter 5), displays variations in hydrophobicity across the sample surface depending on the graphene layer thickness [45]. Although this may affect the ion distribution on the length scale of the electrode surface (i.e., graphene) domains [153], any variation in adsorbed ion structure is expected to be small [154]. Furthermore, X-ray reflectivity probes the laterally averaged electron density (see Chapter 3), and therefore would not be sensitive to ion structuring parallel to the electrode surface.

Counterion condensation

The formation of an IS complex (i.e., a Stern layer) relies on counterions condensing at the electrode surface. Lau et al. [74] describe Stern layer formation as a result of fluctuation correlations of a charged plate in a dielectric medium with only counterions. They introduce three dimensionless parameters that completely describe the phenomenon of counterion condensation within their theory, which uses the formalism of the PB and GC theories. These parameters are the coupling constant (i.e., the strength of fluctuation correlations due to the charged surface), the reduced temperature related to the interactions between ions, and the order parameter (i.e., the fraction of counterions in the condensed phase), given, respectively, by

$$g \equiv \frac{\nu^2 \lambda_B}{\Lambda}, \tag{2.17a}$$

$$\theta \equiv \frac{a}{\nu^2 \lambda_B}, \tag{2.17b}$$

$$\tau \equiv \frac{\nu e n_c}{\sigma_0} \tag{2.17c}$$

where a is the ion radius, n_c is the charge density of condensed counterions, σ_0 is the charge density on the electrode, and all other variables are the same as described for the GC theory. They identify two modes of counterion condensation depending on the reduced temperature. Specifically, below a critical temperature θ_c, charge fluctuations play a significant role, and counterion condensation occurs as a first order phase transition at a critical value of g (Figure 2.4a). Meanwhile, the transition is continuous above θ_c.

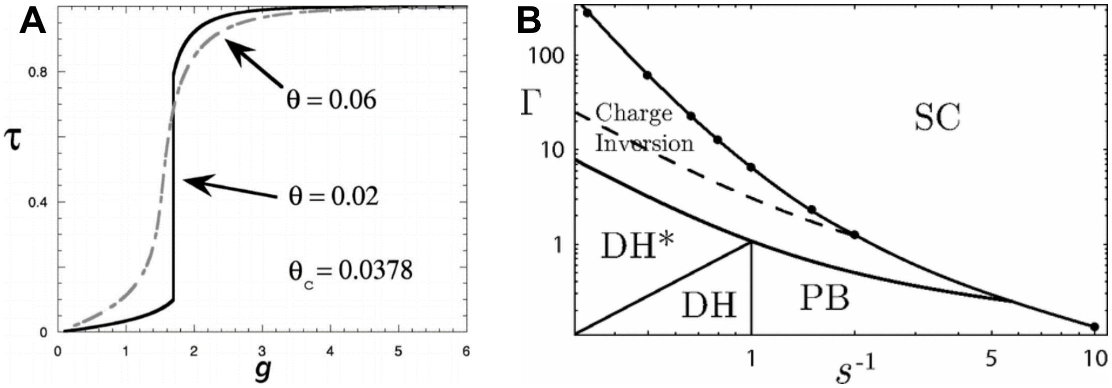

Figure 2.4. Deviations from PB theory. (A) Fraction of condensed ions, τ, at a charged surface increases with the order parameter, g. For reduced temperatures below a critical value, θ_c, counterions undergo a first order phase transition. Above θ_c, the phase transition is gradual. For $g \ll 1$, τ is well-described by PB theory. (B) Phase diagram of double layer as a function of $\Gamma \equiv \lambda_B/32\pi\Lambda$ and $s \equiv 4\nu/\Lambda\lambda_B\sigma_0$. DH: Debye-Hückel (essentially GC theory), SC: strong coupling, PB: Poisson-Boltzmann; DH* ($\Gamma > 1/s$) indicates a region with reduced effective surface charge but not charge inversion. Reprinted (A) with permission from Lau, Lukatsky, Pincus, and Safran, Phys. Rev. B, 65, 051502 (2002). Copyright 2002 by the American Physical Society. Ref. [74]. Reprinted (B) with permission from Lau, Phys. Rev. E, 77, 011502 (2008). Copyright 2008 by the American Physical Society. Ref. [158].

Charge Inversion, Overcharging, and Underscreening

In many cases, the buildup of charge in the double layer exceeds the nominal charge on the electrode surface. Two rationales for this observation are charge inversion and overcharging [155]. The first explanation describes a change in sign of the surface charge that is often attributed to a chemisorption process wherein ions specifically adsorb and undergo an electron transfer (i.e., a redox reaction). The second explanation results from physical ion-ion correlations within the double layer [83, 156]. Although charge inversion and overcharging are often considered as distinct phenomena, ionic correlations can be thought of as leading to an effective charge near a charged plate that alters the potential felt by other ions in the extended double layer. Ion-ion correlations are expected to lead to "charge inversion" in cases of high electrode surface charge (i.e., $> 10\ \mu C/cm^2$) and in electrolytes with di- or multi-valent ions [157] even in dilute conditions [83]. Ion correlations can also lead to an "anomalous" increase in the screening length (indicating that the surface charge is underscreened) compared to GC theory (i.e., the Debye length), which is related to the ion size, concentration, and solvent conditions [60, 84, 85].

In Chapter 5, I consider counterion condensation and charge inversion in addition to the limiting model of GC theory. The experiments are designed with the goal of capturing a diffuse double layer structure, but the limiting conditions of GC theory are not well-understood. Therefore, it is important to keep in mind the complex nature of ion adsorption to gain insights into the double layer structure under the experimental conditions described in Chapter 5. I use the counterion condensation theory of Lau et al. [74] as one point of comparison. Lau further expanded the theory to include co-ions (i.e., having the same charge as an electrode as in a real system) [158] and arrived at the phase diagram for the observation of GC, PB, and charge inversion, shown in Figure 2.4b, which serves as a second reference for the interpretation of our experimental measurements.

Chapter 3: Experimental Techniques

3.1: High Resolution X-ray Reflectivity

X-ray reflectivity (XR) is a quantitative and sensitive probe of the real-space structure of solid/liquid interfaces [40, 159-161]. The use of hard X-rays with photon energies E > 10 keV leads to macroscopic (> 1 mm) penetration lengths through water, enabling the measurement of XR signals from buried solid/liquid interfaces. At these energies, the X-ray wavelength $\lambda < 1$ Å is comparable to inter-atomic distances and can, therefore, directly probe the molecular-scale structure of an interface. The reflectivity signal R(**Q**), measured in reciprocal space, is the fraction of the incident beam that is reflected from the surface as a function of the scattering vector **Q**,

$$R(\boldsymbol{Q}) = T(\boldsymbol{Q})B(\boldsymbol{Q})X(\boldsymbol{Q})\left(\frac{4\pi r_e}{\boldsymbol{Q}A_{UC}}\right)^2 |F(\boldsymbol{Q})|^2 \qquad 3.1$$

and

$$\begin{gathered} \boldsymbol{Q} = \mathbf{K_f} - \mathbf{K_i} \\ |\boldsymbol{Q}| = \frac{4\pi}{\lambda}\sin\left(\frac{2\theta}{2}\right) \end{gathered} \qquad 3.2$$

where $\mathbf{K_f}$ and $\mathbf{K_i}$ are the momentum vectors of the reflected and incident X-rays, respectively, controlled by the X-ray wavelength and the scattering angle 2θ between incident and reflected X-rays (see Figure 3.1a); T(**Q**) describes the **Q**-dependent transmission of the X-ray beam through the sample cell (e.g. influenced by the pathlength of X-rays through a thick water layer); B(**Q**) < 1 is a surface roughness factor resulting in a reduction of the scattered intensity relative to that from a perfectly smooth surface; X(Q) combines any necessary corrections for the detector resolution and the active area of the sample exposed to X-rays (dependent upon the sample size, X-ray beam area, and incident angle); $r_e = 2.818\times10^{-5}$ Å is the classical electron radius; and A_{UC} is the unit cell area

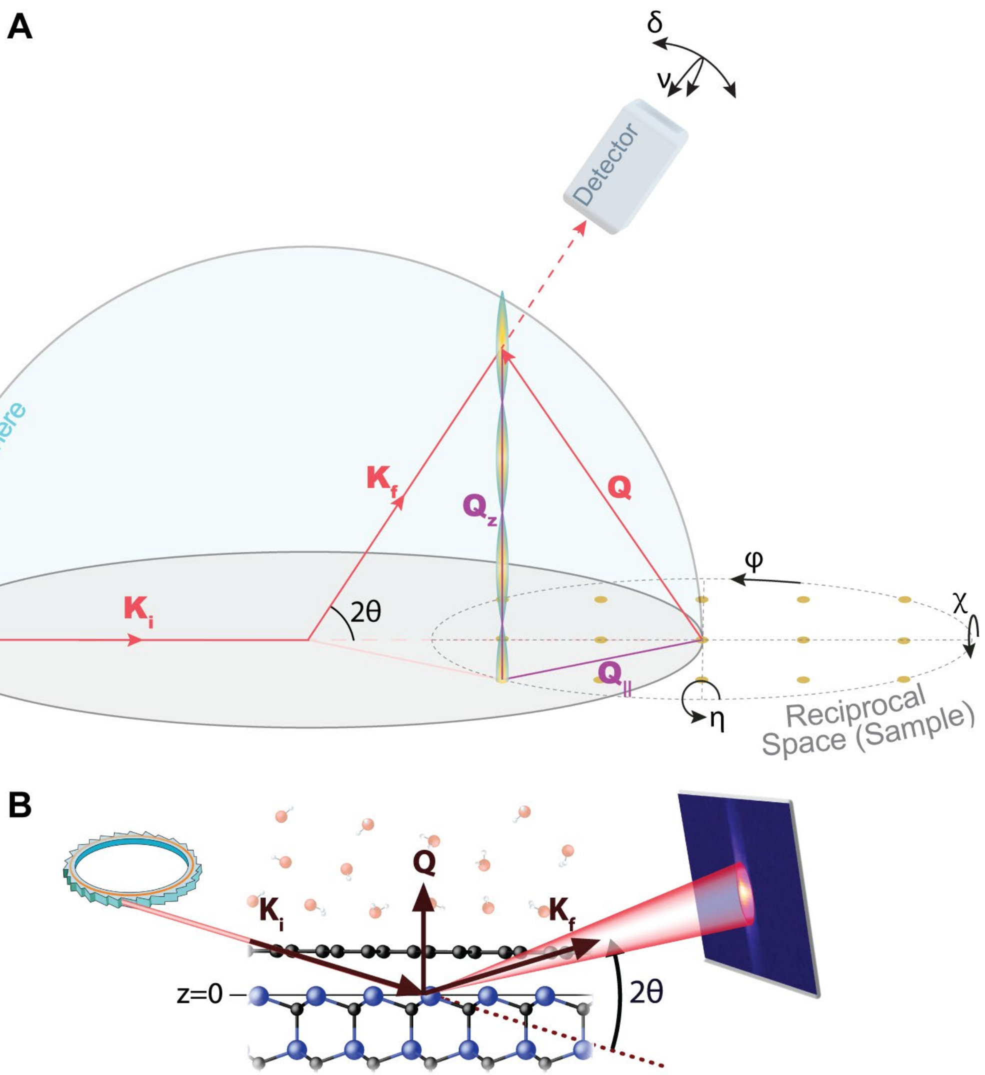

Figure 3.1. X-ray reflectivity (XR) schematics. (A) The XR signal measured at the detector (controlled by angles δ and ν) depends on the intersection of the Ewald sphere with the reciprocal lattice of the sample (with rotational degrees of freedom $\eta, \chi,$ and ϕ). The physical sample sits at the vertex of the incident and reflected X-ray vectors, $\mathbf{K_i}$ **a**nd $\mathbf{K_f}$, respectively. The detector is positioned to probe the scattering condition $\mathbf{Q} = \mathbf{K_f} - \mathbf{K_i} = \mathbf{Q}_{||} + \mathbf{Q}_z$ where $\mathbf{Q}_{||}$ and $\mathbf{Q_z}$ are the in-plane and specular (vertical) momentum transfers, respectively; the scattering angle 2θ is indicated. The $\overline{2}\overline{1}L$ crystal truncation rod is shown. (B) Specular XR ($\mathbf{Q} = \mathbf{Q_z}$), shown for the specific case of the water/graphene/SiC interface (oxygen atoms shown in red, hydrogen atoms in white, carbon atoms in black, and Si atoms in blue), measures the vertical structure (i.e., perpendicular to the substrate surface). The SiC substrate is located at $z \leq 0$; left: synchrotron schematic; right: Pilatus area detector image from experiment at APS.

of the solid surface. F(**Q**) is the complex structure factor equal to the Fourier transform of the electron density $\rho(\boldsymbol{r})$ [162] at along the scattering condition, **Q**,

$$F(\boldsymbol{Q}) = \int_{V} \rho(\boldsymbol{r}) e^{i\boldsymbol{Q}\cdot\boldsymbol{r}} d^3 r \qquad 3.3$$

integrated over the entire volume *V* scattering X-rays.

For a crystalline system, the electron density is localized at discrete lattice points (i.e., atoms in a crystal lattice) with position $\boldsymbol{r} = x\boldsymbol{a} + y\boldsymbol{b} + z\boldsymbol{c}$. Here, (x,y,z) are the fractional coordinates of an atom with respect to the unit cell lattice vectors **a**,**b**,**c**. Similarly, **Q** can be written in terms of the Miller indices HKL [162],

$$\boldsymbol{Q} = 2\pi(H\boldsymbol{a}^* + K\boldsymbol{b}^* + L\boldsymbol{c}^*) \qquad 3.4$$

where **a***, **b***, **c*** are the reciprocal lattice unit vectors. For a bulk crystal, the observed scattering occurs at discrete values of the Miller indices. The structure factor can then be written as a discrete sum over each atom *j* as

$$F(\boldsymbol{Q}) = \sum_{j} f_j(\boldsymbol{Q})\, e^{i\boldsymbol{Q}\cdot\boldsymbol{r}_j} e^{-\frac{(\boldsymbol{Q}\cdot\boldsymbol{u}_j)^2}{2}} \qquad 3.5$$

where f_j is the element-specific form factor (FF) [163] accounting for the Q-dependent decay in the scattering strength due to the spatial distribution of electrons surrounding each atom, and $e^{-(\boldsymbol{Q}\cdot\boldsymbol{u}_j)^2/2}$ is the Debye-Waller (DW) factor accounting for the thermal fluctuations (with root mean square, r.m.s., width $\boldsymbol{u_j} = u_{j,x}\hat{x} + u_{j,y}\hat{y} + u_{j,z}\hat{z}$) of an atom about its mean position. The FF carries the same functional form as the structure factor, namely the Fourier transform of the electron density (Eq. 3.3) but this time describing the electron cloud around a single nucleus rather than the electron density of the larger system. Thus, larger atoms (i.e., with more electrons) scatter X-rays more intensely than lighter atoms.

The scattering of X-rays from the bulk crystal lattice planes gives rise to intense Bragg peaks at **Q** corresponding to integer multiples of the Miller indices with a corresponding lattice spacing d_{HKL} along the scattering direction. When the symmetry of an infinite bulk lattice is broken, e.g., by introducing an interface, a continuous rod of weak intensity is observed between the Bragg peaks in a form known as a "Crystal Truncation Rod" (CTR) [159, 164]. The CTR structure factor takes the form of a geometric series as [159]

$$F_{CTR} = \frac{1}{1 - e^{-i\boldsymbol{Q}\cdot\boldsymbol{d}_{HKL}}} \qquad 3.6$$

where the negative sign in the exponential term results from taking the crystal to be semi-infinite in the negative direction (i.e., the crystal surface is at the origin). The XR intensity from a solid/liquid interface arises from the coherent interference between the structure factor contribution from the bulk crystal, the interfacial region (e.g., the surface of the truncated substrate crystal and the adjacent fluid), and the bulk liquid. The **Q**-dependent intensity of the CTR is directly sensitive to the deviations of the interfacial structure from the expected bulk structure. These changes include displacements of solid surface layers from their expected bulk positions resulting from the termination of the infinite crystal and ordering of the liquid near the solid surface [40, 159].

The resolution of an XR probe is inversely related to the magnitude of the maximum scattering vector of the measurement as $\sim\pi/|\mathbf{Q}_{\max}|$. Low angle XR (denoted as XRR) spans a few degrees in 2θ, (i.e., the region below the first Bragg peak), and is useful to resolve the nanoscale structure of an interface, such as the thickness and density of a thin film layer. Such measurements can be carried out using rotating anode tube sources whose maximum flux is limited to $\sim 10^8$

photons/s. R(**Q**) decreases as $\mathbf{Q}^{-4}$ (see Eq. 3.1 and note that the $|F|^2$ term carries an additional Q^{-2} resulting from the angular charge distribution), so in practice measurements performed with tube sources are limited to low-angle as the signal-to-noise ratio quickly decreases (e.g., with a Cu target, $\lambda_{K\alpha}$ = 1.54 Å, $Q_{max} < 1$ Å^{-1}). Conversely, the flux on the sample at a synchrotron source such as the Advanced Photon Source can be up to $\sim 10^{13}$ photons/s depending on the specifics of the synchrotron device (i.e., an undulator versus a bending magnet source) and of the beamline, such as the energy spread of the beam (e.g., monochromatic versus polychromatic beams), the selected energy, and the use of any filters. With such a high incident flux, the reflected signal even at low-reflectivity scattering conditions can be measured. High angle measurements through multiple Bragg peaks are possible, i.e., with Q_{max} exceeding 5 Å^{-1} (depending on sample considerations, such as the density and roughness), leading to sub-Å (atomic) resolution of the interface structure. The spectral brightness of conventional and synchrotron sources is compared in Figure 3.2 [165].

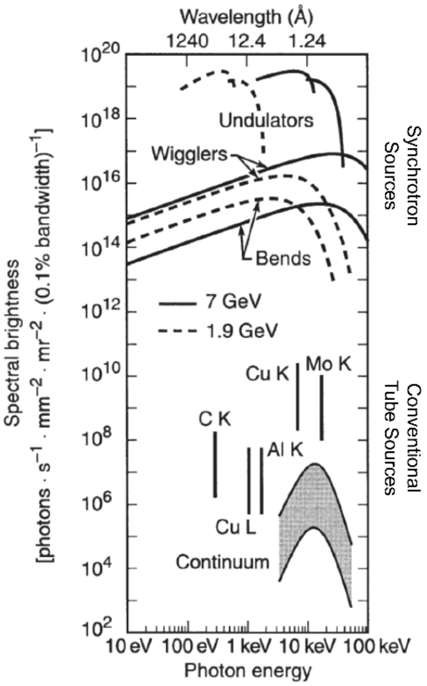

Figure 3.2. Spectral brightness of conventional X-ray tube sources (lower half) versus synchrotron sources (upper half) as a function of X-ray photon energy. The characteristic radiation from tube sources have a fixed energy while synchrotrons emit a range of photon energies with intensities dependent upon the type of source (undulator, wiggler, or bending magnet). Tube sources also emit a continuum of Bremsstrahlung radiation but with much lower brightness. Adapted from Ref. [165].

3.1.1: Specular X-ray Reflectivity and General Data Analysis Approach

As shown in Figure 3.1a, the scattering vector can be separated into perpendicular and parallel components $\mathbf{Q_z}$ and $\mathbf{Q_{||}}$, corresponding to specular (i.e., mirror-like) and non-specular reflections, respectively. Specular XR (Figure 3.1b) measures the electron density distribution along the substrate surface normal direction $\hat{\mathbf{z}}$ while non-**s**pecular measurements are sensitive to both the vertical and in-plane structures. In this thesis, I primarily consider specular XR where the scattering vector is oriented along $\hat{\mathbf{z}}$ with Miller indices H = K = 0 and magnitude Q = $|\mathbf{Q_z}|$. A specular measurement is carried out with detector angle ν fixed at zero, and the vertical angles δ =

2η (see angles in Figure 3.1a) are adjusted to probe the specular truncation rod in the scattering plane defined by the **K_f** and **K_i** vectors, as in Figure 3.1b. Except for small incident angles where the X-ray beam footprint may exceed the sample dimensions (thereby requiring an active area correction), the prefactor X(Q) in Eq. 3.1 is usually unity.

The specular XR signal R(Q) probes the laterally averaged (i.e., over the x- and y-directions) electron density $\rho(z)$. The structure factor of Eqs. 3.3 and 3.5 can now be rewritten in a one-dimensional form in several equations relevant for this thesis:

$$F(Q) = \int_{-\infty}^{\infty} \rho(z) e^{iQz} dz \qquad 3.7a$$

$$= \sum_{j=1}^{N_{elements}} f_j(Q) \int_{-\infty}^{\infty} n_j(z) e^{iQz} dz \qquad 3.7b$$

$$= \sum_{j=1}^{\infty} f_j(Q) \Theta_j e^{iQz_j} e^{-\frac{Q^2 u_j^2}{2}}. \qquad 3.7c$$

Eq. 3.7a allows for the calculation of XR signals directly from a known or simulated electron density distribution, such as that predicted by a first principles molecular dynamics (FPMD) calculation in which the electron distribution is explicitly computed (see Chapter 4). Eqs. 3.7b and 3.7c both describe the structure factor in terms of FFs f_j and the atomic density distribution: in Eq. 3.7b, the atomic density is treated as a continuous number density distribution of each element j, $n_j(z)$, and the sum is taken over all N elements in the system (i.e., Al, O, and H for the case of the Al_2O_3/H_2O interface or Si, C, O, and H for the SiC/EG/H_2O interface); in Eq. 3.7c, the atomic density is given in terms of the individual, discrete atomic layers, j, where Θ_j is the layer occupancy per substrate unit cell area (A_{UC}), z_j is the layer height relative to some reference plane (typically the surface-most substrate layer), and u_j is the r.m.s. layer width in the z-direction.

Ideally, one would be able to retrieve the electron density distribution exactly from an XR measurement via inverse Fourier transform. However, because the reflected intensity measures the modulus square of the structure factor (Eq. 3.1), the phase information, i.e., related to the positional arrangement of atoms and electrons in the system, is lost (the so-called “phase problem”). Therefore, in practice, the electron density profile across an interface is determined through model-dependent analysis of the XR data. Specifically, the electron density distribution is modeled as a series of Gaussians describing each atomic layer *j* with parameters of coverage, height, and r.m.s. width as described above for Eq. 3.7c,

$$\rho_{eff}(z) = \sum_j \frac{Z_j \Theta_j}{u_j \sqrt{2\pi}} e^{\frac{-(z-z_j)^2}{2u_j^2}} . \qquad 3.8$$

Here, the “effective” electron density distribution $\rho_{eff}(z)$ is indicated because the Gaussian distribution is multiplied by the layer atomic number Z_j, which does not account for the spatial distribution of electrons around an atomic core (FF are used for this purpose). Electron densities derived from model-dependent analyses are typically reported according to Eq. 3.8, but the full electron density can be represented more accurately as the convolution of the atomic number density profiles with the inverse Fourier transform of the FFs:

$$\rho(z) = \sum_j \left(\int_{-\infty}^{\infty} f_j(Q) e^{-iQz} dQ \right) * n_j(z). \qquad 3.9$$

In this thesis, I mainly present effective electron density distributions according to standard practice (Eq. 3.8), which also facilitates comparisons between simulated *atomic* distributions and those derived from experimental analysis. In addition, I include the electron densities according to Eq. 3.9 for comparisons with FPMD simulations and explicitly explore the role of the assumption of various FF in Chapter 4.

The structure factor for any set of model input parameters (Eq. 3.8 with the appropriate tabulated FF f_j substituted for the atomic number Z_j) is calculated according to Eq. 3.7c. The accuracy of the model is then evaluated using a χ^2 ("chi-squared") goodness-of-fit metric,

$$\chi^2 = \frac{1}{N} \sum_{Q_0}^{Q_{max}} \left(\frac{R_{meas}(Q) - R_{calc}(Q)}{\sigma(Q)} \right)^2 \qquad 3.10$$

where N is the number of data points and R_{meas}, R_{calc}, and σ are the measured reflectivity, calculated reflectivity from the model, and experimental uncertainty, respectively. $R_{calc}(Q)$ is calculated via Eq. 3.1 with the model structure factor determined via Eq. 3.7c. The model parameter values (z_j, Θ_j, and u_j) are optimized via an iterative non-linear least-squares fitting procedure in which the parameters are adjusted until χ^2 converges. A perfect fit to the data and its associated uncertainties would result in $\chi^2 = 1$.

The XR data analysis approach described here typically makes the implicit assumption that atomic FFs (i.e., those for neutral atoms) accurately describe the electron distributions surrounding each atom. However, the assumption of atomic FF may not always be accurate especially at interfaces where covalent bonding, charge transfer, and electronic delocalization may alter the electron density distribution around an atomic core. In such cases, ionic FF may be suitable. I briefly explore the use ionic FF in Chapter 4.6, but further validation of their applicability (outside the scope of this thesis) is needed.

Finally, the surface of a real crystal is never perfectly smooth (though it may be sufficiently small to be negligible), resulting in a reduced specular scattering intensity compared to the ideal case (Figure 3.3a). An extrinsic roughness parameter may be required for an accurate interpretation of the data. In this thesis, I use the Robinson roughness [166], which models the substrate surface as a series of layers with decreasing partial coverage moving away from the bulk substrate (Figure 3.3b). The first partial layer has fractional coverage β, the subsequent layer has coverage β^2, the next layer occupancy is β^3, etc. Altogether, the roughness factor B(Q) in Eq. 3.1 is given by

$$B(Q) = \frac{1-\beta^2}{1+\beta^2-2\beta\cos(Qc)} \tag{3.11}$$

which translates to a root-mean-square (r.m.s.) roughness of

$$\sigma_{rms} = \frac{\sqrt{\beta}}{1-\beta}c. \tag{3.12}$$

In some cases, either with very small roughness or significant covariance of β with other parameters (such as the occupancy of partial coverage thin film layers), β can converge to zero with a large uncertainty.

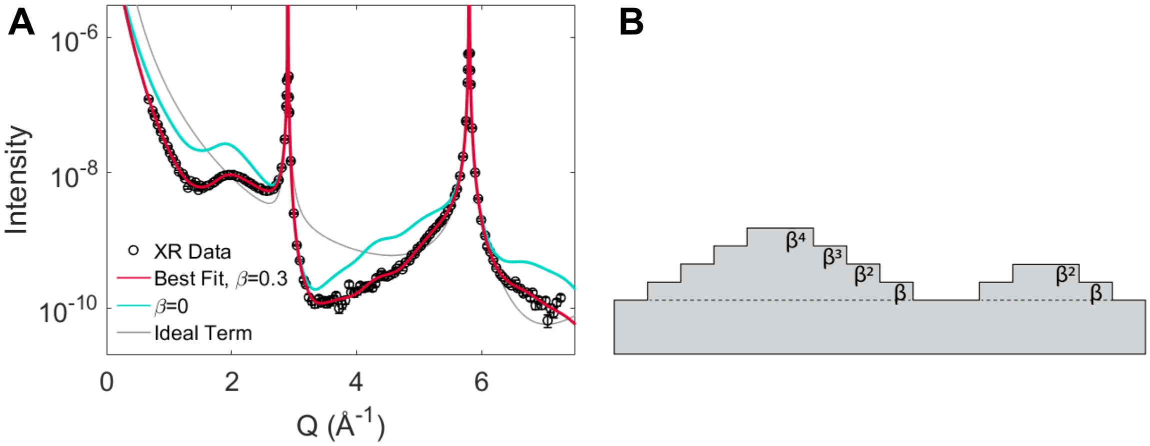

Figure 3.3. Effect of surface roughness on X-ray reflectivity. (A) experimental data with 1σ uncertainties (black circles) for the alumina/water interface (see analysis in Chapter 4) plotted with the reflectivity expected from an ideally-terminated alumina substrate (gray line), the best-fit to the data with roughness parameter $\beta = 0.3$ (red line), and the reflectivity obtained from a structural model with $\beta = 0$ and all other parameters fixed at their best-fit values (turquoise line). (B) Robinson roughness schematic adapted from Ref. [166]; the horizontal dotted line separates the ideal substrate from the rough surface.

3.1.2: Off-specular X-ray Reflectivity

Off-specular XR measurements can be used to probe the in-plane structure of a solid/water interface. Several off-specular CTRs are usually measured to adequately sample reciprocal space. The measurement is similar to the specular case in that H and K are fixed as the detector is scanned vertically to measure the HKL rod, but for an off-specular measurement, $\nu \neq 0$, as shown in Figure 3.1a (the $\overline{2}\overline{1}L$ rod of the reciprocal map is depicted). The sample (equivalently, the reciprocal space) angles and the detector angles must be calculated for the desired HKL, which is non-trivial and can vary depending on the mode used for the measurement—e.g., the incident angle may be fixed and only the detector is moved, or the sample and detector rotation may both vary. Off-specular XR data presented in this thesis were measured with the assistance of Dr. Zhan Zhang, beamline scientist at APS Sector 33-ID-D, using the first method wherein the sample angle was fixed (fixed

$\mathbf{K}_i$), and the required detector angles were calculated using beamline macros after defining two directions of an orientation matrix (defining the specular 001 and one in-plane direction).

The interpretation of off-specular XR data is similar to the method used for the specular analysis, but with some additional requirements. **Q** and F(**Q**) are defined in the general form in terms of the Miller Indices (Eqs. 3.4 and 3.5), active area and detector resolution corrections (X(**Q**) in Eq. 3.1) are often required [159], and the electron density must account for each atom individually rather than treating $\rho(x, y, z)$ as laterally-averaged layers. That is, the coverage of each atom j is the same, $\Theta_j = 1$, and in the substrate crystal, the position parameters are defined as a three-dimensional matrix of fractional coordinates x_j, y_j, z_j of each atom with respect to the lattice constants **a**, **b**, and **c**. The analysis of off-specular data is more complex than the specular case, requiring many more structural parameters. However, the full suite of measurements for a sample (including off-specular and specular CTR data) must provide a consistent picture of the solid/water interface. Therefore, acquiring many off-specular CTRs provides some redundancy to constrain the parameter space. Off-specular XR is not a focus of this thesis, but measurements of the alumina/water interface are included at the end of Chapter 4 with a brief, qualitative interpretation of the data with regard to their deviation from an ideally-terminated substrate crystal.

3.2: Resonant Anomalous X-ray Reflectivity

Various methods have been developed to solve the phase problem, each with its own strengths and weaknesses. These include X-ray standing waves [167], ptychography [168], various phase retrieval/inversion algorithms [169-171], and spectroscopic approaches, such as resonant anomalous X-ray reflectivity (RAXR) [172-174]. RAXR combines the structural information of

XR with the chemical information of X-ray absorption spectroscopy to discern the location of a specific element of interest (i.e., a resonant ion) that may otherwise be difficult to distinguish from the surrounding sea of electrons, such as that arising from water. This method has been used previously to resolve the structure of aqueous adsorbates at several mineral-water [15, 144, 175-182] and electrified metal-water interfaces [183] and is employed in this thesis to measure the EDL structure. As outlined in Chapter 2, the classical model of the EDL follows PB theory, which describes a dilute electrolyte—e.g., 0.1 M RbCl used in the experiments presented in Chapter 5. Because X-rays scatter from all electrons in the system, the dominant contribution to the reflectivity from the electrolyte will come from the water (specifically the O atoms), which has an effective molar density of 55 M, effectively masking the EDL. However, the X-ray photon energy can be tuned to an absorption edge of the element of interest (Rb^+ in this case) to increase its relative contribution to measured reflectivity. Whereas conventional X-ray tube sources produce characteristic X-rays at a fixed energy, synchrotron sources (e.g., an undulator or bending magnet) emit X-rays at a range of energies (Figure 3.2) that can be selected by carefully tuning a monochromator. Thereby, the photon energy can be scanned (or stepped) during an experiment, enabling a RAXR measurement.

As with X-ray absorption spectroscopies, such as X-ray absorption near edge structure (XANES) [184], RAXR exploits the energy-dependent change in the elastic scattering cross-section due to the photoabsorption of X-rays by electrons in discrete atomic core levels, providing a fingerprint unique to each atom (or ion). The photoabsorption process is depicted in Figure 3.4a with the standard nomenclature of K-edge, L-edge, and M-edge electrons describing bound electrons with principal quantum numbers n = 1, 2, and 3, respectively (i.e., 1s, 2s-2p, and 3s-3d electrons where s, p, and d refer to the orbital quantum numbers $l = 0$, 1, and 2, respectively). K-edge absorption energies occur at the highest energies as these are the most tightly bound electrons, requiring more energy to eject from their bound state. In general, the X-ray absorption cross-section, σ_a, of a material is inversely proportional to the cube of the X-ray photon energy, $\sigma_a \propto E^{-3}$. However, at an absorption edge, an additional pathway to absorb photons becomes available, leading to discontinuous increase in the absorption cross-section (Figure 3.4b).

We can expand on the simple description above by treating the electrons as harmonic oscillators bound in the potential energy well of the nucleus [162]. The equation of motion of a

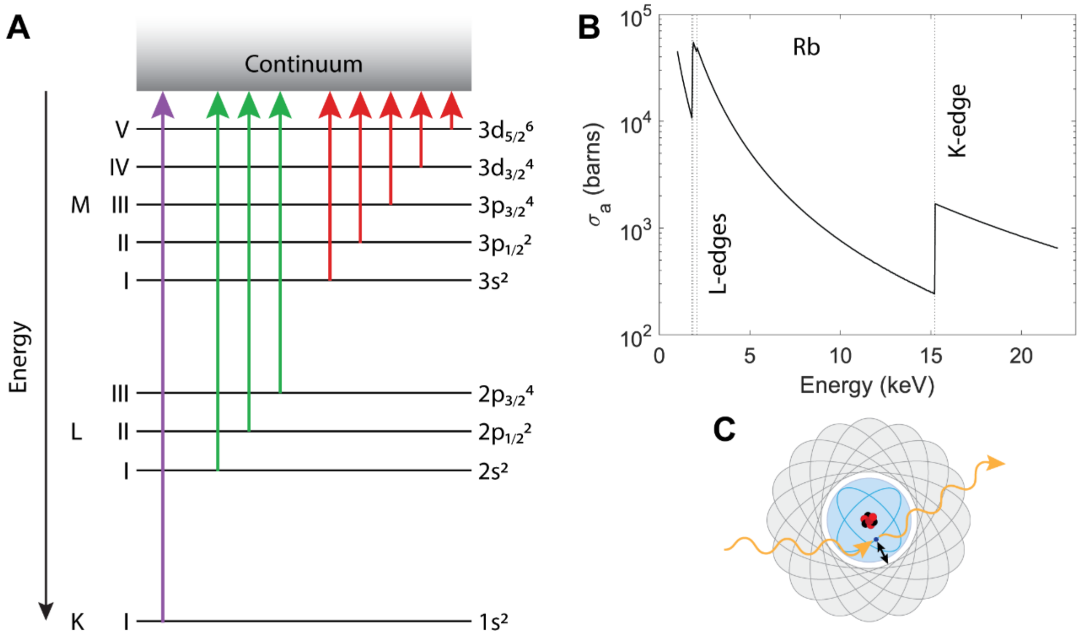

Figure 3.4. Basics of X-ray absorption and resonant scattering. (A) Energy level diagram showing absorption transitions from the K-, L-, and M-shell electrons to the continuum states; the electrons corresponding to the edges are labeled as nl_j^g where n, l, and j are the principal, azimuthal angular momentum, and total ($l + s$, where s is the spin) angular momentum quantum numbers, respectively, and $g = 2j + 1$ is the multiplicity. (B) Absorption cross-section of Rb versus incident X-ray energy with L- and K-edge energies labeled (1 barn = 10^{-28} m^2). (C) Resonance schematic showing incident photons, electron excitation and relaxation back to ground state, and emitted photon. ((a) adapted from Ref. [162]).

bound electron subject to the driving force of the incident X-rays is

$$\ddot{x} + \Gamma\dot{x} + \omega_0^2 x = \frac{e\mathcal{E}_0}{m} e^{-i\omega_\gamma t} \qquad 3.13$$

where m is the electron mass, Γ is the damping coefficient, ω_0 is the natural (or resonant) frequency of the bound electron, and $\mathcal{E}_0 \exp(-i\omega_\gamma t)\,\hat{x}$ is the electric field of the incident X-rays polarized in the $\hat{x}$-direction with photon energy E = $\hbar\omega_\gamma$ ($\hbar$ is the reduced Planck constant); $\dot{x}$ indicates the first derivate (the electron velocity), and $\ddot{x}$ is the second derivative (the electron acceleration). In this classical picture of a damped driven harmonic oscillator, an excitation frequency, ω_γ, approaching the natural frequency of the oscillator, ω_0, gives rise to a resonant change to the scattering cross-section, hence the name RAXR. The physical process remains an elastic scattering event (Figure 3.4c): below the absorption edge, bound electrons absorb incident X-rays and are excited to a higher unoccupied energy level (but not ejected); they subsequently decay back to the ground state and emit a photon with the same energy as the incident X-ray but phase shifted. In a real system, at energies just above an absorption edge, the photoelectrons ejected from the resonant atom have finite kinetic energy and can interact with the local environment, which gives rise to oscillations in the absorption spectra (i.e., the “near edge structure” of XANES).

Finally, to combine the XR part of RAXR with the spectroscopic aspects described above, we rewrite the structure factor to include a resonant term:

$$F_{TOT}(Q,E) = \sum_j f_j(Q)\Theta_j e^{iQz_j} e^{-Q^2u_j^2/2} + \sum_k f_k(Q,E)\Theta_k e^{iQz_k} e^{-Q^2u_k^2/2} \qquad 3.14$$

where the first term is the same as the structure factor in Eq. 3.7c with the sum taken over all $j \neq k$ atoms, and the second term is the structure factor contribution from the distribution of resonant ions k. The energy-dependent scattering factor $f(Q,E)$ of the resonant ion is given by

$$f(Q,E) = f^0(Q) + f'(E) + if''(E) \tag{3.15}$$

where f^0 is the non-resonant ('NR') contribution to the atomic FF as in Eq. 3.7, and f' and f'' are called the dispersion corrections, which arise from the change in absorption cross-section near an edge energy. For tightly bound core electrons (e.g., K-shell), f' and f'' are independent of the scattering vector, Q, but electrons with greater spatial distribution from the nucleus (e.g., L- and M-shell) would require a Q-dependence similar to that of f^0. f'' is directly related to the X-ray absorption as

$$f''(E) = \frac{E}{2hcr_0}\sigma_a(E) \tag{3.16}$$

where $h = 6.626\times10^{-34}$ is Planck's constant, $c = 3\times10^8$ m/s is the speed of light, and hc ≈ 12400 eV Å. f'' and can be measured at the beamline by XANES while f' is calculate from f'' by Kramers-Kronig transformations [162]. Far from an edge, the f'(E) and f''(E) terms are negligible, and the structure factor is dominated by the non-resonant term. However, near the edge energy, the dispersion corrections are significant (Figure 3.5).

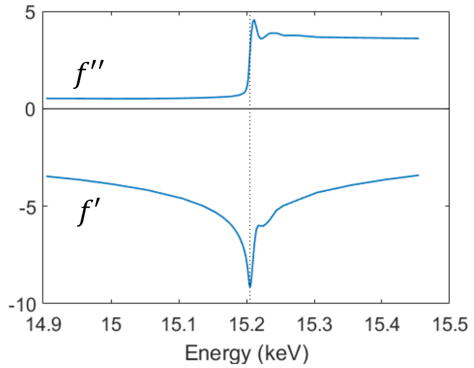

Figure 3.5. Dispersion corrections for Rb (K-edge E_0 = 15.2 keV) determined via transmission XANES measurement at beamline 33-ID-D of the APS. Note the oscillations above the K-edge, which result from interactions with nearby atoms.

The energy-dependent reflectivity can be written in terms of the dispersion corrections as

$$R(Q,E) \propto \left|F_{NR} + \left(f'(E) + if''(E)\right)\mathcal{F}(Q)\right| \qquad 3.17a$$

$$\propto \left|F_{NR} + \left(f'(E) + if''(E)\right)A_R(Q)e^{i\phi_R(Q)}\right|^2. \qquad 3.17b$$

Here, the resonant structure factor has been separated into its energy-dependent and spatial ($\mathcal{F}_R(Q)$) components with the latter being written in terms of the resonant atom's amplitude, A_R(Q), and phase, ϕ_R(Q) [176]. The amplitude is related to the ion coverage and DW factor while the phase is related to the vertical height (see Eq. 3.14). The amplitude and phase can be calculated as, respectively,

$$A_R(Q) = |\mathcal{F}_R(Q)|^2 \qquad 3.18$$

and

$$\mathcal{F}_R(Q) = A_R(Q)(\cos[\phi_R(Q)] + i\sin[\phi_R(Q)]) \qquad 3.19a$$

$$\mathrm{Re}[\mathcal{F}_R(Q)] = A_R(Q)\cos[\phi_R(Q)] \qquad 3.19b$$

$$\mathrm{Im}[\mathcal{F}_R(Q)] = A_R(Q)\sin[\phi_R(Q)] \qquad 3.19c$$

$$\phi_R(Q) = \mathrm{atan}\left\{\frac{\mathrm{Im}[\mathcal{F}_R(Q)]}{\mathrm{Re}[\mathcal{F}_R(Q)]}\right\}. \qquad 3.19d$$

A key result from Eq. 3.19d is that the resonant ion phase is independent of the total coverage.

RAXR is typically carried out by measuring the total reflectivity at a fixed Q_0 and scanning the X-ray energy through the absorption edge, E_0, of the resonant species, giving $R(Q_0,E)$. Due to the dependence of Q on the X-ray wavelength (Eq. 3.2), Q varies during an energy scan:

$$E = \frac{hc}{\lambda} \qquad 3.20a$$

$$Q = \frac{4\pi}{hc}\sin\left(\frac{2\theta}{2}\right)E. \qquad 3.20b$$

Consequently, the scattering angle 2θ must be adjusted at each step of an energy scan in order to keep Q_0 fixed. The required diffractometer angles are calculated on-the-fly during a scan using beamline control software macros (SPEC) and repositioned before a detector image is acquired at the new energy. This is repeated at several Q_0 to sufficiently sample the resonant structure factor. The non-resonant reflectivity, $R_{NR}(Q) \propto |F_{NR}|^2$, is separately measured via specular CTR at $E << E_0$ (or $E >> E_0$) such that the dispersion corrections f' and f'' are negligible. Thereby, the only unknowns become the resonant amplitude and phase, which are determined by model-independent least-squares fitting of the normalized intensity, i.e., with respect to the non-resonant reflectivity:

$$\frac{R(Q_0,E)}{R_{NR}(Q_0)} = \frac{\left|F_{NR}(Q_0) + \left(f'(E) + if''(E)\right)A_R(Q_0)e^{i\phi_R(Q_0)}\right|^2}{|F_{NR}(Q_0)|^2} \qquad 3.21a$$

$$\begin{aligned}\frac{R(Q_0,E)}{R_{NR}(Q_0)} &= 1 + (f'^2 + f''^2)\left(\frac{A_R(Q_0)}{A_{NR}(Q_0)}\right)^2 \\ &+2\frac{A_R(Q_0)}{A_{NR}(Q_0)}\left[f'\cos\left(\phi_R(Q_0) - \phi_{NR}(Q_0)\right) - f''\sin\left(\phi_R(Q_0) - \phi_{NR}(Q_0)\right)\right].\end{aligned} \qquad 3.21b$$

The relative phase $\Delta\phi = \phi_R - \phi_{NR} = Q_0(z_R - z_{NR})$ of the resonant atom with respect to some non-resonant reference plane (typically the substrate surface) gives the height of the resonant atom above the reference surface. $\Delta\phi$ determines the shape of the normalized RAXR spectra (i.e., a step up or a step down as the energy is scanned through the absorption edge) based on the relative contribution of f' and f''. This can be seen from the third term in Eq. 3.21b if we assume that $A_R \ll A_{NR}$ so that the second term is negligible: for $\Delta\phi = n\pi$ (n = 0,1,2,…), the spectrum will take the shape of $\pm f'$ (for even and odd multiples of π, respectively); for $\Delta\phi = n\pi/2$ (n = 1,3,5,…), the spectrum alternates between $\mp f''$. Thus, if the height of the resonant atom above the sample surface changes, so too will the relative phase and the shape of the RAXR spectra (demonstrated in Figure 3.6 for a single adsorbed ion layer in the form of a Gaussian). For a diffuse layer of ions at the surface (i.e., following the GC model of ion adsorption), the resonant atom is distributed in an exponential profile with the coverage varying as a function of the height above the substrate (Eq. 2.13). This will lead to variations in the shape of the RAXR spectra at different Q_0, weighted by the amplitude (see Chapter 5), resulting from the distribution of ion coverages. The challenge then is to interpret the amplitude and phase extracted from the model-independent analysis to arrive at the real-space electron density distribution. Interpreting the amplitude and phase separately as in Eqs. 3.18 and 3.19 is useful for model dependent analysis, as $A_R(Q)$ and $\phi_R(Q)$ can be calculated for a model distribution and compared to the model-independent results.

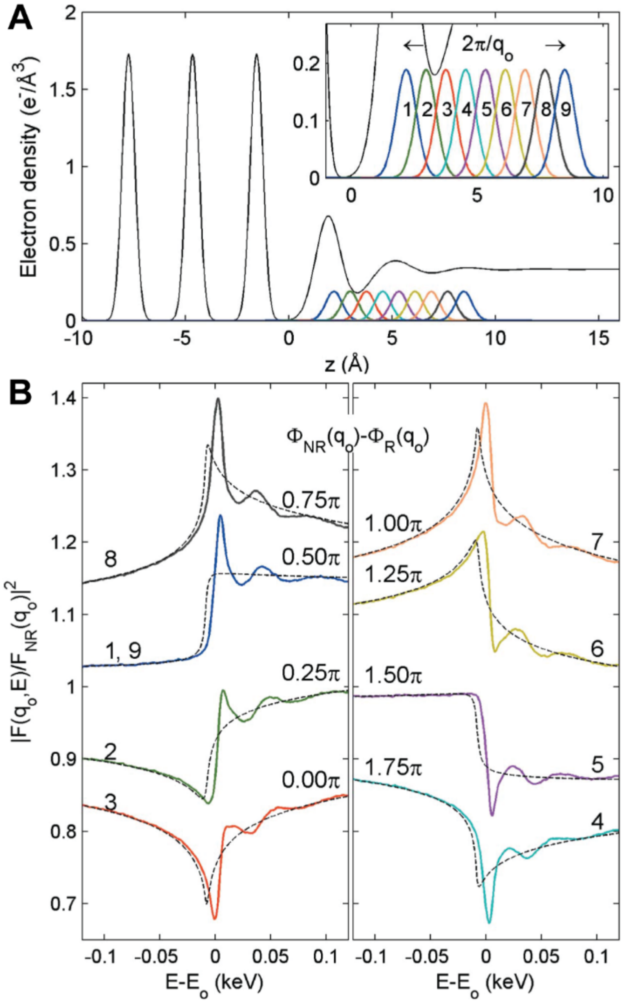

Figure 3.6. RAXR example. (A) The resonant ion distribution is modeled as a Gaussian at different heights above solid surface, resulting in (B) the RAXR spectra with different shapes based on the phase (height) difference between the ion and the adsorption surface. Non-resonant CTR not shown. Reproduced with permission of the International Union of Crystallography from Ref. [176].

3.3: Cyclic Voltammetry

Cyclic voltammetry (CV) [70] is a widely-used and versatile electrochemical measurement technique for characterizing energy storage devices ranging from capacitors to batteries. A CV records the current response of the electrochemical system as a function of the applied potential at a working electrode, I(V), which can be the cathode or anode depending on the objective of the experiment. As the name implies, the measurement is carried out by cycling the voltage at a constant scan rate between two extremes. CVs provide information about redox reactions taking place at the electrode surface, (e.g., how many electrons are transfer during a Faradaic charge transfer process). Reproducibility of the CV over several cycles can provide information about the reaction reversibility and the stability of the electrode and electrolyte over time. Changes in the CV could indicate non-reversible processes such as electrode poisoning or side-reactions in the electrolyte.

CVs fall into two broad groups based on the type of electrochemical processes taking place. The first and probably most familiar CV includes oxidation and reduction peaks in the current response resulting from electron transfer events [185]. The current increases dramatically when the applied voltage reaches the activation energy for a chemical reaction to occur and then drops as the analyte is used up. These peaks are characteristic of batteries. The second type of CV is approximately rectangular in shape and lacks peaks (Figure 3.7). These CVs result from a buildup of charge in a capacitive double layer at the electrode surface, but there is no charge transfer between the electrode and electrolyte. All CVs inherently include a capacitive element as the electrolyte charges must reach the electrode surface before any electron transfer may occur. Therefore, the rectangular CVs characteristic of capacitors are achieved by limiting the voltage window such that Faradaic processes cannot occur.

For an ideal planar capacitor with the specific capacitance $C_A = C/A$ defined according to Eq. 2.2, where A is the electrode area, and an applied potential, V, the surface charge $\sigma = Q/A$ is given by

$$\sigma = C_A V. \qquad 3.22$$

Taking the time derivative of Eq. 3.22 yields

$$j(V) = V\frac{dC_A}{dt} + C_A\frac{dV}{dt} \qquad 3.23a$$

$$j(V) = Vs\frac{dC_A}{dV} + C_A s \qquad 3.23b$$

$$j(V) = C_A s \qquad 3.23c$$

where j(V) is the voltage-dependent current density, and $s = dV/dt$ is the voltage scan rate during a CV experiment; $dC_A/dV = 0$ for an ideal capacitor, yielding Eq. 3.23c. In the latter case, the current response is constant and varies only in sign as the voltage is scanned either in the positive ($s > 0$) or the negative ($s < 0$) direction, as depicted in Figure 3.7a. Eq. 3.23c is often assumed in the literature without acknowledging the underlying assumption of ideality even though a real

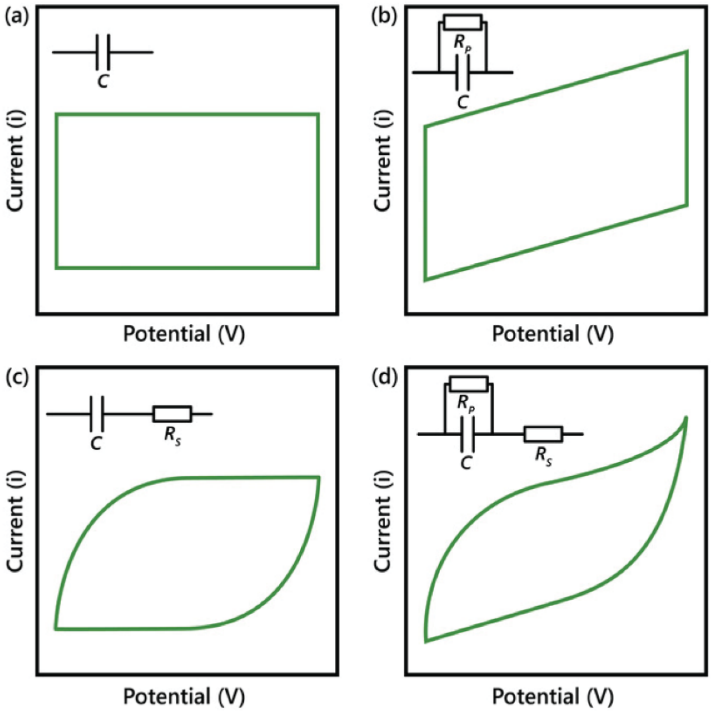

Figure 3.7. Model cyclic voltammograms and equivalent circuit analysis (inset): (A) ideal capacitor, (B) capacitor with parallel resistor R_P, (C) capacitor with series resistor R_S, and (D) capacitor with both R_P and R_S. Reprinted with permission from Ref. [186]. © 2019 WILEY-VCH Verlag GmbH & Co. KGaA, Weinheim.

electrochemical cell always includes other circuit elements that result in deviations from the ideal rectangle (Figures 3.7b-d) [186]. Non-ideal behavior may be modeled by parallel and series resistances as show in in Figures 3.7b-d, which can arise from potentiostat connections, resistance within the electrolyte between the active ("working") electrode and the counter electrode, and the electrodes themselves. Alternatively, we can see from Eq. 3.23b that a sloped CV, such as in Figure 3.7b, would result from a voltage-dependent capacitance, such as that resulting from a change in dielectric response as the voltage is varied. Due to the non-ideal behavior, it is useful to calculate an effective capacitance from the CV.

There are several ways to estimate the capacitance from a CV. The integral capacitance, C_{int}, can be used to estimate the average capacitance of the electrochemical cell, i.e., $C_{int} = (\langle C_{an}\rangle + \langle C_{cath}\rangle)/2$, where $\langle C_{an}\rangle$ and $\langle C_{cath}\rangle$ are themselves the mean capacitances over the anodic (i.e, for $s > 0$) and cathodic (i.e., for s< 0) segments of the CV, respectively. Integrating Eq. 3.23c with respect to the voltage, we obtain

$$C_{int} = \frac{1}{2|s|\Delta V}\int_{V_1}^{V_2} [\, j_{an}(V) - j_{cath}(V)]\, dV \qquad 3.24a$$

$$C_{int} = \frac{A_{CV}}{2|s|\Delta V} \qquad 3.24b$$

where $|s|$ is the magnitude of the scan rate, $\Delta V = V_2 - V_1$ is the voltage window over which the CV is carried out, and A_{CV} is the area inside the CV. C_{int} essentially provides a measure of the overall device performance during cycling. $\langle C_{an}\rangle$ and $\langle C_{cath}\rangle$ can be calculated separately from Eq. 3.24a but integrating over just the relevant segment of the CV and without the factor of ½. The capacitance can also be estimated by measuring CVs at several scan rates and plotting the current at a specified voltage (e.g., $j_{min}(V_1)$) versus the scan rate. According to Eq. 3.23c, the slope gives the capacitance. At higher scan rates, the $j(s)$ curve usually deviates from the expected linear relationship, which indicates that the current response changes from a capacitive (i.e., surface adsorption) regime to a diffusion-limited regime. In the latter case, j becomes linear in $\sqrt{s}$ [187]. Both approaches are used in this thesis to estimate the capacitance and associated surface charge density at steady state (i.e., at a fixed voltage) for comparison with ion coverage determined by RAXR measurements.

In this thesis, I use an XR-compatible three-electrode electrochemical cell to carry out CVs (Figure 3.8). In general, a three-electrode setup includes a working electrode where the electrochemical process of interest (e.g., ion absorption) takes place, a counter electrode where the opposite reaction takes place, and a reference (or pseudoreference) electrode that provides a stable point of reference for the measured voltage (Figure 3.8a). A voltage is applied between the reference and working electrodes to generate a current. The potentiostat lead for the reference electrode has a significant resistance applied across it so that current only flows between the working and counter electrodes. The XR-compatible electrochemical cell is shown in Figure 3.8b and includes a Kapton window, which allows the transmission of X-rays. The working electrode is epitaxial graphene grown on SiC, which is placed horizontally in the center of the cell in a reflection geometry (Figure 3.8c). The counter electrode is a Pt wire/mesh combination (wire diameter = 0.25 mm, 99.99% trace metal basis; mesh wire diameter = 0.06 mm, nominal aperture = 0.25 mm), which is a standard noble metal for use in aqueous electrochemistry. The Pt mesh is wrapped around the Pt wire to increase the counter electrode surface area so that adsorption at the counter electrode is not rate limiting.

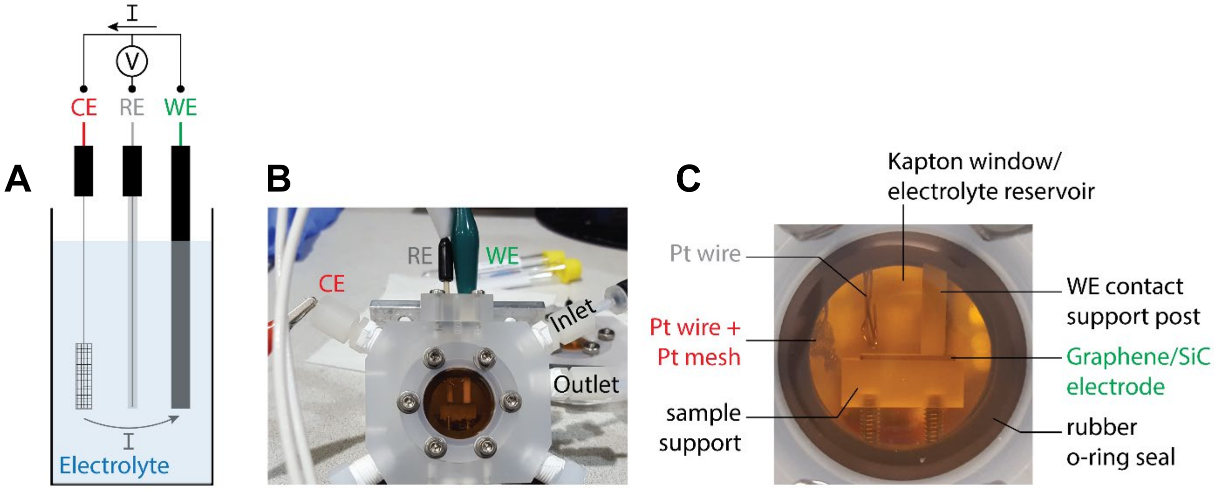

Figure 3.8. Three-electrode electrochemical cell. (A) Standard configuration with a counter electrode (CE) in red including a wire and mesh to increase the surface area, reference electrode (RE) in gray, and working electrode (WE) in green. The electrochemical reaction takes place at the interface of WE and electrolyte. (B) Photo of assembled XR-compatible three-electrode electrochemical cell shown with a leakless miniature Ag/AgCl RE and Pt wire CE. The electrolyte solution can be exchanged through the inlet and outlet valves. (C) Close-up view of the center of the XR electrochemical cell with a Pt wire + Pt mesh CE, Pt wire pseudo-RE, graphene/SiC WE, and auxiliary parts labeled.

Initial in situ electrochemistry measurements were carried out using a miniature Ag/AgCl reference (pictured in the setup in Figure 3.8b), which is a common reference electrode used in aqueous electrochemistry. It includes an internal standard with an Ag wire coated with AgCl and 3.4 M KCl solution. The standard Ag/AgCl potential is +0.23 V with respect to the standard hydrogen electrode (SHE) for the half-reaction reaction

$$\mathrm{AgCl(s)} + \mathrm{e}^{-} \rightleftharpoons \mathrm{Ag(s)} + \mathrm{Cl}^{-}$$

The electrode is nominally leakless with a conductive seal so that the internal KCl solution does not contaminate the electrochemical cell. However, on several occasions during in situ electrochemistry experiments, the electrochemical cell experienced sudden loss of capacitive behavior that could be recovered by switching to a fresh Ag/AgCl reference. We hypothesize that this breakdown in the reference electrode properties results from damage to the seal when inserting the miniature electrode through narrow openings into the XR-compatible electrochemical cell. Therefore, we switched to a Pt pseudoreference (pseudo because it is a Pt wire and lacks an internal electrochemical reaction with known reference potential). The reaction potential of a Pt wire was

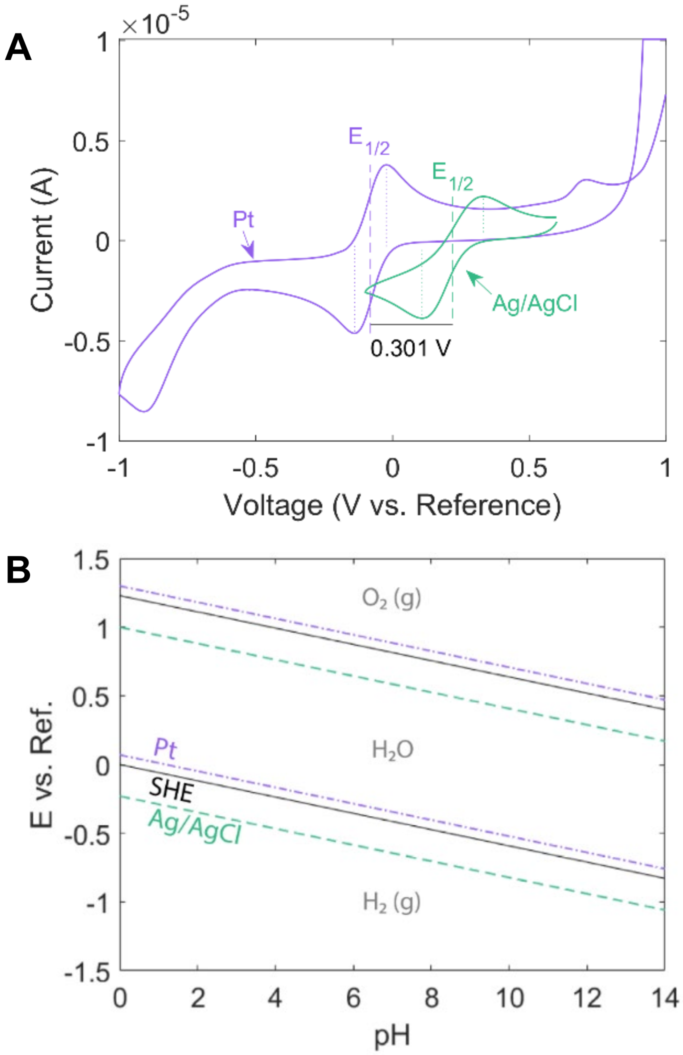

Figure 3.9. Platinum pseudoreference electrode. (A) Calibration of Pt pseudoreference with respect to Ag/AgCl standard reference measured in a 1 mM KFeCN/100 mM KCl solution; the half-cell potential, $E_{1/2}$, is shifted by -0.3 V with a Pt reference compared to Ag/AgCl. (B) Pourbaix diagram showing the water stability window, i.e., the voltage range outside of which hydrogen gas H_2(g) and oxygen gas O_2(g) are evolved, as a function of electrolyte pH and for various reference electrodes. (Pt = purple; standard hydrogen electrode, SHE = black; Ag/AgCl = green).

calibrated with respect to a fresh Ag/AgCl reference electrode and was found to be -0.3 V with respect to Ag/AgCl (Figure 3.9a), which is consistent with a previous report [188], and results in a reaction potential of -0.07 V with respect to SHE. All CV measurements presented in this thesis were carried out with respect to the Pt wire pseudoreference.

One final consideration for aqueous electrochemistry measurements is that the voltage range is limited by the water window, i.e., the region within which water is stable and outside of which hydrogen gas, H_2 (negative potentials), and oxygen gas, O_2, (positive potentials) are generated. The stability window for water as a function of solution pH is shown in the Pourbaix diagram in Figure 3.9b. At neutral pH, water is stable from -0.41 V to +0.81 V versus SHE. Thus, with a Pt reference, water is stable from -0.34 V to +0.88 V, which defines the voltage limits that can be applied for purposes of this thesis.

Chapter 4: Validation of First Principles Simulations of Water Adsorption at the Alumina/Water Interface

Portions of this chapter have been published in Refs. [189] and [190]. The work presented here involved close collaboration with two separate computational groups who ran the simulations. The first set of simulations were carried out by Dr. Kendra Letchworth-Weaver (Argonne), Dr. Alex Gaiduk (UChicago), and Dr. Federico Giberti (UChicago) as part of the Midwest Integrated Center for Computational Materials (MICCoM); the second set of simulations were carried out by Dr. Ying Chen (UCSD) and Dr. Eric Bylaska (Pacific Northwest National Lab). The analysis of the MICCoM simulation accuracy with respect to the experimental X-ray reflectivity data was a joint effort (Chapter 4.6), and I carried out all model-dependent optimization of simulated structures (Chapter 4.7).

4.1: Introduction

First principles molecular dynamics (FPMD) simulations, also called *ab initio* MD and density functional theory MD (DFT-MD), have had a significant impact in materials science, chemistry, and condensed matter physics [111, 191-194] in the last three decades. However, they rely on several design choices, including theoretical and numerical approximations, whose validation is often a challenging and complex task [95, 96, 103, 104, 195-201]. These include the selection of a suitable atomistic model to describe the system of interest (e.g., the number of atoms to represent it) and selection of the appropriate thermodynamic conditions (temperature, density, pressure). The level of theory to describe interatomic interactions, i.e., the exchange-correlation functional, and the methodological approaches to solve the Kohn-Sham equations [202] (i.e., the description of core and valence electrons and basis set expansion of the electronic wave functions) must be specified. Validation of the simulation results requires that all approximations be appropriate, and a tight integration between experiment and computation is essential.

Validation procedures are commonly performed for several properties of bulk solids [102, 104, 203] and of bulk liquid water [95, 97, 103, 105, 107, 195, 198, 200, 201, 204, 205] where many direct predictions of experimental observables (e.g., crystallographic structures, formation energies, diffusion coefficients) from theoretical calculations may be obtained. The electronic properties of oxide/water interfaces are of particular interest for understanding photoelectrochemical water splitting, catalysis, and charge storage capabilities [5, 9, 19, 206], but they present a particular challenge for FP simulations due to the loss of translational symmetry across boundaries. At the same time, such systems may result in high sensitivity to any discrepancies in the molecular-scale interactions in these low symmetry structures, thereby offering an opportunity to understand the strengths and weaknesses of various approximations required for FP calculations.

XR offers a direct test of computational accuracy through the simple and well-defined interactions of X-rays with matter as described in detail in Chapter 3. XR intensities can be calculated from simulated interfacial structures and compared directly with measured XR data. This approach serves as an adjunct to the usual method for evaluating the accuracy of simulations –that is, comparing the simulated atomic distributions with those derived from model-dependent analysis of experimental XR data, which determines a probable structure but not necessarily the *right* structure. It is still useful to compare the real-space structures in order to understand the origins and relative importance of any discrepancies in the simulated XR signals, but comparing to experimental data is a more direct validation route. Comparisons of simulated and experimental XR intensities have recently been carried out for classical MD [51, 108, 207] and FPMD [207] simulations using predicted atomic density distributions and atomic FF (as in Eqs. 3.7b and 3.7c) and in one case using the predicted electron density (Eq. 3.7a) of the solid surface but with a classical continuum model to describe electron density of the liquid [208]. These studies have demonstrated that the high sensitivity of XR to atomic-scale interfacial structures provides a strict test of the accuracy of these simulation approaches.

Here, we compare FPMD simulations of the α-Al_2O_3(001)/water interface with measured XR data using both the simulated atomic density distributions and the simulated electron density distributions for both the solid and the water regions. The latter approach is new to this work. We establish a general validation protocol for FPMD simulations of oxide/water interfaces (outlined in Figure 4.1) that can be applied to other solid/water interfaces for which high-quality X-ray reflectivity data can be obtained. We explore how the choice of exchange correlation functional, pseudopotential, system size, and statistical sampling affect the accuracy of the simulation predictions. The Al_2O_3(001)/water interface was selected because it is well-understood experimentally [209-214] and is relatively simple to simulate (in contrast to isostructural Fe_2O_3, which has similar interfacial water properties [210] but requires hybrid functionals to capture its antiferromagnetic properties arising from the spin-orbit coupling of the Fe *d*-shell electrons [42, 215, 216]). The conventional unit cell of Al_2O_3 (Figure 4.2a) contains 12 aluminum atoms, 18 oxygen atoms and has trigonal class symmetry (space group $R\bar{3}c$). The experimentally determined

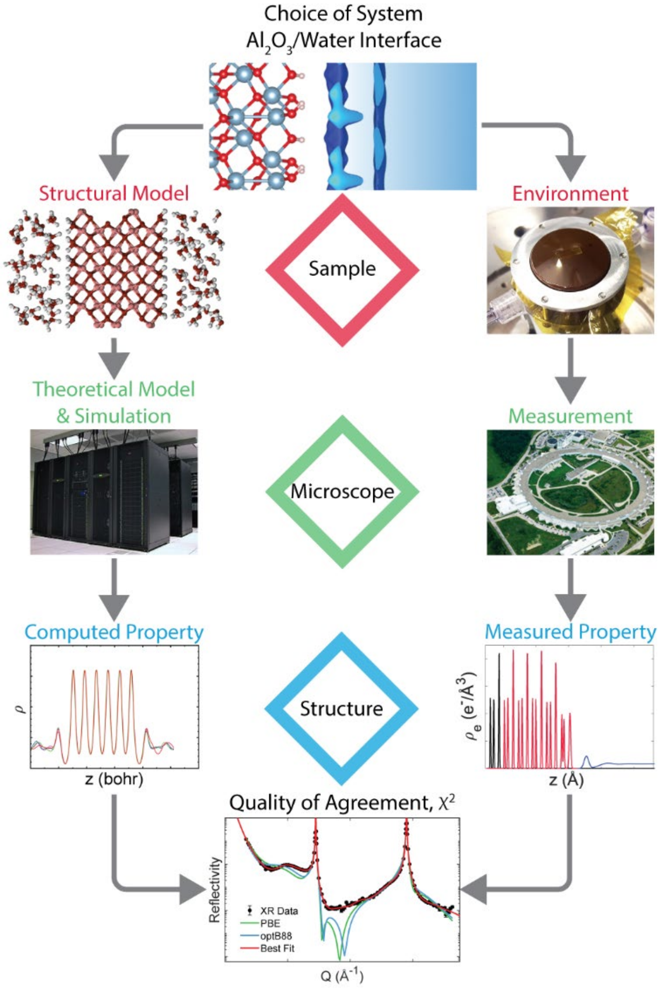

Figure 4.1. Schematic of the validation protocol adopted in this work, showing the close coupling of theory and experiment customized for the specific case of FPMD simulations of the alumina/water interface using X-ray reflectivity.

lattice constants are a = b = 4.767 Å, and c = 12.998 Å with angles $\alpha = \beta = 90°$ and $\gamma = 120°$ [217]. The unit cell contains six lattice planes along the surface normal (001) direction that differ only in their lateral registry (Figure 4.2b). Consequently, in a specular XR measurement, $Al_2O_3(001)$ Bragg peaks are observed at $L = 6n$ ($n = 1, 2, ...$) or, equivalently, at $Q = n$ 2.900 Å^{-1} where $Q = 2\pi L/c$ (see Eq. 3.4). It is convenient to use the unitless reciprocal lattice vector L rather than Q to describe

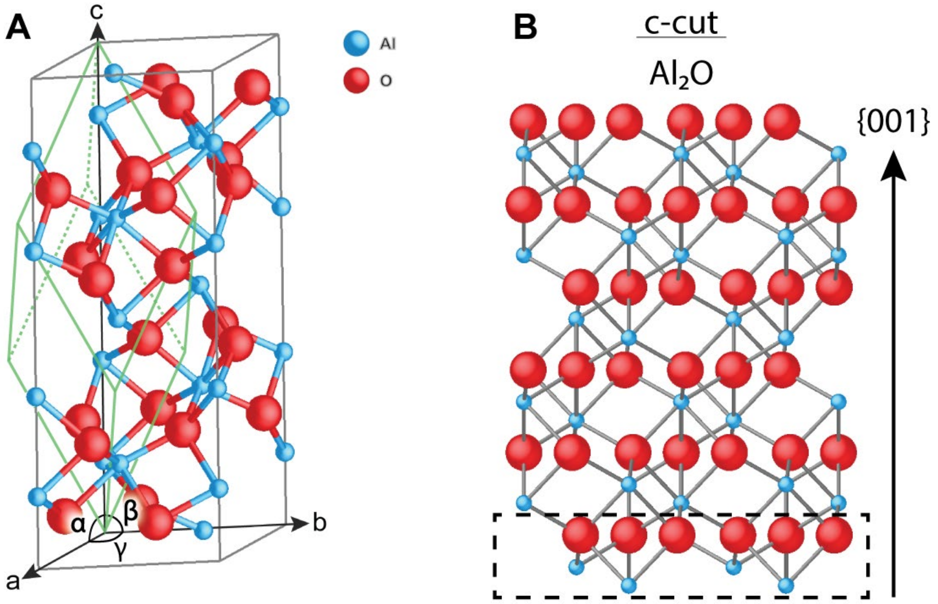

Figure 4.2. Alumina crystal structure. (A) α-Al_2O_3 conventional unit cell (rhombohedral cell shown in green). (B) O-terminated (Al_2O functional group) c-cut alumina (001 surface) viewed from the 100 direction; the dashed box indicates the vertical repeating unit cell.

the scattering condition when making comparisons between simulated and experimental XR signals because the lattice constants may not agree exactly.

4.2: Exchange Correlation and Pseudopotential

In addition to an electron's kinetic energy arising from its radial motion and the potential energy due to the nuclear core, DFT calculations use an exchange-correlation functional to account for electron-electron interactions in many-body systems, such as those arising from the spatial *exchange* of electrons with the same spin (i.e., Pauli exclusion) and from the *correlated* motion of an electron due to the presence of all other electrons in the system [218]. FPMD uses DFT to minimize the total energy of the system with respect to its electron density, ρ_e. The total energy is given by

$$E_{tot}(\rho_e) = T(\rho_e) + U(\rho_e) + E_{XC}(\rho_e) \qquad 4.1$$

where T and U are the total kinetic and potential energies (not accounting for electron-electron interactions), and E_{XC} is the exchange-correlation term. Many different classes of exchange correlation functionals have been developed of the years. These include, in order of increasing complexity, accuracy (often but not always) [95, 219], and computational cost: the local density approximation (LDA) wherein ρ_e is treated as spatially homogenous, the generalized gradient approximation (GGA) in which E_{XC} depends on both the electron density at each point in space, $\boldsymbol{r}$, as well as its spatial variation at that point via its derivative, and hybrid functionals with an additional contribution of Hartree-Fock exact exchange [218]. Within each of these groups there are many flavors of functional that yield different levels of agreement with experimental results. Eq. 4.1 must be minimized with respect to all electrons in a system and at each time step of a dynamical FPMD simulation, creating a significant computational challenge as the number of electrons and the level of theory (i.e., the inclusion of dispersion forces) increase.

One approach to reduce the complexity and increase the efficiency of a DFT calculation is to decrease the number of electrons being modeled explicitly. This can be accomplished through the use pseudopotentials (PPs), which replace core electrons with a fictitious wavefunction and effective potential [220, 221]. The underlying assumption is that core electrons do not participate in chemical reactions, and, therefore, do not need to be modeled explicitly. The PP describes the potential felt by the valence electrons due to the ionic core, i.e., the nucleus plus screening due to the inner electrons. There are many varieties of PP. Among the most popular, and used for simulations presented in this thesis, are norm-conserving PPs [222]. The PP is constructed such that at a cutoff radius, r_c, the pseudo wavefunction, ψ_P, must converge to the all-electron wavefunction of the bare atom, ψ_{AE} (Figure 4.3), and inside the cutoff radius, the norm of the pseudo wavefunction equals that of the all-electron wavefunction: $\langle\psi_P|\psi_P\rangle_{r<r_c} = \langle\psi_{AE}|\psi_{AE}\rangle_{r<r_c}$. The PP must be optimized such that beyond r_c, the residual energy of the pseudo wavefunction is minimized. The residual energy depends on the basis set expansion chosen to solve the Kohn-Sham equations and depends on choices made to balance accuracy (minimize energy) with the goal of computational efficiency [223].

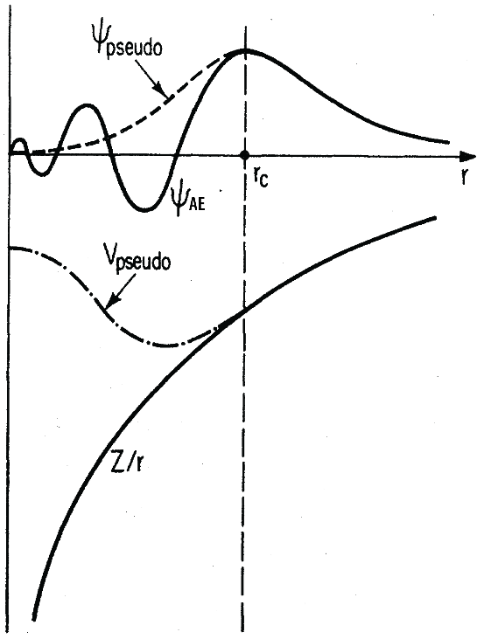

Figure 4.3. Schematic of pseudopotential concept showing the all-electron (solid lines) and pseudo (dashed lines) wavefunctions, ψ_{AE} and ψ_{pseudo}, respectively, and potentials $V = Z/r$ and V_{pseudo}, respectively; r_c is the cutoff radius at which ψ_{pseudo} converges to ψ_{AE}. Adapted from Ref. [221].

For a periodic system (i.e., electrons in a crystal lattice), the electronic wave functions may be expanded in a plane wave basis set (essentially the Fourier components of the wave) following Bloch's theorem [224], $\psi(\boldsymbol{r}) = \exp[i\boldsymbol{k} \cdot \boldsymbol{r}]\, u(\boldsymbol{r})$. An exact description of the wave functions can be obtained by including infinitely many plane waves, which is not feasible. Instead, the expansion only includes plane waves up to some energy cutoff, E_{cut}, that yields accurate predictions of an experimental observable (i.e., a lattice constant). All wavefunctions (including valence and pseudo wavefunctions) are expanded with the same E_{cut}. A larger cutoff energy indicates a larger basis set and greater computational cost, but a smaller cutoff energy may result in convergence errors with respect to PP and observable quantities.

In some cases, it may be appropriate to treat semicore electrons (e.g., d-shell) explicitly in the DFT calculation [225], such as with systems incorporating transition metals where semicore electrons are expected to participate in chemical reactions. In principle, including semicore electrons can provide a more accurate calculation even if these electrons are not expected to participate in chemical reactions, as doing so would explicitly account for more quantum mechanical effects. However, as stated above, including more electrons explicitly increases the complexity of the PP and can introduce additional error to the DFT results if the PP is not properly optimized.

4.3: Experimental Methods and Results

Sample Preparation and Measurement

The specular XR data used for comparison with simulations were measured at beamline 33-ID-D at the APS by Dr. Jeffrey Catalano (Washington University in St. Louis) at a photon energy of 12 keV. A polished 10mm x 10mm (001)-terminated single crystal alumina α-Al_2O_3 substrate was cleaning according to the procedure described in Ref. [210]: four cycles of sonication in HPLC-grade acetone, HPLC-grade MeOH, and 18 MΩ ultra-pure de-ionized water (DIW) (nominal pH = 7) for 15 minutes each, followed by a 12 hour soak in 2% HF and a 4 hour soak in 1M HCl followed by several rinses in DIW. The sample was then annealed at 1100 °C for 24 hours in air before transport to the APS. The sample was mounted in a thin-film cell (Figure 4.4) in DIW for XR measurements.

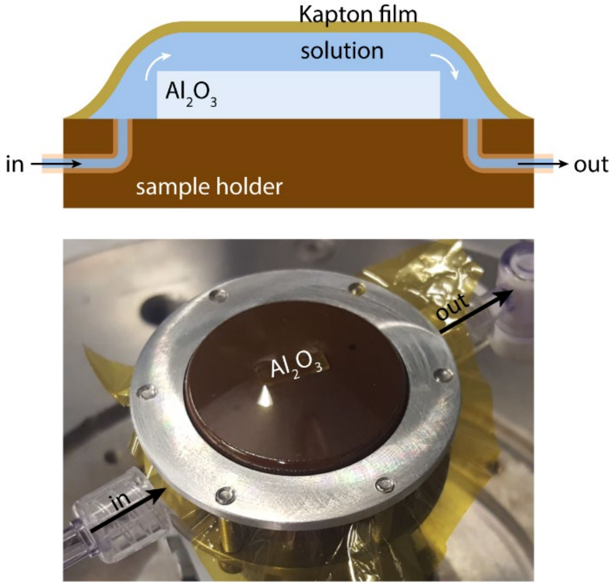

Figure 4.4. Thin film cell for XR measurements of the Al_2O_3/water interface (top: schematic; bottom: photograph with a 3 x 10 mm Al_2O_3 sample).

XR Data Analysis Model

The experimental $Al_2O_3(001)$/water interface structure along the (001) plane normal is characterized by an electron density profile, ρ(z), that was determined by direct comparison of measured specular XR data to calculated XR intensities based on atomistic models of the $Al_2O_3(001)$/water interface. These models consist of a semi-infinite known, fixed bulk alumina structure, five unit cells of Al_2O_3 interface (e.g. five repeating Al-Al-O_3 planes above the bulk structure for a total of 15 atomic layers), an adsorbed water layer, and a layered bulk water model [120, 209, 210]. The position, vibrational amplitude, and coverage for each of the interfacial alumina layers and the adsorbed water layer were optimized following the model-dependent analysis procedure described in Chapter 3. The parameters for the bulk Al_2O_3 crystal were kept fixed in the data analysis. The model also included extrinsic factors for the roughness (see Chapter 3.1.1), the water layer thickness (influencing the attenuation of X-rays through the sample), and an overall scale factor (to align the Bragg peak intensities of the calculated structure and the data).

The positions of each layer in the alumina surface model are independently optimized as are the position of the first hydration layer and the starting position of the extended layered water model (18 parameters total). The extended layered water model describes a series of m Gaussians ($m = 0$, 1, 2…) each with occupation Θ_w defined as

$$\Theta_w = \frac{A_{UC} d_w}{V_w} \tag{4.2}$$

where A_{UC} is the unit cell area of the substrate (19.597 Å^2 for $Al_2O_3(001)$), and $V_w = 29.9$ Å^3 is the volume of a water molecule in the bulk liquid. The position z_m and r.m.s. width u_m of each Gaussian are given by

$$z_m = z_0 + md_w$$
$$u_m = \sqrt{u_0^2 + m\bar{u}^2} \qquad 4.3$$

where z_0 and u_0 are the height and r.m.s. width, respectively, of the zeroth Gaussian of the extended water layer (i.e., closest to the adsorption surface along the surface normal), d_w is the distance between adjacent Gaussians and is uniform, and $\bar{u}$ is the width broadening of the Gaussians so that the vibrational amplitudes increase away from the alumina slab to asymptotically approach the bulk density for water (ρ_w = 0.33 e$^-$/Å^3). This water model contributes three additional parameters (21 total).

The vibrational amplitudes of the alumina surface layers are modeled as an exponential profile with an enhancement of the r.m.s. width at the surface, u_{enh}, and a decay length from the surface into the bulk layers, λ_{enh}. The width of each atomic layer, j, is given by

$$u_j = u_0\left(1 + u_{enh}e^{(z_j - z_{surf})/\lambda_{enh}}\right) \qquad 4.4$$

where u_0 is the element-specific bulk width (0.0514 Å for Al and 0.0563 Å for oxygen in α-Al_2O_3), and the enhancement effect for the layer at z_j (where the substrate is defined at $z < 0$) is referenced to the height of the surface layer z_{surf}. This simple model for the surface vibrational amplitudes forces the r.m.s. layer widths to converge to the bulk values at the bulk position (below the fifth Al_2O_3 unit cell). It also has the benefit that it reduces the number of parameters for the model-dependent fitting routine compared to fitting each layer's r.m.s. width individually, leading to greater confidence in the best fit results. Only two parameters are needed to describe the widths of all 15 interfacial layers, giving a total of 23 parameters in the model-dependent analysis.

Results

The best fit to the XR data yielded $\chi^2 = 1.54$ (Figure 4.5a) with the layer structure given in Table 4.1. The best-fit electron density distribution (Figure 4.5b) reveals an alumina interface described by an oscillatory relaxation pattern within the top five Al_2O_3 layers nearest the interface with the surface-most O layer expanding away from the alumina bulk. The surface vibrational amplitudes are two times the bulk values and manifest as a suppression of the maximum peak density of the surface-most layers. The enhancement decays to bulk-like widths below the second unit cell. The liquid water structure is described by a modulated fluid density with a first adsorbed hydration layer at a distance of 2.52 ± 0.01 Å above the Al_2O_3 surface and an occupation factor of 1.83 ± 0.12 water molecules per surface unit cell (H_2O/UC). The first layer of the weakly modulated extended water is located ~3.1 ± 0.1 Å above the first hydration layer and decays to the bulk water density at $z \sim 10$ Å above the alumina surface. The surface roughness was $\beta = 0.3 \pm 0.01$, corresponding to an r.m.s. roughness of 1.7 ± 0.05 Å (Eq. 3.12), and the water film was found to be 57 ± 9 μm thick.

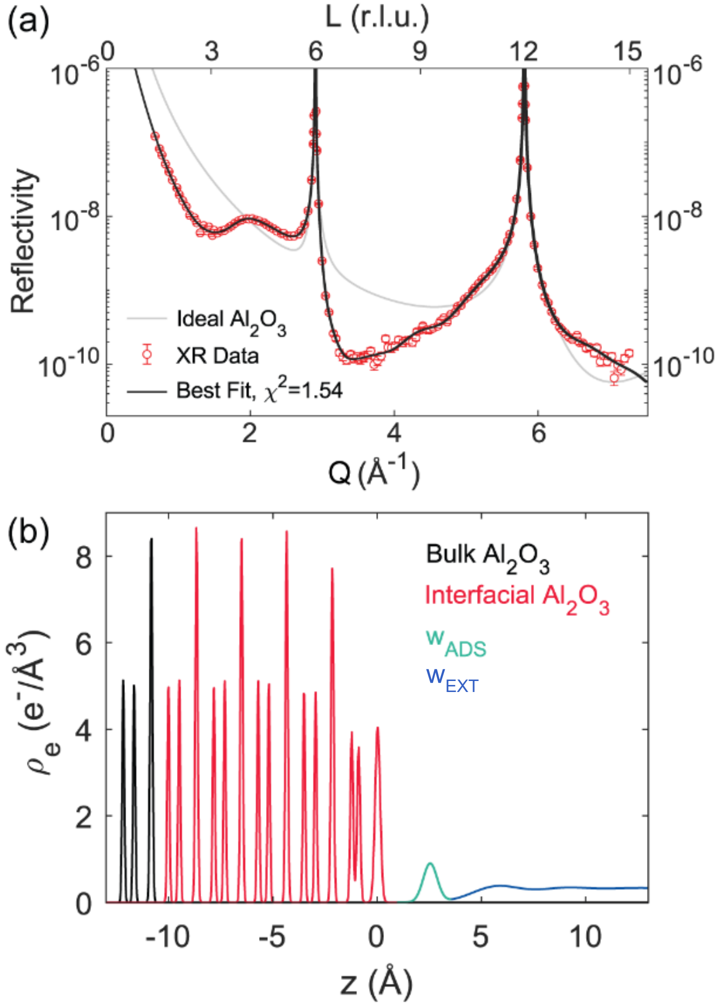

Figure 4.5. Experimental specular XR results for the $Al_2O_3(001)$/water interface. (A) The best fit to the XR data (black line and red circles with error bars as 1σ uncertainties, respectively) gives $\chi^2 = 1.54$; the reflectivity expected from an ideally terminated c-cut alumina substrate is shown for reference (gray line). (B) The best-fit electron density profile reveals Al_2O_3 surface relaxations, a well-defined adsorbed water layer (w_{ADS}), and a weakly modulated extended layered water model (w_{EXT}) with oscillations decying to a uniform bulk density beyond ~10 Å.

Table 4.1. XR best-fit structure for the α-Al_2O_3(001)/water interface (uncertainty on last significant figure in parentheses).

Z	**z (Å)**	**u (Å)**	**Θ (A_{UC}^{-1})**
	Alumina		
13	-10.013(4)	0.0514	1
13	-9.489(4)	0.0514	1
8	-8.663(2)	0.0563(1)	3
13	-7.834(6)	0.0515(2)	1
13	-7.310(7)	0.0515(3)	1
8	-6.502(2)	0.0564(7)	3
13	-5.705(6)	0.052(1)	1
13	-5.194(6)	0.052(2)	1
8	-4.340(5)	0.057(5)	3
13	-3.51(1)	0.053(8)	1
13	-2.952(6)	0.05(1)	1
8	-2.149(6)	0.06(2)	3
13	-1.22(1)	0.07(3)	1
13	-0.888(8)	0.07(3)	1
8	0.022(7)	0.121(17)	3
	Water		
8[a]	2.54(1)	0.34(5)	1.83(12)
8[b]	5.7(1)	1.16(11)	1.98(22)

[a] First adsorbed water layer. [b] First Gaussian of extended water using a layered water model (Eqs. 4.2 and 4.3).

Follow-up Studies

Both c-cut (001) and r-cut (012) α-Al_2O_3 samples were prepared for additional measurements of water adsorption on alumina. Off-specular XR measurements were carried out on the Al_2O_3(001)/water interface at APS Sector 33-ID-D using a photon energy of 20 keV to probe the lateral ordering of water at this interface. Specular XR and RAXR data were collected on both c-cut and r-cut alumina to investigate the effects of pH on water adsorption, to discern the contribution of ions to the electron density of the interfacial layering, and to assess the relative reactivity of these two surfaces of alumina. The solution pH was controlled using 0.01 M HCl (pH = 2), 0.01 M NaOH (pH = 12), or 0.01 M RbOH (pH = 12). Specular XR data were measured at beamlines 13-ID-C at a photon energy of 13 keV and 6-ID-B at a photon energy of 18 keV. RAXR data were also collected at beamlines 13-ID-C and 6-ID-B near the Rb K-edge, E = 15.2 keV. The sample preparation followed the same procedures described above and in Ref. [26] with some modifications as described in Appendix A.1. The analysis of these data is ongoing, and some preliminary analysis is presented at the end of this Chapter and in Appendix A.1.

4.4: Detailed Simulation Methods

4.4.1: MICCoM Simulations for Direct Comparison with XR Results

The following simulations were carried out by K. Letchworth-Weaver (Argonne), A. Gaiduk, and F. Giberti (UChicago) and in collaboration with Giulia Galli (UChicago) and Maria Chan (Argonne) as part of MICCoM's efforts toward the validation of FP calculations of solid/water interfaces.

The structural model chosen to represent the Al_2O_3(001)/water interface consists of a periodically repeated rhombohedral supercell with a $3 \times 2\sqrt{3}$ surface cell and 27.057 Å between replicated periodic images. The alumina was modeled as a solid slab with 6 oxygen layers in the vertical (001) direction, 12 in-plane unit cells, and a fully hydroxylated surface termination (H-[O3-Al-Al]$_5$-O_3-H). The liquid was modeled with 96 water molecules (Figure 4.6). The chosen surface termination is consistent with previous experimental characterization and fitting analysis of the

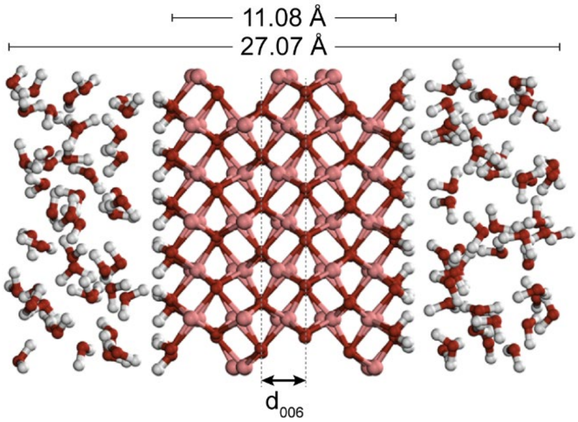

Figure 4.6. Snapshot of the FPMD supercell before equilibration, viewed along the $1\bar{1}0$ direction, with a 6-layer Al_2O_3 slab and 96 water molecules. d_{006} is the slab lattice parameter. O atoms are red, Al atoms are pink, and H atoms are white. (Structural model constructed by A. Gaiduk).

Al_2O_3(001) surface in water at neutral pH [209, 210, 212, 214, 226, 227]. In total, each simulation includes 120 Al atoms, 312 O atoms, and 264 H atoms (696 total atoms).

The initial atomic configuration of the slab was prepared starting from the final snapshot of a previously equilibrated alumina/water interface, which was simulated using FPMD with the PBE functional and included a 3-layer Al_2O_3 slab interfaced with 96 water molecules [228]. That snapshot was expanded along the (001) direction to accommodate a thicker 6-layer Al_2O_3 slab; it was subsequently equilibrated for ~1 ns using classical MD (CMD) in the LAMMPS code [229] with the ClayFF force field [230] to describe the Al_2O_3 and SPC/E [231] to model liquid water. Finally, FPMD simulations were carried out starting from randomly chosen snapshots of the equilibrated classical simulation. These snapshots were equilibrated for ~6 ps by FPMD before trajectory sampling. Each final FPMD prediction used for comparison with the experimental data is the average of the prediction from four independent trajectories sampled for various durations ranging from 2.5 – 10 ps each, which were seeded from four separate CMD snapshots.

The FPMD simulations were performed in the Qbox code [232] where the Kohn-Sham equations are solved using plane-wave basis sets and Optimized Norm-Conserving Vanderbilt pseudopotentials (PP) [223, 233]. All calculations were performed using PPs generated with the PBE exchange correlation functional [234] and designed for use at an energy cutoff of 60 Ry. The PPs were constructed such that the 1s electrons of oxygen and of aluminum were always considered as core electrons and, thus, frozen in their respective atomic configurations. In the case of Al, we considered two different PPs: 1) a PP in which the $3s^2 3p^1$ electrons were considered as part of the valence partition (the "$3e^-$PP") was used for simulations with two different exchange correlation functionals, PBE and optB88 [105], and 2) a PP in which the $2s^2 2p^6 3s^2 3p^1$ electrons were in the valence partition (the "$11e^-$PP") was used for additional optB88 simulations. In total, this leads to 2496 or 3456 valence electrons being treated explicitly when the $3e^-$PP or $11e^-$PP is used for Al, respectively. The simulation supercell was sampled at the Γ point (commensurate with a 3x3x1 k-point sampling of the conventional hexagonal Al_2O_3 unit cell) with periodic boundary conditions and a cutoff energy of 60 Ry for PBE calculations and 80 Ry for optB88 calculations. Runs were [235]carried out at constant temperature (NVT) using a BDP thermostat [236] with T = 400 K for PBE simulations and T = 330 K for optB88 simulations.

PBE is the workhorse functional of DFT. It has been shown to accurately reproduce the geometric and electronic properties of bulk alumina [237] but performs less-well for bulk water [95]. In particular, PBE is known to overestimate HB strengths, resulting in an overstructured liquid with slow diffusion coefficients compared to experiment, a density below 1 g/cm^3, and ice with a higher density than the liquid [238]. PBE calculations of water are usually carried out at T = 400 K to correct this overstructuring [239], but such a high temperature could have undesired effects on the alumina in the case of simulations of the alumina/water interface. Yet, several FPMD calculations of alumina/water interfaces have been carried out using PBE in recent years [228, 240] due to the relatively low computational cost of PBE compared to hybrid functionals, which provide only limited improvements for predictions of bulk water properties [95, 235]. The optB88 exchange correlation functional includes van der Waals (vdW) interactions and has previously been shown to outperform PBE in its predictions of the structural and vibrational properties of liquid water [195]. Moreover, optB88 can reproduce some of the water properties as accurately as the hybrid functional PBE0 [241] but at a significantly lower computational cost [195, 242]. Nevertheless, the simulations carried out in this study incur significant computational cost due to the large number of explicit electrons; thus, we used CMD for further investigation of the effect of the distance of the first water layer from the solid surface on the XR signals.

4.4.2: DOE Geosciences Simulations

The following simulations were carried out by Y. Chen (UC San Diego), E. Bylaska (Pacific Northwest National Lab), and John Weare (UCSD) as part of the Geosciences Research Program from the DOE/BES.

These simulations were performed using the pseudopotential plane-wave program NWPW [243, 244] contained in the NWChem computational chemistry package [245]. Two separate calculations were carried out using PBE, one with and one without the Grimme2 [100, 246] dispersion correction. Grimme2 is a phenomenological correction designed to account for long-range vdW interactions not included in semi-local PBE (unlike optB88, which includes vdW interactions explicitly). For both the PBE and the PBE+Grimme calculations, the structural properties of a perfect bulk alumina crystal were first optimized using a 2 × 2 × 1 Monkhorst-Pack Brillouin zone sampling [247]. The valence electron interactions were approximated using generalized norm-conserving Hamann pseudopotentials [248] generated using PBE in a separable form suggested by Kleinman and Bylander [222, 249]. The electronic wavefunctions were chosen based on previous studies [250] and were expanded using a plane-wave basis with periodic boundary conditions with a wavefunction cutoff energy of 100 Ry and a density cutoff energy of 200 Ry. With PBE, this gave bulk alumina lattice parameters of $a = b = 4.767$ Å, $c = 12.999$ Å, $\alpha = \beta = 90^{\circ}$, and $\gamma = 120^{\circ}$, which are within 0.2% of experimental results ($a = b = 4.757$ Å, $c = 12.998$ Å) [251]. Relaxing the unit cell upon addition of the Grimme2 correction gave lattice parameters of $a = b = 4.746$ Å, $c = 12.911$ Å (0.7 % smaller than the experimental result), and $\alpha = \beta = 90^{\circ}$ and $\gamma = 120^{\circ}$.

Next, an FPMD simulation supercell with lateral dimensions $a = b = 9.534$ Å and length $c = 45.150$ Å, $\alpha = \beta = 90^{\circ}$ and $\gamma = 120^{\circ}$ was generated for simulations of the $Al_2O_3(001)$/water system. The alumina surface was modeled as a 12-layer 2 x 2 slab with deuterated surface oxygens (i.e., $Al_{88}O_{144}D_{24}$, comprising 1086 valence electrons). 64 D_2O (512 valence electrons) were placed in the vacuum between alumina slabs in the periodic cell to obtain a water density ~1 g/cm^3 (see Figure 4.7). The use of deuterium allows for larger MD time steps. The size of the cell and number of water molecules were chosen specifically to capture the known extent of changes to the alumina

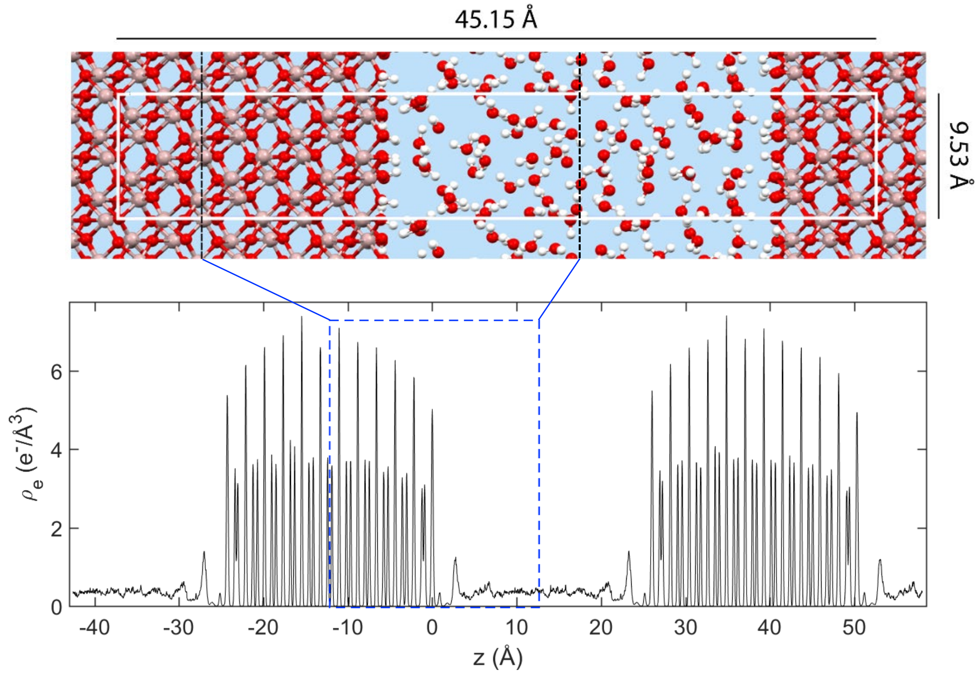

Figure 4.7. Top: a snapshot of the 12-layer Al_2O_3(001)/water system from the PBE-based FPMD simulation is shown with the supercell perpendicular to the alumina (001) surface indicated by the white box. The black vertical dashed lines coincide with the bulk-like center of the alumina slab and bulk-like center of the water region. O atoms are red, Al atoms are pink, and H atoms are white. Bottom: total electron density profile with a repeating supercell. The surface oxygen of one alumina slab is shown at z = 0 Å. The blue dashed box indicates the section used for comparison with XR data. (Snapshot provided by E. Bylaska).

surface structure (i.e., relaxations within at least the three surface layers) and the modulation of the interfacial water [40, 210].

The initial interfacial hydration structures were generated using a mixed FPMD/molecular mechanical (FPMD/MM) model in which the positions of the slab layers were fixed and the water molecules were modeled using the SPC/E interaction potential. This FPMD/MM model has been shown to produce excellent agreement with experimental data for the hydration structure of charged ions in solution (i.e. Zn^{2+} aqua ion) [252]. In the calculations reported here, the FPMD/MM structures were equilibrated by FPMD for 1.5 ps during which time the potential and kinetic energies stabilized. Trajectories were sampled at the Γ-point using the Car-Parrinello method [253, 254], and snapshots were collected every 1.2 fs for 10 ps during which time the simulation did not evolve significantly. These simulations were carried out in the presence of Nosé–Hoover thermostats [255-257] with a time step of 0.12 fs and fictitious mass of 750 au. The temperature and period of the ionic and electronic thermostats were set to 300 K and 1200 au, respectively.

4.5: Calculating XR Intensities from Predicted Structures

Simulated XR intensities for direct comparisons with experimental XR data were computed by K. Letchworth-Weaver using software she developed previously for the calculation of $SrTiO_3$ XR signals [208] and modified for the specifics of the present system. Comparisons and interpretation of the results were carried out by me and K. Letchworth-Weaver. I separately calculated XR intensities from FPMD structures for empirical optimization of these predictions with respect to the XR data. My calculations used MATLAB scripts developed in the Interfacial Processes Group. Both sets of calculations follow the same formalism described here.

For each simulation we identify three regions corresponding to the structures probed by the XR measurement: the bulk crystal, the substrate surface and interfacial liquid, and the bulk liquid. The total structure factor F(Q) is evaluated following Eq. 3.7 by writing $\rho(z)$ as the sum of contributions coming from each of the three regions. The structure factor contribution from the solid/water interfacial region is simply that of the oxide surface and the adjacent fluid as simulated with interfacial density, $\rho_{int}(z)$; the interface is defined over the range $z_B < z < z_w$ where z_B is the middle (i.e., most bulk-like) position within the simulated solid slab, and z_w is the most bulk-like position within the water region. The bulk fluid at $z > z_w$ is represented as a semi-infinite water layer above the simulated interfacial water region with uniform density, ρ_w, chosen to be equal to the experimental electron density of bulk water (0.33 $e^-/Å^3$); its structure factor is ρ_w/iq multiplied by a phase factor to describe its distance from the bulk substrate. The bulk solid structure at $z < z_B$ can be defined in three different ways, each with its own merits and drawbacks: 1) using the known bulk structure as determined by experiments; 2) using the bulk structure as predicted by a fully periodic bulk DFT calculation; or 3) as a semi-infinite extension of the center layer of the solid slab:

(1) Because XR signals are highly sensitive to bulk crystal structures [258], any errors in the simulated bulk (including the lattice constant, internal atomic coordinates, or spatial valence electron distributions) will contribute to significant systematic errors throughout the calculated XR signals. Errors in the simulated lattice constant will shift the sharp, intense Bragg peaks in the computed XR signals away from their positions in the experimental data, leading to significant χ^2 discrepancies. For example, an overestimate of the alumina slab lattice parameter by only 1.7% results in residual errors (expression in parentheses in Eq. 3.10) approaching $\Delta R/\sigma_R$ = 2000 just below the second Bragg peak at Q = 5.8 $Å^{-1}$ (Figures 4.8a-i and 4.8b). Meanwhile, errors in the internal unit cell coordinates (i.e., the Al-Al distance) or valence electron distributions in the bulk will alter the slow modulation of the CTR intensities (e.g., as seen in the relative intensities near the Bragg peaks). Such errors can be minimized by incorporating the experimentally known substrate crystal structure while using the simulation to define only the interface (Figure 4.8a-ii and 4.8b). However,

this results in an implicit structural mismatch between the bulk and interfacial components that can manifest as differences in peak densities of the electron density distribution due to disagreement of the layer r.m.s. widths (Figure 4.8a-ii) and as a slope on the surface relaxation, i.e., the fractional displacement of atomic layers with respect to their expected bulk positions (Figure 4.9). Ultimately, this mismatch leads to extrinsic and unphysical oscillations in the calculated XR intensities due to the presence of a discrete boundary between the bulk and interface regions.

This approach is best suited to a model-dependent optimization of the simulated structure with respect to XR data (as in Chapter 4.7) wherein the predicted interfacial structure is adjusted following the usual model-dependent least-squares fitting procedure that is used for the analysis of experimental data (see Chapter 3.1.1). By optimizing the interface structure, the discrete boundary between experimental bulk and simulated interface is eliminated and χ^2 minimized.

(2) Fully periodic DFT calculations comprising a single unit cell with periodic boundary conditions have been found to give lattice constants within 1% of expected Al_2O_3 values [189, 237]. Meanwhile, the lattice parameter of the solid in an extended slab geometry, as used for oxide/water interface simulations, is typically larger than that of a fully periodic DFT calculation [189, 259]. Therefore, use of the DFT bulk to define the bulk structure factor for XR calculations would lead to more accurate Bragg peaks than using the slab lattice parameter, albeit still with a significant contribution to the χ^2 value. This approach would also be consistent with the conceptual framework of FPMD wherein the interface (slab geometry) and bulk (periodic DFT) are evaluated independently, and the expansion of

the slab lattice parameter compared to the bulk DFT is ignored. As long as the periodic DFT lattice constant is within a certain threshold of the experimental bulk value (e.g., 1%), the approximations used to carry out the simulations are deemed appropriate. However, because the XR probe simultaneously sees the bulk, the interface, and the transition between the two, combining the periodic DFT bulk structure with the slab interface can introduce a structural mismatch between the solid bulk and interface regions, just as using the experimental bulk structure would.

(3) Treating the bulk solid as a semi-infinite extension of the middle "bulk-like" layer of the slab ensures that there is no discontinuity between the bulk and interfacial regions. To mitigate errors in the computed XR intensities resulting from the overestimates in lattice spacing, comparisons with the reflectivity data can be made in units of reciprocal lattice index L. This effectively scales the z-axis so that all simulations have a substrate lattice spacing equal to the experimental value (Figure 4.8a-iii and 4.8c). However, a consequence of this choice is that all other aspects of the structure, including the Al_2O_3 substrate internal aluminum coordinate (i.e., the Al-Al distance at the middle of the Al_2O_3 slab) and the simulated water profile are also scaled. These effects must be kept in mind when interpreting the sources of χ^2 errors.

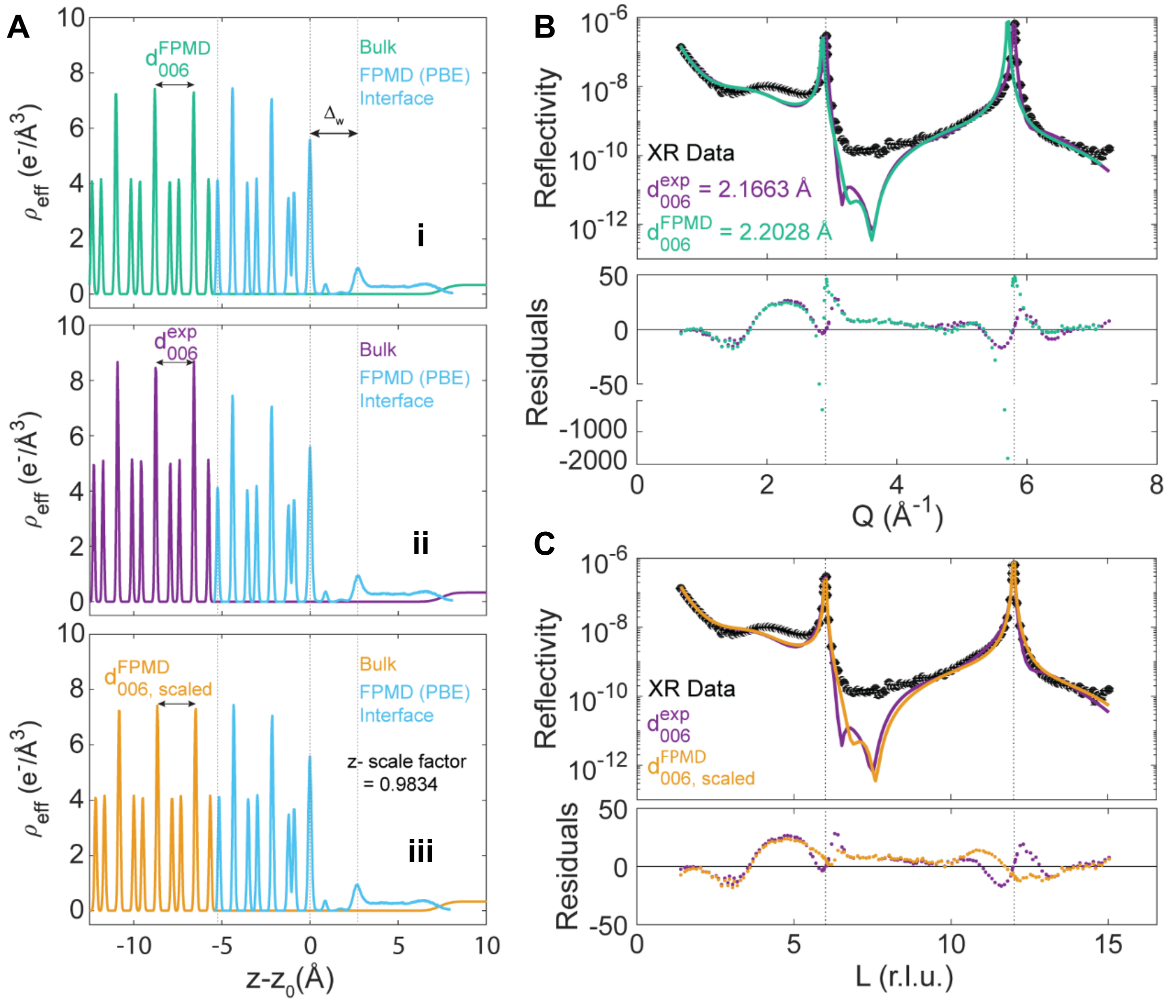

Figure 4.8. Definition of the substrate bulk structure for the calculation of XR intensities from simulated electron density distributions. (A) The effective electron density profiles are shown with the Al_2O_3 surface oxygen at z_0 as the reference plane. The predicted interfacial structure from FPMD (PBE), including the alumina surface and adsorbed water layer (light blue), is placed between bulk Al_2O_3 and bulk water layers colored based on the bulk substrate definition: i) using the slab lattice parameter d_{006}^{FPMD}, Al-Al spacing, and vibrational amplitudes (green); (ii) using the experimental lattice constant d_{006}^{exp}, Al-Al spacing, and vibrational amplitudes (purple); and (iii) using the slab structure effectively scaled in the z-direction by d_{006}^{FPMD} due to comparisons of the XR intensities with respect to the reciprocal lattice unit L (r.l.u.; yellow). The adsorbed interfacial water height Δ_w is indicated. (B) The comparison of the XR intensities (top) and residuals (bottom) as a function of Q calculated from the structures in (A-i,ii) shows orders of magnitude errors near the Bragg peaks (dotted vertical lines) when the slab lattice parameter is used. (C) The comparison of the XR intensities (top) and residuals (bottom) in terms of L (r.l.u.) effectively scales out the lattice parameter overestimate, corresponding to the structure in (A-iii); the Bragg peaks align and the residual errors are reduced.

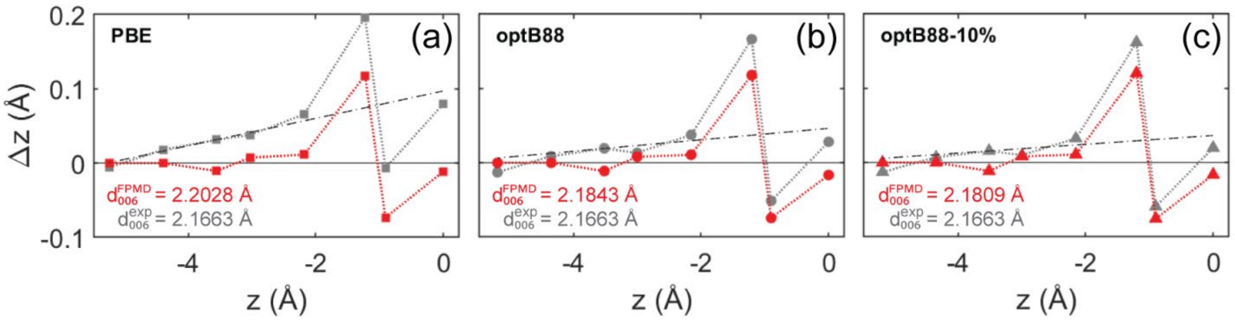

Figure 4.9. Effect of the choice of "bulk" lattice constant on the calculated Al_2O_3 surface relaxation, i.e., the deviation Δz of the surface atom positions from their expected bulk positions for (A) PBE, (B) optB88, and (C) optB88 with a 10% reduction of the supercell size along the Al_2O_3 (001) direction. The surface relaxations computed using the simulated d_{006}^{FPMD}(red) show an asymptotic decay in Δz from the alumina surface (z = 0) to the bulk-like positions whereas those calculated using the known experimental bulk d_{006}^{exp} (gray) include an implicit structural mismatch that leads to a slope on Δz ('· —' lines). The FPMD calculations shown here are from the six-layer alumina slab simulations.

For direct comparisons of the as-simulated FPMD structures with experimental XR data (Chapter 4.6), we chose to define the bulk substrate structure following the third approach. Specifically, the substrate crystal structure is calculated as a repeating periodic array of the bulk-like middle of the Al_2O_3 slab (i.e. the three planes Al-Al-O_3) with a slab lattice parameter d_{006} equal to the oxygen-oxygen vertical inter-layer spacing (Figures 4.6 and 4.8); this bulk crystal has a total structure factor given as the product of the structure factor of a single unit cell with density $\rho_B(z)$ and the CTR structure factor (Eq. 3.6). Altogether, the full structure factor for the FPMD simulation is written as

$$
\begin{aligned}
F(Q) &= F_{CTR}F_{BULK} + F_{int} + F_{H2O} \\
&= \frac{\int_0^d \rho_B(z)e^{iQz}dz}{1 - e^{-iQd_{006}}} + \int_0^{z_w} \rho_{int}(z)e^{iQz}dz + \frac{\rho_w}{iQ}e^{iQz_w}
\end{aligned}
\qquad 4.5
$$

where the position of the bulk layer, z_B, has been taken to be equal to 0. The structure factors in Eq. 4.5 can be calculated directly from the full electronic structure prediction from FPMD, new to this work, or from the simulated atomic densities and FF as in previous studies [51, 108, 189]. The direct use of FPMD electron density distributions accounts for any changes to valence electron configurations and directly tests the ability of DFT to predict the associated XR signals. Meanwhile, the use of simulated atomic densities is beneficial in evaluating the accuracy of the simulated structure (i.e., the location of a particular atomic layer) with respect to the best-fit structural model and its uncertainties. We employ both calculation schemes in this study to evaluate the consistency between and relative accuracies of the simulated electronic distributions and those assumed by FF.

One final consideration is that the FPMD simulations consider perfectly smooth interfaces whereas the experimental sample includes some amount of surface roughness as described in Chapter 2.1.1. Therefore, an additional roughness parameter following Eq. 3.11 should be applied to simulated XR intensities so that the accuracy of intrinsic structures is not masked by extrinsic factors. In practice, the roughness can easily be included as a fitting parameter in the χ^2 calculations, even in the case where the accuracy of the FPMD structures is evaluated directly (i.e., without any adjustment of the as-predicted structure).

4.6: Direct Comparison of Simulated XR intensities with XR Data

4.6.1: Choice of Theoretical Model

The results of all FPMD simulations used for direct comparisons are summarized in Table 4.2, including slab lattice spacings and χ^2 levels of agreement with the XR data calculated from elemental number densities and FF or directly from the DFT electron density distributions. Starting with the simulations carried out using the PBE functional, we see that the simulated electron density profile (Figure 4.10a) obtained as the average of four 10 ps trajectories is qualitatively consistent with the experimentally-derived electron density profile. However, we identify several structural discrepancies with the experimental best-fit model (Figure 4.5 and Table 4.1). The PBE slab lattice parameter differed from the experimentally known value by +1.7% (Table 4.2). In contrast, the fully periodic, optimized bulk PBE simulation gave an Al_2O_3 lattice parameter of 2.19 Å, ~1.2% larger than the experimental value. PBE also overestimates the interfacial water height above the oxide surface Δ_w by ~0.2 Å compared to the experimental best-fit (2.52 $\pm$ 0.01 Å) and underestimates the occupation factor Θ of the first hydration layer (i.e., the integrated area of the first water peak with respect to the Al_2O_3 surface unit cell area), giving 1.3 H_2O/UC compared to 1.83 $\pm$ 0.12 H_2O/UC found in the experimental analysis. The water structure from PBE is consistent with that from a previous study [228] and with the PBE results presented later in this thesis (Chapter

Table 4.2. Qualities of agreement, χ^2, from comparisons of MICCoM FPMD simulations with experiment.

Exchange Correlation	**PP**	**ΔV[a] (%)**	**t (ps)[b]**	**d_{006}^{FPMD} (Å)[c]**	**$d_{Al\text{-}Al}$ (Å)[d]**	**Δ_w (Å)**	**Θ (H_2O/UC)**	**χ^2**	
								Atomic FF	**DFT e^-**
PBE	3	0	40	2.2028	0.5131	2.74	1.3	102	119
optB88	3	0	12.8	2.1982	0.5190	2.68	1.5	66	91
	11	0	11.6	2.1843	0.4986	2.68	1.5	100	197
	11	10	13.2	2.1809	0.4999	2.64	1.7	69	133
	3	10							57[e]
Experiment				2.1663	0.5230	2.52	1.83	1.54	

[a]Volume change of the simulation cell via compression along alumina (001)-direction relative to the volume used in the PBE simulation; [b]Total simulation time after averaging over 4 independent trajectories; [c]Al_2O_3 slab lattice parameter; [d]Vertical spacing between adjacent aluminum atoms in the bulk-like middle of the Al_2O_3 slab; [e]Calculation uses the atomic positions from the optB88 11e^- PP trajectory with compression but dressed with the 3e^-PP core and valence configurations.

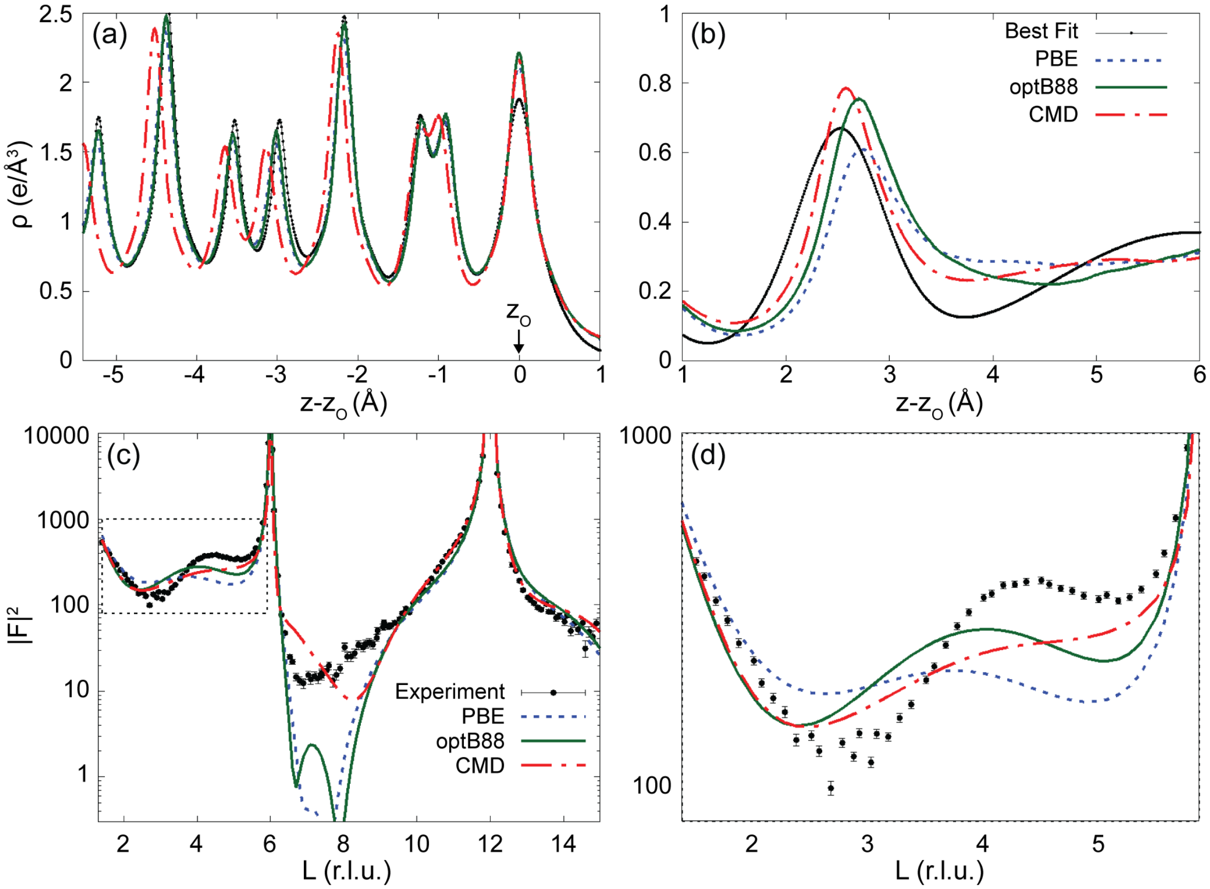

Figure 4.10. Simulated electron densities and XR intensities from different theoretical methods compared to the experimental result. All simulated data are computed using form factors; FPMD results are those of the 3e$^-$ PP simulations in Table 4.2. (A) Electron density profiles of the simulated Al_2O_3 surface from the PBE (blue dotted line) and optB88 (green solid line) simulations plotted with the surface oxygen at z_O as the reference plane, showing subtle deviations from the experimental best fit (black line); the differences are more visible in an equivalent CMD simulation (red) due to a larger discrepancy in the Al_2O_3 lattice parameter. (B) The electron density profiles of the interfacial water region reveal predicted interfacial water heights exceeding that obtained from XR experiments with the CMD result in closest agreement and the PBE result in worst agreement with the experimental best fit. (C) The simulations reproduce the general shape of the XR data (experimental errors shown as 1σ uncertainties) but with notable differences in the region below the first Bragg peak (dotted box) and for $L \sim$ 6-9. (D) A close-up view of the region in the dotted box from (C) shows that the simulated XR intensities from FPMD qualitatively reproduce oscillations in the XR data better than that from CMD; the optB88 functional outperforms PBE, reflecting important qualitative improvements in the optB88 electron density distribution. The surface roughness factor was 0.28, in agreement with the value obtained from the experimental analysis. (Individual figure panels provided by K. Letchworth-Weaver).

4.7), which used a different simulation software (Qbox versus NWChem) and different FPMD parameters as described in Chapter 4.3. This suggest that the PBE exchange correlation functional, independent of other FPMD factors, does not accurately describe the interactions of the Al_2O_3/water interface.

The optB88 exchange correlation functional provides several improvements over PBE. The simulated alumina slab lattice spacing from optB88 exceeds that of the experiment by +1.5% as opposed to PBE's +1.7% (both using the $3e^-$PP). Further gains are obtained from optB88 with an $11e^-$PP, yielding a slab lattice parameter +0.8% compared to that of the experiment (the periodic bulk optB88 DFT calculation gave an Al_2O_3 lattice parameter of 2.17 Å, ~0.3% larger than the experimental value). These differences in the Al_2O_3 bulk lattice spacing do not lead to substantial qualitative differences between the electron density profiles of the Al_2O_3 surface obtained from PBE, optB88, and the experimental best fit model (comparisons of the results obtained using the $3e^-$PP are shown in Figure 4.10a). However, such differences are important in determining the accuracy of the computed XR intensities as all comparisons are performed with respect to L (i.e., after normalizing the lattice constant errors).

We observe clear differences in the interfacial water distributions as well (Figure 4.10b). The optB88 functional predicts an interfacial water height of 2.68 Å (independent of the choice of PP), in closer agreement with the expected experimental value (2.52 Å) than the height predicted by PBE (2.74 Å). The optB88 functional also predicts an occupation factor of the first hydration layer of 1.5 H_2O/UC, which is more consistent with the experimental best-fit result (1.83 ± 0.12 H_2O/UC). These results suggest that the optB88 functional, which includes vdW interactions, provides an improved description of interfacial water properties relative to PBE.

The noted improvements in the electron density distribution obtained with the optB88 functional and 3e$^-$PP translate to superior χ^2 agreements in the calculation of the optB88 3e$^-$PP XR intensities (Figure 4.10c,d and Table 4.2). Namely, χ^2 decreases from 102 for PBE to 66 for optB88 when using atomic FF, or from 119 to 91 for PBE and optB88, respectively, when using DFT electron densities directly. However, such an improvement is not observed when using optB88 with the 11e$^-$PP despite its more accurate prediction of the lattice parameter. In this case, χ^2 = 100 using FF, equivalent to the PBE result (102), and χ^2 = 197 using DFT charge densities.

The different χ^2 of the 3e$^-$PP and 11e$^-$PP optB88 calculations suggest that there are errors present in the 11e$^-$PP leading to inaccuracies in the atomic structural prediction (seen in the χ^2 results using FF) as well as in the valence electron distribution (revealed by the χ^2errors using the DFT charge densities). One possible explanation for the worse χ^2 accuracy for the 11e$^-$PP optB88 calculation using FF is that this simulation gives a less accurate prediction of the internal aluminum-aluminum layer spacing d_{Al-Al} at the slab center compared to the 3e$^-$PP optB88 case (Table 4.2). These values are 0.4986 Å and 0.5190 Å, respectively, whereas the experimental value is 0.5230 Å. This highlights the sensitivity of the XR data to small displacements. We explore the sensitivity to the DFT electron distribution in detail in Chapter 4.6.3.

Lastly, comparison with an equivalent CMD simulation (i.e., with six alumina oxygen layers and 96 water molecules) further points to the interfacial water height as an especially important factor in improving χ^2. The Al_2O_3 slab lattice parameter from CMD is 2.2551 Å and the interfacial water height is 2.55 Å. The large alumina lattice spacing results in a significant discrepancy in the alumina surface layer positions compared to those from both the experimental best fit and FPMD (Figure 4.10a). Meanwhile, the CMD water height is nearly equivalent to the value obtained from the experimental best-fit model (Figure 4.10b). The resulting CMD χ^2 of 55 (using atomic FF) is significantly better than those obtained with the FPMD, indicating that the improved prediction of the water height compared to the FPMD results outweighs the errors due to worse agreement of the lattice constant from CMD. Furthermore, the CMD XR signal is more qualitatively consistent with the experimental XR data at $L \sim$ 6-9 than the FPMD XR intensities, which show an order of magnitude deviation from the XR data at these scattering conditions (Figure 4.10c). When the CMD-simulated water layer is rigidly shifted away from the solid Al_2O_3 surface and brought in line with the FPMD values, the CMD XR intensity begins to qualitatively reproduce the low-intensity region observed in the FPMD intensities (Figure 4.11). These results suggest that an accurate reproduction of structural details in the interfacial water structure, especially the interfacial water height, is critical (but not sufficient) to obtain a high-level agreement with the measured data.

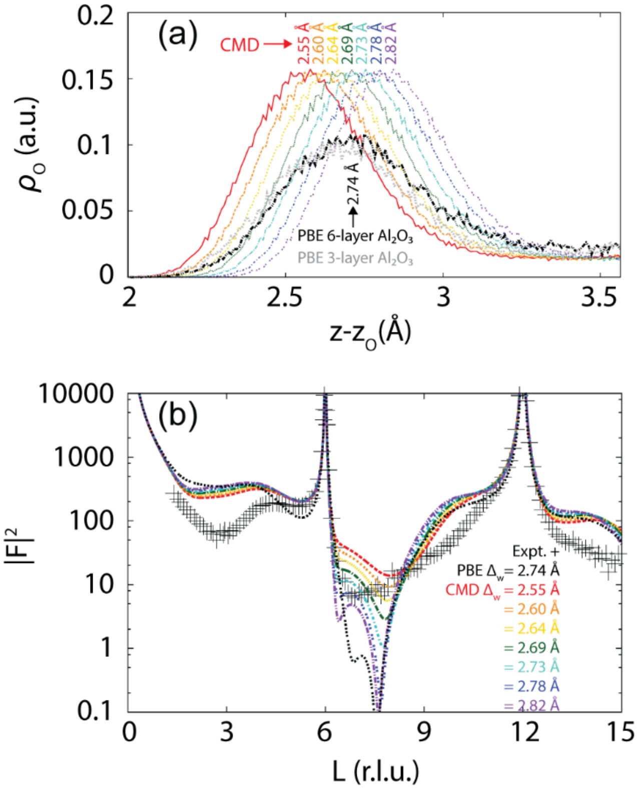

Figure 4.11. CMD water height displacement. (A) The oxygen atomic densities ρ_O from PBE and CMD at several water heights are given as the distance between the alumina surface oxygen and the peak water oxygen of the first hydration layer (z-z_O); ρ_O of the PBE 3-layer Al_2O_3 (gray) from Ref. [228]. (B) Larger water heights Δ_w in CMD yield a lower XR intensity at the midzone ($6 < L < 9$) but do not reproduce the PBE result. (Experimental data shown as '+'; simulated $|F|^2$ do not include a surface roughness factor; simulations by F. Giberti).

4.6.2: Volume of the Simulation Supercell

Both the simulated interfacial water heights in excess of the value indicated by the experiment and the adsorbed water densities (i.e., occupation factors) that were lower than the experimental result suggest that the volume of the supercell chosen in our NVT simulations (3117 $Å^3$) may have been too large. In principle, one may determine the optimal volume by using NPT simulations. However, adopting such a protocol for large simulations such as the ones in this study is currently prohibitive from a computational standpoint. Therefore, we explored the sensitivity of the simulated interfacial water density profile and the resulting XR intensities to the selection of simulation volume by reducing the supercell z-dimension size by 10% using simulations performed at the optB88 level.

The volume compression in our optB88 simulations ("optB88-10%") led to an interfacial water structure in better agreement with the experimental XR best-fit result. The 10% reduction of the *supercell* volume produced a ~17% decrease in the volume of the water region due to the relative incompressibility of Al_2O_3 compared to H_2O. The alumina slab electron density profile and lattice spacing did not change significantly (Figure 4.12a and Table 4.2). The interfacial water profile (Figure 4.12b) has an integrated first hydration layer density of 1.7 H_2O/UC and an interfacial water height of 2.64 Å (0.04 Å closer to the Al_2O_3 surface that without compression). We also observe significant changes to the second hydration layer, including an increased density and a peak shift from >6 Å to 5.25 Å. Finally, the asymptotic bulk-like water density (i.e., the density at the point farthest from the solid surface) was 0.29 $e^-/Å^3$, in closer agreement with the experimental value of 0.33 $e^-/Å^3$ than the result from the optB88 simulation using a larger volume, which was 0.22 $e^-/Å^3$. A caveat is that the experimental XR best-fit shows the interfacial water oscillations decaying to a bulk-like value at >10 Å from the solid surface (Figure 4.5b), which exceeds the dimensions of the water region in the simulations. As the simulation volume is not sufficiently large to capture the full extent of interfacial water oscillations or a true bulk water distribution, this will also affect the accuracy of the computed XR signals and may obscure the magnitude of χ^2 improvements originating from an apparent improvement in the first hydration layer.

The computed XR intensity from the optB88-10% simulation with the 11e$^-$PP (Figure 4.12c) is in substantially better agreement with the XR data than that from the initial optB88 11e$^-$PP calculation (Table 4.2). We obtain χ^2 = 69 when using atomic FF and χ^2 = 133 when using the

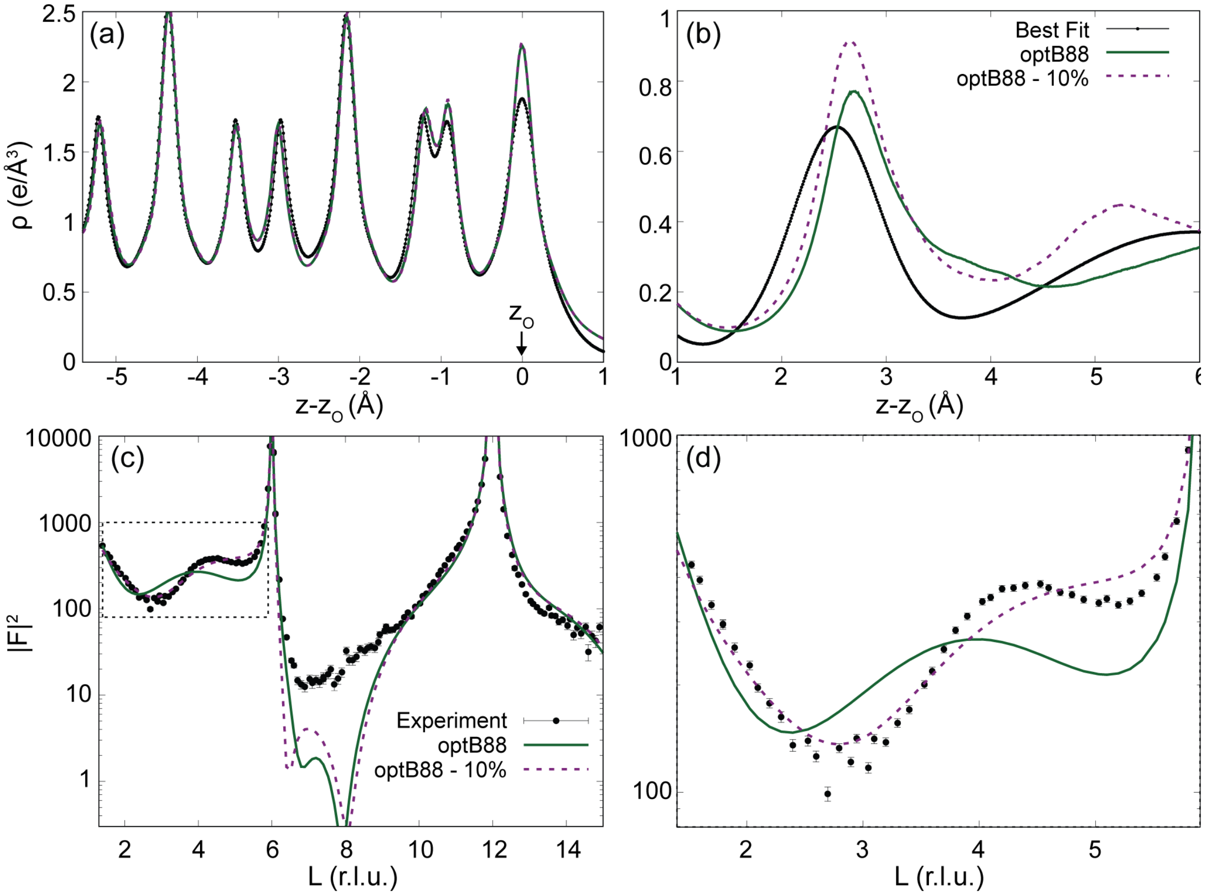

Figure 4.12. Effect of a 10% size reduction of the unit cell along the Al_2O_3 surface normal for the case of FPMD simulations with the optB88 functional and 11e$^-$PP computed using atomic FF. (A) The electron density profiles $\rho(z)$ of the Al_2O_3 interface show equivalent qualitative agreement with the experimental best-fit structure (black) before compression (green) and after compression (purple); the structures are given with the alumina surface oxygen layer z_O as the reference plane. (B) The interfacial water densities increase with volume reduction, and the interfacial water height is in closer agreement with the experimental result. (C) The simulated XR intensities $|F|^2$ versus reciprocal lattice unit L (r.l.u.) are generally similar before and after decreasing the simulation cell size but with notable changes in the oscillations below the first Bragg peak (dotted box), as highlighted in (D), bringing the simulated XR signal in closer qualitative agreement with the XR data (experimental errors are shown as 1σ uncertainties). (Individual panels provided by K. Letchworth-Weaver).

electron density prediction directly from DFT. The majority of the χ^2 improvement appears to originate from a substantial improvement in the oscillations in the simulated XR signals below the Bragg peak (Figure 4.12d), indicating that these low-L XR intensities, in addition to those at $6 < L < 9$, provide a sensitive fingerprint of the interfacial water structure. Although a compression test was not performed with the 3e$^-$PP, a χ^2 calculation using the *atomic* positions as predicted by the optB88-10% 11e$^-$PP and dressed with the DFT electron configuration of the 3e$^-$PP yielded $\chi^2 = 57$ (compare to $\chi^2 = 133$ with the 11e$^-$PP electron configuration). This again points to significant errors in the 11e$^-$PP electronic structure prediction. Overall, these results highlight the importance of a suitable choice of simulation volume, a nontrivial task.

4.6.3: Sensitivity to Valence Electron Distribution and DFT-Simulated Electron Densities

We showed that the XR data are sensitive not only to the atomic positions, but also to the electron distribution surrounding each atom. To isolate the impact of the charge densities, we compare three calculations using a single prediction of the atomic density distribution, that of the 11e$^-$PP optB88-10% simulation, but with different descriptions of the electron configuration: atomic FF, 3e$^-$PP DFT electrons, and 11e$^-$PP DFT electrons. The resulting electron density distributions are similar (Figure 4.13a-c), but the calculation using the DFT electrons from the 11e$^-$PP simulation shows a distinct broadening of the electron density within the Al_2O_3 slab (Figure 4.13b). This apparent charge delocalization leads to an overestimate of the electron density between atomic layers and an associated reduction in the density at the Al peak positions. We observe a nearly identical delocalization when carrying out calculations from the same snapshot using either

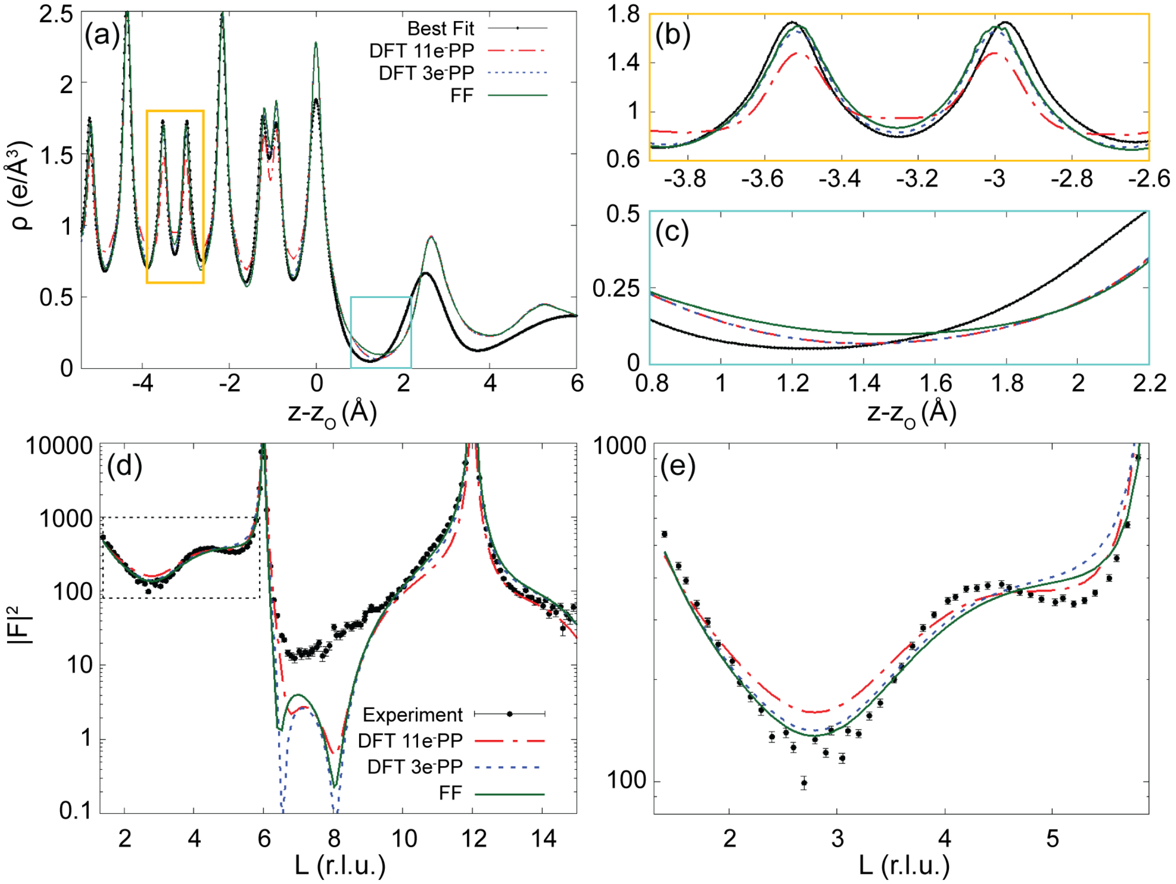

Figure 4.13. Effect of different electron density configurations on the XR signal demonstrated using the atomic density prediction from the optB88-10% simulation with 11e$^-$PP. (A) The full electron density profiles calculated directly from the electron density predictions of the 11e$^-$PP (red), using the 3e$^-$PP electron distribution (blue), or using atomic FF (green) are compared to the experimental best-fit (black) with all profiles aligned at the alumina surface oxygen position z_O. The simulated structures show detailed variations in (B) the inter-layer region of the alumina slab (gold box) and in (C) the bonding region at the interface with water (teal box). (B) In the alumina slab, the 11e$^-$PP electron distribution exhibits an excess density between atomic layers and a decreased Al peak density. (C) In the bonding region, the electron densities directly from DFT are similar to each other (the 3e$^-$PP and 11e$^-$PP cases overlap) and are in closer agreement with the experimental best fit than the density calculated with atomic FF. (D) The XR intensity $|F|^2$ as a function of reciprocal lattice unit *L* (r.l.u.) computed with the 3e$^-$PP agrees best with the XR data (black; experimental errors shown as 1σ uncertainties) while the intensity computed directly from the 11e$^-$PP electron density distribution is the least accurate (see Table 4.2). (E) Detailed view of the variation in the low-*L* region of the computed XR intensities (dotted box in (D)). (Individual panels provided by K. Letchworth-Weaver).

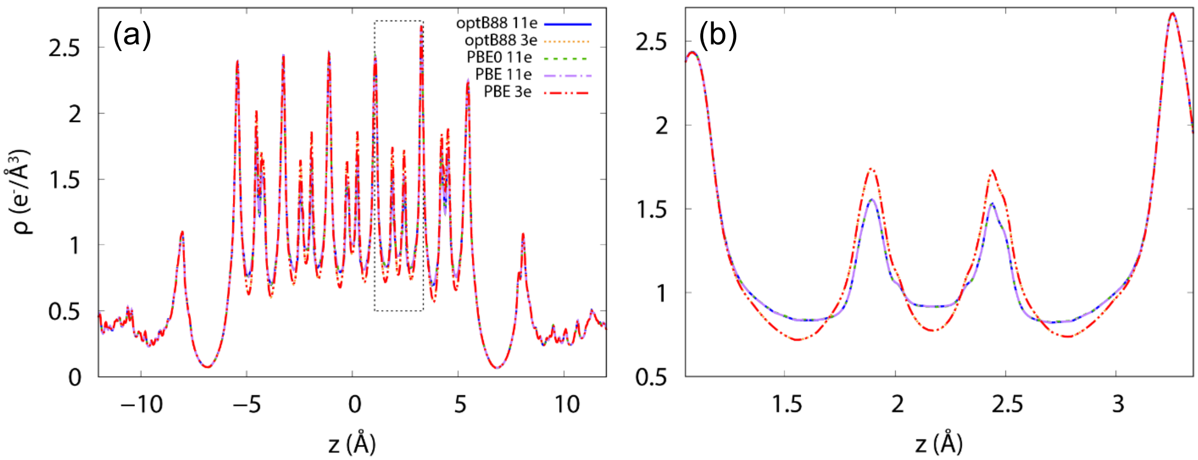

Figure 4.14. Effects of PP choice on electron delocalization in Al_2O_3, calculated using PBE, optB88, and PBE0. (A) Total electron densities $\rho(z)$, including the Al_2O_3 slab centered at z = 0 Å and the water regions, from a single snapshot show similar structures with equivalent atomic layer positions for all calculations (optB88 11e$^-$PP in blue and 3e$^-$PP in gold; PBE0 11e$^-$PP in green; PBE 11e$^-$PP in purple and 3e$^-$PP in red). (B) Close-up of the region in the dotted box in (A) shows that the electron density delocalization arises from the choice of PP rather than the exchange correlation functional. (Calculations by K. Letchworth-Weaver).

PBE or the hybrid functional PBE0 [241] with the 11e$^-$PP (Figure 4.14), indicating that the inaccuracy in the description of charge densities largely originates from the use of the PP derived with 2s2p electrons in the valence partition.

The electron density broadening around the Al atoms appears to be associated with a lower XR intensity just below the second Bragg peak ($10 < L < 12$), i.e., a scattering condition indicative of the bulk substrate structure, as described in Chapter 4.5. Specifically, a decreased XR intensity is observed at $10 < L < 12$ for the calculation using the 11e$^-$PP electron configuration with $\chi^2 = 133$ (Figure 4.13d) but not for the calculations using atomic FF ($\chi^2 = 69$) and the 3e$^-$PP ($\chi^2 = 57$), both of which are in close agreement with the experimental data at these L. Hence, we conclude that inaccuracies of the 11e$^-$PP for Al are a primary contributor to the observed differences in χ^2 values. We also note significant differences between the 3e$^-$PP and 11e$^-$PP XR intensities below the first

Bragg peak (Figure 4.13e), which result entirely from the differences within the alumina since the 3e$^-$PP and 11e$^-$PP DFT electron density distributions are identical in the water region (this is expected since these PPs describe the electron configurations for the Al atoms). This highlights that the low-*L* signal contains information not only about the water structure as we showed earlier, but also about the substrate.

The simulated electron density distributions in the region between the solid surface and interfacial water (the "bonding region"; Figure 4.13c) also show important differences with the experimental best-fit structure. Overall, the calculated densities display good qualitative agreement with the experimental density (the minimum position is shifted due to the larger interfacial water height from optB88-10%, but the amplitudes are similar). However, the distribution calculated using atomic FF shows a higher density in this region than those using DFT charge densities and the experimental best fit. This likely contributes to the lower accuracy obtained when using atomic FF rather than the 3e$^-$PP (χ^2 = 69 versus 57, respectively). It is important to note here that the XR best-fit density, which is also calculated using atomic FF, does not include H atoms due to their relatively weak X-ray scattering cross section, but these atoms are present in the simulations. Thus, the higher charge density from the optB88-10% atomic FF calculation appears to be associated with the use of FF for neutral atoms (O, H), which does not account for the possibility of charge transfer at the interface. To test this idea, we computed the electron density distributions and XR intensity from the same atomic density distribution but using ionic FF (O^{2-}, H^+, and Al^{3+}). The use of ionic FF leads to an electron density distribution in the bonding region in closer qualitative agreement with that predicted by optB88-10% DFT charge densities and, consequently, in closer agreement with the experimental best-fit density (Figure 4.15a). The electron density within the alumina is also reduced compared to the atomic FF case, but the change is subtle and does not necessarily improve the level of agreement with the experimental best fit within the solid (Figure 4.15b). Overall, the use of ionic FF with the optB88-10% simulation gives a more accurate XR signal with respect to experiment than any of the previous calculations ($\chi^2 = 45$; Figure 4.15c), suggesting that the XR data are sensitive to the nature of the charge distribution at the interface.

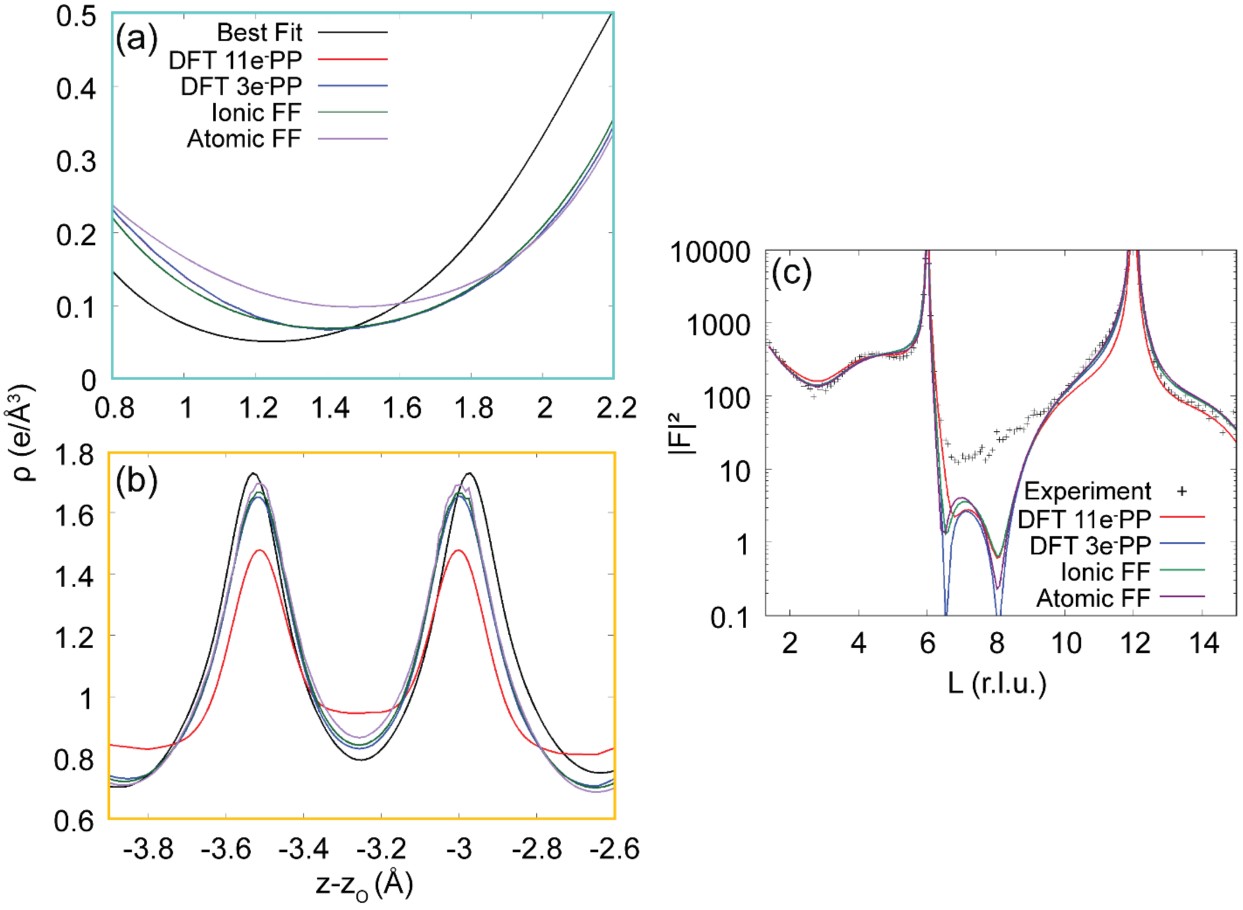

Figure 4.15. Effect of ionic FF on the electron density distributions and XR signals using the atomic density distribution predicted by optB88-10% with the 11e$^-$PP. (A) In the water region, the ionic FF calculation (green) has a lower electron density than that computed from the 11e$^-$PP DFT electron configuration (red), 3e$^-$PP DFT electron configuration (blue), and atomic FF electron distribution (purple) and is in closest agreement with the experimental best fit (black). (B) The electron density in the bulk-like alumina region is slightly decreased with ionic FF compared to the atomic FF case. (C) The XR intensities are compared to the experimental data shown as '+' symbols. (Plots provided by K. Letchworth-Weaver).

These results illustrate the importance of an accurate calculation of electron density distributions directly from DFT for comparison with experimental XR data so as to avoid the need for any *ad hoc* choices of FF. They also suggest that ionic FF may be better suited to describe Al_2O_3/water interface interactions and charge transfer than atomic FF—it is possible that the XR best-fit electron density in the bonding region with atomic FF is representative of the measured system because protons are excluded from the analysis model. However, given the high sensitivity of the XR measurement to substrate structures, it is not possible at this point to separately discern the sensitivity of the XR data to the electron density of the bonding region. Overall, the χ^2 values obtained here for the FPMD calculations are all significantly larger than those obtained through the experimental analysis (χ^2=1.54; Figure 4.5), indicating that the accuracy of the simulations is not yet fully quantitative.

4.6.4: Role of Trajectory Sampling

As a final step of the validation protocol, we analyzed how the statistical sampling of FPMD trajectories may affect the accuracy of computed XR signals. As noted previously, we carried out four independent MD trajectories for each FPMD simulation condition, which allows us to evaluate the range of possible predictions for a given set of FPMD approximations. We evaluate the trajectories obtained for the optB88-10% simulation using the $3e^-$PP, which yielded an average accuracy of χ^2 = 57, and the trajectories for the PBE simulation focusing on the atomic density distributions.

The four optB88-10% trajectories *s*0-*s*3 were each sampled for 3.4 ps and show similar electron density predictions (Figure 4.16a) with differences appearing primarily in the interfacial water distribution (Figure 4.16b). The $s2$ trajectory shows the largest deviation from the average electron density distribution $\langle s \rangle$ over the four trajectories. The mean variance over all trajectories with respect to the average electron density (i.e., $\langle s_n - \langle s \rangle \rangle$ where n = 0-3) is $1.91\times10^{-8} \pm 0.0165$ $e^-/Å^3$. In the alumina solid, the variance of each individual electron density from $\langle s \rangle$ is within the standard deviation, indicating that the FPMD simulation is well-converged within the solid. The levels of agreement with the XR data range from $41 < \chi^2 < 92$ with $s2$ giving the largest χ^2, in line with its large discrepancy in the interfacial water structure. 2-3 order-of-magnitude differences are seen in the computed XR intensities in the low-intensity region ($6 < L < 8$; Figure 4.16c), and up to a factor of ~2 differences appear in the region below the first Bragg peak (Figure 4.16d).

The differences in PBE trajectories follow the same trends as those observed for optB88-10% with the $3e^-$PP DFT electrons, indicating that the statistical variance between trajectories is a general phenomenon for FPMD simulations and is independent of the choice of exchange correlation functional, electron description, and other approximations. In particular, the simulated intensities of the four trajectories are nearly indistinguishable at most momentum transfers, but they vary by up to an order of magnitude for L = 6-8 (Figure 4.17a). Trajectories $s1$ and $s3$ exhibit the largest visual differences in the computed XR intensities but have similar elemental number density distributions (Figure 4.17b). The largest cumulative deviation between $s1$ and $s3$ occurs within the water region. From these results and those from optB88-10% with the $3e^-$PP, we conclude that the interfacial water region is the main contributor to the variability in χ^2 for each FPMD methodology, and it is an important factor in the strong variation of the computed XR intensities at L = 6-8 across the different simulations.

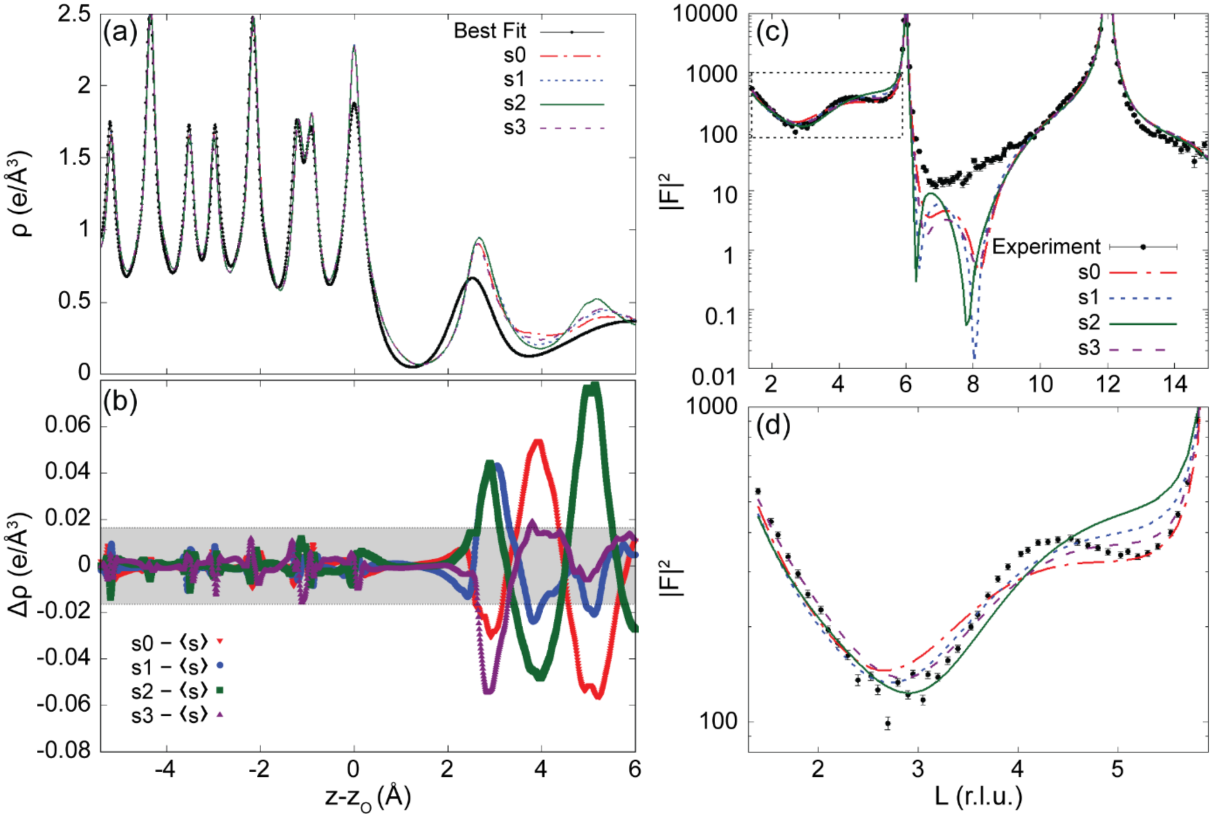

Figure 4.16. Role of sampling from four independent trajectories, s0-s3 (s0 red: s1: blue, s2: green, s3: purple), for the optB88-10% simulation using the 3e$^-$PP electron distribution. (A) The trajectories all have similar electron density distributions but with clear variations in the interfacial water region, z - $z_O > 0$ where z_O is the alumina surface oxygen layer position. (B) The difference in density, $\Delta\rho$, between each trajectory and the average of all four trajectories, $\langle s \rangle$ (which gives $\chi^2 = 57$), is largest in the water region with the s2 trajectory (green squares) showing the largest deviation; density differences for s0 - $\langle s \rangle$ are shown as red inverted triangles, for s1 - $\langle s \rangle$ as blue circles, and for s3 - $\langle s \rangle$ as purple triangles. The total variance for all trajectories averages to zero with a standard deviation of 0.0165 e$^-$/Å^3 (shaded box). (C) The XR intensities, $|F|^2$, versus reciprocal lattice unit, L (r.l.u.), vary both in the low intensity region ($6 < L < 8$) and in (D) the region below the first Bragg peak (dotted box in (C)). χ^2 values range from 41 (s0) to 92 (s2). The experimental result is shown for reference (black; experimental errors shown as 1σ uncertainties). (Individual panels provided by K. Letchworth-Weaver).

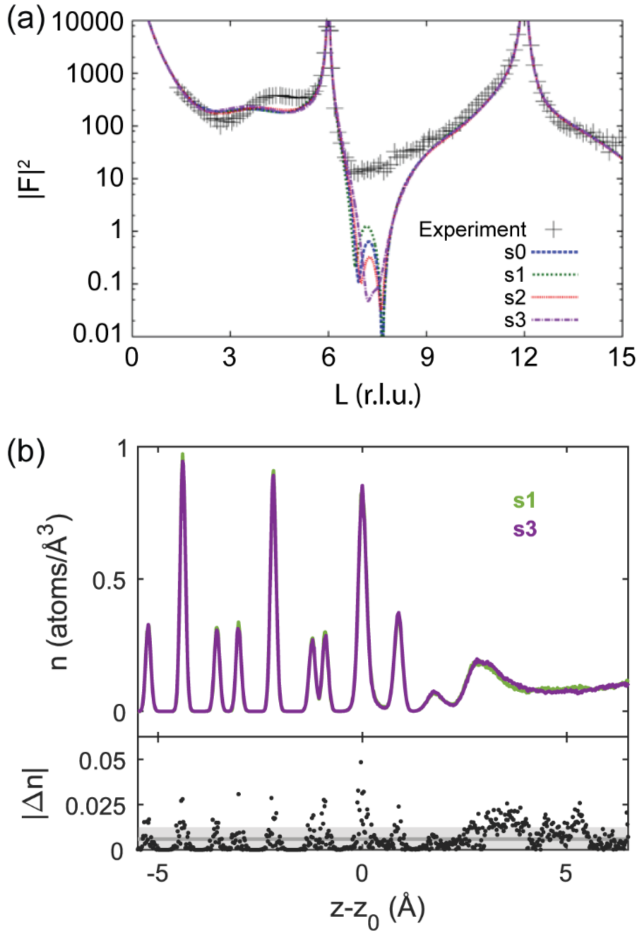

Figure 4.17. Role of sampling from four independent PBE trajectories s0-s3 (s0: blue, s1: green, s2: red, s3: purple). (A) Comparison of computed XR intensities $|F|^2$ versus reciprocal lattice unit L (r.l.u.) using the $3e^-$PP electron configuration shows a range of agreement with the experimental data with $107< \chi^2 <133$ (average = 119). (B) Top: atomic density profiles n(z) from trajectories s1 and s3 are nearly indistinguishable despite showing substantial differences in computed XR intensities (A); Bottom: the magnitude of the difference in atomic densities |Δn| (dots) averages 0.0058 ± 0.0065 atoms (gray line and shaded area).

These results show how the presence of sharp minima in XR intensities are intrinsically challenging to reproduce by DFT. Even subtle differences in the electron density distributions from trajectory to trajectory (within a given DFT methodology) can lead to significant differences in the computed XR signals that influence the calculated χ^2 level of accuracy. Therefore, the robust sampling of multiple trajectories, as previously suggested for pure water [198], is crucial to accurately describe these low-intensity features in the simulated XR signals. We propose that the high sensitivity of these minima in the XR data can, in principle, be used as a stringent test of FPMD-predicted charge densities at oxide-water interfaces, such as those that are controlled by hydrogen bonding.

4.6.5: Summary

The comparisons presented here highlight the benefits of directly pairing computational and experimental results. The initial comparisons, i.e., with a focus on the real-space structures, between the predicted electron density distributions and the experimental best-fit electron density profile showed that the FPMD can achieve qualitative accuracy. However, the quantitative agreement with the XR data was unsatisfactory. The alumina slab lattice parameter and interfacial water height from PBE gave the lowest level of agreement with the experimental result among the FPMD simulations carried out here, but even they were accurate to within ~0.2 Å. Yet, we found that the XR data are highly sensitive to these small deviations, providing a pathway to carefully investigate the accuracy of the various choices and approximations that are required to carry out FPMD simulations. These include the choice of exchange correlation functional (PBE versus optB88 in the present analysis), the choice of simulation volume (which affects not only atomic layer positions but also the water density), and the model to describe the electron density distribution via FF, a PP with valence electrons treated explicitly (the $3e^{-}$PP), or a PP with both valence and semicore electrons treated explicitly (the $11e^{-}$PP).

The goal of these solid/water interface FPMD calculations is to predict the interactions occurring at the interface. Therefore, it is crucial to evaluate the accuracy of the water structure in particular. Here, we identified several improvements in the water structure predicted by optB88 compared to PBE, indicating that vdW interactions play an important role at this interface and that an interfacial water height closer to the alumina surface is necessary to achieve agreement with the XR data. However, we still did not achieve a simulation with quantitative accuracy at the level seen in the experimental best-fit model, highlighting that further improvements are needed to achieve accurate predictions of solid-water interfacial structure *in silico*. Moreover, there are still significant errors remaining in the Al_2O_3 substrate, which, given the sensitivity of XR to bulk structures, obfuscates the χ^2 contributions from the water. In the next section, I show how we can eliminate the substrate errors and evaluate the accuracy of the water structure separately.

4.7: Optimization of FPMD structures with Empirical Fitting to XR Data

The procedure described here outlines in detail how to evaluate the accuracy of simulated interfacial water structures independent of any errors in the simulated substrate. Starting from the simulated FPMD structure, the predicted solid surface structure is optimized in order to minimize its errors with respect to the XR data. In the processes, we can also evaluate the sensitivity of the XR measurement to other features of the solid/liquid interface, including the bulk substrate lattice constant and vibrational widths and the surface relaxations within the solid. First, we parameterize the simulated structure, or in other words map it onto the parameter space of the experimental XR data analysis procedure described in Chapter 2.1.1. The simulated FPMD atomic layer positions z_j, r.m.s. widths u_j, and coverages θ_j of each atomic layer j in the solid interface (Eq. 3.8) are determined by fitting the effective electron density distributions to a series of Gaussians. The parameters derived from the FPMD serve as the initial electron density model from which we can calculate the structure factor (Eq. 3.7c) and associated reflectivity (Eq. 3.1). Subsequently, we iteratively fit the parameters until χ^2 converges.

The method is demonstrated step-by-step for the set of simulations that included a 12-layer Al_2O_3 slab described in Chapter 4.4.2. Only the first and last steps of this process (parameterization and final optimized structures, respectively) are given for the 6-layer MICCoM simulations. For the 12-layer alumina simulations, all XR calculations use atomic FF. For the 6-layer alumina simulations, I evaluate the accuracy of the water structure when the electron density distribution is defined both using atomic FF and the DFT-derived electron configuration, similar to the tests carried out in Chapter 4.6.3. To distinguish the PBE calculations from the two separate groups of simulations, I use the shorthand "PBE-*n*" where n = 6 or 12 according to the number of oxygen planes in the alumina.

4.7.1: Initial Comparisons with Experiment and Parameterization of Simulated Structures

Figure 4.18 shows the fitted PBE-12 and PBE-12+Grimme electron density profiles, and the layer heights, r.m.s. widths, and coverages are tabulated in Table A1. The fitting was carried out first on the total electron density profiles, i.e., summed over all elements (Figure 4.18a,b), and shows that the alumina layers are well-described by Gaussians. Although we do not parameterize the water layer because the goal is to optimize and eliminate errors in the substrate, we still fit the first two hydration layers to get an estimate of the water height and coverage. We assumed the adsorbed water peak near 2.6-2.7 Å in the total electron densities could be modeled as a single oxygen layer (Z = 8), but in reality this layer density is the sum of densities from overlapping oxygen and hydrogen distributions. Therefore, we also separately fit the element-specific O and H electron density profiles (as in Eq. 3.7b) for the PBE-12 and PBE-12+Grimme simulations (Figures 4.18c-f) to assess the validity of using a single layer to model the water peak. The difference in water coverage in the first hydration layer determined using the element-specific and the total electron density fits were negligible: for PBE-12, $\Theta_{\mathrm{O}} = 1.33 \pm 0.09$ H_2O/UC and $\Theta_{\mathrm{TOTAL}} = 1.39 \pm 0.15$ H_2O/UC, and for PBE-12+Grimme, $\Theta_{\mathrm{O}} = 1.38 \pm 0.03$ H_2O/UC and $\Theta_{\mathrm{TOTAL}} = 1.28 \pm 0.11$ H_2O/UC (see Tables A1 and A2). Equivalent fitting results for the PBE-6, optB88, and optB88-10% total electron density profiles (not shown) are given in Table A3.

From the above fitting, we can carefully evaluate the agreement between the predicted structures and the experimental best fit. A comparison of the interfacial FPMD and XR best fit electron densities shows that the PBE-12 and the PBE-12+Grimme simulations both capture many of the features observed in the experimental structure (Figure 4.19 and Table 4.3; see Figures 4.10 and 4.12 for PBE-6, optB88, and optB88-10% comparisons). The overall density profiles are visually similar (Figure 4.19a), and both experiment and computational approaches find that the vibrational amplitudes, *u*, and interfacial atom locations deviate from the expected bulk-like values, especially in the topmost layer (Figures 4.19b,c and Tables A1 and A3).

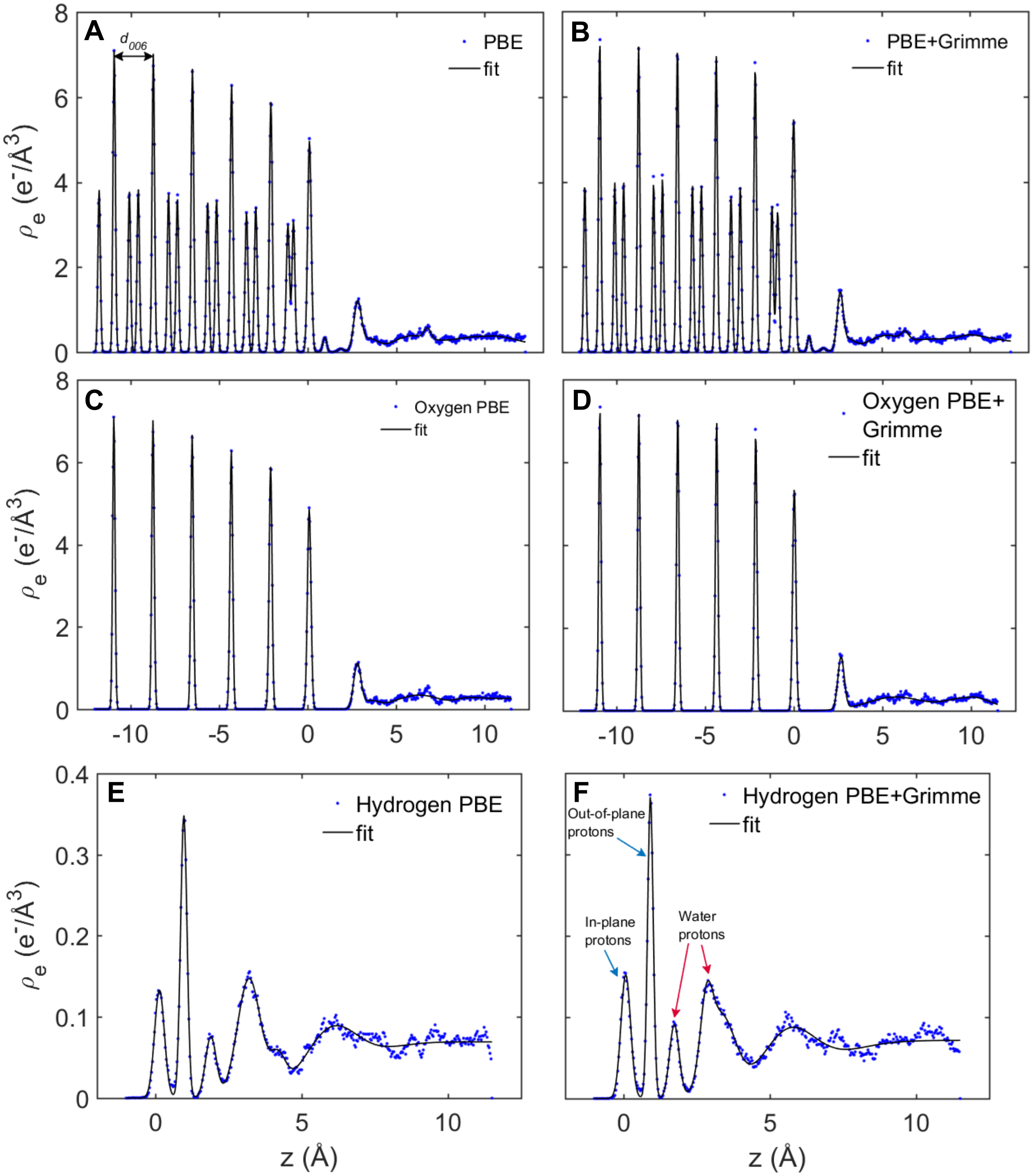

Figure 4.18. Fitting of (A) PBE-12 and (B) PBE-12+Grimme total electron density profiles to determine atomic positions and vibrational amplitudes for parameterization of FPMD structures. Separate fits of the oxygen-specific profiles in (C) PBE-12 and (D) PBE-12+Grimme and the hydrogen-specific profiles in (E) PBE-12 and (F) PBE-12+Grimme resulted in negligible changes to the O coverage in the first adsorbed water layer compared to the values from fitting the total electron densities. Arrows in (F) indicate protonation in and out of the plane of the alumina surface and protons bound to the first adsorbed water layer.

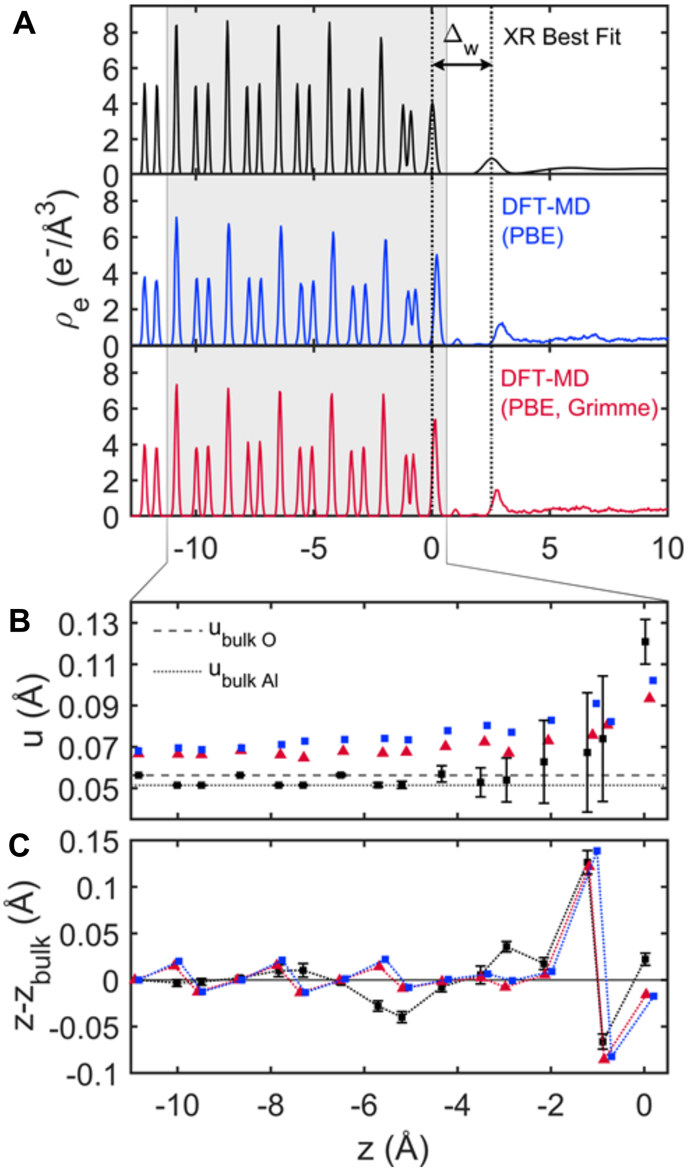

Figure 4.19. Comparison of experimental best-fit structure (black) with the predictions from the PBE-12 (blue) and PBE-12+Grimme (red) FPMD simulations. (A) The experimental effective electron density profile (top) agrees qualitatively with that from PBE-12 (middle) and PBE-12+Grimme (bottom). The shaded gray area indicates the alumina surface layers; dotted vertical lines indicate the positions of the XR best-fit alumina surface oxygen and first hydration layer with interfacial water height Δ_w. (B) The simulations predict bulk alumina vibrational amplitudes *u* larger than those determined experimentally, shown as a dashed line for O layers and a dotted line for Al layers. (C) Displacements of each atomic layer relative to its expected bulk position z_{bulk} (defined using the experimental lattice constant for the XR best fit and the slab lattice parameters for the FPMD simulations) indicate surface relaxations four unit cells deep in the best-fit structure but only in the topmost unit cell in the FPMD structures.

The simulations also show key differences with the experimental best fit. The alumina slab lattice parameter from PBE-12 was ~2.1% larger than the experimental value (Table 4.3), which is notably larger than the slab lattice parameter of the PBE-6 simulation (Table 4.2). The inclusion of the Grimme correction improved the prediction of the alumina slab lattice parameter to ~1.3% larger than the known value, which is similar to the value obtain with the optB88 exchange correlation functional using a 3e$^-$PP but not as accurate as the value obtained with optB88 and an 11e$^-$PP. As with the set of simulations using a 6-layer alumina slab, the 12-layer slab lattice parameters are larger than those from the corresponding fully periodic bulk DFT calculation, which differed from the known structure by only +0.2%. It is interesting to note that the expansion of the lattice parameter from bulk to slab geometry was worse in the case of the 12-layer alumina slab simulations than in the case of those using a 6-layer slab. While the expansion effect appears to be universal to FPMD calculations using such a geometry [259], it is clear that other choices made in the calculations also play a role. In addition to employing a different alumina slab size, the two sets of simulations were also carried out on different platforms, with different descriptions of the valence electrons (i.e., the PP), and using different thermostats.

Table 4.3. Structure characteristic lengths (Å).

Feature	XR Best Fit	PBE-12	PBE-12+Grimme
d_{006}	2.1663	2.2112	2.1944
$\langle u \rangle^a$	0.061(3)	0.077(6)	0.071(3)
$dz_{rms}{}^b$	0.041	0.042	0.038
$\delta_{rms}{}^c$	-	0.0236	0.0227
Δ_w	2.519(14)	2.729(8)^d	2.628(5)

^{a}Mean vibrational amplitude within the top 5-layers of Al_2O_3 (uncertainties in parentheses); ^{b}r.m.s. displacement from the expected bulk atom positions in the top 5 Al_2O_3 layers; ^{c}r.m.s. deviation from XR best fit after bulk corrections; ^{d}Uncertainties for Gaussian fits of the predicted electron density profiles.

It is also apparent that the PBE-12 and PBE-12+Grimme electron density profiles have alumina peaks that are broader and shorter than those in the XR best-fit model (Figure 4.19a), which results from the predicted vibrational amplitudes, u, being larger than expected (Figure 4.19b). PBE-12 overestimates u of atoms in the alumina surface layers by an average of 0.016 Å, or 26% larger than the vibrational widths derived from the experimental XR data analysis (Table 4.3). PBE-12+Grimme performs slightly better, overestimating the vibrational amplitudes by 0.01 Å on average, or roughly 16%. In general, all simulations predict bulk-like vibrational amplitudes larger than the known bulk alumina values (shown for PBE-12 and PBE-12+Grimme in Figure 4.19b), and the simulations using the 12-layer alumina slab give less accurate bulk r.m.s. widths than those using the 6-layer slabs (see Tables A1 and A3). However, it is not possible at this time to determine if the larger slab size is responsible for this result due to the number of other differences between the simulations described previously.

Another source of discrepancies is in the predicted alumina interfacial surface relaxation profiles, i.e., the vertical layer displacement from the expected bulk position. Here, the expected bulk position is defined using the internally-consistent lattice spacing, i.e., the experimental lattice constant for the XR best fit and the slab lattice parameters for FPMD structures so as to avoid a "background" slope on the surface relaxations as seen in Figure 4.9 for the 6-layer alumina FPMD calculations. PBE-12 and PBE-12+Grimme reveal significant vertical displacements only in the first Al_2O_3 unit cell (Figure 4.19c), which is also observed for the PBE-6, optB88, and optB88-10% simulations (Figure 4.9). This differs from the XR best-fit result, which includes a non-negligible oscillatory relaxation profile that extends four layers into the alumina surface (Figure 4.19c). In addition, all of the simulations predict an inward relaxation of the surface-most alumina oxygen layer, whereas the experimental best fit shows that this layer relaxes outward from the bulk. The r.m.s. difference between the predicted PBE-12 and the XR best fit alumina surface atom positions is 0.024 Å (Table 4.3). The PBE-12+Grimme simulation performs similarly, deviating from the XR best fit relaxation profile by 0.023 Å.

The differences in the interfacial water region are similar to those seen with the PBE-6, optB88, and optB88-10% simulations. A notable, but expected, difference is the appearance of peaks in the simulated profiles at $0 < z < 2.5$ Å due to the presence of hydrogen atoms that are not in the experimental density profile (Figure 4.19a). The simulations also show interfacial water heights Δ_w in excess of that in the experimental best fit with Δ_w(PBE-12) = 2.73 Å (Table 4.3) in agreement with the PBE-6 result (Table 4.2). The inclusion of the Grimme correction slightly improved the prediction of the interfacial water height to Δ_w(PBE-12+Grimme) = 2.63 Å (Table 4.3), which agrees with the value obtained using the optB88 functional after controlling for the simulation supercell volume (Table 4.2). However, the Grimme correction decreased the accuracy of the first hydration layer density with respect to the experimental best fit (Θ = 1.4 H_2O/UC, 1.3 H_2O/UC, and 1.83 H_2O/UC for PBE-12, PBE-12+Grimme, and the XR best fit, respectively).

Before we can optimize the simulated structures, there are several considerations for inputting the structures described above into the XR analysis framework. The code requires input of the atomic positions for the solid surface layers as $1 + dz$ where dz is the layer displacement from the expected bulk position z_{bulk}. $dz > 0$ describes displacements toward the water while $dz < 0$ describes displacements toward the bulk substrate. Therefore, we must convert the absolute layer positions z_i obtained from Gaussian fits of the simulated density distributions (Tables A1 and A3). For the empirical optimization procedure, we define z_{bulk} using the experimental bulk structure rather than the simulation slab lattice structure. This initially creates a mismatch between the bulk and interface lattices as described in Chapter 4.5. However, the disagreement between these two regions will be eliminated as the surface layer positions move to reduce χ^2 and will ultimately give the best level of agreement with the XR data due to the high sensitivity of XR to bulk structures [258].

The XR analysis code also models the r.m.s. layer widths of the substrate according to an exponential with a surface enhancement effect that decays into the bulk substrate (Eq. 4.4), so we need to convert the individual Gaussian layer widths from the simulations accordingly. We fit the alumina slab vibrational amplitudes u_j in Tables A1 and A3 to the functional form of Eq. 4.4 to estimate the surface enhancement and decay parameters predicted by the simulations. We observed that different atom layers within a single vertical unit cell (e.g., repeating Al-Al-O_3) followed slightly different exponential decays from one another (Figure 4.20). For example, all "bottom" Al layers (i.e., closer to the bulk substrate) had a different vibrational amplitude surface enhancement and decay length than all "top" Al layers (i.e., closer to the alumina surface). Furthermore, each had a bulk-like r.m.s. width greater than those determined experimentally. Therefore, we introduced additional parameters to incorporate the simulated structures into the XR analysis code. Instead of having a single surface enhancement and a single decay length to describe all alumina surface layers, we specified $u_{enh}(\mathrm{Al_{bot}})$, $u_{enh}(\mathrm{Al_{top}})$, and $u_{enh}(\mathrm{O})$ and $\lambda_{enh}(\mathrm{Al_{bot}})$, $\lambda_{enh}(\mathrm{Al_{top}})$, and $\lambda_{enh}(\mathrm{O})$. We additionally modified Eq. 4.4 as

$$u_j = u_0\left(k_a + u_{enh,a}e^{z_j/\lambda_{enh,a}}\right) \qquad 4.6$$

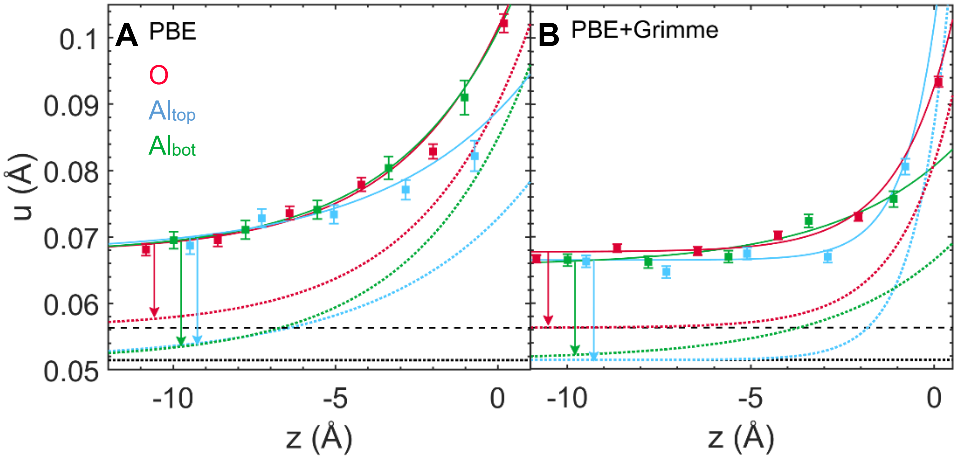

Figure 4.20. Fitting of atom-specific vibrational amplitude surface enhancements in (A) PBE-12 and (B) PBE-12+Grimme FPMD simulations. Symbols are the r.m.s. widths determined from Gaussian fits to the simulated electron density distributions (error bars are the uncertainties on those fits), and lines through the data are the exponential fits according to Eq. 4.5 (O atoms in red, Al_{top} atoms in blue, and Al_{bot} atoms in green). The color-coordinated arrows and dotted exponential curves indicate a bulk correction imposed on the simulated r.m.s. widths during the subsequent empirical optimization procedure in order to bring the simulated bulk widths in line with the known experimental values (u_{Al} = 0.05144 Å as black dotted line; u_O = 0.0563 Å as black dashed line).

where the r.m.s. width of each layer j is described by the known experimental bulk vibrational amplitude u_0 (as in Eq. 4.4), k is a constant associated with the difference of u in the simulated slab centers compared to the known bulk u values, and the subscript ‘a’ specifies the “atom type” (Al_{bot}, Al_{top}, or O). The same process is carried out for the PBE-6, optB88, optB88-10% simulations, not shown.

Finally, the simulated interfacial water structure is not parameterized and, therefore, must be “embedded” between the parameterized alumina interface and a bulk water layer (Figure 4.21). This is accomplished by defining an error function window around the simulated interfacial water layer such that the simulated alumina density is excluded, as demonstrated in Figure 4.21. Semi-infinite error functions are also applied to the alumina substrate (in the negative direction) and to the bulk water (in the positive direction) to ensure a continuous electron density distribution between the boundaries of the embedded FPMD region and the rest of the structure. The total electron density is given by

$$\begin{aligned}\rho(z) = {} & \rho_{subst}(z) \times \frac{1}{2}\left[1 - \mathrm{erf}\left(\frac{z - z_s}{\sigma_s}\right)\right] + \\ & \rho_{\mathrm{FPMD}}(z) \times \frac{1}{4}\left[1 + \mathrm{erf}\left(\frac{z - z_s}{\sigma_s}\right)\right] \times \left[1 - \mathrm{erf}\left(\frac{z - z_w}{\sigma_w}\right)\right] + \\ & \rho_w \times \frac{1}{2}\left[1 + \mathrm{erf}\left(\frac{z - z_w}{\sigma_w}\right)\right]\end{aligned} \qquad 4.7$$

where $\rho_{subst}(z)$ is the electron density of the parameterized solid alumina substrate with the complementary error function, 1 – erf, applied to the “top” edge of the substrate at $z = z_s$ with edge width σ_s; $\rho_{\mathrm{FPMD}}(z)$ is the electron density of the embedded FPMD region with an error function applied to the “bottom” end at the boundary between the solid substrate and FPMD water region ($z = z_s$, width = σ_s) and the complementary error function applied to the “top” end at the boundary

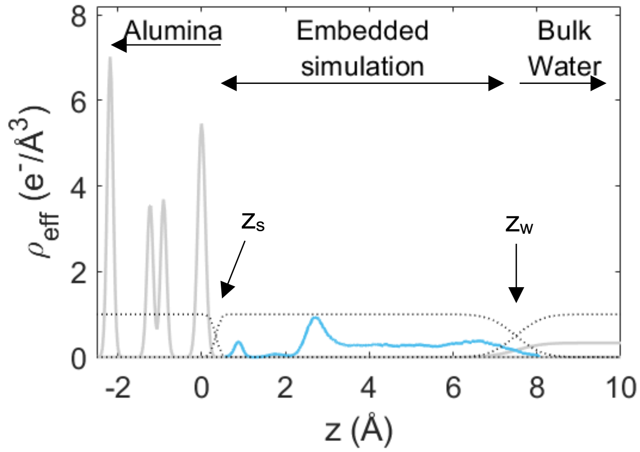

Figure 4.21. Diagram of embedded interfacial water profile as part of parameterization procedure for eventual optimization of simulated structures with respect to XR data, shown for the optB88 case. An error function window (dotted black line) is defined around the specified section from the simulation to be embedded (blue). Complementary error functions are applied to the adjacent alumina and bulk water regions to ensure a continuous electron density distribution. z_s and z_w indicate the boundaries of the substrate and the bulk water, respectively, according to Eq. 4.7.

between the FPMD water and bulk water at $z = z_w$ and with r.m.s. edge width σ_w; $\rho_w = 0.33$ e$^-$/Å^3 is the density of bulk water described as an error function profile extending infinitely in the positive-z direction from z_w and with r.m.s. edge width σ_w.

We verify the accuracy of the parameterized structure qualitatively by visual inspection of the effective electron density distributions compared to the as-simulated FPMD structures and quantitatively by comparing the computed χ^2 values (using atomic form factors) from the two approaches. In the first case, we extend the error function window to include the entire simulated structure, including alumina and water, between a bulk substrate and bulk water layer and overlay with the parameterized alumina surface electron density distribution. This is demonstrated in Figure 4.22a-c for the PBE-6, optB88, and optB88-10% simulations and shows that the parameterized structures accurately reproduced the as-simulated alumina interfaces. Minor differences are observed in the peak densities, likely due to the simplifying assumption that r.m.s. layer widths can be modeled by an exponential decay, which is a good approximation but not exact (Figure 4.20). Next, we calculate the XR intensities from the as-simulated and the parameterized structures and compare their level of agreements with the XR data. The results show high consistency between the XR signals (PBE-6, optB88, and opB88-10% in Figure 4.22d-f; PBE-12 and PBE-12+Grimme in Figure 4.22g,h) with some minor differences in the computed XR as a result of small errors in the parameterization of the r.m.s. widths. As expected from the direct comparisons of FPMD and XR data in Chapter 4.6, it is apparent that the calculated signals deviate significantly from the experimental data. The χ^2 values for these initial comparisons are given in Table 4.4. The simulations with the 12-layer alumina slab Calculations were also carried out with the slab lattice structures (i.e., as extracted from the middle layer of the simulated alumina slabs), which gave a superior level of agreement for PBE but worse agreement for the optB88 calculations.

Table 4.4. Initial χ^2 accuracy of simulated FPMD XR intensities from fully "embedded" structures (including Al_2O_3 surface and interfacial water between bulk alumina and bulk water) and from structures with a "parameterized" Al_2O_3 surface with embedded FPMD interfacial water.

Simulation	d_{006} (Å)[a]	Embedded[b]	Parameterized[b]
PBE-6	2.2028	104	-
	2.1663	112	124
optB88 (11e$^-$PP)	2.1843	105	-
	2.1663	83	90
optB88-10% (11e$^-$PP)	2.1809	75	-
	2.1663	54	51
PBE-12	2.1663	219	223
PBE-12+Grimme	2.1663	122	128

[a] d_{006} values used to define the bulk Al_2O_3 substrate for empirical analysis were either those determined by the simulation (the slab lattice parameter) or the known experimental lattice spacing of 2.1663 Å. [b] χ^2 calculations use atomic form factors.

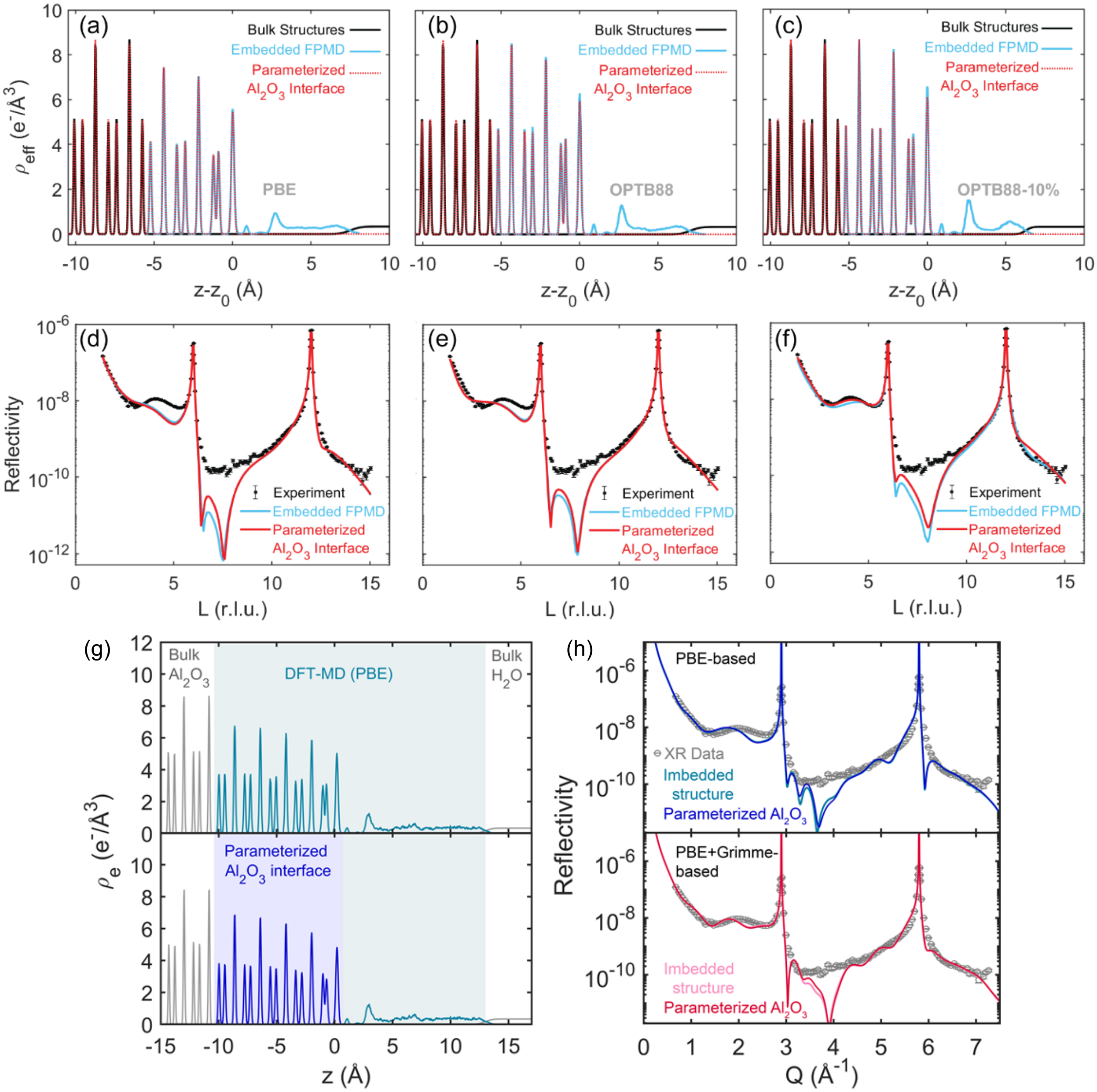
(a)
(b)
(c)
Bulk Structures
Embedded FPMD
Parameterized
Al_2O_3 Interface
PBE
OPTB88
OPTB88-10%
ρ_{eff} ($e^-/Å^3$)
z-z_0 (Å)
(d)
(e)
(f)
Reflectivity
Experiment
Embedded FPMD
Parameterized
Al_2O_3 Interface
L (r.l.u.)
(g)
Bulk
Al_2O_3
DFT-MD (PBE)
Bulk
H_2O
Parameterized
Al_2O_3 interface
ρ_e ($e^-/Å^3$)
z (Å)
(h)
PBE-based
XR Data
Imbedded
structure
Parameterized Al_2O_3
PBE+Grimme-
based
Imbedded
structure
Parameterized Al_2O_3
Reflectivity
Q ($Å^{-1}$)

Figure 4.22. Accuracy of embedded FPMD simulations for empirical fitting. The (A) PBE-6, (B) optB88, and (C) optB88-10% effective electron densities of the fully embedded structures (i.e., as-simulated including alumina and water regions; blue) overlap well with the parameterized Al_2O_3 interface structures (red), showing qualitative accuracy for the parameterization process. The simulated XR intensities calculated from the fully embedded and parameterized (D) PBE-6, (E) optB88, and (F) optB88-10% density profiles show similar disagreements with the experimental XR data (black circles with error bars shown as 1σ uncertainties) with minor differences resulting from the parameterization of the Al_2O_3 surface. (G) Comparison of the fully embedded PBE-12 FPMD electron density profile (top) and that with the parameterized Al_2O_3 interface (bottom). Embedded structures are shown in teal, parameterized region in blue, and bulk structures in gray. (H) XR signals calculated from the fully embedded (teal) and parameterized (blue) PBE-12 structures (top) show similar levels of agreement with the XR data (gray circles); XR signals from the fully embedded (pink) and parameterized (red) PBE-12+Grimme structures (not shown) also show similar levels of agreement with the XR data.

Finally, the position of the error function step edges and their r.m.s. widths (Eq. 4.7) were found to have a non-negligible effect on χ^2. These parameters were optimized as a function of the parameters z_i and σ_i ($i = s, w$) (only for the PBE-6, optB88, and optB88-10%), but within certain constraints:

(1) For PBE-6 and optB88, χ^2 could be reduced by truncating the embedded FPMD water structure at some *z* within the first hydration layer (i.e., by increasing z_s or σ_s such that a portion of the first peak was removed) or by truncating the FPMD structure in the region of the second hydration layer (by decreasing z_w or increasing σ_w such that a portion of the second peak was removed). Such structures then only partially describe the FPMD predictions and were avoided.

(2) I determined that the χ^2 of the optB88 calculations could be improved by significantly reducing z_s to the point of partially including the electron density of the alumina surface oxygen. This then leads to an overlap with the density in the surface layer

from the parameterized interface and effectively double counts a portion of the electron density there. These structures were avoided.

(3) Also in the case of the optB88 calculation, certain combinations of z_w and σ_w that produced a sharp step edge between the FPMD water region and the bulk water region also led to an improvement in χ^2. The abrupt step results from an erf cutoff that extends beyond the end of the simulation. Such cases were determined to produce non-physical electron density profiles.

Altogether, a series of rules for the error function positions and edge widths were devised to enable a physical and accurate assessment of the predicted water densities: 1) the included section of the FPMD simulations must be sufficiently separate from the parameterized alumina interface so as to avoid double counting of electron densities; 2) the onset of the FPMD water region must include the complete first hydration layer, i.e., including the full width of the electron density distribution of this layer; 3) the second hydration layer peak of the simulated FPMD cannot be truncated by the error function window; and 4) the boundary between the FPMD water and bulk water must present a physical, continuous transition from one to the other. The PBE-12 and PBE-12+Grimme analysis was carried out before I explicitly defined these rules. Nevertheless, the analysis of the 12-layer simulations qualitatively satisfies them, so the χ^2 presented herein are expected to be close to the optimal values that would be obtained if z_i and σ_i were to be optimized with those simulations.

4.7.2: Sensitivity to Alumina Bulk-Interface Lattice Mismatch

We scaled the alumina slab interface so that the inter-layer spacing would be consistent with the experimental value. In practice, this requires adjusting the input parameters z_j without allowing them to move freely (i.e., without optimizing with respect to χ^2) because optimizing the layer positions would simultaneously change the surface relaxation profile. To maintain the same surface relaxation profile and only rectify the lattice spacing disagreement (essentially remove the slope seen on the surface relaxation profile when the simulated layer positions are referenced to the experimental bulk lattice; Figure 4.9), I converted the simulated atomic displacements from bulk, dz, to the corresponding fractional coordinates δz:

$$\delta z = \frac{dz - z_0}{d_{006}^{exp}} \tag{4.8}$$

where all layers are referenced to the zeroth layer in the unit cell z_0 such that in a perfect bulk the first layer of the adjacent unit cell has δz = 1. Subsequently, the new atomic layer position parameters with the appropriate lattice constant scaling were obtained by multiplying δz by the corresponding FPMD slab lattice parameter and adding 1. The resulting XR intensities were significantly more accurate with an improvement from $\chi^2 = 223$ to $\chi^2 = 91$ for the scaled PBE-12 structure (Figure 4.23a-i-ii) and from $\chi^2 = 128$ to $\chi^2 = 61$ for the scaled PBE-12+Grimme structure (Figure 4.23b-i-ii). Most of the χ^2 reduction originates near the alumina Bragg peaks at momentum transfers Q = 2.9 Å^{-1} and 5.8 Å^{-1}, as expected. Thus, the inaccuracy of the bulk alumina lattice constant in the FPMD supercells, though small, contributes significantly to the disagreement with XR data.

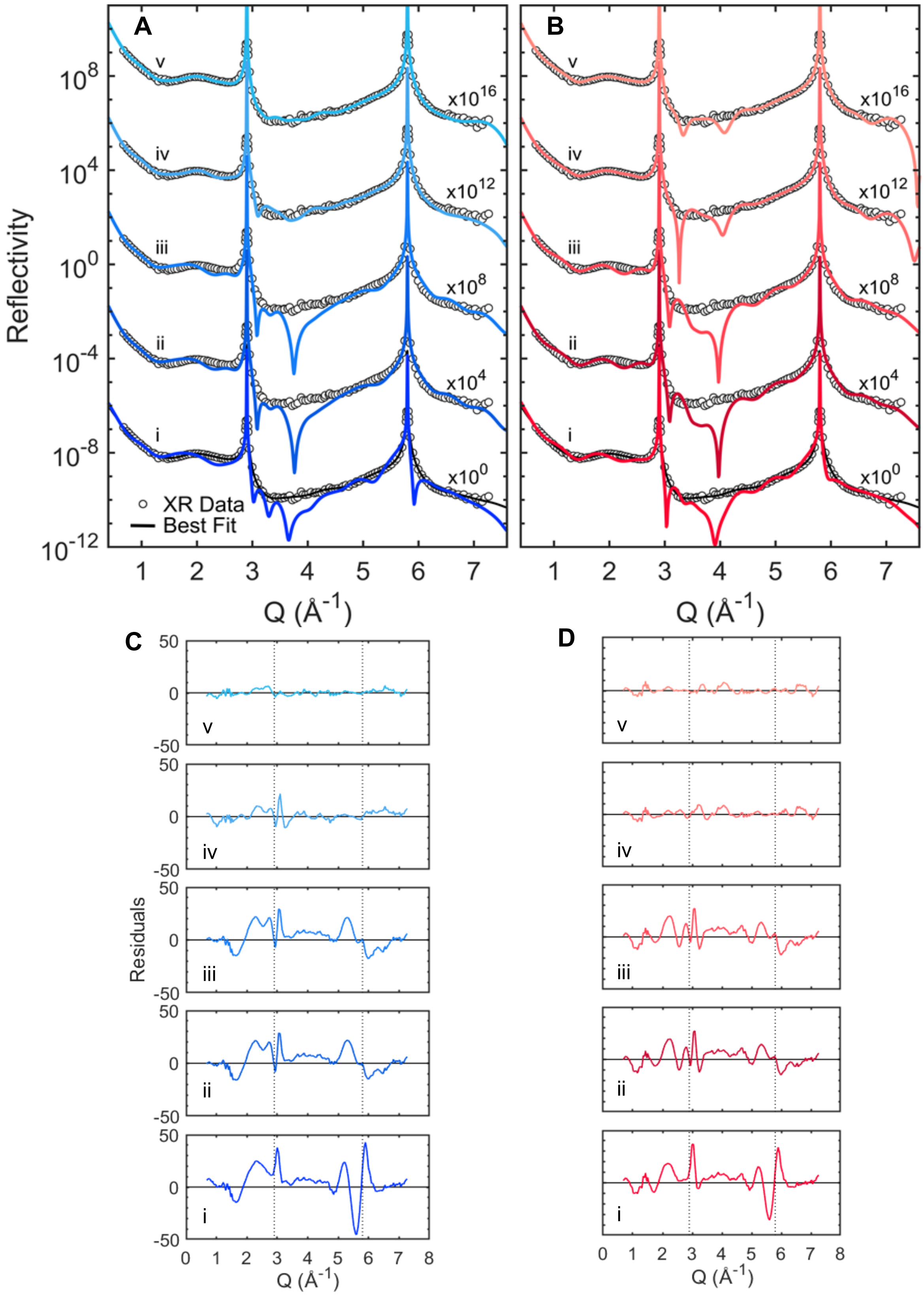
A
B
C
D
Reflectivity
10^8
10^4
10^0
10^{-4}
10^{-8}
10^{-12}
v
iv
iii
ii
i
x10^{16}
x10^{12}
x10^8
x10^4
x10^0
○ XR Data
— Best Fit
Q (Å^{-1})
Residuals
50
0
-50
0 1 2 3 4 5 6 7 8

Figure 4.23. A series of XR curves (i-v) calculated from FPMD-based effective electron density distributions show improvements with each optimization step that was performed starting from (A) the PBE-12-simulation and (B) the PBE-12+Grimme simulation. The XR intensities are calculated for: (i) initial prediction, χ_A^2 = 223 and χ_B^2 = 128 for PBE-12 and PBE-12+Grimme, respectively; (ii) structures with a scaled lattice constant, χ_A^2 = 91 and χ_B^2 = 60; (iii) structures with corrected bulk vibrational amplitudes, χ_A^2 = 94 and χ_B^2 = 63; (iv) optimized alumina surface relaxations, χ_A^2 = 22 and χ_B^2 = 11; and (v) optimized water heights, χ_A^2 = 6 and χ_B^2 = 8. Calculated intensities are compared to the XR best fit (χ^2 = 1.54, black line) and XR data (gray circles) for reference and offset as indicated for clarity. (C) and (D) show the residual errors of each simulated XR intensity for optimization steps i-v starting from PBE-12 and PBE-12+Grimme, respectively. All simulated XR signals include the optimization of the extrinsic interfacial roughness parameter.

4.7.3: Sensitivity to Vibrational Amplitudes

Next, the simulated vibrational amplitudes were corrected based on the excess seen at the bulk-like positions by setting the factor $k_a = 1$ in Eq. 4.6 so that u decays to the known bulk values. This had only a small effect on the quality of fit of the calculated XR intensities from both simulations, resulting in χ^2 = 94 for the PBE-12-derived structure (Figure 4.23a-iii) and χ^2 = 60 for the PBE-12+Grimme-derived structure (Figure 4.23b-iii). The vibrational amplitude surface enhancement parameter and decay were kept fixed at the input values. Therefore, the correction for the bulk u values effectively leads to a decrease in the r.m.s. width of the alumina surface oxygen layer from the predicted PBE-12 and PBE-12+Grimme values, which were already slightly smaller than the value derived from the experimental data. The smaller than expected r.m.s. width of the surface-most layer may contribute to the small relative change in χ^2 accuracies despite an improvement in the bulk widths. Still, these results together with the large derived uncertainties in u in the XR best fit (Figure 4.19 and Table 4.1) indicate a relative insensitivity of XR to small changes in interfacial vibrational amplitudes. At this point, errors in the bulk alumina have been corrected, so the remaining χ^2 discrepancies are due to differences between the predicted and measured interfacial structures.

4.7.4: Sensitivity to Alumina Interface Structure

The alumina atom position parameters were optimized (from the previously lattice- and vibrational amplitude-corrected structures) using the XR data least-squares fitting routine until the χ^2 agreement with the XR data converged. The water position above the alumina surface was shifted along with any change in position of the alumina surface oxygen layer to maintain the interfacial water height at the value predicted by FPMD. Following this step, all remaining errors are due the interfacial water profile, including its height above the alumina surface, the occupation within the first hydration layer, and the oscillatory decay to bulk water. The agreement of the calculated XR intensities with the XR data improved to $\chi^2 = 22$ and $\chi^2 = 11$ for the PBE-12-based and PBE-12+Grimme-based simulations, respectively (Figure 4.23a-iv and 4.23b-iv, respectively, and Table 4.5). These improvements (nearly 80% for both simulations) highlight the extreme sensitivity of high-resolution XR measurements to sub-Å displacements in the interface region given that the initial predicted FPMD surface relaxations (Figure 4.19c) differed from the XR best fit structure by only ~0.02 Å, on average, in both PBE-12 and PBE-12+Grimme (Table 4.3). The χ^2 improvement results (in part) from substantially reduced oscillations in the XR intensities near Q ≈ 3-4 Å^{-1} compared to the previous step of the optimization procedure (Figures 4.23ab-iii-iv). Notably, we previously attributed low-intensity reflectivity at these scattering conditions to discrepancies in the water structure (Chapter 4.6.4). Here, only the solid structure has changed while the water structure is incorporated as predicted. Together, these results indicate that the calculated interference of X-rays scattered from all layers within the alumina interface with those scattered from the adjacent water was inconsistent with the behavior defined by the XR data.

Table 4.5. χ^2 values for optimized alumina solid structures derived from FPMD, using atomic FF (and DFT electrons for the 6-layer slab simulations) with a fixed FPMD water structure.

Simulation	**Atomic FF**	**DFT e$^-$**
	Optimized (χ^2_{fA})^a	**Optimized (χ^2_{fDFT})^a**
PBE-6	11.2	5.6
optB88 (11e$^-$PP)	17.0	14.8
optB88-10% (11e$^-$PP)	5.6	5.5
PBE-12	22	-
PBE-12+Grimme	11	-

[a] *fA* and *fDFT* indicate, respectively, the final χ^2 values calculated with the water structure incorporated either using elemental number density profiles and atomic FF or directly from the simulation DFT electron density.

An oscillatory surface relaxation pattern similar to the one found in the XR best fit emerged following the alumina surface refinements (Figure 4.24a). This suggests that oscillatory behavior is necessary for agreement with the XR data. Additionally, while the agreement of the optimized alumina relaxation patterns with that derived in the XR best fit has improved, the residual discrepancies between the predicted XR signals and the XR data (Figure 4.23c-iv and d-iv) indicate that there remain additional inconsistencies with respect to other features of the FPMD-based interfacial structure (i.e., in the bonding region between solid and liquid and in the water structure).

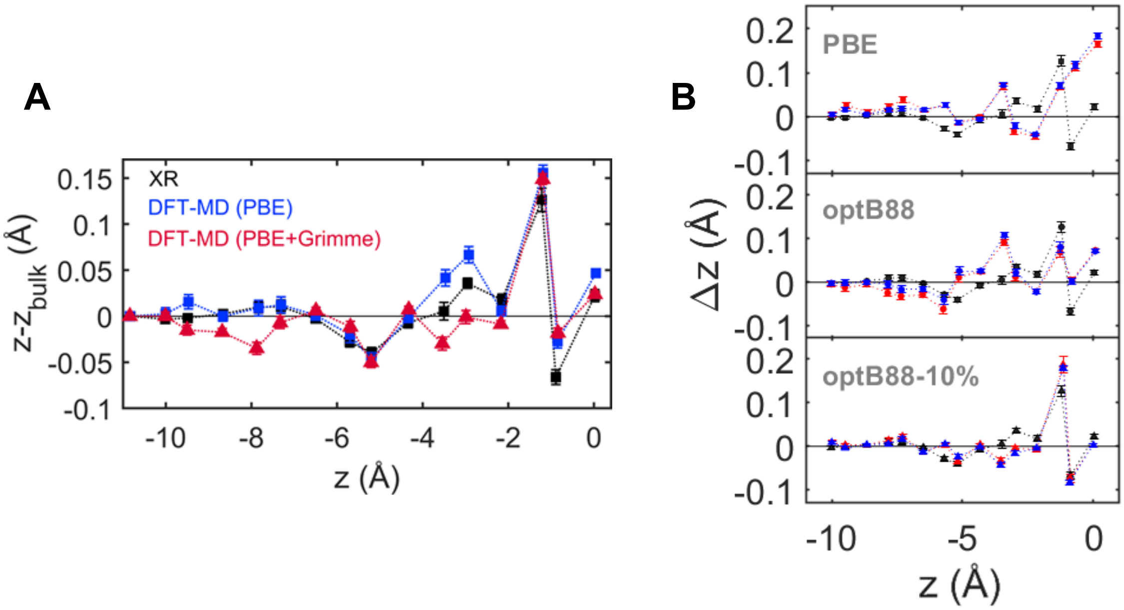

Figure 4.24. The optimized alumina relaxation behaviors obtained with a fixed water profile height as defined by FPMD. (A) The surface displacement fields had r.m.s. differences from the XR best fit relaxation (black) of 0.0192 Å for the PBE-12-based simulation (blue) and 0.0245 Å for the PBE-12+Grimme-based simulation (red). (B) The optimized surface relaxation profiles derived from PBE-6 (top), optB88 (middle), and optB88 with 10% compression (bottom) are compared to the experimental best-fit result (black); surface relaxations optimized with an FPMD water profile defined using the predicted elemental number densities and atomic FF (red) are not statistically different from those optimized using an FPMD water structure defined directly using DFT the electron distributions (blue).

The final χ^2 of XR intensities computed from the optimized structures from PBE-6, optB88, and optB88-10% (Table 4.5; Figure 4.25a,b) were overall similar to those from the optimized structures derived from PBE-12 and PBE-12+Grimme. We obtained χ^2_{fA} = 11.2, 17, and 5.6 for PBE-6-derived, optB88-derived, and optB88-10%-derived structures, respectively, when the FPMD water electron density distributions were described using atomic FF (the subscript “fA” indicates final with atomic FF). These results indicate that the optB88-10% simulation predicted the most accurate interfacial water structure among the FPMD simulations compared in this thesis.

This further supports the idea that vdW interactions play an important role at this oxide/water interface, and vdW functionals are needed to accurately predict realistic interfacial phenomena for such systems.

We also carried out calculations with the FPMD water layer described by DFT electron densities directly using the 3e^{-}PP for PBE-6 and 11e^{-}PP for both optB88 and optB88-10% (recall that the 11e^{-}PP defines the core-valence interactions for the Al atoms, so the electron density distribution in the water region is the same as that obtained with the 3e^{-}PP). The structure factor of the rest of the electron density profile (i.e., bulk and interfacial alumina and bulk water) was calculated using atomic FF. The χ^2_{fDFT} ("$fDFT$" indicates final with DFT e^{-}) are universally better than those obtained with the water electron density described by atomic FF, yielding χ^2_{fDFT} = 5.6, 14.8, and 5.5, for structures derived from PBE-6, optB88, and optB88-10%, respectively. The high accuracy when using the PBE-6 water structure with DFT e^{-}, comparable to that of the optB88-10% results, was surprising given that the result with the PBE-6 elemental water density and atomic FF was not as good. It was also surprising that both methods to calculate the optB88 water electron density distribution gave the worst χ^2 results despite optB88 giving a smaller water height and a larger water occupation in the first hydration layer than PBE.

The origin of the remaining χ^2 errors is not immediately obvious by looking at the interfacial electron density distributions (Figure 4.25a), but the resulting XR signals (Figure 4.25b) show better qualitative agreement with the data for the DFT-based calculations versus those using atomic FF. We highlight, in particular, the remaining discrepancies with the XR data in the region between the Bragg peaks (6.5 Å^{-1} < L < 9 Å^{-1}), which we previously identified as being associated with, but not exclusively due to, the interfacial water. The optimized alumina surface relaxation

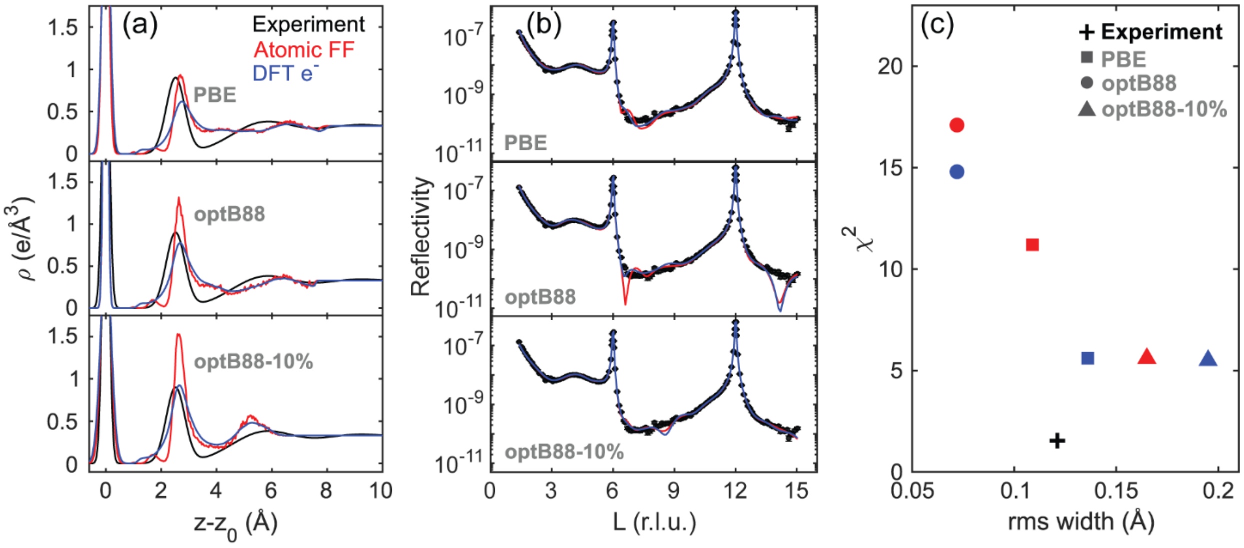

Figure 4.25. Optimized alumina interface structures with fixed simulated water from FPMD. (A) Total electron densities from PBE-6, optB88, and optB88-10%. (B) The final simulated XR intensities after optimizing the Al_2O_3 surface. (C) The χ^2 associated with the structures in (A) are correlated with the r.m.s. width of the alumina surface oxygen. Red data indicate a water structure that was calculated from atomic number densities and atomic FF; blue data indicate a water structure calculated directly from DFT electron density predictions; black data indicate the experimental result.

patterns derived from these 6-layer alumina simulations (Figure 4.24b) do not explain the observed χ^2 trends for this set of calculations. In all cases, the oxygen layer relaxes outward from the bulk (qualitatively consistent with the experimental best fit, whereas the initial FPMD simulations showed the surface oxygen relaxing inward; see Figure 4.9). However, the optimized relaxation derived from the PBE-6 simulation shows the greatest distortion of the top unit cell (the surface-most Al-Al-O_3) with all three of these layers monotonically relaxing away from the bulk. For comparison, the XR best-fit structure and the optimized surface relaxations from PBE-12, PBE-12+Grimme, and optB88-10% all show that the top Al layer relaxes inward toward the bulk. From these results, one might expect that the PBE-6-derived structure should result in the worst χ^2 among the simulations compared here, but this is not the case.

We also found that the optimized alumina surface relaxation was independent of how the water structure was calculated (i.e., using number densities and atomic FF versus electron distributions directly from DFT). The r.m.s. deviations of the optimized relaxation profiles from the experimental best-fit model show no statistical differences for a given simulation: for PBE-6, the optimized Al_2O_3 relaxation patterns deviated from the experiment by 0.070 ± 0.003 Å (number density) and 0.072 ± 0.003 Å (DFT electron density); for optB88, these deviations were 0.042 ± 0.003 Å (number density) and 0.043 ± 0.003 Å (DFT electron density); and for optB88-10%, these deviations were 0.025 ± 0.004 Å (number density) and 0.027 ± 0.003 Å (DFT electron density).

Details of the water structure beyond the first hydration layer also do not explain the observed χ^2 trends. The PBE-6 and optB88 second hydration layers are qualitatively more similar to one another and to the experimental best fit than those in the optB88-10% calculation (i.e., in terms of the maximum peak density and the distance between hydration layers; Figure 4.25a). One might expect these details to contribute to a worse χ^2 for the optimized structures derived from the optB88-10% simulation, which is not what we observe. The XR best fit shows a low-density region between the first and second hydration layers ($z \sim 3.5$), which is qualitatively reproduced by the optB88-10% simulation and to a lesser extent in the optB88 simulation. The expected χ^2 contributions from this feature would lead optB88 to outperform PBE-6, in line with the expected outcome due to the first hydration layer height and water occupation predictions. Again, these expectations deviate from the observed trends in χ^2.

Ultimately, we find that the trend in χ^2 is correlated with the vibrational enhancement of the alumina surface oxygen peak (Figure 4.25c). An r.m.s. width of the alumina surface oxygen layer (located at $z = 0$ in Figure 4.25a) that is equal to or larger than in the experimental best-fit value leads to a smaller χ^2. In all of the FPMD simulations, the initial prediction showed an r.m.s. widths of the surface oxygen layer smaller than that in the experimental best fit (see Figures 4.10a, 4.12a, and 4.19b). For PBE-6 with the water structure calculated from all DFT electrons and for the compressed optB88 calculations, the optimization procedure drives the surface oxygen peak r.m.s. width to be broader than in the experiment, thereby providing a $\chi^2 \sim 5.5$. A wider peak means that the electron density of this layer is more spread out such that some of it extends into the bonding region between the alumina and the adjacent water and suggests that a higher electron density in this region may be favorable for achieving agreement with the experimental data. This result further reinforces the finding that the XR measurement is sensitive to the electron density distribution within the bonding regions, which may be indicative of the oxidation state and bonding character at the interface.

4.7.5: Sensitivity to Interfacial Water Height

Throughout this analysis, we have identified the interfacial water height, Δ_w, as a significant contributing factor in the level of accuracy of the simulated XR intensities. Namely, larger water heights have been found to be not only less consistent with the experimental best fit but also with the XR data directly. However, significant errors within the substrate Al_2O_3 obscured the Δ_w contributions to χ^2. Now that the substrate errors have now been minimized, we again test the effects of water height on the XR data using the PBE-12- and PBE-12+Grimme-derived structures. The FPMD water profiles were rigidly shifted toward the alumina surface while allowing all other aspects of the alumina interfacial structure to relax in response. χ^2 was calculated at each step until the minimum χ^2 was obtained. This resulted in an optimal height of 2.53 ± 0.01 Å for both simulated water structures, consistent with the distance found in the XR best fit (2.52 ± 0.01 Å). The optimized structures gave calculated XR signals with $\chi^2 = 5.9$ and $\chi^2 = 7.6$ for the PBE-12-derived and PBE-12+Grimme-derived structures, respectively (Figure 4.23a-v and 4.23b-v, respectively) and visually reproduce most of the features in the experimental XR data. However, intensity oscillations can still be seen in the PBE+Grimme-based XR at $Q \approx 3$-4 Å^{-1}. This, and the observation that the quality of agreement is still worse than that obtained by a model fit, indicates that these residual discrepancies are due to the specific modulation of the interfacial water density in the predicted water structure. We did not optimize the water heights for the PBE-6, optB88, and optB88-10% water structures, but the results from PBE-12 and PBE-12+Grimme suggest that further χ^2 improvements could be gained by doing so.

Following optimization of the interfacial water height, we observed further changes to the alumina relaxation pattern. These changes in the r.m.s. deviation of the alumina atom positions from the XR best-fit structure, δ_{rms}, showed a marked improvement for the PBE-12-derived structure, resulting in a negligible $\delta_{rms} = 0.0096$ Å (compare to the original $\delta_{\mathrm{rms}} = 0.0236$ Å). However, for the PBE-12+Grimme-derived structure, $\delta_{\mathrm{rms}} = 0.0221$ Å (originally $\delta_{\mathrm{rms}} = 0.0227$ Å). The difference in χ^2 between these final FPMD-derived structures again highlights the significance of these small deviations. It also indicates that the detailed optimized parameters for incompletely optimized structures (that is, we have not fully optimized the interfacial water profile, including its coverage and second hydration layer properties) should interpreted with caution.

Residual inconsistencies between the FPMD and best-fit water structures include the coverage and vibrational amplitude of water molecules in the first adsorbed water layer at ~2.5 Å above the alumina (Figure 4.26). The PBE-12 water occupancy of ~1.4 H_2O/UC and width of 0.21

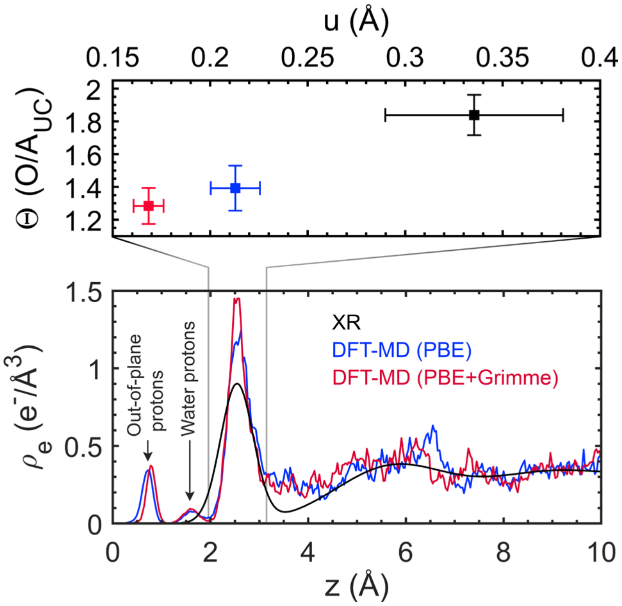

Figure 4.26. The heights of the first adsorbed water layer from PBE-12 (blue) and PBE-12+Grimme (red) agree with that of the XR best fit (black) after optimization with respect to χ^2. Significant differences remain in vibrational amplitudes, u, and coverages, Θ, in the first adsorbed water layer and in the shape of the water distribution near 3-4 Å. The density associated with protons is indicated (i.e., those terminating the alumina surface and those in water) but is not probed in the XR result. Uncertainties in the FPMD coverage and width are from Gaussian fits to the electron density profiles.

Å, and the PBE-12+Grimme occupancy of 1.28 H_2O/UC and width of 0.17 Å are underestimated relative to those in the XR best fit (1.83 ± 0.12 H_2O/UC and 0.34 ± 0.06 Å, respectively). The same behavior of underestimating hydration layer vibrational width was observed for PBE-FPMD predictions of the first hydration shell around a number of transition metal ions [110] and for the PBE-6 simulation (Figures 4.10b and 4.25a). Numerical integration of the first adsorbed water layer and the adjacent shoulder at z ~3-4 Å gives a coverage of 2.06 H_2O/UC for the PBE-12 prediction and 2.04 H_2O/UC for the PBE-12+Grimme prediction, in closer agreement with the value determined in the XR best fit. This suggests that FPMD captures the total amount of adsorbed water observed in the XR best fit, but the average height and vertical distribution of this water are distinct due to inadequate interactions between the solid surface and the water described by PBE (which is also consistent with the large interfacial water height predicted by PBE).

4.8: Discussion and Future Directions

Following the protocol outlined in Figure 4.1, we systematically tested theoretical and numerical approximations made in first principles simulations of the Al_2O_3-water interface, and we assessed how they affect the accuracy of the predicted structures by comparing directly with simulated XR intensities. Approximations include the choice of exchange correlation functional, pseudopotential, size of the system, and the approach to calculate experimental observables. We used X-ray reflectivity as the experimental validation tool due to its high sensitivity to both bulk and interfacial structures and found, crucially, that XR exhibits extreme sensitivity to electron densities as well as to atomic coordinates. For example, the delocalization of electrons around atomic cores in the bulk substrate depending on the choice of PP was shown to contribute significantly to inaccuracies in computed XR signals. In addition, we demonstrated an enhanced sensitivity of low-intensity regions in the XR data to details of the interfacial water distribution and later showed that these low intensities arise not just due to variations in the interfacial water structure but more specifically due to the precise interference of X-rays scattered from the solid interface and from the water. Finally, through a model-dependent optimization of the Al_2O_3 surface starting from the predicted structures, we were able to separate inaccuracies associated with the simulated oxide substrate structure so that we could evaluate the relative accuracy of interfacial water predictions from FP. The direct comparisons and empirical fitting approaches provide two complementary pathways to validated simulated FPMD structures. The former gives a complete picture of the raw-FPMD simulation accuracy while the latter is useful to assess the sensitivity of the XR measurement to specific predicted features independent of the rest of the structure.

Although none of the simulations evaluated in this work were able to achieve full quantitative agreement with the XR data, the comparisons between simulation and experiments have provided insights as to what improvements are needed from FP calculations to do so. A fundamental first step is recognition that a fully quantitative and direct evaluation of the *interface* accuracy using XR relies on having accurate predictions of both the bulk substrate and bulk water structures. The XR measurements probe the bulk and interfacial regions simultaneously, so a rigorous and direct validation approach, i.e., without the need for empirical optimization of predicted structures, requires equally accurate calculations for the bulk and the interface and the transitions between these regions. We observed significant contributions to the level of agreement with the XR data originating from the bulk Al_2O_3 structure (i.e., the slab lattice parameter, atom coordination, and valence electron distributions). We also found that for a given *a priori* choice of number of water molecules and system volume, it is challenging to get an accurate prediction of the bulk (and interfacial) water densities via an NVT simulation. These errors of NVT simulations obscure contributions from the interface. With accurate asymptotic predictions of the bulk solid and liquid phases in the FPMD simulation cell, one should be able to assess the accuracy of interfacial properties (i.e., the interfacial water height and density and details of the second hydration layer) without resorting to a model-dependent analysis.

4.8.1: Slab Bulk

The source of the disagreement in slab and periodic bulk DFT lattice constants is unclear. One hypothesis is that the slabs are not large enough to recover the bulk lattice constant from periodic DFT calculations due to interactions between the two slab surfaces. The fact that all of the simulations predict surface relaxations only in the surface unit cell indicates that these surface effects are effectively screened and, therefore, should not affect the oxygen-oxygen layer spacing at the slab center. However, Sundaresan et al. reported a larger-than-expected Al_2O_3 lattice constant for nanoparticles < 20 nm in diameter, though the value was not given [260]. While our simulations are periodic in the lateral directions, and therefore the slab is infinite in x and y, the *z*-dimension is well within the range where such a nanoscale effect may be realized. Another possibility is that the expansion of the slab lattice parameter is an artifact arising from errors in the choice of functional, PP, or other approximations required by the DFT. This idea is supported in part by the fact that the larger 12-layer PBE alumina slab had a lattice spacing in worse agreement with the experimental value than did the 6-layer PBE alumina slab. This suggests an instability in the DFT design that will not be solved by simply increasing the slab size. In the end, understanding the lattice expansion phenomenon in a slab geometry will require large-scale, systematic studies of DFT parameters, which is outside the scope of this thesis.

4.8.2: Interfacial Properties

The qualitative consistency in predicted surface relaxations predicted from different FPMD simulations (i.e., only in the surface-most unit cell) may indicate that long-range interactions which penetrate into the alumina substrate in the experiment are either screened by the first unit cell (as discussed in the context of the slab bulk lattice parameter) or are not present in the simulations. That is to say, the semi-local and vdW exchange correlation functionals used and the phenomenological Grimme correction are insufficient to describe the alumina/water interface. A point of caution here is that the XR data analysis finds a local minimum based on a pre-conceived interface model and does not include explicit chemical constraints on the structural optimization. Therefore, it is possible that a different interface structure with a different alumina surface relaxation profile (and larger interfacial water height) could also accurately reproduce the experimental data, although the present simulations have not demonstrated that. However, the fact that the optimized FPMD-derived structures converged to an oscillatory surface relaxation pattern and interfacial water height in good agreement with the best-fit structure provides confidence that these features of the experimental best fit, which have been seen in previous analysis of XR measurements of the same system [210], are required by the XR data and are not artifacts of the starting model. We suggest that residual discrepancies in Al_2O_3 surface displacements and the hydration structure within the FPMD-derived structures are associated with very small energy differences, which underscores the importance of being able to identify sub-Å deviations between the FPMD and XR approaches. Such structural differences affect predictions of surface reactivity, as reflected in previous studies in which a ~0.1 Å vertical displacement at the interface observed as a function of pH was associated with a change in protonation state due to an adsorbed hydroxyl vs. a water molecule [27].

The difference in the average first water layer height between 2.52 Å from the XR data and 2.6-2.7 Å predicted by FPMD may suggest a discrepancy in the interaction strength between the adsorbed water and the alumina terminal hydroxyls. We employed two different FPMD approaches to include vdW interactions—namely, the vdW exchange correlation functional optB88 and the Grimme energy correction—which marginally improved the interaction strength as seen by a decrease in interfacial water height. However, the optimized χ^2 derived from the PBE-12+Grimme was worse than that obtained from the optimized PBE-12 structure (and worse than obtained with optB88 without a water height adjustment) because the shape of the PBE-12+Grimme simulated interfacial water profile was less consistent with the XR. Grimme corrects for long-range energetics and is known to give a more correct density of water than PBE [200], but it does not capture mid-range interactions, which our results suggest are important for the interfacial water adsorption.

The interfacial water height also has implications for the lateral arrangement of water molecules at the alumina (001) surface (Figure 4.27a). The average nearest neighbor oxygen distance in bulk water is d_{OO} ~ 2.7-2.8 Å between hydrogen bonded (HB) water molecules [261, 262] whereas the experimental best-fit (and FPMD-optimized) water height was Δ_w~ 2.52 Å. This Δ_w would suggest an unusually short HB if the water oxygen were located directly vertically above an alumina surface oxygen (along the 001 surface normal vector). However, the specular XR measurements probe only the projection of the O-O vector along the alumina (001) surface normal direction. If we assume a d_{OO} of 2.7 Å, the water height of 2.52 Å is consistent with a water adsorption site that is laterally displaced by d_{XY} ~ 1 Å on average from the alumina surface oxygen site, as illustrated in Figure 4.27a. Meanwhile, the PBE interfacial water height prediction (~2.7 Å) suggests that the O-O vector angle with respect to (001) is small. For comparison, a hexagonal close packed arrangement of water molecules at the alumina surface would lead to Δ_w ~ 2.4 Å, which is considerably smaller than our best-fit water height.

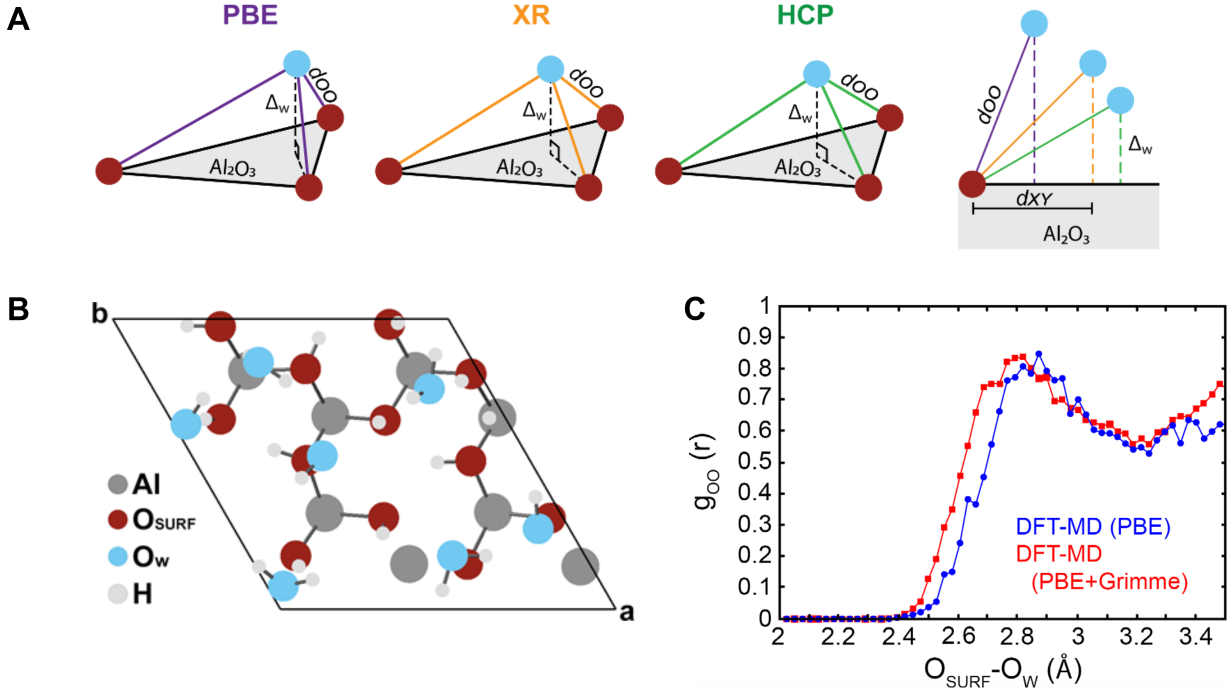

Figure 4.27. Proposed in-plane water ordering on Al_2O_3 based on vertical water height and predicted lateral distribution from FPMD. (A) Schematics of PBE (purple), XR (orange), and HCP (green) in 3D and the corresponding lateral projections seen by the specular XR measurement. Δ_w is the interfacial water height, d_{OO} is the O-O distance between hydrogen-bonded water molecules, assumed here between alumina surface oxygens (O_{SURF}; red) and adsorbed water oxygens (O_w; blue), and d_{XY} indicates the lateral displacement between O_{SURF} and O_w if d_{OO} is assumed. (B) A snapshot of the in-plane alumina (001) unit cell (a x b) from the PBE-12 simulation reveals the O_w adsorption sites relative to the alumina O_{SURF}. (C) Radial distribution functions (normalized to the unit cell volume, V_{UC}) for the PBE-12 and PBE-12+Grimme calculations show nearest neighbor distances between O_{SURF} and O_w of ~2.9 Å and ~2.8 Å, respectively.

Of course, the O-O spacing between the alumina surface and adjacent adsorbed water layer could also exceed the bulk-like HB distance. A snapshot of the lateral water organization from the PBE-12 simulation reveals that the adsorbed water O are located primarily near the alumina surface oxygen atoms but with a visible lateral shift (Figure 4.27b). The corresponding simulated radial distribution function (RDF) between the surface O and the nearest neighbor water O, averaged over all snapshots from the PBE-12 simulation, shows an O-O separation of ~2.9 Å (Figure 4.27c), slightly in excess of the expected distance for a HB. The equivalent RDF for the PBE-12+Grimme simulation gives a peak distance of ~2.8 Å (Figure 4.27c). The combination of the simulated vertical interfacial water heights and the RDFs suggests an average lateral displacement of adsorbed water relative to alumina surface oxygen sites of ~1 Å for both simulations, consistent with that inferred by XR with the assumption of a bulk-like d_{OO}. These results affirm that the HB interactions between the alumina surface and adsorbed water are weaker in the simulations (even when vdW interactions are included) compared to what is inferred from the experimental data.

Off-specular XR measurements can directly probe the lateral water organization. Data measured at APS Sector 33-ID-D (Figure 4.28) show significant deviations in several off-specular CTRs from the intensities expected from an ideally-terminated $Al_2O_3(001)$ crystal. These discrepancies arise from many different factors, including alumina surface rearrangements and interfacial water structure, as we have demonstrated throughout this work. Careful analysis of these data is an important next step in further understanding the properties of HB interactions at the alumina/water interface. Based on similar measurements of adsorbed water on the isostructural α-$Fe_2O_3(001)$ surface [210, 263], one might expect these data to reveal lateral water ordering close to that inferred from the specular XR best fit and from the FPMD RDFs for PBE-12 and PBE-12+Grimme—namely, a ~1 Å lateral displacement of the water O atom positions from the alumina surface O. For Fe_2O_3, the vertical interfacial water height was 1.9 Å [210], and off-specular XR revealed a lateral displacement of water molecules from adjacent surface O groups of ~1.8 Å [263], resulting in a d_{OO} consistent with a HB length.

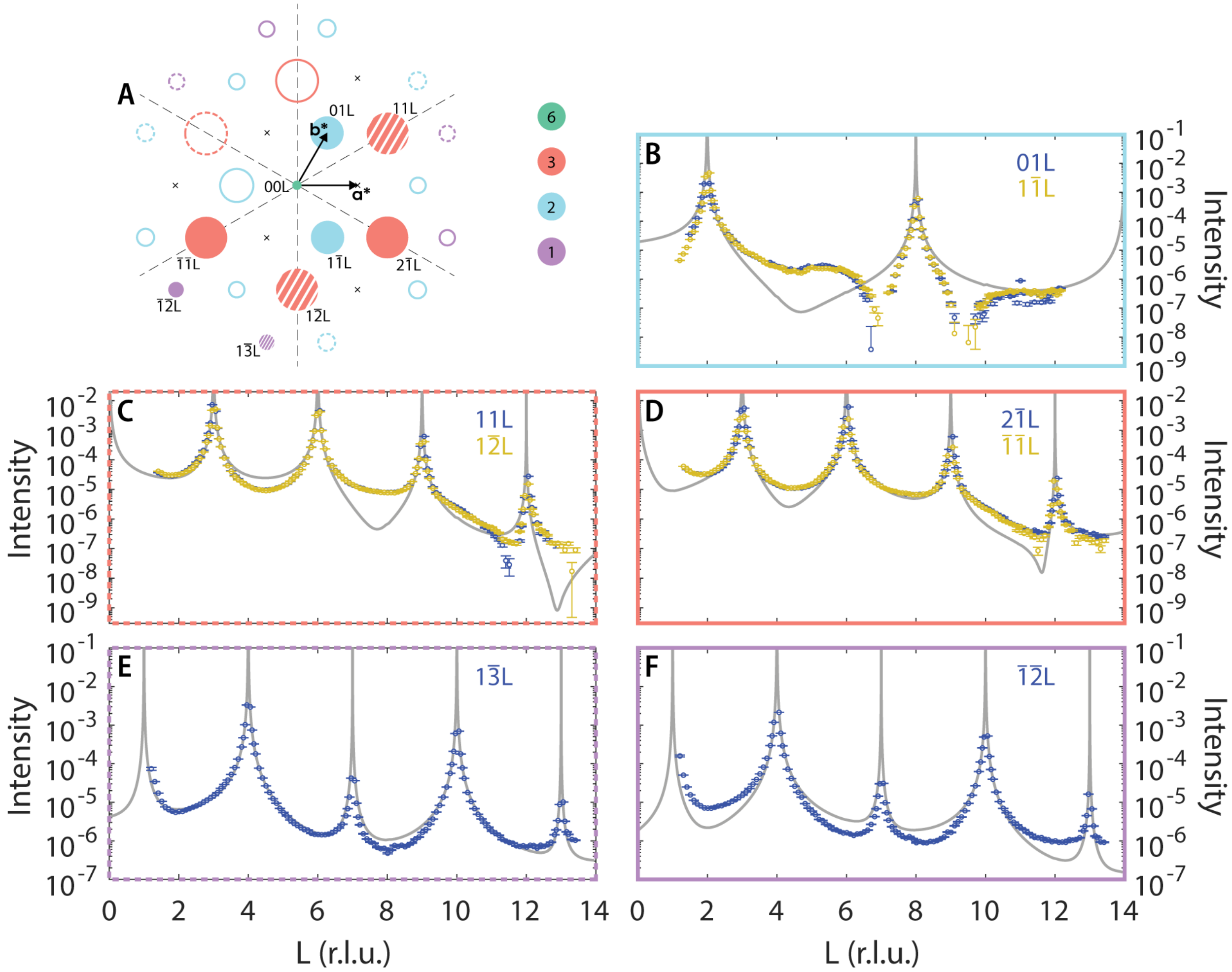

Figure 4.28. Off-specular XR measurements of the Al_2O_3(001)/water interface. (A) Schematic of all measured rods (including specular) and their symmetry equivalents projected onto the *L*=0 plane. The three-fold symmetry of α-Al_2O_3 is apparent. Filled circles are the measured rods with HKL labeled; striped versus solid colors indicate reflections related by a glide plane (dashed gray lines). Empty circles were not measured. The reflections are grouped by radii, representing the relative intensities of the first Bragg peak, and by color based on the *L* of the first Bragg peak (*L* = 1, purple; *L* = 2, blue; *L* = 3, salmon; *L* = 6, green). An '×' indicates a forbidden reflection. (B-F) XR data (blue and yellow) are grouped by symmetry equivalence according to the fill colors and patterns in (A), indicated by the outline of the figure panel. The data are shown relative to the expected reflectivity from an ideally terminated Al_2O_3 (001) bulk crystal (gray lines). Data measured at APS sector 33-ID-D at and X-ray photon energy of 20 keV. See Appendix A.1 for sample preparation details.

Another potential source of discrepancy between the simulated and measured water structures derives from the specific protonation state of the surface. The differences in the water heights seen here are similar to those observed previously at the TiO_2(110)/water interface that were associated with changes of the surface charge and proton site distributions [24]. The FPMD simulations all assumed a fully protonated Al_2O_3 surface (i.e., with one proton per surface oxygen), consistent with previous simulations [228, 264] and experimental results [209, 210, 212, 214, 226] at neutral pH. However, it is known that the alumina surface protonation is controlled by pH (characterized by a point of zero charge) [213, 214, 265] and that this behavior can be influenced by surface morphology and defects [211, 266, 267]. The experimental Al_2O_3 sample was cleaned and annealed to eliminate surface defects, and thus the assumption of a fully protonated surface in DIW (nominal pH = 7) is expected to be reasonable. Still, SFG studies of this system showed a subtle change in spectral response between a pH of 6 and 8 [53], which may be consistent with a slight change in the surface charge that could reasonably affect the HB strength and, consequently, the interfacial water height. These behaviors are currently be explored with additional specular XR measurements as a function of pH (Appendix A.1) and resonant XR measurements to determine how changes in the XR data versus pH reflect differences in the water structure versus effects of ion adsorption. These effects should also be incorporated explicitly in FP calculations.

4.8.3: Choice of DFT Functional

The studies presented in this thesis have used the PBE and optB88 exchange correlation functionals. PBE, in particular, serves as the workhorse functional of DFT. It is computationally tractable, commonly used, and has been shown to provide a reliable and flexible description of interactions in solutions [110, 252]. There are, however, well-documented problems with the accuracy of PBE (and other DFT approximations) for the study of water interactions [95], and liquid water simulations have been shown to be sensitive to the different theoretical and numerical approximations. For example Grossman et al. [107] found that liquid water was slightly over-structured (increased coordination/activity and slower self-diffusion rate) for choices of DFT and integration parameters similar to those used in the PBE-12 simulations. Inclusion of the Grimme dispersion correction [95] had little effect on the over-structuring of liquid water at the Al_2O_3/water interface. Increasing the thermostat temperature to 400 K, such as in the PBE-6 simulations discussed here, is an oft-employed ad hoc approach to resolve some of these well-known issues. Nevertheless, the water structures from the PBE-12 and PBE-6 simulations were similar despite the temperature difference, highlighting errors inherent in PBE.

There are many other flavors of DFT that may be good candidates for the validation protocol described here. Hybrid functionals [241, 268-270] can perform better than semi-local functionals for bulk water [95, 271] and for some bulk solid phases [272] including Al_2O_3 [273]. However, most hybrid functionals cannot accurately describe interfaces between systems with different dielectric properties such as alumina and water, and it is currently unclear how to properly describe vdW interactions [201, 205] within the context of hybrid functionals. In addition, they are significantly more computationally expensive than semi-local and nonlocal DFT, which is already any issue in the simulations presented here because of the large number of electrons being modeled.

The strongly constrained and appropriately normed (SCAN) functional [274] incorporates an improved description of weak interactions including hydrogen bonding and vdW relative to PBE and overall has performed remarkably well for bulk water [204, 275]. It is more computationally advantageous than hybrid functionals and was recently shown [264] to outperform a hybrid functional (HSE) [268, 269] for the prediction of vibrational properties at the $Al_2O_3(001)$/water interface and the prediction of the adsorbed water height above the alumina surface (2.62 Å). The results in Ref. [264] derive from simulations with only three Al_2O_3 layers and fewer water molecules than we used here, which would contribute significantly to the level of accuracy of simulated XR intensities. Nevertheless, the available results point to SCAN as a promising functional for predictions of oxide/water interfaces and worth future study using the validation framework.

4.8.4: Conclusion

This study shows how quantitative comparisons of XR and FPMD simulations can assess the accuracy of our understanding of a simple, well-defined structure: the Al_2O_3(001)/water interface. The FPMD-predicted structures give good visual agreement with the structures determined by the experimental best fit, showing that they qualitatively capture many physiochemical behaviors at this interface. However, significant quantitative differences between the measured and simulated XR signals demonstrate sub-Å differences between predicted structures and experimental data that are important for the accurate description of interfacial phenomena. The small but significant effects of electron density description by FF or PP, of the charge distribution in the low-density region between the solid and liquid, and of sub-Å displacements in the bulk and interfacial substrate and the water height accentuate the deep structural insights that can ultimately be derived from these comparisons, especially with regard to HB networks and proton transfer dynamics at the interface. Finally, these studies pave the way for future FPMD-XR analyses of other systems to refine predicted structures and, as a natural next step, to provide a starting point for XR data analysis of more complex systems without the need for a pre-conceived model of the interface.

Chapter 5: Ion Adsorption at the Charged Graphene Surface

5.1: Introduction

Resonant anomalous X-ray reflectivity (RAXR) has been used to probe the structure of adsorbed ions on several mineral surfaces where the surface charge is either fixed (e.g., muscovite mica with a high charge of 1 e^- per surface unit cell area [40]) or may be controlled by changing the solution pH with respect to the point of zero charge (e.g., Al_2O_3) [15, 144, 175, 178-180, 182, 276]. Here we set out to measure the adsorbed ion structure at a potential-controlled electrode surface. This work enables measurements of the electrical double layer (EDL) as a function of surface charge in real time by altering the applied potential and also provides a direct comparison with electrochemical measurements. In previous studies of ion adsorption using RAXR, the strength of ion sorption has been relatively strong, leading to strong resonance modulations in the RAXR spectra (Figure 5.1a). For example, the high surface charge of mica (1 e^-/A_{UC} is equivalent to -34 μC/cm^2) leads to a well-defined Stern layer of adsorbed Rb^+ even for a dilute concentration of 3 mM RbCl (Figure 5.1b) [15]. Conversely, the diffuse double layer inherently arises due to weak interactions with a charged surface, and the contribution to the resonance spectra is expected to be significantly smaller. Qualitatively, this can be inferred from the equation for the structure factor (Eq. 3.14) which says that a more distributed atomic (or ionic) layer (i.e., through the DW factor) will decrease the structure factor contribution from that element. A diffuse profile described by an exponentially decaying ion distribution (Eq. 2.13) would have a similar effect. Therefore, a successful measurement of a diffuse ion profile will benefit from a substrate with low electron density (i.e., a small atomic FF), which will lend a smaller contribution to the total structure factor than a typical, high-*Z* metal electrode (e.g., Ag or Pt). With this in mind, we selected a graphene electrode to facilitate measurement of the EDL.

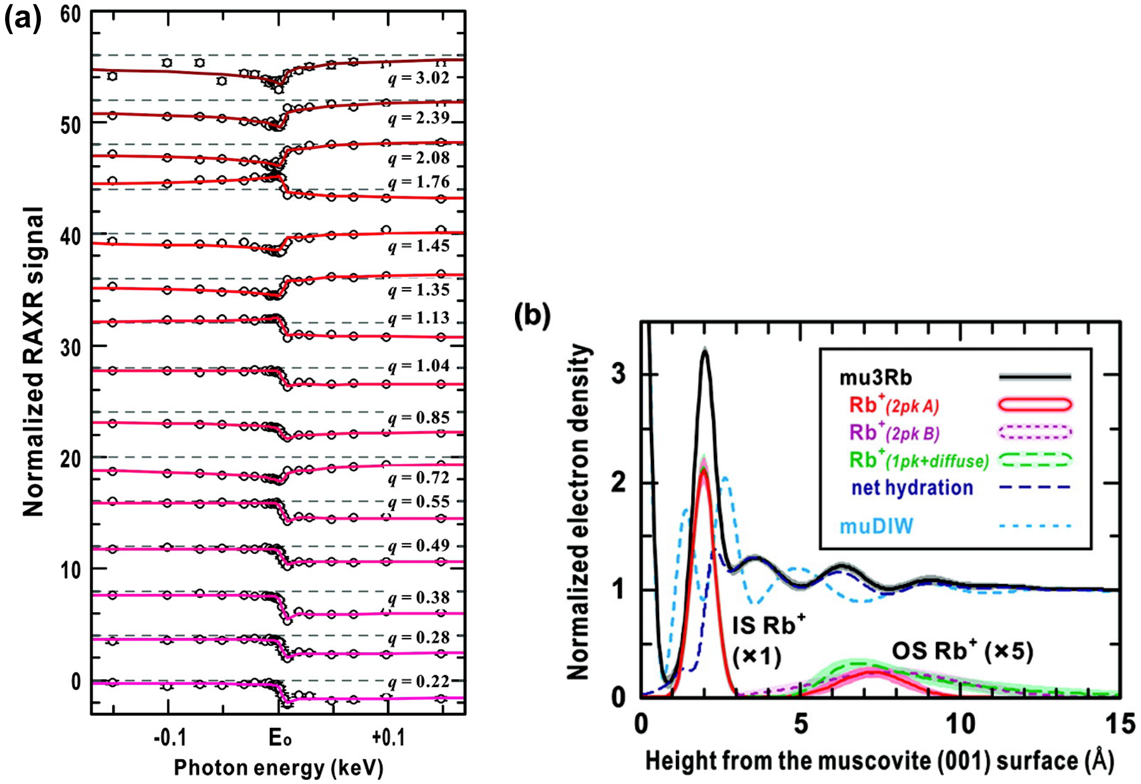

Figure 5.1. Example of RAXR measurement of strongly adsorbed Rb$^+$ on muscovite mica in 3mM RbCl(aq). (A) Normalized RAXR spectra show clear resonance modulations through the Rb K-edge over a range of scattering conditions (0.22 Å^{-1} < Q < 3.02 Å^{-1}; spectra are offset for clarity). (B) Three models for the adsorbed Rb$^+$ ion distribution with similar χ^2 levels of agreement with the experimental data ($1.3 < \chi^2 < 1.5$) all show an inner sphere (IS) adsorption complex. Electron densities derived from CTR measurements in DIW (light blue dots) and in 3mM RbCl (black line) are given. Reprinted with permission from Lee, Fenter, Nagy, and Sturchio, *Langmuir*, 28, 8637-8650 (2012). Copyright 2012 American Chemical Society. Ref. [15].

5.1.1: Graphene on SiC

Graphene is the atomically-thin building block of the two-dimensional (2D) carbon allotrope graphite and has been the subject of extensive research over the past two decades due to its unique properties as a 2D material [277]. Its light weight, strength resulting from its sp^2 hybridized honeycomb lattice [278], thermal [279] and electrical [280] conductivity, and capability to be fabricated in different architectures [90, 281-283] and with different surface functionalizations [284-287] make it a material of interest for numerous applications, including as protective coatings [288] and as an electrode in field effect transistors [289-291] and electrical double layer capacitors (EDLCs) [88, 285, 286, 292].

Graphene may be obtained by several methods. These include mechanical exfoliation from graphite using tape [280], chemical vapor deposition on metal (e.g., Cu) from a carbon-containing precursor [293], and epitaxial growth by thermal desorption of Si from a SiC substrate either in ultra-high vacuum (UHV) [294-296] or in a partial atmosphere of an inert gas [297]. Growth on SiC approach is best suited for large-area production of high-quality epitaxial graphene [297-299], which is a prerequisite for the use of graphene as an electrode material in EDLCs where the charge storage scales with the area of the adsorption surface. However, the electronic properties of graphene grown on SiC vary from those of isolated graphene. Intrinsically, a single layer of graphene zero gap semiconductor [280], but its band gap can be tuned by applying a voltage [280, 291, 300], by chemical doping [301], and by interactions with a substrate [302-306].

The thermal graphitization of SiC proceeds via the high-temperature evaporation of Si from the interface and subsequent restructuring of remaining C atoms into the familiar 2D honeycomb structure (Figure 5.2a) with in-plane lattice constant $a_G = 2.46$ Å and c_G = 3.35 Å [307]. This graphene synthesis method is commonly carried out on the hexagonal polymorphs of SiC, i.e., 4H- and 6H- SiC (Figure 5.2b) with lattice constants $a = b = 3.08$ Å, $c_{4H} = 10.08$ Å, and $c_{6H} = 15.12$ Å [308]. Layer-by-layer growth is oriented along SiC step edges [309, 310], and the film thickness and graphene ordering depends on the temperature, atmospheric conditions, and the polarity of the

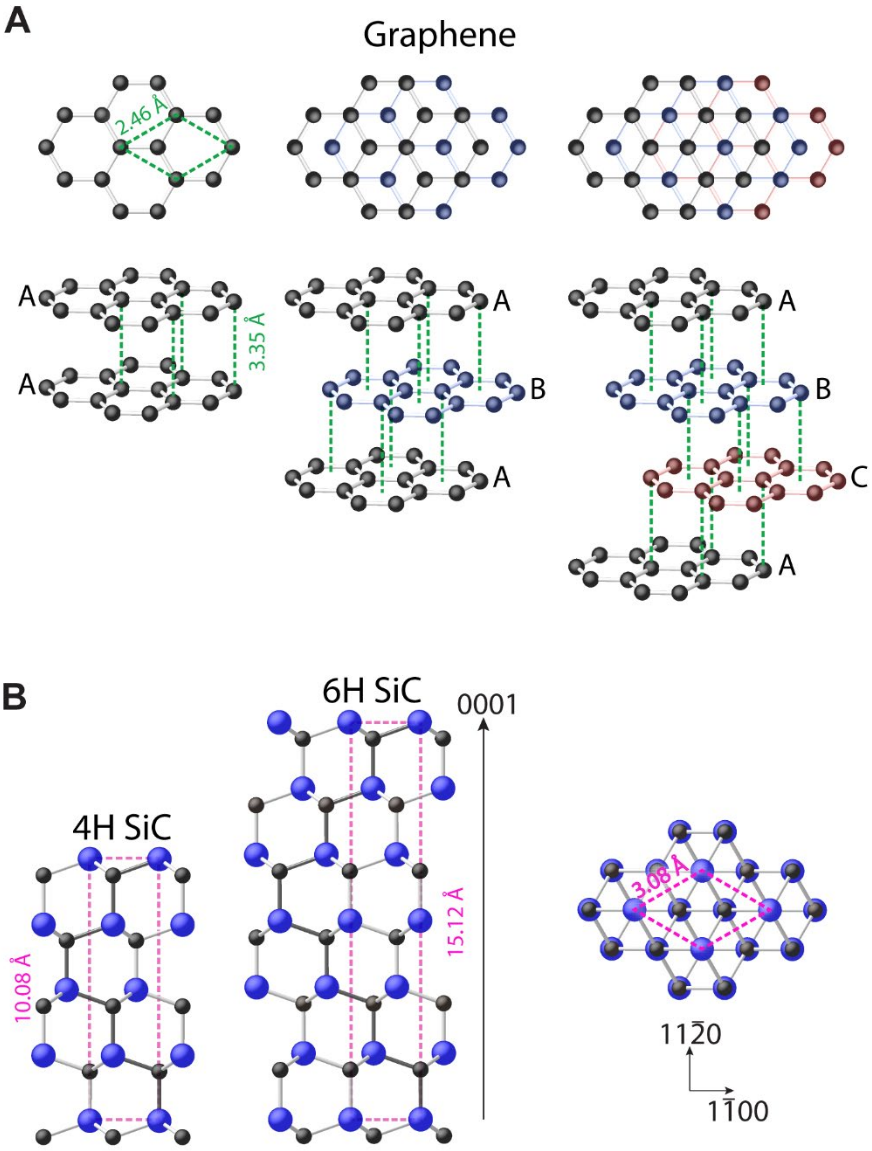

Figure 5.2. Graphene and SiC crystal structures. (A) In-plane (top) and vertical (bottom) graphene structures showing different stacking sequences (AA, AB, and ABC). (B) The 4H-SiC and 6H-SiC polytypes differ in the vertical layer sequence (indicated by thick black bonds; left) but have equivalent in-plane structures (right). The unit cells are indicated by dotted lines.

SiC—that is, whether the graphitization takes place on the Si-face (0001) or C-face ($000\bar{1}$) [311, 312]. Specifically, 2D graphene growth on the Si-face follows the formation of an intermediate C-rich buffer layer in a $6\sqrt{3} \times 6\sqrt{3}$ surface reconstruction [313] that is coupled strongly to the underlying SiC substrate through partial sp^3 hybridization [311]. Graphitization proceeds slowly on this face, leading to few-layer graphene films [314], and the bonding of the buffer layer to the substrate contributes to the high degree of order of graphene films grown on this face [311]. The graphene layers tend to stack in three configurations (AA, AB, ABC) shown in Figure 5.2a with interlayer spacing $c_G \sim 3.35$ Å where the Bernal type (AB) is the most common [312]. Conversely, graphene layers on the C-face interact weakly with the substrate (there is no buffer layer), and growth is fast and uncontrolled, leading to comparatively thick, disordered films [315]. Substrate defects have a profound impact of the quality of the graphene, and careful pre-treatment (e.g., H_2 etching) is necessary to obtain uniform growth [316-318].

The interaction of graphene on the Si-face with the underlying substrate leads to an opening of the band gap at the Dirac point [319] with a dependence on layer thickness (i.e., a decreasing gap with thicker graphene) [302, 320, 321] (Figure 5.3a,b). The graphene stacking order also contributes to the measured band structure of graphene resulting from the degree of π orbital

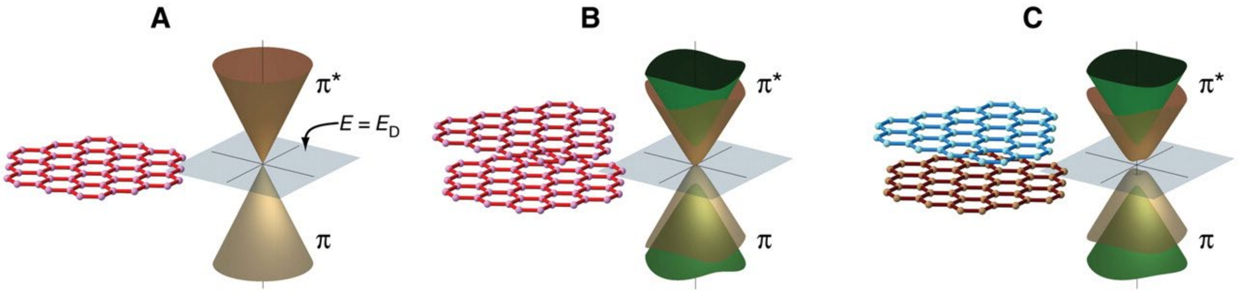

Figure 5.3. Graphene energy bands depending on layer structure. (A) Single layer graphene, (B) AA-stacked bilayer (BL) graphene, and (C) asymmetrically stacked BL graphene. E_D is the Dirac point of the energy bands. From Ohta et al., Science **313**, 951-954 (2006). Reprinted with permission from AAAS. Ref. [301].

overlap from the different layers (Figure 5.3c) [312]. As a result of the band opening, electrons are confined within the graphene layers and behave as a 2D electron gas [322], which gives rise to a quantum capacitance, C_q [289, 323-326]. C_q scales with the density of states, and is, therefore, voltage and thickness dependent and is typically on the order of a few μC/cm^2 [289, 290]. This small capacitance can dominate the total capacitance of EDLCs depending on the electrolyte conditions [323-325] where it acts in series with the double layer capacitor, and the total capacitance, C_{tot}, is given by

$$\frac{1}{C_{tot}} = \frac{1}{C_q} + \frac{1}{C_s} + \frac{1}{C_{GC}}. \tag{5.1}$$

Here, C_s is the capacitance of a Stern layer, which may be treated as a parallel plate capacitor, and C_{GC} is the Gouy-Chapman capacitance in the case of a diffuse ion profile. The Stern and GC capacitances combine to form the electrical double layer capacitance, C_{EDL}, as shown in Figure 5.4. If no Stern layer is present, the EDL capacitance is simply that of the diffuse ion layer.

In this Chapter, I first investigate the structure of water on graphene grown on both 6H- and 4H-SiC, in the absence of ions. Molecular dynamics simulations provide additional insights to the water distribution and behavior at the graphene surface and suggest that an intrinsic

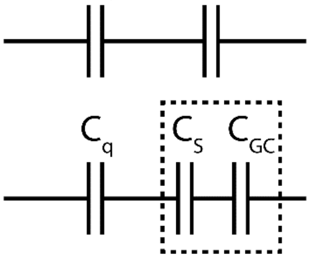

Figure 5.4. Graphene/electrical double layer (EDL) circuit diagram. C_q is the graphene quantum capacitance and C_{EDL} is the EDL capacitance (top). The EDL capacitance can be separated into a Stern layer capacitance (C_S) and Gouy-Chapman diffuse layer capacitance (C_{GC}) if specifically adsorbed ions are present.

interfacial water polarization affects the adsorption of cations and anions differently. Then I explore the structure of cation (Rb^+) adsorption at the electrified graphene surface in a weak coupling limit (i.e., small surface charge). I observe significant discrepancies between electrochemical measurements and resonant X-ray reflectivity measurements and discuss possible explanations for the differences.

5.2: Experimental Methods

X-ray reflectivity measurements were carried out on several different samples of epitaxial graphene (EG) grown on the Si-face of semi-insulating 6H-SiC obtained from D. Kurt Gaskill's group at the Naval Research Laboratory and on one sample of EG grown on the Si-face of 4H-SiC purchased from Graphenesic AB (Stockholm, Sweden). All EG/SiC samples were prepared by thermal decomposition of SiC in an inert atmosphere of Ar gas [297]. The large, oriented graphene terraces produced by this method are beneficial for XR measurements as the large surface domains lead to sharper diffracted signals on the detector and improves the peak signal-to-background ratio. In contrast, EG/SiC samples grown in UHV conditions produce smaller, unoriented graphene domains [320, 327], which leads to broad X-ray reflections that are challenging to integrate and analyze [328]. The sample dimensions were cut to approximately 3 mm×10 mm each in order to fit in the transmission electrochemical cell (Figure 3.8) used for in situ XR and RAXR measurements.

The samples were cleaned by several alternating rinses of methanol and de-ionized water (DIW) to remove surface contamination and characterized by AFM to estimate sample quality (i.e., roughness, layer morphology, and layer coverages). Four-point probe measurements were carried out using the S-302 Resistivity Stand from Lucas Signatone Corporation (Gilroy, CA, USA) with potentiostatic control via CH760E bipotentiostat (CH Instruments, Inc., Austin, TX, USA) to evaluate the resistivity of the samples. For a conductive thin film, the sheet resistivity ρ_s (as opposed to bulk resistivity) is calculated from Ohm's Law as

$$\rho_s = \frac{\pi}{\ln 2} t\, \xi \frac{V}{I} \tag{5.2}$$

where the constant prefactor accounts for a film with thickness t that is less than half the probe tip spacing [329], and ξ is a geometric correction factor that depends on the shape of the sample (i.e., circular or rectangular) and is required when the sample dimensions are small such that current edge effects must be considered [330]. The sample conductivity is

$$\sigma_s = \frac{1}{\rho_s}. \tag{5.3}$$

Samples suitable for use as electrodes in studies of the electric double layer (EDL) were selected based on AFM characterization and good conductivity as determined by four-point probe (i.e., having a sheet resistance, ρ_s/t, on the order of a few kΩ/square or less).

All samples were assembled into the transmission electrochemical cell for transport to the APS. Samples used for studies of the water structure on graphene were kept dry for transport to the APS, and XR measurements were carried out on the samples in air before DIW was introduced to the cells. Samples used as electrodes for studies of the EDL structure were characterized by cyclic voltammetry (CV) in DIW and in 0.1 M RbCl using either a CHI660D or CHI760E potentiostat before taking to the APS for in situ XR measurements, which were also carried out in 0.1 M RbCl. The initial CV measurements serve as a point of comparison for those carried out at the beamline and provide a more accurate assessment of the capacitance of the assembled cells (see Chapter 5.4).

The CHI760 potentiostat was used for electrochemical measurements at the beamline and was controlled externally by the beamline software, SPEC. The potentiostat voltage was defined as a motor with values set according to an input table. CVs were carried out by stepping the voltage in 0.01 V increments with a voltage window set according to the range over which capacitive behavior was expected. The voltage was held at a fixed negative value within the capacitive voltage window during RAXR measurements to measure the adsorbed Rb^+ distribution. “Cleanup” CVs were performed between RAXR scans to check the stability of the EG/SiC electrode following repeated X-ray exposures and ensure that RAXR data used to evaluate the EDL structure are reliable.

XR measurements were carried out at beamline 33-ID-D of the APS using various fixed X-ray photon energies, which are given in the respective results sections. For the measurement of Rb^+ adsorption on graphene, resonant measurements were always carried out by scanning the energy through the Rb K-edge, nominally $E_0 = 15.2$ keV, with a scan range from E_0+250 eV to E_0-250 eV. As the precise value of E_0 could vary (typically no more than few eV) depending on extrinsic factors of the beamline configuration, E_0 was measured at the start of each beamtime with the assistance of Dr. Sang Soo Lee (Fenter group, ANL). The linear absorption as a function of X-ray photon energy was measured through a transmission XANES cell placed at the front of the beamline (where the X-rays enter the 33-ID-D hutch) and filled with an aqueous RbCl solution. The precise value of E_0 is the energy corresponding to the minimum in the derivative of the absorption spectrum. Non-resonant reflectivity was measured away from the K-edge (either above or below, as indicated in the results sections) where the anomalous dispersion terms (Eq. 3.15 and Figure 3.5) are negligible.

5.3: Water on Graphene

5.3.1: Model for XR Data Analysis

The XR data were analyzed following the model-dependent least-squares fitting procedure described in Chapter 3. The model for the SiC/EG/water interface consists of a semi-infinite bulk SiC substrate defined by the polytype (either the 6H- or 4H-SiC; Figure 5.1) [308], six alternating C-Si interfacial layers for the 6H-SiC polytype (total of 12 atomic planes) and four alternating C-Si interfacial layers for the 4H-SiC polytype (total of eight atomic planes), up to eight carbon (graphene) layers, and the layered water model previously described (see Chapter 4.3 and Ref. [120]). Individual adsorbed water layers (i.e., as in the $Al_2O_3(001)$/water structure) were found to be unnecessary to converge the model to the XR data for SiC/EG/water. The parameters for the interfacial SiC, graphene, and water structures were optimized while the bulk SiC structure was fixed.

In general, the SiC/EG/water interface model contains many more parameters than were used for the Al_2O_3/water interface model in Chapter 4. Unlike $Al_2O_3(001)$ which has a single well-defined substrate surface, the thermal decomposition of SiC to grow EG leads to several interfacial layers that may experience surface relaxations and partial occupancy [327, 331, 332]. Therefore, the model includes position parameters for each of the SiC surface layers, each EG layer, the first Gaussian of the extended water model, and the peak spacing between adjacent Gaussians of the layered water (up to 22 position parameters for 6H-SiC and up to 18 for 4H-SiC). Layer occupation factors were included for up to four Si surface layers and for each graphene layer (for an additional 12 parameters). Models that included partial C layers in the SiC substrate surface led to worse levels of agreement with the XR data, which is consistent with previous results that found no evidence of depletion in these layers [331]. Therefore, the occupation factors for C in the SiC were fixed at the bulk coverage (1/UC). The vibrational amplitudes of the surface-most Si layer, each graphene layer, and the first Gaussian of the layered water model were optimized, as was the vibrational enhancement of subsequent water layers such that the water density oscillations decay to the bulk water density (11 additional parameters). Extrinsic factors included the surface roughness, water layer thickness, and a scale factor. In total, up to 48 or 44 parameters for 6H- and 4H-SiC, respectively, were possible for the least-squares analysis of the SiC/EG/water XR data.

Typically, the graphene films were found to have fewer than five partial layers, so in practice the number of position, occupation, and r.m.s. width parameters were reduced from the maximum number possible. In addition, the roughness parameter and water thickness parameter were always fixed after the first few iterations of the least-squares minimization. As noted in Chapter 3.1.1., the Robinson roughness model [166] describes partial coverage layers of the substrate material (Figure 3.3), so the β roughness parameter covaries significantly with the coverage parameters for the SiC/graphene interface. For all samples that were measured, β converged to zero with a large uncertainty, so this parameter was fixed at zero. The X-ray attenuation through a transmission cell is nearly constant over the Q range that was probed in these measurements (Figure B1), leading to a significant covariance with the extrinsic intensity scaling factor. Thus, the water layer thickness was fixed at an arbitrary value, and its effects were accounted for by the scale factor.

We modified the layered water model (Eqs. 4.2 and 4.3) to incorporate multiple graphene surfaces, G_n ($n = 0, 1, 2, \ldots$) [67], and assumed that water interacts in the same way with each exposed graphene layer. That is, above each exposed graphene surface exists the same intrinsic water structure with m Gaussians but vertically displaced and with fractional coverage due to the position z_n, width u_n, and coverage Θ_n of the exposed graphene layer. Altogether, the layered water structure can be described by

$$\begin{aligned} z_{m,n} &= z_m + z_n \\ u_{m,n} &= \sqrt{u_m^2 + u_n^2} \\ \Theta_{w,n} &= \Theta_w \frac{\Theta_n - \Theta_{n+1}}{\Theta_{ML}} \end{aligned} \tag{5.4}$$

where the graphene monolayer coverage on SiC is $\Theta_{\mathrm{ML}} = 3.147$ carbon atoms per SiC unit cell, and the positions z_m, r.m.s. widths u_m, and occupation factor Θ_w for the extended layered water structure are given by Eqs. 4.2 and 4.3.

We partially constrained the surface SiC and G_0 parameters in the XR analysis based on the work of Emery et al. [331]. That study combined the chemical and structural sensitivity of X-ray photoelectron spectroscopy (XPS), X-ray standing waves (XSW), and XR to rigorously characterize the structure of the SiC/EG/air interface and address long-standing debates about the buffer layer, G_0, between SiC and epitaxial graphene. The XPS/XSW measurements were consistent with a carbon-rich buffer layer composed of two chemically-distinct layers, S1 with sp^2 hybridization and S2 with sp^3 hybridization and bonded to Si atoms of the substrate [303, 305, 333-335] and ruled out a proposed Si adatom model [332, 336]. Although Emery et al. found that the EG/SiC interface was largely identical across all samples studied (UHV-grown vs. Ar-grown with 1.3 or 1.7 ML graphene), we allowed the structure parameters in this work to vary up to 10% from their results. In general, the present results are in agreement with those previously reported.

5.3.2: Simulation Methods

Two classical MD simulations were carried out by Dr. Felipe Jiménez Ángeles (Olvera group, Northwestern) and provide further insights to the properties of water adsorbed on graphene. One simulation included an ideal graphene slab constructed of four graphene layers with complete coverage (i.e., spanning the simulation x- and y-dimensions). The second simulation included an irregular surface with four layers with coverages defined according to the experimental best fit for one of the samples (EG/6H-SiC). The electron density distributions of the water structure predicted by the simulations are compared to the experimental results. In addition, the dipole moment orientations $\boldsymbol{\mu}$ of water molecules at the interface and the instantaneous polarization near the graphene surface are calculated from the MD simulations. The instantaneous polarization is calculated as $\mathbf{p}(\mathrm{r}, \mathrm{z}) = \Delta\mathbf{m}/\Delta\mathrm{V}$ where $\Delta\mathbf{m} = \sum_i \boldsymbol{\mu}_i$ and $\boldsymbol{\mu}_i$ is the dipole moment of all water molecules in the volume ΔV at (r,z). Further details of the simulation methodology can be found in Ref. [130].

5.3.3: Results

The adsorbed water structure on graphene was investigated on two samples, one with a 6H-SiC substrate and one with a 4H-SiC substrate. Figures 5.5a,b and 5.5c-e show AFM height scans of the epitaxial graphene on 6H- and 4H-SiC in air, respectively, and reveal smooth sample

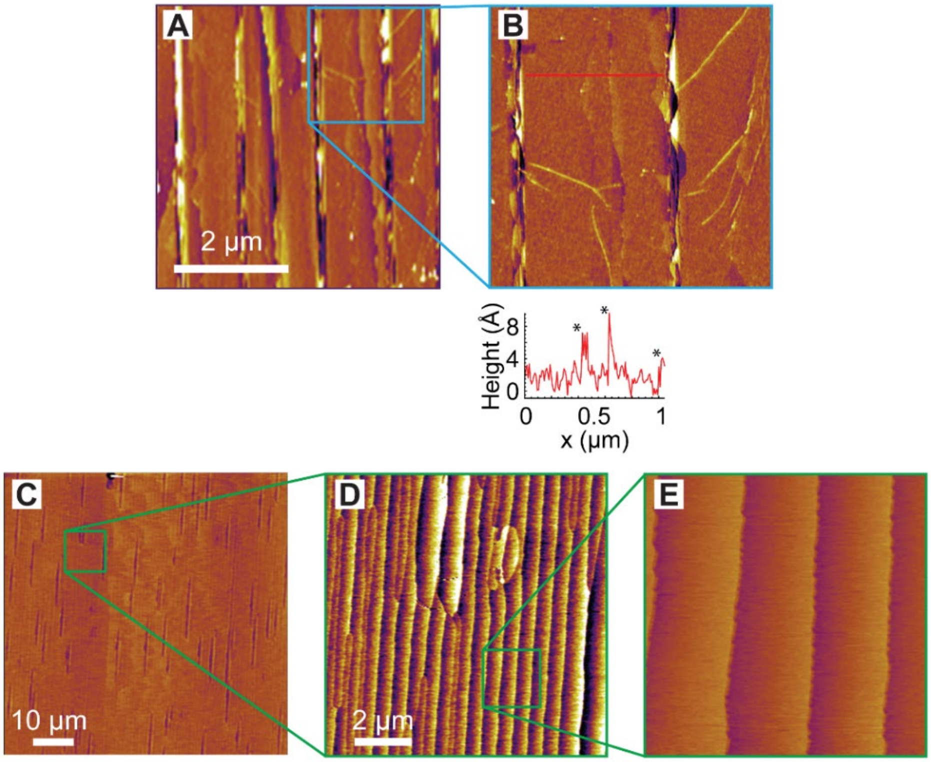

Figure 5.5. AFM height images of epitaxial graphene (EG) grown by thermal decomposition of SiC. (A) A 5×5 µm^2 region of the EG/6H-SiC sample shows large terraces ~1 µm wide with several partial graphene layers that are more easily seen in (B) the zoomed in region spanning 4 µm^2 (top); the height profile (bottom) along the horizontal red line in the AFM shows three peaks (‘*’) with heights of ~3.5 Å above the surrounding surfaces, highlighting the edges of four partial graphene layers. Bright and dark vertical lines are the terrace edges. (C) A 70 *µ*m ×70 *µ*m area of the EG/4H-SiC sample shows uniform EG growth across most of the sample with vertical structures covering ~15-20% of the surface area. (D) The ridges appear to be wider graphene terraces. (E) A region zoomed in to 4 µm^2 on a uniform section of the sample shows complete coverage of graphene layers across the terraces.

surfaces (average surface roughness = 38 pm on the 6H-SiC substrate, and the EG/4H-SiC surface appears perfectly smooth). The lateral terrace widths are ~1 µm and ~0.5 µm on the 6H- and 4H-SiC samples, respectively. On the 6H- sample, we also see several partial layers of graphene on each terrace (Figure 5.5b) while on the 4H- sample the graphene coverage appears uniform on each terrace across the majority of the sample (Figure 5.5e). Approximately 15-20% of the 4H-

SiC substrate surface is covered by ridges (Figure 5.5c), which appear to be thicker regions of graphene (Figure 5.5d) that may result from step bunching. Due to the limited resolution of the AFM, its chemical insensitivity, and the fact that it does not see the layers below the surface, we cannot determine the number of graphene layers precisely from the AFM. Nevertheless, this qualitative picture provides an additional reference point against which to evaluate the XR best-fit results.

Figure 5.6 shows the XR data and best-fit structures measured on both samples in air and in DIW. The XR measurements on the EG/6H-SiC sample were carried out at an X-ray photon energy of E = 15.2 keV, and the measurements on the EG/4H-SiC sample were carried out at a photon energy of E = 18 keV. The optimized XR model parameters (z, u, and Θ) for each atomic layer are summarized in Tables 5.1 and 5.2 for the 6H-SiC sample and the 4H-SiC sample, respectively. The XR data show a low-intensity at $Q \sim 1$ Å^{-1} for both samples measured in air, but upon the addition of water the intensity at this scattering condition increases due to the presence of an additional oscillation in the reflectivity (Figure 5.6a). This change in in intensity just below the first graphene peak was also observed for other measurements (not shown) and appears to be a signature of the adsorbed water. Overall, the interfacial structure of SiC/EG/DIW is similar for 6H-SiC and 4H-SiC (Figure 5.6b), as I discuss in detail below. The MD simulations also generally agree with the hydration layer distribution derived from the experiments and provide further insights to the physiochemical phenomena occurring at the graphene/water interface.

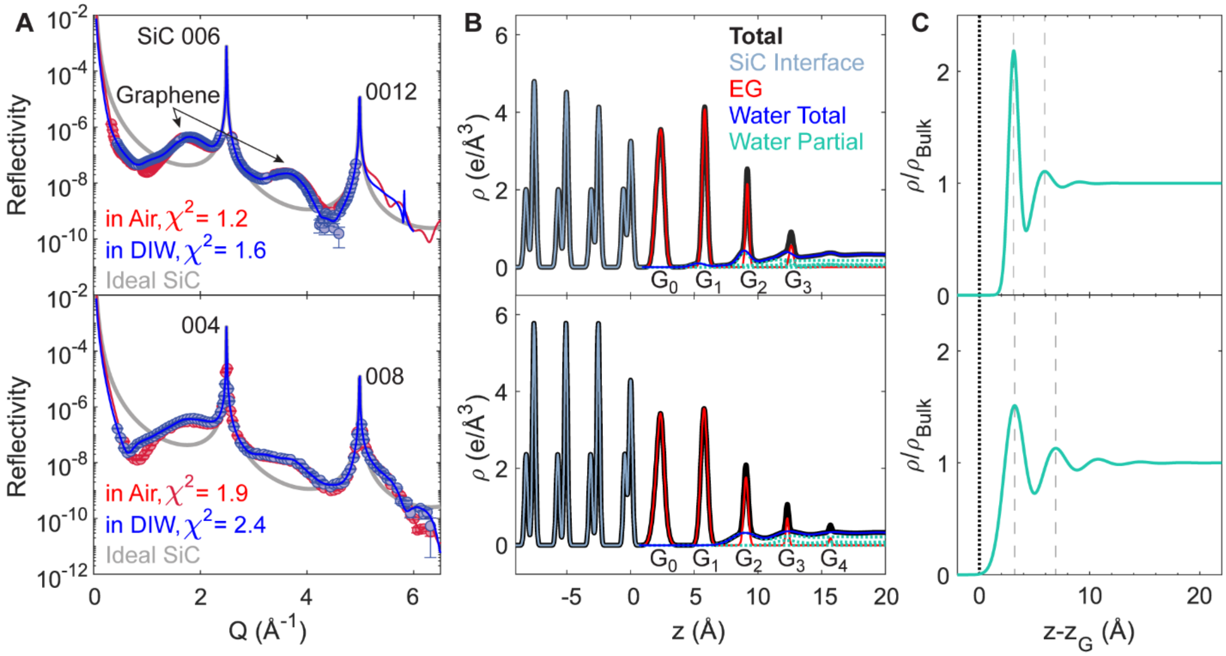

Figure 5.6. Adsorbed de-ionized water structure on EG/SiC. Top row: 6H-SiC substrate sample; bottom row: 4H-SiC substrate sample. (A) XR data (circles) and best fits of samples in air (red) versus in water (blue) and the expected reflectivity from an ideally-terminated SiC(0001) substrate (gray). Error bars are given as 1σ uncertainties with 2% minimum error bars (6H-SiC) and with 4% minimum error bars enforced (4H-SiC); SiC and graphene peaks are labeled and are similar for both samples. (B) The best-fit electron density distributions of samples in DIW reveal that sample 1 (χ^2 = 1.6) has three partial graphene layers, G_1-G_3, above the G_0 buffer layer, and sample 2 (χ^2 = 2.2) has a complete graphene layer, G_1, and three partial layers, G_2-G_4, above the G_0 buffer layer; the adsorbed water layers are approximately coincident with the graphene layers; the distributions are resolution-broadened with effective r.m.s. width of each layer j given by $u_{eff,j} = \left[u_j^2 + (0.55/Q_{max})^2\right]^{1/2}$ (C) The intrinsic water structures are similar for both samples with the hydration first peak at ~3.1 Å above the graphene surface ($z_{G;}$ vertical black dotted line); the spacing between adjacent hydration layers (indicated by vertical gray dashed lines) in the sample 1 best-fit is smaller than the structure derived from the CTR data for sample 2.

Table 5.1. XR best-fit results for the 6H-SiC(0001)/EG/water interface with uncertainties on the last significant figures in parentheses. Values without uncertainties were fixed during analysis.

	In DIW			In Air		
Layer	**z (Å)**	**u (Å)**	**Θ (A_{UC}^{-1})**	**z (Å)**	**u (Å)**	**Θ (A_{UC}^{-1})**
6H-SiC(0001)						
C	−13.226(5)	0.0922	1	-13.215(5)	0.0922	1
Si	−12.598(2)	0.0837	1	-12.603(1)	0.0837	1
C	−10.723(7)	0.0922	1	-10.68(1)	0.0922	1
Si	−10.076(3)	0.0837	1	-10.078(2)	0.0837	1
C	−8.20(2)	0.0922	1	-8.17(1)	0.0922	1
Si	−7.557(5)	0.0837	0.988(8)	-7.575(2)	0.0837	1
C	−5.66(2)	0.0922	1	-5.65(3)	0.0922	1
Si	−5.026(5)	0.0837	0.93(2)	-5.086(4)	0.0837	1.0004
C	−3.08(2)	0.0922	1	-3.09(6)	0.0922	1
Si	−2.49(1)	0.0837	0.85(3)	-2.56(1)	0.20(2)	1.0097
C	−0.56(7)	0.0922	1(1)[a]	-0.60(9)	0.0922	1
Si	0.02(2)	0.11(13)[a]	0.75(4)	-0.08(1)	0.22(8)	0.784(12)
Graphene						
S1 (G_0)	2.41(3)	0.224(25)	2.86(11)	2.3(2)	0.38(23)	2.571(68)
S2 (G_0)	1.99(5)	0.19(3)	0.86(44)[a]	2.1(5)	0.15(26)	0.784[c]
G_1	5.82(4)	0.154(22)	2.66(12)	5.55(2)	0.152(14)	3.147[d]
G_2	9.16(7)	0.07(27)[a]	0.98(18)	9.11(1)	0.07	1.149(28)
G_3	12.6(1)	0.12(71)[a]	0.32(3)	12.42(3)	0.06	0.529(15)
G_4	-	-	-	15.79(7)	0.06	0.115(14)
Water						
H_2O	5.29(34)	0.43(37)	0.66[b]			
d_w = 2.42(1.46)[a]		$\bar{u}$ = 1(1)[a]				

[a] Large uncertainties indicate a general insensitivity to these structures and magnify uncertainties for other parameters in cases where they covary. As such, these parameters were fixed in the final iterations of the least-squares optimization. [b] Calculated from d_w according to Eq. 4.2. [c] Used modified model that enforces equality with Si surface coverage. [d] Fixed at bulk value after several fitting iterations in which the coverage of this layer exceeded 1 ML ($\Theta_{ML} = 3.147$ C/SiC).

Table 5.2. XR best-fit results for the 4H-SiC(0001)/EG/water interface with uncertainties on the last significant figures in parentheses. Values without uncertainties were fixed during analysis.

	In DIW			**In Air**		
Layer	**z (Å)**	**u (Å)**	**Θ (A_{UC}^{-1})**	**z (Å)**	**u (Å)**	**Θ (A_{UC}^{-1})**
4H-SiC(0001)						
C	-8.19(2)	0.0871	1	-8.16(1)	0.0922	1
Si	−7.569(3)	0.0791	1	-7.564(3)	0.0837	1
C	−5.70(3)	0.0871	1	-5.61(2)	0.0922	1
Si	−5.063(9)	0.0791	1	-5.047(5)	0.097(5)	1
C	−3.12(4)	0.0871	1	-3.05(2)	0.0922	1
Si	−2.525(9)	0.0791	1	-2.539(6)	0.139(12)	1
C	−0.44(6)	0.0871	1	-0.53(4)	0.0922	1
Si	0.01(2)	0.10(5)	0.84(7)	-0.046(7)	0.148(12)	0.86(3)
Graphene						
S1 (G_0)	2.3(2)	0.37(13)	3.04(15)	2.27(3)	0.44(4)	2.63(5)
S2 (G_0)	2.4(4)	0.19	0.84[a]	2.27(4)	0.19	0.86[a]
G_1	5.8(1)	0.24(3)	3.14(17)	5.64(2)	0.234(8)	3.14[b]
G_2	9.1(1)	0.15	1.06(14)	9.04(2)	0.15	1.07(7)
G_3	12.3(1)	0.07	0.27(13)	12.23(6)	0.07	0.25(8)
G_4	15.7	0.07	0.07(6)	15.73(9)	0.07	0.11(5)
Water						
H_2O	5.45(21)	0.93(44)	0.9(1)[c]			
$d_w = 3.5(5)$		$\bar{u} = 1$				

[a] Used modified model that enforces equality with Si surface coverage. [b] Fixed at bulk value (1 ML graphene) after several fitting iterations in which the coverage of this layer exceeded 1 ML. [c] Calculated from d_w according to Eq. 4.2.

G0 Buffer Layer

The best-fit structures resulting from analysis of the XR data measured in DIW and in air for both samples were generally equivalent but with several differences that highlight the sensitivities and challenges of XR data analysis. For the EG sample grown on 6H-SiC, we identified a G_0 buffer layer with a mean height of 2.31 ± 0.02 Å above the SiC surface and FWHM of approximately 0.72 Å when measured in DIW and a mean height of 2.36 ± 0.18 Å with FWHM

~0.82 Å in air. The best fit for the EG/4H-SiC sample was similar with a mean G_0 height of 2.29 ± 0.19 Å and FWHM ~0.80 Å in DIW and a height of 2.32 ± 0.03 Å with FWHM ~0.93 Å in air. These results are consistent with previous experimental [331, 332] and FPMD reports [303]. Others have reported G_0 heights of ~2.5 Å [334, 336].

The spacing between the two G_0 subpeaks S1 and S2 was found to be 0.42 ± 0.05 Å for the DIW/EG/6H-SiC XR measurement and 0.19 ± 0.56 Å for the air/EG/6H-SiC data, both of which are consistent with the separation distance reported by Emery et al. (0.35 Å) [331]. Although these vertical S1-S2 distances are below the resolution of the XR measurement (recall, $r = \pi/Q_{max} \sim 0.64$ Å in this case), we were unable to obtain a good fit to the data using a single G_0 peak, suggesting that the XR measurement may be sensitive to the asymmetry of this layer. The spacing between S1 and S2 was conserved throughout the fitting iterations as both layers moved together with respect to the SiC surface (and the parameters covary significantly), lending support for the shape of the buffer layer. Moreover, the distance from S2 to the topmost Si layer of the substrate was found to be 1.97 ± 0.05 Å for the DIW/EG/6H-SiC case and 2.21 ± 0.53 Å for the air/EG/6H-SiC case, in agreement with earlier reports [331, 334] and close to the vertical Si-C bond distance within the substrate (~1.8-1.9 Å; see Table 5.1). The latter observation further supports the structural model of the S2 C atoms being covalently bonded to the terminal Si of the substrate.

The best fit to the DIW/EG/4H-SiC XR data (with a resolution of ~ 0.5 Å) had a vertical S1-S2 spacing of 0.13 ± 0.47 Å with the S2 peak converging to a height above the SiC surface greater than that of the S1 peak (~2.4 Å and ~2.27 Å, respectively). Meanwhile, the fit to the XR data measured in air yielded coincident S1 and S2 peaks. These results are inconsistent with sp^3-type bonding of the S2 C atoms. However, the S2 layer height was poorly constrained with an uncertainty that would lead to a Si-S2 vertical distance of ~2 Å at the lower bound, consistent with sp^3 bonding. Previous studies have suggested that the buffer layer structure on 4H-SiC(0001) is equivalent to that on 6H-SiC [332]. Therefore, we conclude that the results of this XR analysis are fully consistent with current understanding of the buffer layer structure for EG/SiC(0001).

The best-fit structures reveal a G_0 coverage equivalent to 1.18 ± 0.03 ML and 1.23 ± 0.05 ML of graphene for the DIW/EG/6H- and DIW/EG/4H-SiC samples measured in DIW, respectively, and a coverage of 1.07 ± 0.02 ML and 1.11 ± 0.02 ML for the air/EG/6H- and air/EG/4H-SiC data, respectively. These results differ from previous reports that identified a layer with graphene-like density (i.e., ~1 ML) [67, 305, 331]. Attempts were made to constrain the G_0 density to that of a single graphene layer, but such a density was always found to be inconsistent with the data. The excess carbon density we identified in the G_0 layer may account for a surface oxide species [331, 337-340] not included in our model. Emery et al. identified via XPS the presence of SiO_x in several EG/SiC samples, which they were unable to accurately model in the XR data analysis. They estimated the oxygen coverage to vary from 2 O/nm^2 in an Ar-grown sample to 6 O/nm^2 in a UHV-grown sample. The excess carbon density of the G_0 layer in our Ar-grown samples can instead be attributed to an oxygen content ranging from ~2 O/nm^2 to ~7 O/nm^2. The G_0 coverages found for the best fits in DIW were larger than those found in air, but it is unclear if this results from the adsorption of water in the G_0 layer or a covariance of the G_0 coverage parameter with parameters describing the water layer (modeled as an O layer due to the relative insensitivity of X-rays to hydrogen), especially in the case where surface oxide species may be present.

SiC Surface

We identify a partially depleted SiC surface, consistent with the thermal desorption of Si during graphene growth. The model chosen for analysis of the DIW/EG/6H-SiC XR data was different from that chosen in the other three cases discussed here and included independent S2 and surface Si layer coverages. Based on the results of the DIW/EG/6H-SiC analysis, the model was revised for all subsequent EG/SiC XR analyses to enforce equality between the terminal Si layer coverage and that of the S2 layer (i.e., a single parameter was used to describe the coverage of both layers). The best fit to the DIW/EG/6H-SiC data resulted in Si depletion down to the fourth surface layer of the SiC while the C layers within SiC were not depleted. The coverage of the topmost Si layer was consistent with the coverage of the S2 layer of G_0, though we report a large uncertainty on the S2 coverage; see Table 5.1. Therefore, we fixed the S2 coverage parameter after several fitting iterations where it was converging to values consistent with the amount of surface Si depletion. That is, the coverages of the two layers indicate a one-to-one bonding between dangling Si atoms and sp^3-hybridized carbons, consistent with the proposed EG growth mechanism and previous reports [294, 295, 331, 341].

For the air/EG/6H-SiC measurement and both measurements of the sample with the 4H-SiC substrate (i.e., with the revised model using a single parameter to describe the terminal Si and S2 coverages), the SiC surface was depleted only in the surface-most Si layer. The coverage of this layer was independent of the sample environment and was ~20% depleted in the 6H-SiC sample and ~15% depleted in the 4H-SiC sample. For both measurements carried out in DIW, the topmost Si layer was displaced away from the bulk and toward the G0 buffer layer, whereas in air the topmost Si layer was displaced toward the bulk substrate. The latter results agree with those of Emery et al. wherein the XR data were measured with the samples in vacuum.

Epitaxial Graphene

We found a graphene film structure on the 6H-SiC sample consistent AFM images in Figure 5.5a,b. The best fit to the data measured in DIW revealed three free-standing graphene layers, G_1 - G_3, above the G_0 buffer layer on the 6H-SiC sample with a total of 1.25 ± 0.07 ML of EG; the best fit to the data measured in air revealed four graphene layers G_1 - G_4 totaling of 1.57 ± 0.01 ML of EG with the G_1 layer having complete coverage. The difference in graphene coverage between the DIW and air results (and the different Si surface depletion identified above) is likely due to these XR measurements being carried out on different spots on the sample and also points to an inhomogeneity in EG growth across the sample that may depend on the precise positioning of the substrate in the tube furnace. The graphene layer spacing was consistent across both XR analyses with a mean spacing of ~3.40 Å, in agreement with the known value [307]. For the best fit in DIW, G_1 was located 3.50 ± 0.04 Å above G_0 and for the best fit in air G_1 was located at 3.3 ± 0.2 Å, which generally agree with previous reports that show a G_0 – G_1 distance of 3.5 Å [305, 331, 335].

The best-fit graphene structures for the 4H-SiC measurements were similar to those on the 6H-SiC substrate and are also generally consistent with the AFM images (Figure 5.5c-e). We identified four graphene layers G_1 - G_4 totaling ~1.4 ML EG and with a complete G_1 layer. The mean layer spacing between free-standing graphene layers was also found to be ~3.3 Å, and G_1

was found to be located at 3.5 ± 0.2 Å and 3.37 ± 0.04 Å above G_0 for the best fits to the data measured in DIW and in air, respectively.

Adsorbed Water

The best-fit water structures from both data sets are similar and show a weakly modulated water profile with density peaks that correlate with the locations of the graphene layers (Figure 5.6b). The intrinsic interfacial water structures on the EG/6H-SiC and EG/4H-SiC samples (Figure 5.6c) show a first hydration layer height above the exposed graphene surfaces of 3.1 ± 0.3 Å, which is consistent with a slightly hydrophobic interface [38, 39]. Although the water distributions show different vertical distances between the first and second hydration layers between the two samples (Figure 5.6c), the uncertainty on the d_w parameter was large in both cases (Tables 5.1 and 5.2), and the results are equivalent within error. Similarly, the peak density of the first hydration layer was >2× the bulk water density in the case of the DIW/EG/6H-SiC analysis but only ~1.5× the bulk density for the DIW/EG/4H-SiC analysis. Since the hydration layer occupancy is defined by d_w (Eq. 4.2), these peak densities are also poorly constrained.

The classical MD simulation carried out with a partial graphene surface predicts a water distribution generally equivalent to that determined experimentally. Namely, the MD hydration structure is weakly modulated with peak positions that are approximately coincident with the graphene layers (Figure 5.7a). The simulation predicts approximately the same interfacial water height above each exposed graphene surface, z ≈3.3 Å (Figure 5.7b), in agreement with the experimental results. However, MD shows a broadening of the first hydration layer r.m.s. width for thicker graphene regions (i.e., u_{G3} where the total thickness of the graphene slab is ~10 Å is larger than u_{G0}; Figure 5.7b). This phenomenon is not observed in the experimental results because the model used in the XR data analysis assumes the same hydration layer structure above each exposed surface. The XR best-fit parameters show that the vibrational amplitude of the first hydration layer is not well-constrained by the XR data. It is possible that fitting different, overlapping intrinsic water profiles, such as those predicted by the MD, to a single model would lead to a best-fit structure with greater uncertainties on the r.m.s. widths, encompassing the range of vibrational amplitudes that are present. These complexities notwithstanding, the MD hydration layer widths agree with the XR result for the DIW/EG/6H-SiC measurement by the third layer

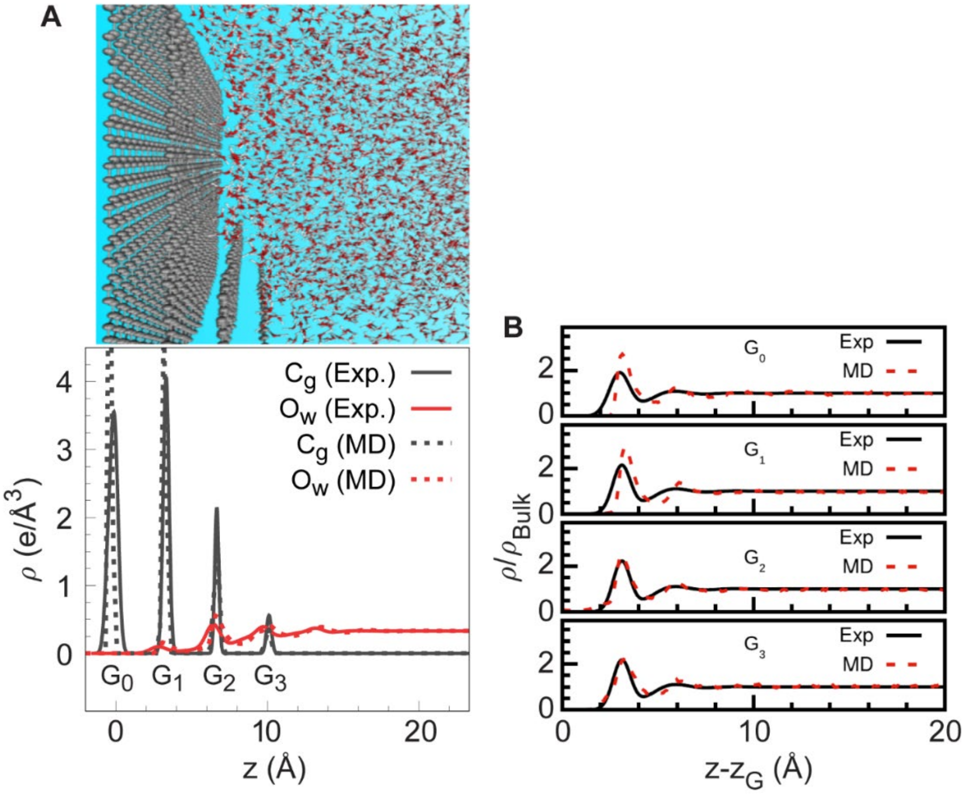

Figure 5.7. Comparison of MD adsorbed water structure on an irregular graphene surface with XR best fit. (A) MD snapshot of irregular graphene surface (top) and resulting layered water profile (bottom, dotted lines) shows agreement with the experimental best-fit structure of water adsorption on the EG/6H-SiC sample (solid lines). (B) The water density profiles on each exposed surface G_0-G_3 are shown normalized to the bulk water density. MD simulations carried out by F. Jimenez Angeles.

(G_2), supporting the experimentally-derived result. The peak widths of the intrinsic water structure determined for the DIW/EG/4H-SiC measurement appear broader than those determined for the 6H-SiC sample (Figure 5.6c), but the structures are equivalent within the best-fit parameter uncertainties.

The intrinsic water structure determined by MD (Figure 5.8a), i.e., from the simulation employing a perfect four-layer thick graphene slab, is the same as that observed above the G_0 layer in the simulation with an irregular surface. This suggests that the width broadening discussed above may result from finite size effects of the simulation or edge effects from the partial graphene layers rather than changes in the graphene thickness. The intrinsic MD water distribution shows a peak oxygen density that is more than twice that of the bulk, in agreement with the XR best-fit structure for the EG/6H-SiC sample. The density oscillations decay rapidly with a small secondary hydration layer at $z \approx 0.6$ nm and a nearly bulk-like third hydration layer at $z \approx 1$ nm, also in agreement with the experimental result. The hydrogen atom distribution calculated via the MD simulation shows a layered proton distribution with a narrow first peak, which suggests a nonzero interfacial water polarization. Since the X-ray scattering from hydrogen atoms is relatively weak, the XR best-fit structure is defined according to the oxygen atom distribution only and cannot be used to determine the proton distribution directly. Nevertheless, the close agreement between the XR and MD oxygen distribution lends support to the MD prediction.

The location of the hydrogen density peak at the first hydration layer coincides with the oxygen density peak but is broader, indicating that a fraction of the water dipole moments are oriented perpendicularly away from the graphene surface. This is partially driven by transient hydrogen bonds between water molecules of the first and second hydration layers (see inset in

Figure 5.8a) and the inability of water molecules to form hydrogen bonds with the graphene surface. The distribution function of the water dipole orientation with respect to the graphene surface normal, $P(\cos\Omega)$ (Figure 5.8b) reveals a first hydration layer in the region h_1 ($z < 5$ Å

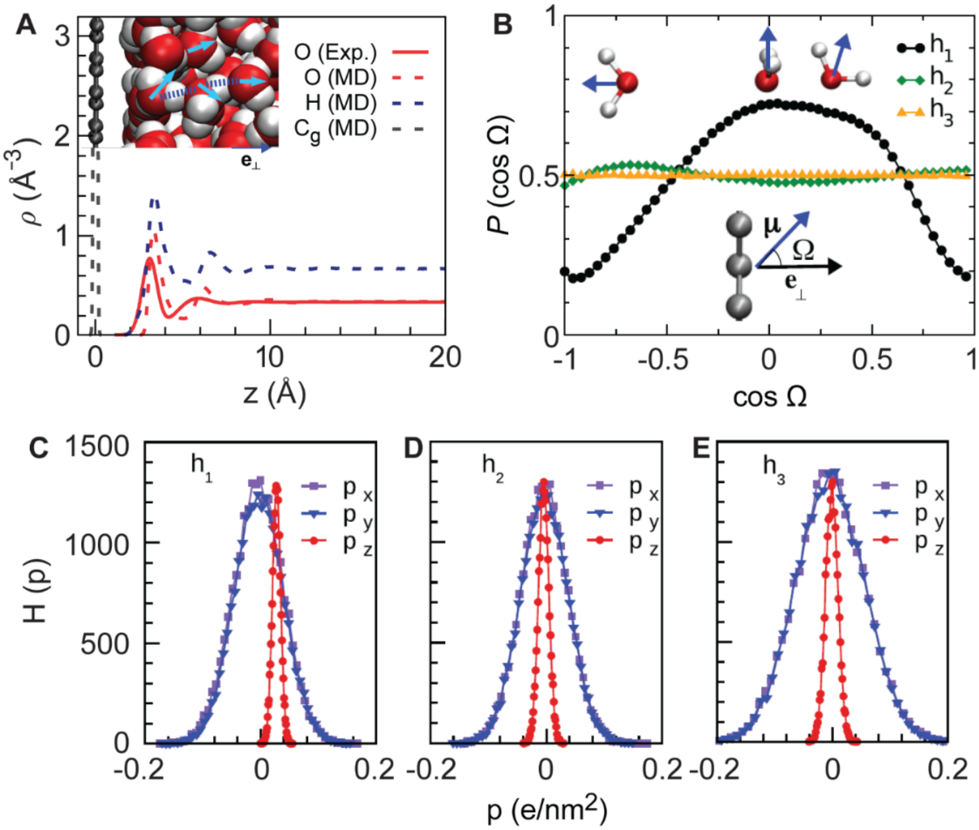

Figure 5.8. Polarization of water at the graphene surface calculated from MD. (A) Similar intrinsic water density profiles are observed in the experimental best-fit (EG/6H-SiC sample; red solid line) and via MD simulations (dashed lines; O, red; H, blue; C, gray); the inset shows an MD snapshot of the water-graphene interface along the surface normal direction with unitary vector $\mathbf{e}_\perp$; light blue arrows represent the water dipole moment, and dashed blue lines represent temporary hydrogen bonds. (B) The water orientation probability distribution function $P(\cos\Omega)$ is shown within three water regions with distinct heights above the graphene surface: $h_1 \equiv 0 \leq z < 5$ Å, $h_2 \equiv 5$ Å $\leq z < 10$ Å, and $h_3 \equiv 10$ Å $\leq z < 15$ Å; the angle between the water dipole moment $\boldsymbol{\mu}$ and the graphene surface normal is given by Ω, $\mu_0 \equiv |\mu| = 0.489\,e$ Å is the dipole moment of the SPC/E water model, and e is the positive elementary charge; from left to right, insets show representative configurations of water for $\cos\Omega = -1$, 0, and > 0, respectively. (C-E) Histograms of the instantaneous water polarization components $H(p_i)$ ($i = x, y, z$) show broad distributions for p_x and p_y centered at zero in the three water regions h_1-h_3; p_z is persistently narrower than in the x and y directions with a preferential polarization in the +z-direction within 5 Å of the graphene/water interface. MD results provided by F. Jimenez Angeles.

from the graphene surface) with the majority of water dipole moments oriented parallel to the graphene plane ($\cos \Omega = 0$). However, an asymmetry in the distribution exhibits a slight preference for the water dipole moment to orient away from the graphene surface, in agreement with the water orientation inferred from the hydrogen atomic density distribution. In the region h_2 (5 Å $\leq z < 10$ Å), the preferential orientation of water molecules is diminished, and in the region h_3 (10 Å $\leq z < 15$ Å) and beyond, all water dipole moment orientations are equally probable.

The MD simulations also reveal a nonzero, persistent water polarization in the *z*-direction within the interfacial region (Figures 5.8c-e). Histograms of the instantaneous water polarization $H(p_{x,y,z})$ show narrow p_z distributions (indicative of a dipole fluctuation suppression identified previously [44]) with an average polarization $P_z \equiv \langle p_z \rangle \approx 0.03$ e/nm^2 in the h_1 region (Figure 5.8c), $P_z \approx -0.004$ e/nm^2 in the h_2 region (Figure 5.8d), and $P_z = 0$ in the h_3 region (Figure 5.8e). The water polarization distributions in p_x and p_y are universally broader than p_z, indicating no suppression of dipole fluctuations parallel to the graphene plane, and P_x and P_y are always equal to zero. These results reveal a confinement-induced, intrinsic polarization of water molecules along the graphene surface normal direction, which in turn leads to an anisotropic dielectric permittivity with a significantly reduced out-of-plane component compared to the bulk [136]. In addition to the change in dielectric response, which has been identified previously [41, 44, 46], the MD simulations show that this polarization leads to a resistance to reorient and displace interfacial water molecules in the presence of ions with an energetic cost that differs for anions and cations. Consequently, there is a directional dependence on the interaction between an anion and cation near the surface (see Ref. [130] for more details). This contrasts with the classical expectations from Coulomb's law wherein the interactions between the anion and cation should depend only on the properties of the dielectric medium. These properties are fundamental to understanding ion-specific effects and ion adsorption at interfaces.

5.3.4: Discussion

The analysis of XR data measured in different environments (air versus water) and for samples grown on the Si-face of two different SiC substrates (6H versus 4H) revealed consistent EG/SiC interfacial structures across all measurements. These included partial depletion of the terminal Si layer of the substrate, a buffer layer that can be described by two C-rich layers with different hybridizations (sp^2 and sp^3), and several partial layers of two-dimensional graphene. The layered interfacial water structures were also similar for both samples with an identical height of the first hydration layer above the adsorbing graphene surfaces, which was also in agreement with the adsorbed water height predicted by MD simulations.

One pattern that emerges from the side-by-side comparison of measurements carried out in air versus in water is that the introduction of water has a small but apparently significant effect on the surface relaxation of the SiC interface. Specifically, the terminal Si layer is shown to relax inward toward the bulk substrate in air but expand away from the bulk substrate in the presence of water. This change in relaxation leads to a slightly reduced G_0-Si distance in water compared to the distance in air. In addition, the results suggest that the G_0 layer r.m.s. width decreases in the presence of water compared to the r.m.s. width in air, though again, the uncertainty on the layer widths was large. This behavior has not explicitly been identified before as previous reports considered the EG/SiC [312, 331, 332] and the DIW/EG/SiC interfaces [67] in isolation. The observation of changes to the Si interface and G_0 buffer layer in the presence of water may reflect the unique band structure of this interface due to strong interactions between G_0 and the substrate that leads to an n-type doping [302, 303, 342-344]. The presence of any surface oxide species SiO_x could also contribute to electrostatic interactions with water. Finally, these results may suggest that EG grown on SiC exhibits a certain degree of wetting transparency, a phenomenon that is still debated [345-348] and has been studied primarily in cases with weak graphene-substrate interactions. Wetting transparency is crucial if graphene is to be used as a coating material without disrupting the properties of the underlying substrate. It is unclear if the G_0 layer with its sp^2 and sp^3 character would display similar wetting transparency properties as 2D graphene. Of course, the XR analysis relies on the selection of a suitable model *a priori*, so it is possible that choices made in setting up the model could contribute to the observed behavior. Nevertheless, the high accuracy of the best-fit structures (based on χ^2~1-3 where a perfect fit to the data within its experimental uncertainties would result in $\chi^2 = 1$) and agreement with the MD prediction of the water structure, supports the choice of model. The effects of water on the SiC substrate and G_0 should be investigated further.

Comparison with Previous DIW/EG/SiC Results

XR measurements by Zhou et al. [67] identified a similar water height on free-standing graphene (3.2 Å) but found a significantly reduced interfacial water height of 2.3 Å on the G_0 buffer layer, which suggested that G_0 exhibits a hydrophilic character. Our best-fit structure for the EG/6H-SiC sample revealed a partially exposed G_0 surface (0.85 ML coverage of G_1), and yet the XR data were well-described using a single model for water adsorption on all exposed C surfaces including G_0. It is possible that our data could also be described accurately with an additional water layer adsorbed closer to G_0, but such a layer was not necessary and would further complicate an already complex model. With this in mind, we explore possible explanations for real differences in G_0 properties across samples.

Zhou et al. reported water contact angle (WCA) measurements that imply a more hydrophilic G_0 and which are equivalent to the WCA on bare SiC [345]. The WCA measurements showed a linearly increasing trend with graphene layer thickness (larger WCA indicates greater hydrophobicity), which would also be consistent with wetting transparency of graphene on SiC. However, our experimental evidence of wetting transparency appears uncorrelated with the adsorbed water height. Zhou et al. reported best-fit occupancies of ~90% G_0 coverage on two of their samples, whereas our best-fit structures showed complete G_0 coverage (with excess density that may be attributable to SiO_x species [331]). Incomplete G_0 coverage could indicate a partially exposed SiC surface (i.e., incomplete graphitization of the substrate during growth) [318] or a reconstructed G_0 layer [319] that promotes stronger water adsorption. Zhou et al. also reported MD and FPMD simulations of defect-free surfaces that predict water heights above G_0 consistent with that observed above free-standing graphene, and in agreement with our results. The FPMD simulations included effects of the SiC substrate and the corrugation of the buffer layer (which are not included in MD simulations) but found only a ~0.2 Å decrease in the adsorbed water height above G_0 compared to free-standing graphene. Only upon inclusion of vacancies in the G_0 layer consistent with the coverage found experimentally and -OH defects were they able to simulate a G_0-water height of 2.33 Å. We conclude that while we can reasonably expect water to adsorb more closely to the buffer layer than to the subsequent graphene layers as a result of the SiC substrate and corrugated surface, we expect the effect to be minor in the absence of substantial defects.

UHV-grown EG/SiC samples such as those examined in Ref. [67] are known to possess a greater amount of defects than graphene grown in a furnace in an Ar atmosphere [311]. However, based on the results of Emery et al. wherein UHV-grown and Ar-grown EG/SiC were found to have equivalent interface structures [331], we would not expect the EG growth methodology to substantially contribute to the differences observed between our and Zhou's G_0-water distance. The quality of the sample depends on the vacuum level and any pre-treatments of the SiC to remove oxides [337, 338, 340, 349]. No pre-treatments were reported by Zhou et al. They also reported Raman data with significant D and D+D' peaks, which result from edge and other defect states [321, 345, 350-352]. In fact, it has been shown that the introduction of such defect peaks upon oxygen plasma etching of EG/SiC is associated with a decrease in WCA [345]. Although Raman measurements are not presented for the samples studied in this work, the insights gained from Ref. [67] suggest that our samples were likely relatively defect-free, in which case the water structures above the buffer layer and subsequent graphene layers are very similar and can be described well by a single water model given certain resolution limits of the XR measurement.

Insights from MD Simulations

The main insight gained from MD relevant for this thesis is the intrinsic and directional polarization of water within 5 Å of the graphene surface. Ion-specific effects at interfaces are typically attributed to properties of the ion (e.g., the radii, valence, and internal polarizability) [353], but the solvent properties are often neglected. Indeed, the theories of the electrical double layer (EDL) formation described in Chapter 2 ignore solvent effects (outside of assuming the dielectric permittivity is that of the bulk medium). While a reduction in dielectric response perpendicular to the graphene surface was previously identified [44, 46], our MD results also show that the polarization of water molecules and the inhibition of their rotational motion adjacent to the graphene surface alters electrostatic interactions between ions in a way that cannot be explained simply by the reduced dielectric constant. This phenomenon may affect the structure of the EDL at the graphene surface, which I explore next.

5.4: RbCl Double Layer on Graphene

5.4.1: Electrochemical Characterization

The potential-controlled EDL structure was measured on a different EG/6H-SiC sample. The AFM of this sample (Figure 5.9a) shows graphene terraces with an average width of ~1.2 μm and with some partially exposed graphene layers, similar to the previous EG/6H-SiC sample (Figure 5.5a,b). The average surface roughness was calculated to be zero. The resistivity was calculated from the inverse slope of the I(V) curve in Figure 5.9b times the appropriate prefactors from Eq. 5.2 and was found to be 3.2 μΩ m. The inset in Figure 5.9b shows the placement of the colinear four-point probe tips during measurement. The geometric correction factor for a rectangular sample depends on the ratio of the small dimension of the sample (3 mm) to the tip spacing, p = 0.04 in (~1.02 mm) in this case, and gives $\xi \approx 0.6$ [330]. The film thickness is non-uniform across the sample surface due to the partial coverage of EG layers. However, a mean thickness can be estimated from the results of the non-resonant XR data analysis (see Section 5.4.2 and Table B1 in Appendix B.2 for best-fit parameters) using the total graphene layer coverage and graphene d-spacing plus the height of the free-standing graphene above the G_0 buffer layer. This yields a rough estimate of the

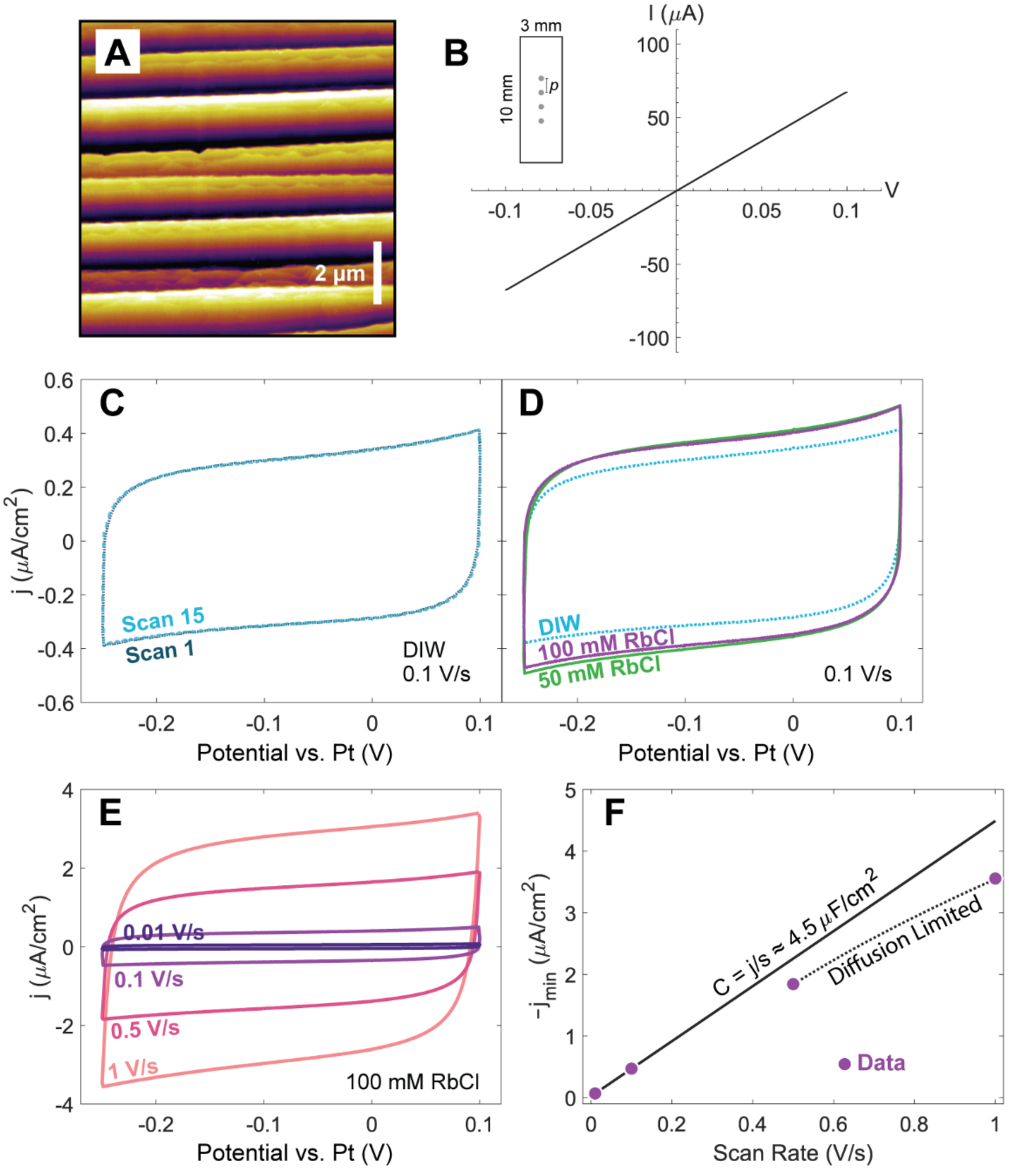

Figure 5.9. Electrochemical characterization of EG/6H-SiC. (A) An AFM image of a 10μm × 10μm section of the sample shows 1 μm wide smooth terraces with some partial graphene layers visible. (B) Resistivity measurement by four point probe; inset: schematic of four point probe tip placement on electrode for measurement (tip spacing p). (C) Scans 1 and 15 of a cyclic voltammogram (CV) in DIW are essentially identical, showing sample stability over repeated cycling. (D) CVs performed in 50 mM RbCl and 100 mM RbCl show increased capacitance compared to the CV carried out in DIW. (E) CVs at different scan rates s in 100 mM RbCl. (F) The capacitance estimated from the minimum voltages from (E) as a function of scan rate is C ~ 4.5 μF/cm^2.

layer thickness as ~8 Å. Thus, the film conductivity is ≈312.5 kS/m, in line with previous reports of graphene conductivity [354].

The sample was loaded in the transmission electrochemical cell with DIW, and several CVs with increasing voltage limits were performed at a voltage scan rate of s = 0.1 V/s. The maximum voltage window that maintains capacitive behavior (i.e., Faradaic charge transfer events were not observed) was approximately 0.35 V ranging from -0.25 V to +0.1V with respect to the Pt wire reference electrode (Figure 5.9c). The CVs also showed that the sample is stable over this voltage range, with fully reversible charging from the first to last scans. The open circuit potential (OCP) measured for this sample in DIW was -0.063 V. The DIW was then drained from the cell and replaced with a 50 mM RbCl solution, which was allowed to equilibrate. The solution was exchanged once more before further CV measurements were carried out in case residual DIW diluted the electrolyte. The OCP in 50 mM RbCl was measured twice, back-to-back without any intermediate steps, as 0.005 V and -0.012 V, which suggests the level of precision of the measurement. A CV scan was then carried out in 50 mM RbCl before the solution was exchanged with 100 mM RbCl. The OCP was not measured in 100 mM RbCl but is not expected to differ significantly from that in 50 mM RbCl given the similarity in the CV curves (Figure 5.9d) and the fluctuation in OCP measured for other similar samples in 0.1 M RbCl (up to 40 mV differences between repeated OCP measurements).

The CVs performed in 50 mM RbCl and 100 mM RbCl show an increase in capacitive current compared to the measurement in DIW (Figure 5.9d). This is indicative of the increased capacitance expected when ions are present. The cathodic sweep (i.e., scanning the voltage in the negative direction) of the 100 mM RbCl shows a minor reduction in the current response compared to the case in 50 mM RbCl, which indicates a reduced capacitance with a higher ion concentration and may reflect either ionic correlations or crowding effects. The integrated capacitances (Eq. 3.24) from the CVs shown in Figure 5.9d yield $C_0 = 3.0$ μF/cm^2, $C_{50} = 3.9$ μF/cm^2, and $C_{100} = 3.6$ μF/cm^2 where the subscript number indicates the concentration of RbCl in units of mM.

A series of CVs were performed in 100 mM RbCl with s ranging from 0.01 V/s to 1 V/s (Figure 5.9e) to obtain an estimate of the capacitance in a regime more comparable to the steady state condition employed for the RAXR measurements of the EDL structure. The magnitude of the cathodic current at the most negative voltage (i.e., $|j(\text{-}0.25\text{ V})|$) plotted with respect to the scan rate gave an estimate of the capacitance according to Eq. 3.23c of C = 4.5 μF/cm^2. The integrated capacitance from the CVs in Figure 5.9e according to Eq. 3.24 yields a similar capacitance estimate at the slowest scan rate, C(s = 0.01 V/s) = 4.7 μF/cm^2.

A capacitance of 4.5 μF/cm^2 is similar to values previously measured [323] and simulated by FPMD [325, 355] for graphene electrodes in aqueous solution. However, this is significantly smaller than the capacitance expected from PB theory and indicates that the graphene quantum capacitance dominates, as expected. The surface charge density from PB theory is expected to follow the Grahame equation (Eq. 2.10), which gives ~240 μC/cm^2 in the double layer for a 100 mM RbCl solution at an applied voltage of -0.25 V and corresponds to a capacitance of ~955 μF/cm^2. This is approximately 200 times the value obtained from the CV measurements (Figure 5.10). From Eq. 5.1, and neglecting for now the possibility of a Stern layer, we estimate the graphene quantum capacitance to be ~4.52 μF/cm^2.

In the small voltage limit of GC theory (i.e., $|V| = k_BT$), the measured capacitance of 4.5 μF/cm^2 yields a stored charge of -0.12 μC/cm^2, equivalent to 0.38×10^{-3} e$^-$ per graphene unit cell,

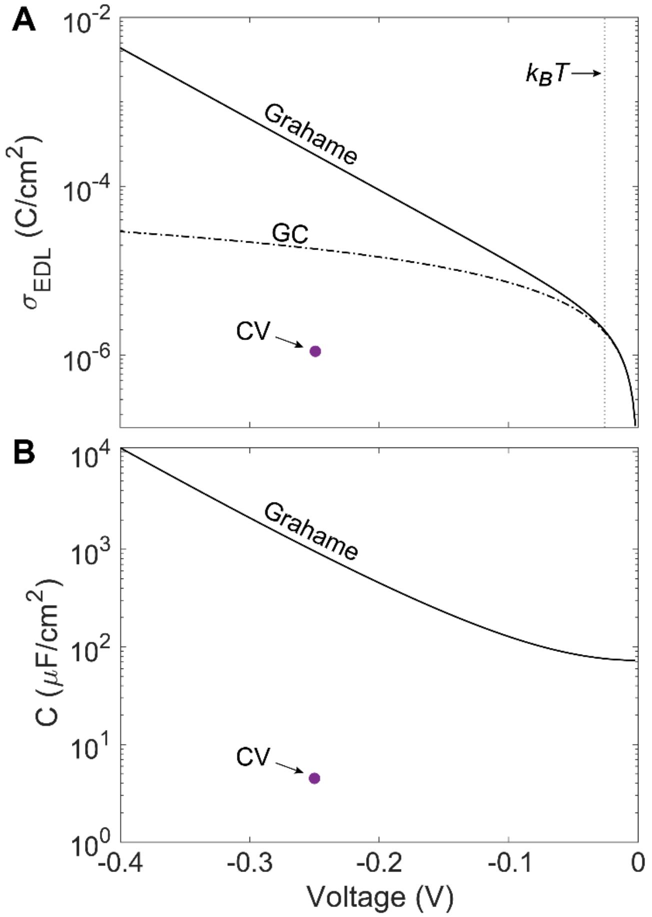

Figure 5.10. Surface charge and capacitance from Poisson-Boltzmann theory and that measured from cyclic voltammetry. (A) The surface charge versus voltage expected for a 0.1 M RbCl solution is calculated using the Grahame equation (—) and compared to the limiting case of Gouy-Chapman theory (—.); the GC theory strictly applies only for $V < k_BT$ (vertical dotted line) but is extended to more negative voltages for comparison; both are significantly larger than the surface charge for C = 4.5 μF/cm^2 with an applied voltage of -0.25 V (purple circle). (B) The capacitance from the Grahame surface charge is calculated from $C = \sigma/V$ and is ~200 times larger than the measured average capacitance from the CV for an applied potential of -0.25 V. The CV data are plotted at the limit of the CV voltage window, -0.25 V.

which is significantly smaller than the intrinsic surface charge on mica (-34 μC/cm^2). At this surface charge, the adsorption strength is expected to be much smaller than that on mica. However, the higher ion concentration of 100 mM RbCl should promote a higher charge density near the surface compared to what would be observed for a 3 mM RbCl solution with the same electrode charge. Specifically, the Debye length decreases with increasing concentration (Λ_3 = 56 Å, and Λ_{100} = 9.7 Å where the subscript again indicates the mM concentration; Eq. 2.14). This would result in an increase in the double layer contribution to the total structure factor in the XR measurements compared to a weakly adsorbed double layer in a 3 mM RbCl solution.

We can also consider how the adsorption is expected to change at voltages outside the GC limit ($|V| > k_B T$). At the edge of the capacitive region in Figure 5.9 (i.e., at -0.25 V), the measured capacitance yields a stored charge of -1.13 μC/cm^2. This is still small, and we expect the ion adsorption behavior to fall into a weak coupling regime within the counterion condensation theory of Lau et al. [74]. The corresponding order parameter (Eq. 2.17a) and reduced temperature (Eq. 2.17b) for 100 mM RbCl in water at room temperature are $g \sim 0.7$ and $\theta \sim 0.2$, respectively. These values indicate that correlation fluctuations will play a small role in the double layer formation with the ions undergoing a smooth transition from the uncondensed to condensed phases. This theory predicts that ~15% of the ions in the double layer would condense at the surface (Figure 2.4a). From Eq. 2.17c, this yields a Stern layer density of ~8.7×10^{-4} Rb^+ per substrate unit cell area (A_{SiC} = 8.22 Å^2). However, when we consider the presence of co-ions [158], Lau's theory predicts that the double layer will agree with the GC prediction (i.e., a diffuse ion cloud), and no Stern layer should form (Figure 2.4b). (Lau et al. define the Debye length in terms of the surface charge rather than the ion concentration [74]. As such, the expected surface charge from our capacitance would still fall within the GC domain).

If we consider the dielectric decrement in in the interfacial region, i.e., $\epsilon_\perp = 2$ within 1 nm of the graphene surface [46], the Lau model including co-ions suggests a modified GC-like double layer resulting in an effective electrode charge lower than the nominal charge (the DH* region of the phase diagram in Figure 2.4b) [158]. However, we still would not expect charge inversion to occur. Based on this analysis, we do not expect to see a significant amount of counterion condensation at the charged graphene surface within the capacitive region. The estimate of ~15% counterion condensation can be taken as an upper limit.

5.4.2: Non-Resonant Specular XR Results

Non-resonant XR data (E = 14 keV) were measured with the EG/SiC sample in DIW and in 100 mM RbCl (Figure 5.11a). As expected, we identify no clear difference between the two CTRs over the Q-range measured due to the weak contribution to the structure factor from the relatively dilute RbCl concentration, even when enhanced locally at the interface. The resulting best-fit structures for both data sets are also generally equivalent. In DIW (Figure 5.11a top panel), we found four partial graphene layers (G_1-G_4) above the G_0 buffer layer (θ_{G0} = 1.26±0.02 ML, z_{G0} = 2.23±0.07 Å above the terminal SiC layer with the S2 sublayer located at ~2.11 Å above the Si, and G_0 FWHM~0.7 Å). The G_1 layer was located at 3.4±0.1 Å above the mean G_0 position, the total graphene coverage was 1.5±0.1 ML with a mean *d*-spacing of 3.33±0.38 Å, and the first adsorbed water layer was found to be located at 3.4±0.2 Å above the exposed graphene surfaces. The best fit to the data measured in 100 mM RbCl (Figure 5.11b bottom panel) revealed five partial graphene layers (G_1-G_5) above G_0 (Θ_{G0} = 1.24 ML, z_{G0} = 2.28±0.02 Å above the terminal SiC layer with the S2 sublayer located at 1.93±0.01 Å above the Si, and G_0 FWHM~0.7 Å). G_1 was located at 3.49±0.04 Å above the mean G_0 position, the total graphene coverage was 1.6±0.3 ML with mean *d*-spacing 3.36±0.02 Å, and the first adsorbed water layer was found to be located at

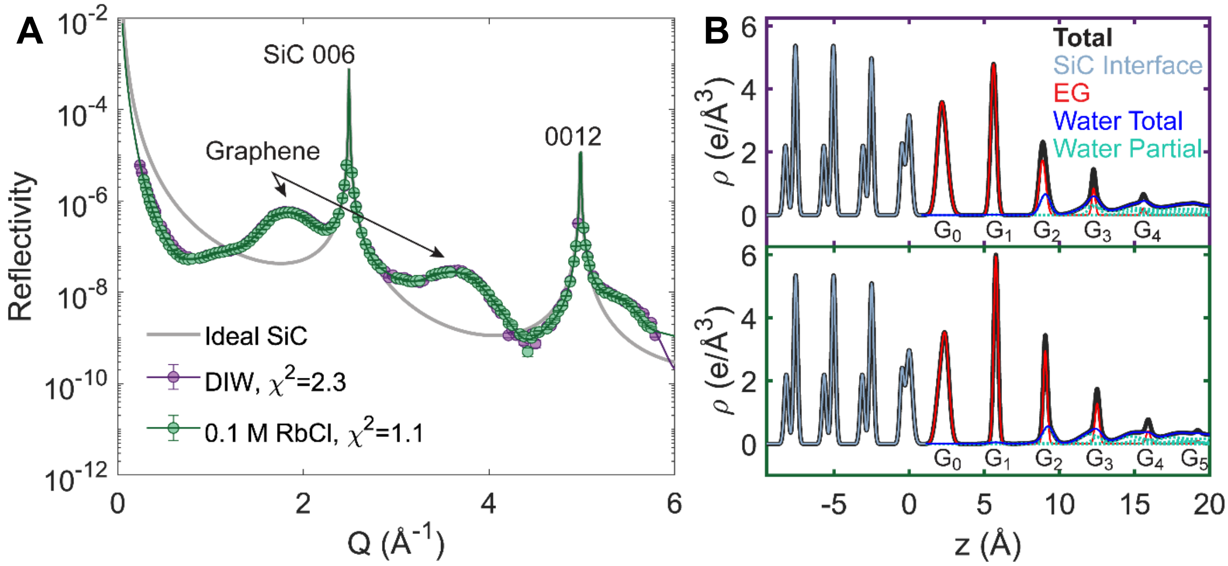

Figure 5.11. X-ray reflectivity data and best-fit structure for EG/6H-SiC in DIW and in 0.1 M RbCl measured at OCP. (A) The CTR data do not show obvious differences between the measurement in DIW (purple) versus that in 0.1 M RbCl (green). The best fit in DIW had $\chi^2 = 2.3$ with 3% minimum error bars; the best fit in 0.1 M RbCl had $\chi^2 = 1.1$ with 2% minimum error bars. (B) The best-fit electron density in DIW (purple outline, top) was found to have 4 partial graphene layers while the best fit in 0.1 M RbCl (green outline, bottom) was found to have 5 partial layers (see Table B.1 for best-fit parameters).

3.5±0.2 Å above each exposed graphene surface. Both fits revealed complete coverage of the G_1 layer. The best-fit parameters for both data sets are given in Table B1 in Appendix B.2.

5.4.3: RAXR Measurement Setup

Cyclic Voltammetry at the Beamline

The CV measurements performed at the beamline are shown in Figure 5.12. An initial CV (CV_0) was performed before the sample was exposed to X-rays to ensure that the capacitive behavior of the sample was maintained during transport to the APS. We found that the fastest scan rate possible when controlling the potentiostat via the beamline software, SPEC (via step-wise voltage changes of 0.1 V) was ~0.038 V/s because communication from the software is a rate limiting step. At this voltage scan rate, we expect the current response to be similar to that measured at 0.01 V/s (Figure 5.9e). Indeed, we find that the CV measured at the beamline is similar but with an increased slope, indicative of a parallel resistance (Figure 3.7b), which may be due to the software control. Overall, the device operated as expected in the initial CV. However, a CV carried out immediately after the specular CTR measurement was completed showed a positive current offset, Δj(CTR), compared to CV$_0$ (Figure 5.12a). This suggests that there was a build-up of positive charge on the electrode due to the X-ray exposure, which is likely due to photoabsorption by the semi-insulating SiC substrate. Upon repeated voltage cycling, we observed that the current slowly decreased and eventually recovered the general shape and magnitude of CV$_0$. Notably, the anodic current (at positive voltage) of the recovered CV (CV$_R$) was lower than that of CV$_0$, indicating an irreversible change in the system.

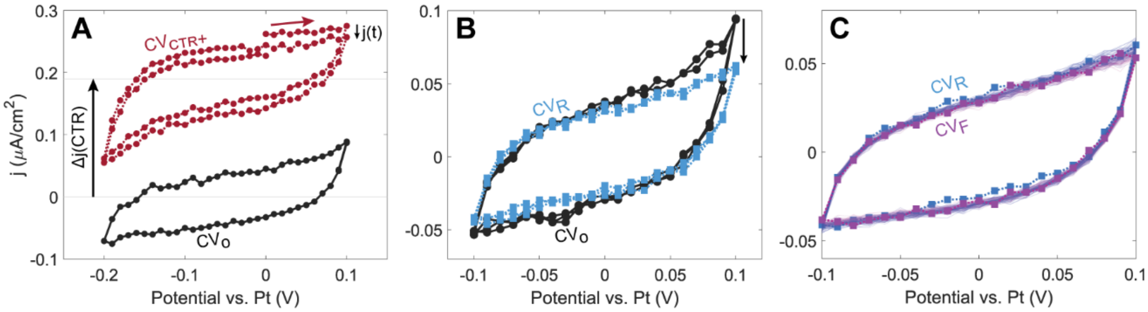

Figure 5.12. CVs at beamline with CH potentiostat controlled by SPEC. CV$_0$ is the reference CV carried out before XR measurements were carried out. Immediately after the first CTR was measured, the CV exhibited an increased current offset by $\Delta j(CTR)$, yielding the CV called "CV$_{CTR+}$". The current decreases with repeated CV cycles and time (j(t)). (B) after several CV cycles and ~1 hour, the current has generally recovered (CV$_R$) to the reference CV$_0$ but with an irreversible decrease in the maximum current density at oxidative potentials (+0.1 V) indicated by the down arrow. (C) Each CV carried out between RAXR scans is plotted with the first CV (CV$_R$) and the final CV (CV$_F$) highlighted in blue and purple, respectively, and show that the electrochemistry was stable throughout the RAXR measurements in which the X-ray flux on the sample was kept low.

Because the sample was found to be sensitive to X-ray exposure, the flux was kept low during RAXR scans. The current generated by the X-rays may perturb the double layer, leading to unreliable RAXR results when the goal is to measure the steady state structure. The filter transmission and exposure time at each scattering condition to be probed were determined manually before starting a suite of RAXR measurements. The required conditions were set such that the total detector counts did not exceed ~600 counts per second (cps) at the maximum energy of a RAXR scan (E_0 + 0.3 keV). Several RAXR scans were performed for each momentum transfer and summed together as the first step of the data analysis in order to improve the signal-to-background ratio. The number of repeat RAXR scans for each Q was set so that the total counts would sum to ~3000 cps at E_0 + 0.3 keV. At small Q (i.e., just above the SiC critical angle, 0.04 Å^{-1}, where the reflected intensity is 10^{-2}), the desired counts could be achieved with a filter transmission of ~10^{-6} and an exposure time of $<$0.3 s, where the transmission is given by

$$\frac{I}{I_0} = e^{-\mu(E)t}; \qquad 5.5$$

I_0 is the X-ray intensity measured by an ion chamber placed before the filters, I is the X-ray intensity measured by a second ion chamber after the filters, $\mu(E)$ is the energy-dependent attenuation coefficient of the filters (a combination of Al and Ti at beamline 33-ID-D), and t is the pathlength of X-rays through the filters. At Q $>$ 0.2 Å^{-1} where the reflectivity decreased by ~3 orders of magnitude, the filter maximum transmission was set to 6×10^{-4} with an exposure time of 1s per image.

A filter transmission greater than 10^{-3} was found to result in a finite current generated through several samples during RAXR measurements (Figure B2). The RAXR measurements are carried out at steady state conditions (i.e., fixed potential), so the measured current should be zero.

In addition, CV measurements were carried out between each energy scan to ensure the electrochemical properties of the cell were maintained (Figure 5.12c). The maximum Q reported later in this Chapter is ~0.32 $Å^{-1}$ because above this value the CVs began to change. The limited flux on the sample results in low counting statistics at each point in the RAXR spectra. Even after summing together multiple images at each energy from multiple repeated RAXR scans, the statistics remain quite poor (as will be shown in Chapter 5.4.4) compared to RAXR measurements carried out in other systems (see Figure 5.1). Unfortunately, the need to avoid X-ray induced currents meant that a full suite of RAXR measurements took 10-14 hours depending on the number of spectra acquired at each Q, prohibiting the acquisition of additional data to improve the counting statistics further.

Linear Attenuation Correction

The attenuation of X-rays depends strongly on the geometry of the sample cell (Figure B1). In past RAXR studies of ion adsorption on mineral surfaces, measurements were carried out in a thin film cell (as used in Chapter 4 to measure the adsorbed water structure on Al_2O_3) [15, 144, 180, 181]. In a thin film cell, the linear attenuation of X-rays is significant at grazing incidence and decreases with increasing scattering angle. In addition, the water thickness is not uniform because the Kapton film encapsulating the liquid film wraps around the sample edges (Figure 5.13a). Consequently, the X-ray pathlength and attenuation correction through the fluid layer at small Q is not simply calculated using a fixed layer thickness. The transmission electrochemical cell used here has the benefit that the width of the water region is uniform during the measurement (Figure 5.13b), so the X-ray pathlength is well-defined by the scattering angle. The attenuation of

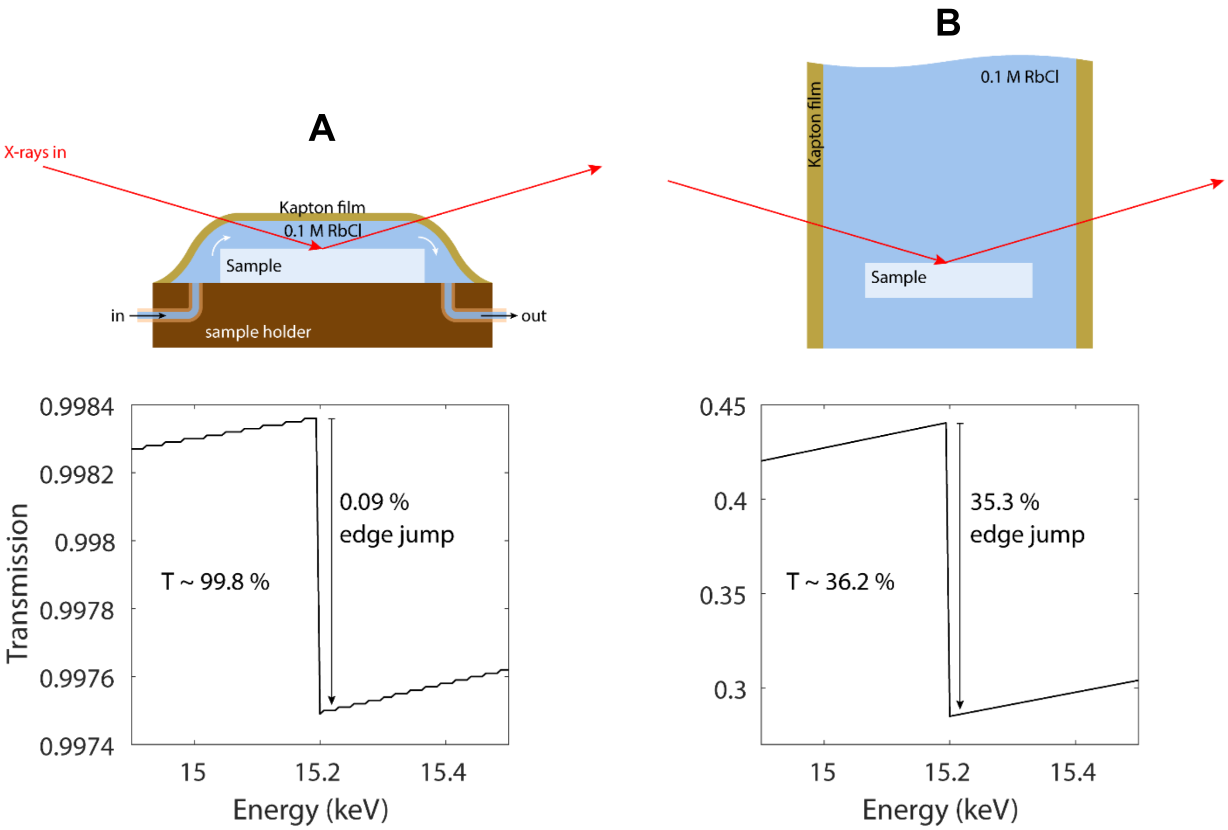

Figure 5.13. Sample cell schematics (top) and corresponding energy-dependent X-ray transmission (bottom) through a 0.1 M RbCl aqueous solution near the Rb K-edge, E = 15.2 keV. (A) thin film cell showing nearly complete transmission and a bulk resonance attenuation of <0.1% (calculated for a 10 μm thick solution layer at normal incidence). (B) Transmission electrochemical cell showing <40% transmission through a 5 mm thick solution layer and ~35 % resonance attenuation due to the bulk solution.

X-rays is effectively constant over the range of Q measured in a typical CTR measurement (and in the RAXR measurement presented here). For a ~5 mm thick cell thickness (i.e., water pathlength along the beam direction), the X-ray attenuation through the cell is ~40% (for E less than the Rb^+ K-edge). While this facilitates the analysis of non-resonant XR data as described in Chapter 5.3.1, it adds a major complication to the measurement of weak resonance signals from adsorbed ion species. Specifically, linear attenuation through the bulk electrolyte contributes a significant change in the reflectivity signal (via the attenuation coefficient $\mu(E)$ in Eq. 5.5; Figure 5.13b) that has the shape of inverse f'' (see Chapter 3.2 for description of the anomalous dispersion corrections). For a 5 mm thick 0.1 M RbCl solution, there is a ~35% change in the linear attenuation as the X-ray energy is scanned through the Rb^+ K-edge. The resonance contribution to the measured reflectivity arising solely from the adsorbed ions at the EG/SiC is not immediately obvious upon inspection because the contribution from the linear attenuation dominates the signal (Figure B3). Therefore, a linear attenuation correction must be applied carefully to the measured RAXR signals to extract the interfacial contribution. Fortunately, the same correction can be applied to all RAXR spectra ($Q_{max} = 0.32$ Å^{-1}) presented in this Chapter.

Several approaches were attempted to achieve an accurate linear attenuation correction. Each method is described in detail in Appendix B.1 (Figure B4). Ultimately, we determined the best approach is to measure the linear attenuation of X-rays through the electrochemical cell placed directly on the diffractometer (Figure 5.14a), after aligning the in-plane angle (i.e., ϕ to align the sample miscut reflection; Figure 5.14b) so that the pathlength of the X-rays through the sample is comparable to the pathlength during the diffraction measurement. The attenuation is measured with the incident X-ray beam oriented parallel to the sample surface ($\eta = 0$; see Figure 3.1a), and the sample cell is displaced down by 1 mm so that the X-rays pass directly through the bulk electrolyte (without touching the sample). The Pilatus area detector is rotated out of the beamline, and the change in intensity through the sample cell as a function of energy (Figure 5.14c) is measured between an ion chamber placed before the sample and a pin diode placed after the sample along the X-ray beam direction. The measured linear attenuation through the sample cell is then fit to obtain a smooth curve and subsequently is divided out of the measured RAXR spectra.

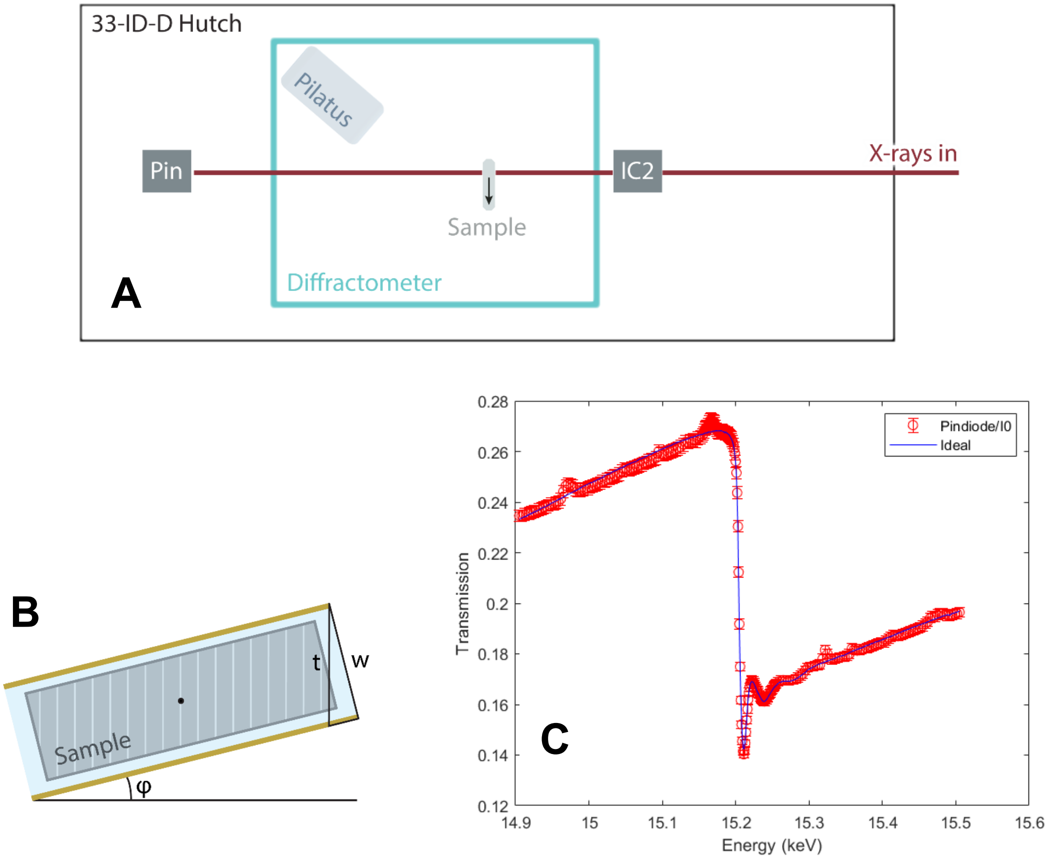

Figure 5.14. Linear attenuation correction for RAXR measurements. (A) The transmitted X-ray intensity through the electrochemical cell is detected by a pin diode ("Pin") placed after the sample along the X-ray beam path and measured relative to an ion chamber ("IC2") placed in front of the sample. The full X-ray beam is used (i.e., without any beamline filters). The sample cell is displaced down so that the X-rays pass through the bulk electrolyte (and avoid the interface), and the Pilatus X-ray area detector is rotated out of the beam path. (B) Top view showing the sample ϕ rotation (about the black dot at the center of the sample) and effective X-ray pathlength through the sample cell, $t = w/\cos\phi$ where w is the width of the solution at normal incidence; the light lines on the sample represent the miscut, and the gold edges are the Kapton windows. (C) The measured transmission through the electrochemical cell includes "blips" in the signal due to the pin diode. The fitted transmission signal (smooth blue line) was divided out of the measured RAXR spectra to correct the linear attenuation through the bulk-electrolyte.

Because each sample has a different miscut and, thus, requires a different in-plane rotation to align the reflection on the detector, the linear attenuation measured through one sample is not directly transferable to another sample even if the electrolyte solution is the same—the X-ray pathlength will vary. This measurement should be carried out each time a cell is mounted on the diffractometer to ensure the linear attenuation correction is performed properly.

RAXR at Fixed Angle, Variable Q

Beamline 33-ID-D uses a Newport six-circle diffractometer in a Kappa geometry (Newport Corporation, Irvine, CA, USA). The goniometers are controlled by servo motors, which are designed for high accuracy, high speed applications. Despite this, these motors still have a finite accuracy arising from use of an encoder to define the motor position, which can introduce error to XR measurements. The motors rotate the diffractometer angles as close to the desired angles as possible and maintain the position within a certain angle range through a constant current supply. If the desired diffractometer movement is beyond the resolution of the encoder, the final motor position and resulting scattering vector may not be the desired one. This is demonstrated in Figure 5.15a, which shows two back-to-back detector images taken during a CTR scan. The reflection

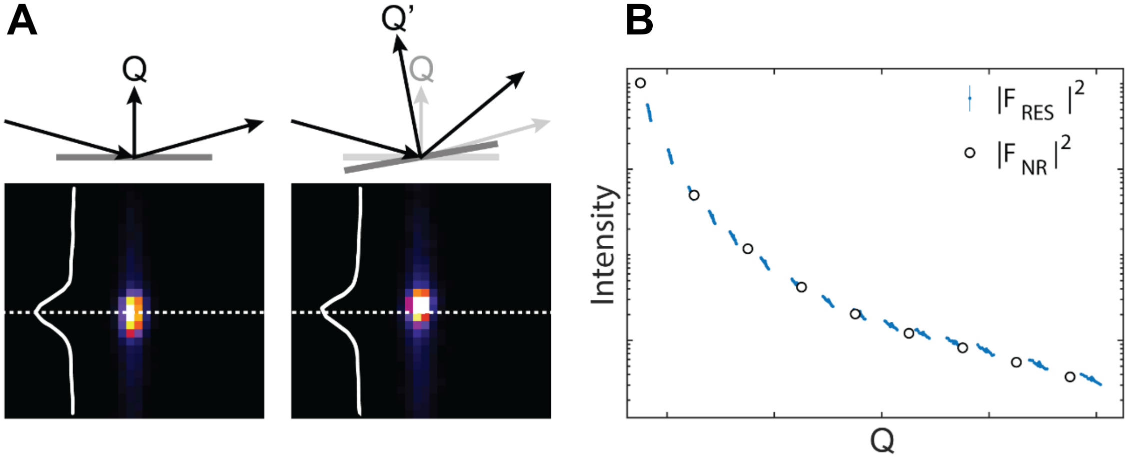

Figure 5.15. Rationale for RAXR measurement at fixed angle. (A) Detector images during CTR measurement showing a fluctuation in reflection peak position and effect on the scattering condition being probed (the relative change in Q' is exaggerated for visual clarity). (B) The small resonance intensities ('RES', blue) relative to the non-resonant CTR ('NR', black circles) exemplify the importance of accuracy in Q during RAXR measurements.

peak position shifts slightly between the two scans, resulting in the scattering condition, Q', rather than the desired Q (i.e., $\delta \neq 2\eta$ in a specular geometry). In a CTR scan, such a small displacement from the expected Q does not significantly impact the interpretation of the measured data as long as most of the data points are at the expected Q (χ^2 is inversely related to the number of points, so a small Q' error at any one point does not contribute significantly to the overall goodness-of-fit; see Eq. 3.10). However, in a RAXR measurement with a very small resonance modulations (after linear attenuation corrections; Figure 5.15b), it is important to account for as many sources of uncertainty as possible. Small Q displacements can contribute significant error to the measurement, especially at low angles were the reflected intensity changes rapidly as one moves along the CTR.

We modified the RAXR methodology to account for this "wobble" in the motor position. As described in Chapter 3.2, a traditional RAXR scan is carried out at fixed Q, which means that the diffractometer angles need to be adjusted in response to a change in energy at every energy step (Eq. 3.20). Here, we perform RAXR measurements at fixed diffractometer angle rather than fixed Q. This results in a change in Q over the course of a RAXR scan with energy range ΔE given by

$$\frac{\Delta Q}{Q_1} = \frac{\Delta E}{E_1} \qquad 5.6$$

where Q_1 and E_1 are the scattering condition and energy at the start of the RAXR energy. The typical range for our RAXR measurements about the Rb K-edge (E_0 = 15.2 keV) is from 15.5 keV < E < 14.9 keV, resulting in a 3.8% change in Q. Doing a RAXR measurement this way requires an adjustment to the model-independent analysis (Eq. 3.21) as well. Instead of normalizing an entire RAXR spectrum by the non-resonant structure factor at a specific Q_0 (i.e., $|F_{NR}(Q_0)|$), we need to normalize each point in a RAXR spectrum by the corresponding $|F_{NR}(Q(E))|$.

5.4.4: RAXR Results

Model-Independent Analysis

The RAXR measurements were carried out in 0.1 M RbCl with the EG/SiC electrode potential held at -0.1 V. The data were normalized by the linear attenuation correction shown in Figure 5.14c and then by the non-resonant structure factor defined by the best-fit structure to the CTR data measured in 0.1 M RbCl (Figure 5.11). The model-independent fit to the spectra (i.e., to determine the amplitude and phase of each spectrum according to Eq. 3.21) is shown in Figure 5.16 for $0.045 < Q_{E0} < 0.316$ where Q_{E0} is the scattering vector of each spectrum at the K-edge energy (E_0 = 15.2 keV). The Rb^+ electron density derived from this analysis is shown in Figure 5.17 overlaid on the non-resonant best-fit electron density. It shows a broad ion distribution with a peak density of 0.03 e/Å^3 located at z ~ 9.7 Å, which is approximately 0.5 Å above the first hydration layer adsorbed on the G_1 graphene layer (z = 9.23 Å). The distribution is skewed in the $+z$ direction, which qualitatively appears as an exponentially decaying profile with a DW factor. However, the resolution of the RAXR measurement is 9.9 Å ($r = \pi/Q_{max}$). Therefore, we cannot draw strong conclusions from the model-independent analysis alone.

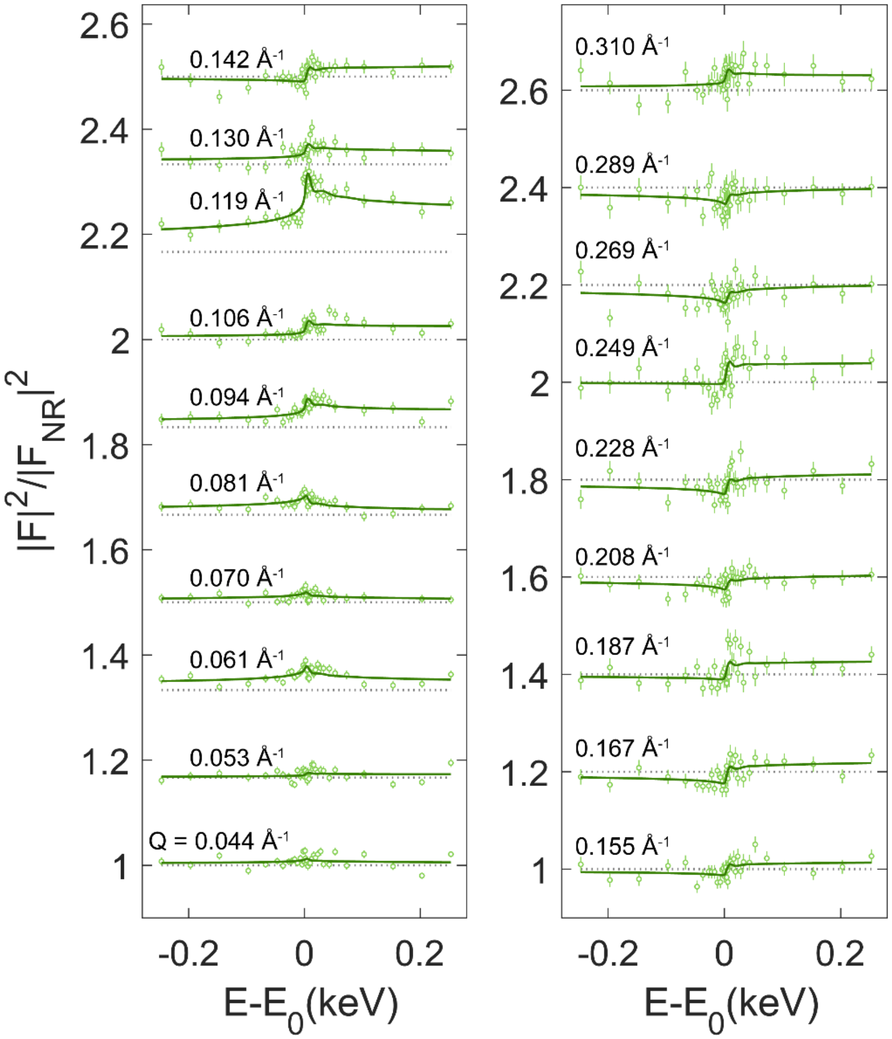

Figure 5.16. Model-independent RAXR results for 0.1 M RbCl at -0.1 V potential bias on a EG/SiC electrode. E_0 = 15.2 keV. The spectra are shown normalized to the non-resonant reflectivity $|F_{NR}|^2$ and are vertically offset for clarity. Horizontal dotted lines indicate the normalized intensity expected if there is no resonance signal. The Q at E_0 is labeled for each spectrum.

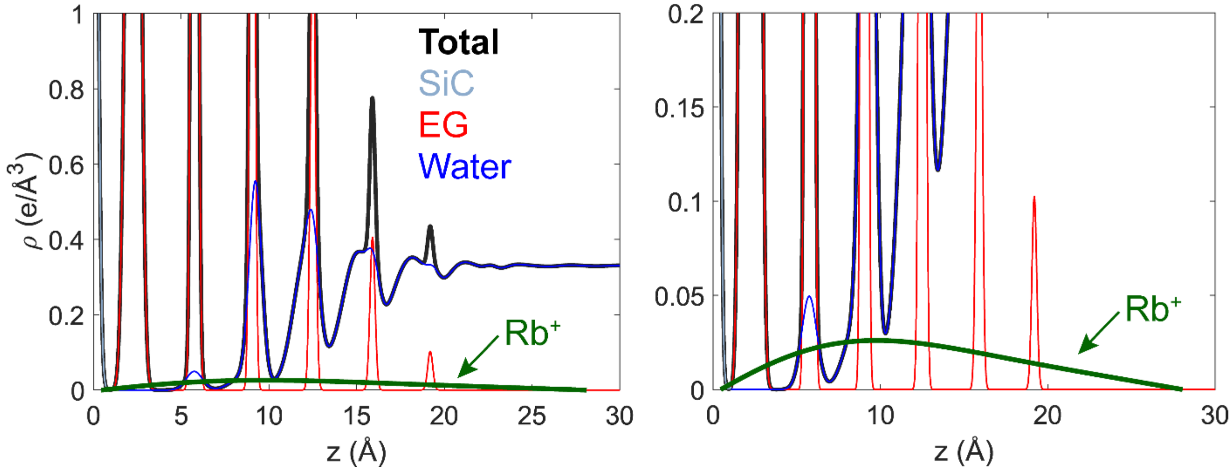

Figure 5.17. Model-independent Rb^+ distribution at the EG/SiC interface. The total electron density profile (black), SiC interface (gray), EG (red), and water (blue) structures are the same as the best-fit distribution in Figure 5.11 for the CTR measured in 0.1 M RbCl. The Rb^+ distribution derived from the RAXR spectra is broadly distributed with a peak density at z~9.7 Å and is resolution-limited. Left: zoomed out view showing the total water distribution; right: zoomed in view of Rb^+ profile showing a skew toward +z indicative of a diffuse ion profile.

Model-Dependent Analysis

We used two models in the model-dependent analysis. The first is the diffuse ion profile from GC theory, and the second is a “capped” ion profile that has a maximum ion density near the interface (i.e., a cap on the packing density). The rationale behind the second model is that the measurement resolution is too small to resolve an individual Stern layer. The model-independent analysis suggests the ion distribution might be quite broad and can be approximated by a flat density region near the interface followed by a density decay.

The structure factor for a diffuse ion profile from GC is given by

$$\begin{aligned}\mathcal{F}_R &= \int_{z_0}^{\infty} \Theta(z) e^{iQz} dz \\ &= \int_{z_0}^{\infty} \Theta_0 e^{-z/\Lambda} e^{iQz} dz\end{aligned} \qquad 5.7$$

where the lower limit of integration, z_0, is the onset position of the ion distribution with respect to the reference surface (i.e., the electrode surface) where the ion profile begins (e.g., the radius of the bare ion at minimum), and the density is written in terms of the ion distribution, $\Theta(\mathrm{z})$, rather than the electron density distribution, $\rho(z)$, noting that the atomic FF f_j of the resonant ion is separate from the spatial structure factor, $\mathcal{F}_R$ (see Eq. 3.17); Θ_0 is the ion density at the start of the diffuse profile, assuming it follows the functional form of Eq. 2.13 as shown in Figure 5.18a. Eq. 5.7 yields

$$\mathcal{F}_R = \frac{\Theta_0 \Lambda}{1 - iQ\Lambda} e^{(iQ - 1/\Lambda)\mathrm{z}_0}, \qquad 5.8$$

and the total ion density is given by

$$\begin{aligned}\Theta_T &= \int_{z_0}^{\infty} \Theta_0 e^{-\mathrm{z}/\Lambda}\, dz \\ &= \Theta_0 \Lambda e^{-\mathrm{z}_0/\Lambda}.\end{aligned} \qquad 5.9$$

Θ_T is equivalent to a double layer charge density of $\sigma_{DL} = \Theta_T e$, where e is the elementary charge, and must be equal to σ_{EG}. For our electrochemical system with C ≈ 4.5 μF/cm^2, the graphene charge density would be -1.5×10^{-3} e$^-$ per graphene unit cell (or equivalently 2.3×10^{-3} e$^-$ per SiC unit cell) at an applied potential of -0.1 V. Substituting Eq. 5.9 into Eq. 5.8 gives the structure factor in terms of the total ion density,

$$\mathcal{F}_R = \frac{\Theta_T}{1 - iQ\Lambda} e^{iQz_0}. \tag{5.10}$$

The amplitude and phase of the resonant ion structure factor calculated from Eqs. 3.18 and 3.19d, respectively, are

$$A_R(Q) = \frac{\Theta_T}{\sqrt{1 + (Q\Lambda)^2}} \tag{5.11}$$

and

$$\phi_R(Q) = \mathrm{atan}\left[\frac{Q\Lambda\,cos(Qz_0) + sin(Qz_0)}{cos(Qz_0) - Q\Lambda\,sin(Qz_0)}\right]. \tag{5.12}$$

These are plotted in Figures 5.18b and 5.18c, respectively. From Eq. 5.11, we see that $A_R(Q = 0)$ yields the total ion coverage, which can be compared directly to the expected charge in the double

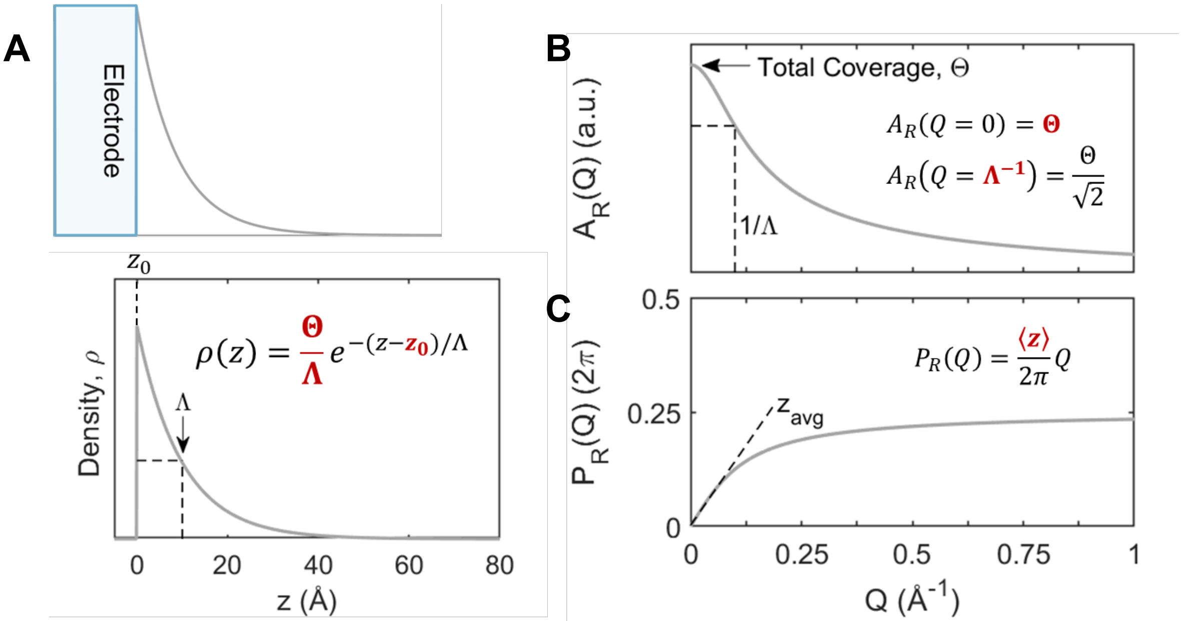

Figure 5.18. Structure factor for the Gouy-Chapman (GC) model of the EDL. (A) Schematic of exponential diffuse ion profile adjacent to the electrode (top) and the associated ion density profile (bottom) highlighting parameters for the start of the diffuse profile above the electrode surface, z_0, the Debye length, Λ, and the total ion coverage, Θ (bottom). (B) The amplitude associated with the GC EDL. (C) The phase of the GC EDL in units of 2π ($\phi_R = 2\pi P_R$).

layer given by the Grahame equation (Eq. 2.10) and to the electrode surface charge, σ_{EG}. In the limit of small Q, Eq. 5.12 reduces to

$$\phi_R(Q) \approx Q(\Lambda + z_0) = Q\langle z\rangle \qquad 5.13$$

where $\langle z\rangle$ is the average height of the ions above the electrode surface. Eq. 5.13 shows that the phase is linear at small Q with the average ion height given by the slope.

Figure 5.18 shows the form of $A_R(Q)$ and $\phi_R(Q)$ for a GC diffuse profile adjacent to a simple electrode surface. However, the partial layer coverage of EG/SiC requires Eqs. 5.11 and 5.12 to be modified to account for G*ₙ* (*n* = 0, 1, 2, …) graphene layers (Figure 5.19a), similar to the modification to the extended layered water model given in Eq. 5.4. The ion density and structure factor become

$$\Theta'(z) = \sum_n \Theta(z)\frac{\Theta_n - \Theta_{n+1}}{\Theta_{ML}}e^{z_n/\Lambda} \qquad 5.14$$

$$\mathcal{F}_R{}'(Q) = \sum_n \mathcal{F}_R\frac{\Theta_n - \Theta_{n+1}}{\Theta_{ML}}e^{(iQ-1/\Lambda)z_n}, \qquad 5.15$$

assuming that the double layer structure is identical above each exposed graphene surface. In the model dependent analysis using GC theory, the fitting parameters are the Debye length, the ion coverage, and the start of the ion distribution above the reference surface.

A schematic of the "capped" ion model is shown in Figure 5.19b. In this model, the parameters include the total ion density, Θ, the onset height of the ion distribution above the electrode, z_0, and an additional variable to define the maximum 3D density near the surface, ρ_{max}. If the 3D ion density near the surface calculated using an exponential profile (i.e., ρ_0 according to GC theory, Eq. 2.13) exceeds the maximum allowed density, ρ_{max}, a flat region is observed near the interface, and the diffuse region is shifted away from the surface. As a result, the average height

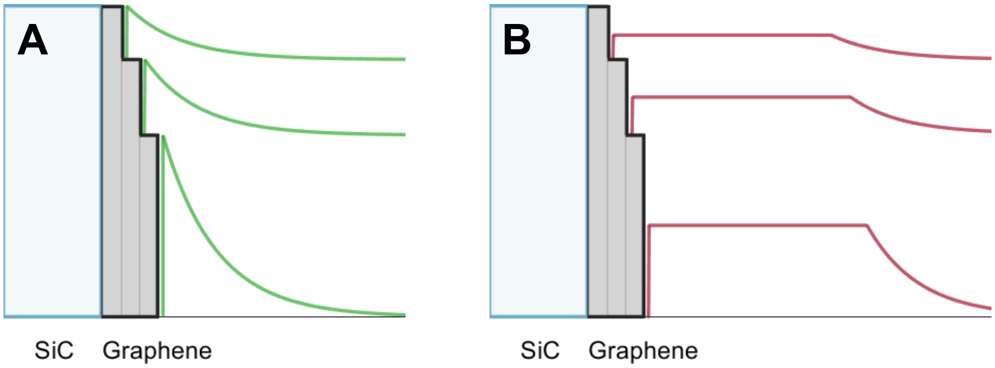

Figure 5.19. Double layer schematics accounting for graphene topography with three exposed graphene surfaces about a SiC substrate. (A) GC diffuse double layer modulated by graphene layer coverage and height. (B) "Capped" ion profile with maximum packing density near the interface followed by an exponentially decaying diffuse ion profile.

of the ions is farther from the interface than if the ions were allowed to pack more densely at the interface. In this model, we assume that the decay length in the diffuse region is that predicted by GC, i.e., $\Lambda = 9.7$ Å for a 0.1 M RbCl solution.

We now perform model-dependent analysis of the amplitude, $A_R(Q)$, and phase, $P_R(Q) = \phi_R(Q)/2\pi$, that were previously extracted from the RAXR spectra via model-independent analysis. The results are shown in Figure 5.20 and summarized in Table 5.3. We notice upon inspection that the total ion coverage in the EDL measured by RAXR (qualitatively determined from the $A_R(Q = 0)$; Figure 5.20a) is inconsistent with the expected charge density based on our CV measurements (Chapter 5.4.1). The capacitance of 4.5 μF/cm^2 results in an ion coverage of 2.3×10^{-3} Rb$^+$/A$_{SiC}$ for an applied potential of -0.1 V. The total ion coverage measured by RAXR also appears to be higher than the ion coverage derived from PB theory (i.e., using the Grahame equation, Eq. 2.10) from which we expect $\Theta_T \sim 0.07$ Rb$^+$/A$_{SiC}$ if we assume a constant bulk dielectric permittivity of $\epsilon = 80$ for bulk water. We tested three GC-type models (i.e., an

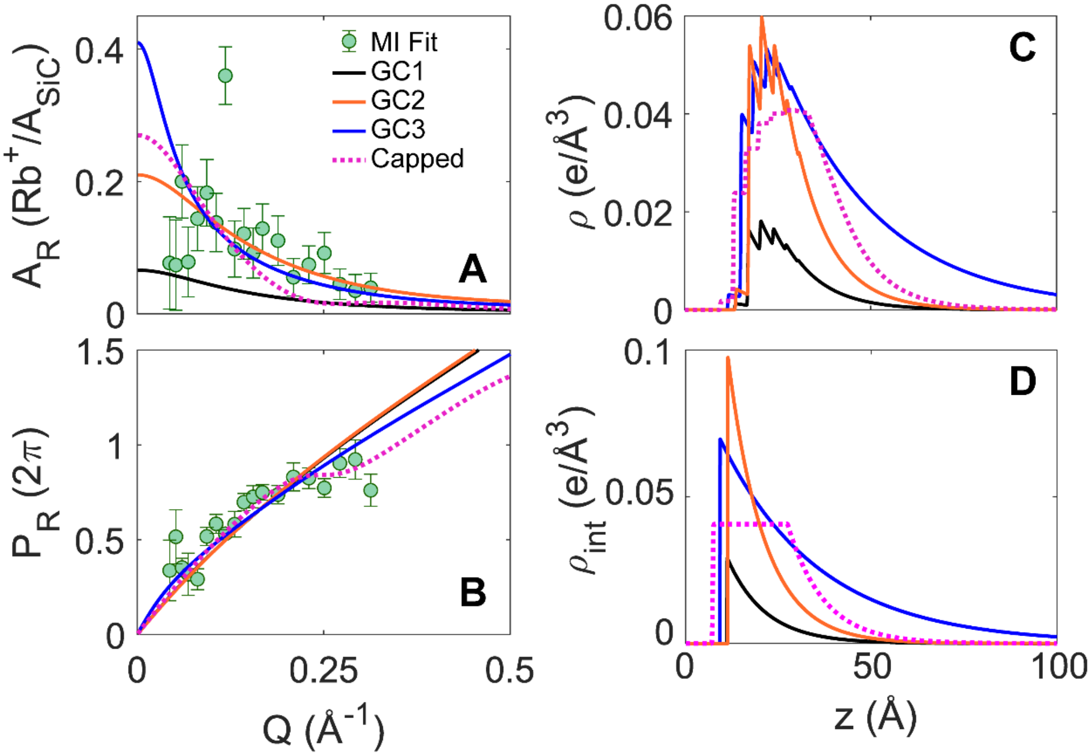

Figure 5.20. Model-dependent RAXR analysis using three exponentially decaying (GC-type) EDL models (solid lines; GC1, black; GC2, orange; GC3, blue) and a "capped" model with maximum packing density (dashed magenta line). (A) The amplitude, (B) phase, (C) model electron density profiles with graphene layer modulation (see Table B1 for layer heights and coverages), and (D) intrinsic electron density distributions are compared. The amplitude and phase data extracted from the model-independent analysis of the experimental RAXR spectra (Figure 5.16) are shown as green circles. See Table 5.3 for model parameters and χ^2 values.

Table 5.3. Best-fit parameters for model-dependent analysis of RAXR amplitude and phase, including the Debye length, Λ, ion coverage, Θ, distance of closest approach to the electrode, z_0, and maximum electron density near the surface.

Model	Λ (Å)	Θ (Rb$^+$/A$_{SiC}$)	z_0 (Å)	ρ_{max} (e$^-$/Å^3)	χ^2
GC1	10.2	0.07[a]	11.2	-	4.8
GC2	9.7[b]	0.21	11.4	-	3.0
GC3	26.5	0.41	9.3	-	2.7
Capped	9.7[b]	0.27	7.3	0.04	2.5

[a] Fixed at value calculated from Eq. 2.10 with an applied potential of -0.1 V. [b] Fixed at Debye length expected from Eq. 2.14 for a 0.1 M RbCl solution.

exponentially decaying profile with the structure factor defined by Eqs. 5.10 and 5.15 and amplitude and phase of the form of Eqs. 5.11 and 5.12, respectively) with different sets of fitting parameters. In the first case (GC1), we fixed the ion coverage to the PB value and fit the Debye length and profile onset height; in the second case (GC2) we fixed the Debye length to 9.7 Å and fit the ion coverage and onset height; and in the third case (GC3), all three parameters were fit. The total χ^2 is the average of the χ^2 fits to the amplitude and phase data separately, i.e.,

$$\chi_T^2 = \frac{\chi_A^2 + \chi_P^2}{2} \qquad 5.16$$

with χ_A^2 and χ_P^2 each calculated from Eq. 3.10 with the reflected intensity $R(Q)$ substituted for the relevant quantity (either $A_R(Q)$ or $P_R(Q)$).

Among the three GC models, GC3 gave the best fit to the data with $\chi_T^2 = 2.7$ for $\Theta_T = 0.41$ Rb$^+$/A$_{\mathrm{SiC}}$, Λ = 26.5 Å, and $z_0 = 9.3$ Å. However, GC2 (Λ = 9.7 Å) had a similar goodness-of-fit with $\chi_T^2 = 3.0$ for coverage and height parameters $\Theta_T = 0.21$ and $z_0 = 11.4$ Å, respectively. Overall, these two models appear to be consistent with the extracted amplitude and phase data. GC1 ($\Theta_T = 0.07$ Rb$^+$/A$_{\mathrm{SiC}}$) was less consistent with the experimental data, yielding $\chi_T^2 = 4.8$ with $\Lambda = 10.2$ Å and $z_0 = 11.2$ Å. Apart from the ion coverage, GC1 and CG2 give a similar diffuse ion profile distribution (i.e., the shape), which again suggests that the ion coverage expected from PB theory is not consistent with the data.

The capped ion model offers a slight improvement over the GC models in terms of the χ_T^2 level of agreement with the experimental A_R and P_R but is generally equivalent. With this model, we obtain $\chi^2 = 2.5$ with a total ion coverage $\Theta_T = 0.27$ Rb$^+$/A$_{\mathrm{SiC}}$, a maximum density $\rho_{max} =$ 0.04 e/Å^3, and an onset height of $z_0 = 7.3$ Å. In the capped model and the three GC models, the phase data at low Q are generally similar (Figure 5.20b). This indicates that, although the four models give different shapes for the ion distribution, the average ion height is approximately the same and is ~30 Å above the reference surface. The capped profile also shows a modulation in the phase data around Q ~ 0.25 $Å^{-1}$, which results from the width of the flat portion of the profile (~20 Å; Figures 5.20c,d).

All four models that were tested yielded a total ion coverage of the same magnitude as the expected value from PB theory. The best-fit ion coverage from the GC_2 model is three times the expected ion coverage from PB theory and is qualitatively consistent with the DH* regime describe by Lau [158] (see Figure 2.4b) if we incorporate a low dielectric region ($\epsilon_{\perp} \approx 2$) within a few molecular layers of the interface as discussed in Chapter 5.4.1. In this regime, charge fluctuation correlations lead to an increase in counterion concentration adjacent to the interface. However, the discrepancy with the EG/SiC electrode charge calculated using the capacitance measured from CV persists. To maintain charge neutrality with the EG/SiC electrode at -0.1 V ($\sigma_{EG} \sim 2.3\times10^{-3}$ e^{-}/A_{SiC}), an ion coverage of 0.21 Rb^{+}/A_{SiC} measured by RAXR implies a nearly equal excess Cl^{-} concentration in the EDL. Such a high density of co-ions in the double layer is inconsistent with PB theory and with other weak-field regimes.

5.4.5: Discussion and Conclusions

Overall, the data appear to be consistent with a GC-type diffuse ion profile, but the limited resolution of the RAXR measurement precludes a fully atomistic interpretation of the EDL structure. The total ion coverage measured by RAXR exceeds the expectations of the classical theories and is also two orders of magnitude larger than what is expected from the capacitance measurement of the electrochemical cell ($\Theta_T \gtrsim 0.2$ Rb^{+}/A_{SiC} from RAXR versus 2.3×10^{-3} Rb^{+}/A_{SiC}

based on the capacitance measurement). This inconsistency has not been resolved and requires further investigation. The observed total ion density in the EDL can be explained simply by accounting for the known decrement in the dielectric permittivity near the interface. However, the reduction in dielectric permittivity arises from the intrinsic polarization of water at the graphene surface, which would likely change under an applied electric field. In particular, the MD simulations presented in Chapter 5.3 indicate that the water molecules orient with the unbound oxygen electrons pointed toward the graphene plane (on average). A negative bias applied to the electrode would repel the free electrons, thereby altering the free energy landscape even if the voltage is not sufficient to flip the interfacial water dipole. The MD simulations suggested that anion and cation adsorption differ at the graphene interface due to the intrinsic polarization of interfacial water. This raises the question of how the energetics of ion adsorption change in an electric field as a result of (or accounting for) the changes in the water polarization.

The large uncertainties on the amplitude and phase data extracted from our RAXR measurements could be reduced by improving the counting statistics of the RAXR spectra but still avoiding X-ray beam effects on the sample. This would require a change to the experimental methods. With unlimited time, the measurements could be carried out for the same system but with many more repeat energy scans at each scattering condition. However, this is impractical at this time. It would be worthwhile to explore other electrode materials that are not beam-sensitive.

Chapter 6: Future Studies

In this thesis, I explored the interfacial structure of solid/water interfaces from two different but complementary directions. The first aim focused on the validation of first principles (FP) simulations of oxide water-interfaces. With the growing need for efficient energy storage and conversion materials, there has been a significant effort to understand physiochemical phenomena at oxide/water interfaces via FP calculations [28, 42, 111, 240, 264]. These simulations have the potential to accurately predict chemical reactions, such as water splitting. However, our ability to rely on the predictions as we search for new materials or to optimize existing materials requires that all approximations used in the simulations be carefully validated. In Chapter 4, I presented a highly collaborative work in which we explored several different FP methodologies in detail to evaluate their effects on an experimental observable—namely, the X-ray reflectivity signal from the Al_2O_3(001)/water interface.

The high sensitivity of XR measurements to buried solid/liquid interfaces opens up new avenues to validate FP simulations beyond a focus on the accuracy of atomic density distributions, which relies on model-derived structures from experimental XR data. A direct comparison between FP structures and XR data is completely model-independent. The protocol outlined in Chapter 4 highlights the strengths and weaknesses of various approximations required by the simulations and points to areas for improvement. The protocol can be applied in the future to the study of other well-defined solid/water interfaces. Finally, the results show that simulated structures can serve as a starting point for optimization with respect to XR data. This would be especially useful in cases where the experimental structure is unknown, and therefore it is difficult to determine a reasonable starting model for the experimental data analysis.

The second project presented here aimed to directly probe the diffuse double layer for the first time. The endeavor proved more challenging than originally expected, but the insights gained have paved the way for future exploration of weakly adsorbed ion structures. The work presented here explored the double layer for one salt (RbCl) at a single ion concentration and at one electrode potential. The electrode material does not enter the equation in GC theory, but I identified a significant discrepancy between the capacitance measured with a graphene electrode—dominated by the graphene quantum capacitance—and the charge stored in the double layer. This incongruity should be explored further. The measurement could be repeated with a different electrode, such as glassy carbon, which (1) does not have a quantum capacitance, (2) may stand up better to X-ray exposure, and (3) has a lower density than EG/SiC (due to the Si in the substrate). The last point should improve the contrast between the non-resonant structure factor and that from the resonance ion. If glassy carbon is not X-ray sensitive (or less so than EG/SiC), one could measure out to higher Q, and thereby increase the resolution of the double layer structure. This would also improve the signal-to-noise ratio in the RAXR measurements. If the EDL structure is verified using a different electrode and the same electrolyte and charging conditions used here, this would raise questions about the use of quantum materials as electrodes.

It would also be useful to measure the EDL structure at a lower ion concentration. This will decrease the linear attenuation contribution to the measured resonance spectra and increase the relative contribution from the adsorbed ion species. In addition, future studies should explore lower voltages to determine at what point the EDL structure begins to deviate from the classical PB and GC theories, and RAXR measurements of the EDL with divalent and multivalent ions would also serve to elucidate gaps in our understanding of ion adsorption at aqueous interfaces.

Finally, large ion clusters containing resonant atoms (i.e., polyoxometalates) would be useful to explore how ion size effects alter the EDL structure. CTR measurements alone may be sufficient to detect polyoxometalates due to their large electron densities.

Appendix A: Supplement to Chapter 4

A.1: Al_2O_3/Water Interface pH-Dependent CTRs

The analysis of these data is ongoing and is being spearheaded by Dr. Young Jae Kim (Interfacial Processes Group, Argonne). The results will elucidate questions that arose from the direct comparisons of simulated FPMD structures with XR data regarding pH effects on the alumina surface and how this affects water adsorption.

Sample Preparation

Two polished 3 mm ×10 mm single crystal Al_2O_3(001) samples from CrysTec, GmbH (Berlin, Germany) were cleaned by four rinse cycles of alternating HPLC-grade acetone, HPLC-grade methanol, and 18 MΩ de-ionized water (DIW). The samples were then soaked for 4 hours in 1 M HCl. After rinsing again in DIW and drying, the samples were annealed in ambient atmosphere at 1000 °C for 24 hours. Subsequently, the samples were stored in DIW for transport to APS sector 13-ID-C where pH-dependent measurements were carried out. AFMs of the cleaned samples are shown in Figure A1 and show smooth surfaces. The sample 1 surface has a patterned structure even after treatment, but the topography/pores are large compared to molecular lengths, so the structuring on the surface is not expected to lead to confinement and subsequent changes in the water structure.

These samples were used again at 6-ID-B during a later beamtime. They sat in DIW for ~2 months between the beamtimes. They were re-cleaned at annealed in preparation for the 6-ID-B beamtime in an abbreviated process similar to the one described by Catalano et al. in Ref. [26].

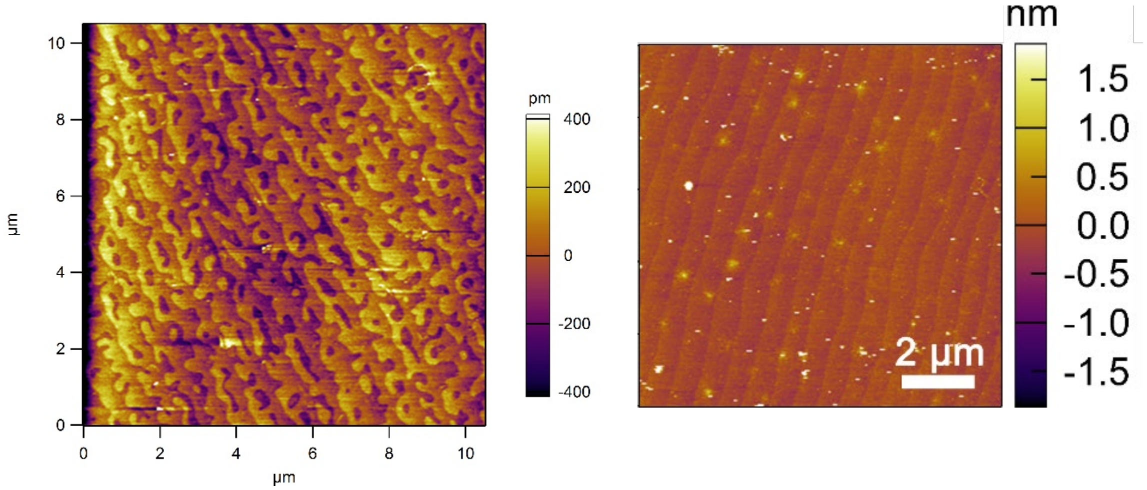

Figure A1. AFMs of Al_2O_3 (001) sample 1 (left) and sample 2 (right). Sample 1 had an r.m.s. roughness of 145.7 pm and miscut angle of 0.035°; sample 2 had an r.m.s. roughness of 942.6 pm and a 0.026° miscut.

Five rinse cycles of alternating sonication (15 min each) in acetone and methanol were carried out. The samples was then sonicated in DIW for 15 minutes and sat in DIW overnight. The samples were then sonicated in 1 mM HCl in a "light rinse" for 30 mins and subsequently heated at 350 °C for 4 hours in an ambient atmosphere. After cooling to 60 °C, the samples were placed in a vial with DIW and taken to the beamline.

XR Data

The integrated CTR data from both beamlines at acidic (pH 2), neutral (nominal pH 7), and basic condition (pH 12) are shown in Figure A2. There is essentially no change in the CTR intensities going from pH 2 to pH 7. There appears to be a small change when going from pH 7 to pH 12. Similar measurements were carried out by Xu et al. who also did not observe a change in the interfacial water structure on c-plane Al_2O_3 over the range $5 < pH < 9$ [178]. Their data were similar to the data I measured on sample 2 at 6-ID-B and on the sample measured at 13-ID-C. In particular, the shape and intensity of the second midzone (between the Bragg peaks) are similarly rounded rather than being flat, as seen in the sample 1 6-ID-B data (Figures A2d and A2f). In addition, we identify an oscillation in the intensity as the scattering condition approaches the second Bragg peak, which also appears in the data in Ref. [178]. Their analysis revealed a consistent water height of ~2.85 Å, which is notably larger than the water height observed on the sample discussed in Chapter 4 of this thesis.

Our sample 1, which has a flat midzone in the CTR, is similar to other CTR data measured for the Al_2O_3(001)/water interface at neutral pH by Catalano [210]. In that study, Catalano found a best-fit water height of ~2.46 Å, which is closer to the water height found in the best-fit for the Chapter 4 measurement. The difference in water height appears to correlate with the shape of the midzone intensity, which is consistent with the insights gain from the direct comparison of XR data with FPMD simulations for this system (see Chapter 4.6).

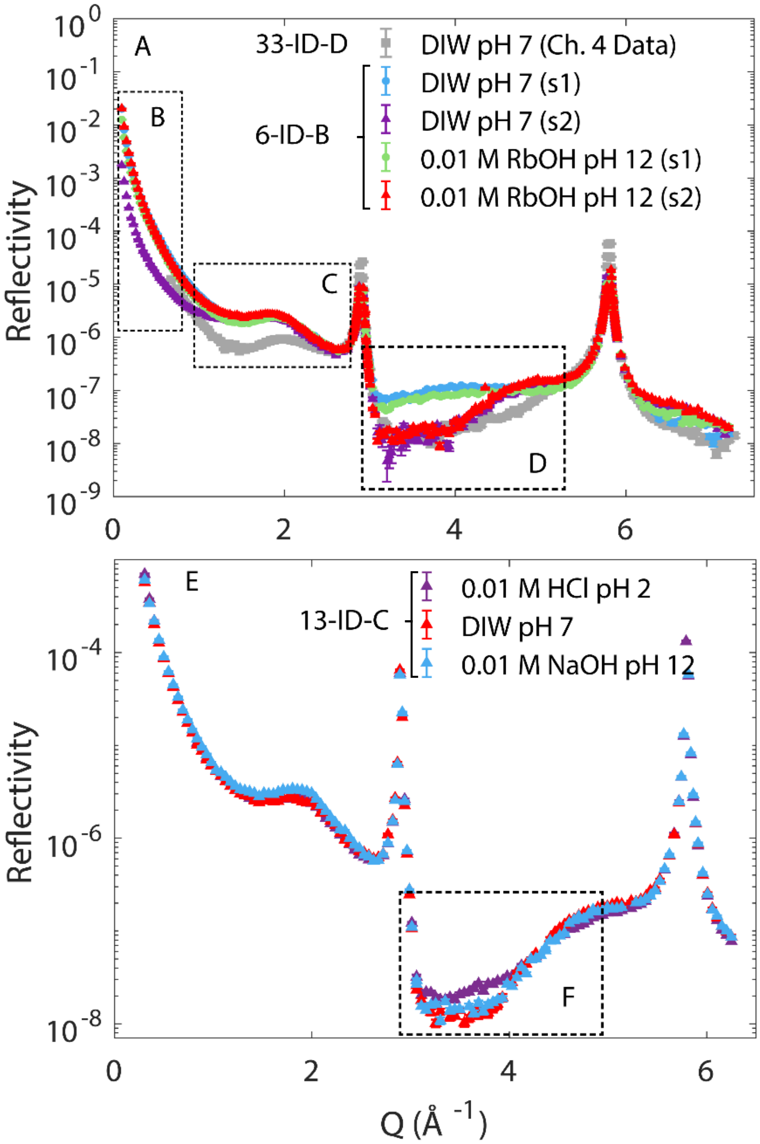

Figure A2. pH-dependent specular XR data on c-plane Al_2O_3. (A) CTR data for two samples, s1 (circles) and s2 (triangles), measured at pH 7 and pH 12 at APS beamline 6-ID-B (E = 18 keV) show little change with pH but significant differences between samples. These data also differ significantly from the Al_2O_3(001)/water data presented in Chapter 4 (gray squares). (B) The low intensity of s2 in DIW results from linear attenuation of the X-rays due to a thicker water layer during this measurement. (C) samples s1 and s2 have similar intensities below the first Bragg peak while that of the Ch. 4 CTR is significantly lower and reminiscent of the intensity reduction due to a rough surface (see Figure 3.3a). (D) Significant variability is observed between samples (but not at different pHs) in the second midzone, the intensity of which is correlated with the water height (see Chapter 4). (E) A set of measurements carried out at APS beamline 13-ID-C (E = 13 keV) using sample s2 (triangles) in pH 2, 7, and 12 show a small change at acidic pH in (F) the midzone.

A.2: Fitted Parameters of FPMD Al_2O_3/Water Atomic Density Distributions

Table A1. Structures extracted from 12-layer Al_2O_3 FPMD simulations by fitting total electron density to layered Gaussians according to Eq. 3.8.

	PBE-12			**PBE-12+Grimme**		
Z	**z (Å)**	**u (Å)**	**Θ (AUC^{-1})**	**z (Å)**	**u (Å)**	**Θ (AUC^{-1})**
Alumina						
13	-11.6912	0.0684	0.9875	-11.6857	0.0673	1
8	-10.84	0.0681	2.9641	-10.84	0.0667	2.9802
13	-9.9815	0.0695	0.9921	-9.9921	0.0665	0.9969
13	-9.4808	0.0687	0.9971	-9.4909	0.0663	0.9942
8	-8.63	0.0695	2.9812	-8.6456	0.0683	2.9917
13	-7.7704	0.0711	0.9934	-7.7978	0.0662	0.9897
13	-7.2717	0.0728	0.9909	-7.2974	0.0647	0.9935
8	-6.4188	0.0736	2.9826	-6.4518	0.0679	2.9824
13	-5.5595	0.0741	0.9896	-5.6037	0.067	0.993
13	-5.0563	0.0734	0.9889	-5.0979	0.0675	0.9973
8	-4.2094	0.0779	2.9721	-4.2586	0.0702	2.9912
13	-3.3652	0.0804	0.9863	-3.4224	0.0724	0.9968
13	-2.8389	0.0771	0.9891	-2.9027	0.067	0.9829
8	-1.9908	0.0829	2.9583	-2.0575	0.073	2.9871
13	-1.0229	0.091	1.02	-1.1072	0.0757	0.9786
13	-0.7106	0.0822	0.9504	-0.7876	0.0806	1.001
8	0.1926	0.1022	3.0917	0.1151	0.0934	3.124
1	1.0555	0.1095	1.8596	0.9888	0.0947	1.7183
Water						
1	1.9463	0.1476	0.5228	1.7946	0.1445	0.6323
8[a]	2.9214	0.2129	1.3921	2.7429	0.1684	1.2836
8[b]	5.8543	1.0719	2.2928	5.1508	0.9947	1.6251

[a] First adsorbed water layer; [b] Second layer using a layered water model (Eqs. 4.2 and 4.3).

Table A2. Element-specific structures from 12-layer FPMD Gaussian fits.

PBE-12			**PBE-12+Grimme**		
z (Å)	**u (Å)**	**Θ (AUC^{-1})**	**z (Å)**	**u (Å)**	**Θ (AUC^{-1})**
		Oxygen			
-10.84	0.0683	2.9996	-10.84	0.0667	2.9925
-8.6293	0.0696	3.0124	-8.6456	0.0683	3.004
-6.4178	0.0732	3.0023	-6.4518	0.0679	2.9946
-4.2074	0.0775	2.9957	-4.2586	0.0702	3.0035
-1.9883	0.0823	2.9823	-2.0575	0.073	2.9993
0.1926	0.1001	2.995	0.1147	0.0915	3.001
2.9078	0.2041	1.3323	2.7523	0.1795	1.3773
3.6412	0.4646	0.4579	5.8359	1.5988	3.2598
6.4205	1.3953	2.9423	9.9071	1.1878	2.2156
		Hydrogen			
0.2254	0.1685	1.1064	0.1462	0.1655	1.2367
1.057	0.1093	1.8776	0.9889	0.0951	1.735
1.9822	0.1847	0.6838	1.8061	0.1636	0.7266
3.2883	0.3996	2.8847	2.9026	0.2061	0.8294
4.2726	0.2639	0.5258	3.4001	0.4819	2.3176
6.0656	0.9278	3.429	5.6672	0.9229	3.0681

Table A3. Fitting results for 6-layer Al_2O_3 FPMD simulations by fitting total electron density to layered Gaussians according to Eq. 3.8.

	PBE-6			**optB88**			**optB88-10%**		
Z	**z (Å)**	**u (Å)**	**Θ (AUC^{-1})**	**z (Å)**	**u (Å)**	**Θ (AUC^{-1})**	**z (Å)**	**u (Å)**	**Θ (AUC^{-1})**
				Alumina					
13	0.2557	0.0636	0.7583	0.2487	0.0566	1.0026	0.2488	0.0546	1.0002
8	1.1013	0.0658	2.279	1.0921	0.0578	3.0075	1.0904	0.056	3.0088
13	1.9363	0.0665	0.7585	1.9244	0.0582	1.0016	1.9208	0.0561	1.002
13	2.4657	0.0641	0.7574	2.4411	0.0565	1.0012	2.438	0.055	1.0012
8	3.3154	0.0703	2.2776	3.2871	0.0619	3.0068	3.2821	0.0601	3.0083
13	4.2674	0.0756	0.755	4.2377	0.0667	1.0005	4.2332	0.0639	0.9975
13	4.5874	0.0722	0.7632	4.5429	0.0626	1.0047	4.535	0.06	1.0006
8	5.4954	0.0928	2.3782	5.4441	0.0818	3.1281	5.4358	0.0799	3.1202
1	6.3705	0.0972	1.2892	6.3406	0.0845	1.8739	6.3369	0.0809	1.8259
				Water					
1	7.2412	0.1306	0.2605	7.1656	0.1464	0.6833	7.1389	0.1523	0.7735
8	8.1965	0.1985	0.7052	8.1286	0.1878	1.2885	8.0826	0.1801	1.5364
8	10.2828	1.2984	1.7688	8.8067	0.5369	0.8905	8.639	0.4721	0.8797
8	-	-	-	10.9562	1.1827	1.6238	10.6605	0.6496	1.9885

Appendix B: Supplement to Chapter 5

B.1: X-ray Attenuation and Effects on EG/SiC Sample

The X-ray pathlength through the sample cell depends on the geometry, and is given for the thin film ('TF') cell and electrochemical ('EC') cell, respectively, as

$$L_{TF} = \frac{8\pi tE}{Qhc} \qquad B.1a$$

$$L_{EC} = \frac{w}{\sqrt{1-\left(\frac{Qhc}{4\pi E}\right)^2}} \qquad B.1b$$

where t is the vertical thickness of the water layer in a thin film cell (typically tens of μm), w is the horizontal width of the water layer in an electrochemical cell (on the order of mm), E is the X-ray energy, and $hc = 12400$ eV·Å. From Eq. B.1a, we see that in the limit of small Q, L_{TF} asymptotically approaches infinity, resulting in a significant linear attenuation correction (Eq. 5.5 and the prefactor T(Q) in Eq. 3.1). In reality, the maximum L_{TF} is the width of the water layer along the X-ray beam direction, which is not uniform at normal incidence due to the finite height of the X-ray beam (~ 80 μm) and the curvature of the Kapton film as it wraps around the sample edges (see Figure 5.13a); it also depends on the lateral dimensions and in-plane rotation of the sample. At high Q the pathlength asymptotically approaches zero (Figure B1).

Conversely, Eq. B.1b shows that for the electrochemical cell, $L_{EC} \approx w$ in the limit of small Q and L_{EC} asymptotically approaches infinity when the denominator goes to zero, i.e., for Q = $4\pi E/hc$. For a specular CTR carried out at E = 14 keV, $L_{EC} \to \infty$ at Q = 14.2 Å^{-1}, which is well beyond the maximum Q of a typical CTR measurement, ~ 6 Å^{-1}. At 14 keV, L_{EC} increases ~10%

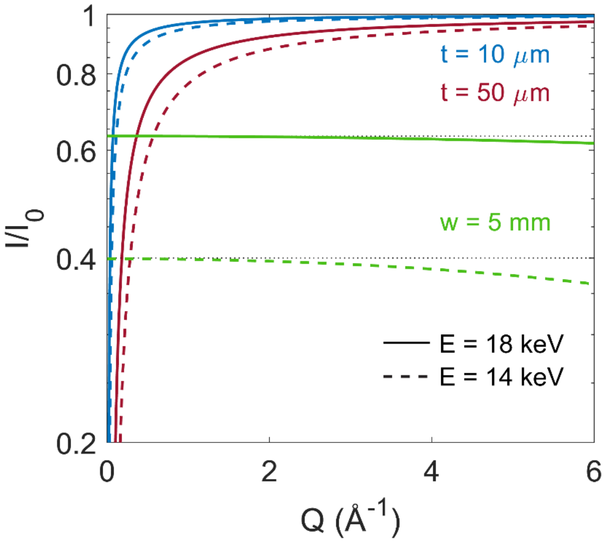

Figure B1. X-ray transmission through sample cells in different geometries and at different energies. Solid lines are calculated at E = 18 keV, dashed lines are calculated at E = 14 keV, blue curves are for a thin film cell with water layer thickness equal to 10 μm, red curves are for a thin film cell with water layer thickness equal to 50 μm, and green curves are for a transmission cell with a 5 mm wide water window along the beam direction. Black dotted lines are an aid to identify the small deviations of the transmission at high Q in the transmission cell.

from $0 < Q < 6$ Å^{-1}; at 18 keV the increase is reduced to 6% (Figure B1). This small change in the linear attenuation leads to significant covariance with the overall scale factor in the non-resonant XR data analysis. The range over which resonant spectra were measured is limited to $Q_{max} \sim 0.3$ Å^{-1}. Therefore, the X-ray pathlength and resulting linear attenuation correction is the same for all RAXR spectra (after accounting for the resonance modulation at the Rb K-edge).

A high X-ray flux was found to induce a current on the EG/SiC samples with a persistent effect on the CV measurements (Figure 5.12). This effect could be mitigated by using filters that kept the flux on the sample low. For a filter transmission below ~ 10^{-3}, the current was not affected (Figure B2).

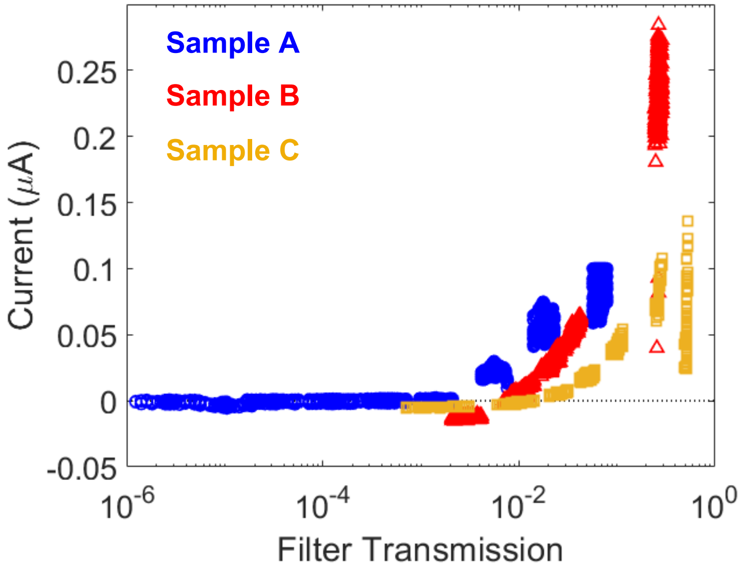

Figure B2. Current generated by X-ray exposure during RAXR measurements as a function of filter transmission and for three different EG/SiC samples.

Finally, as a result of the thick water window of the electrochemical cell, the linear attenuation at E = 15.2 keV (the Rb K-edge) contributes a significant resonance modulation to the total measured signal at the X-ray detector (Figure B3). All RAXR spectra essentially look the same, and the resonance modulations from the interfacial ion structure are not obvious. This is made more challenging because the flux on the sample was limited as described above and in Chapter 5.4.3. The linear attenuation correction needs to be performed carefully so as to not lose any of the already weak resonance modulation arising from the interface. We tested three different methods to measure the linear attenuation before arriving at the methodology described in Chapter 5.4.3. The first three approaches are shown in Figure B4.

The first approach relied on a transmission XANES measurement (Figure B4a), which is always performed to determine the precise value of E_0 as described in Chapter 5.2. If the XANES measurement is carried out with the same electrolyte concentration as the one used to probe the

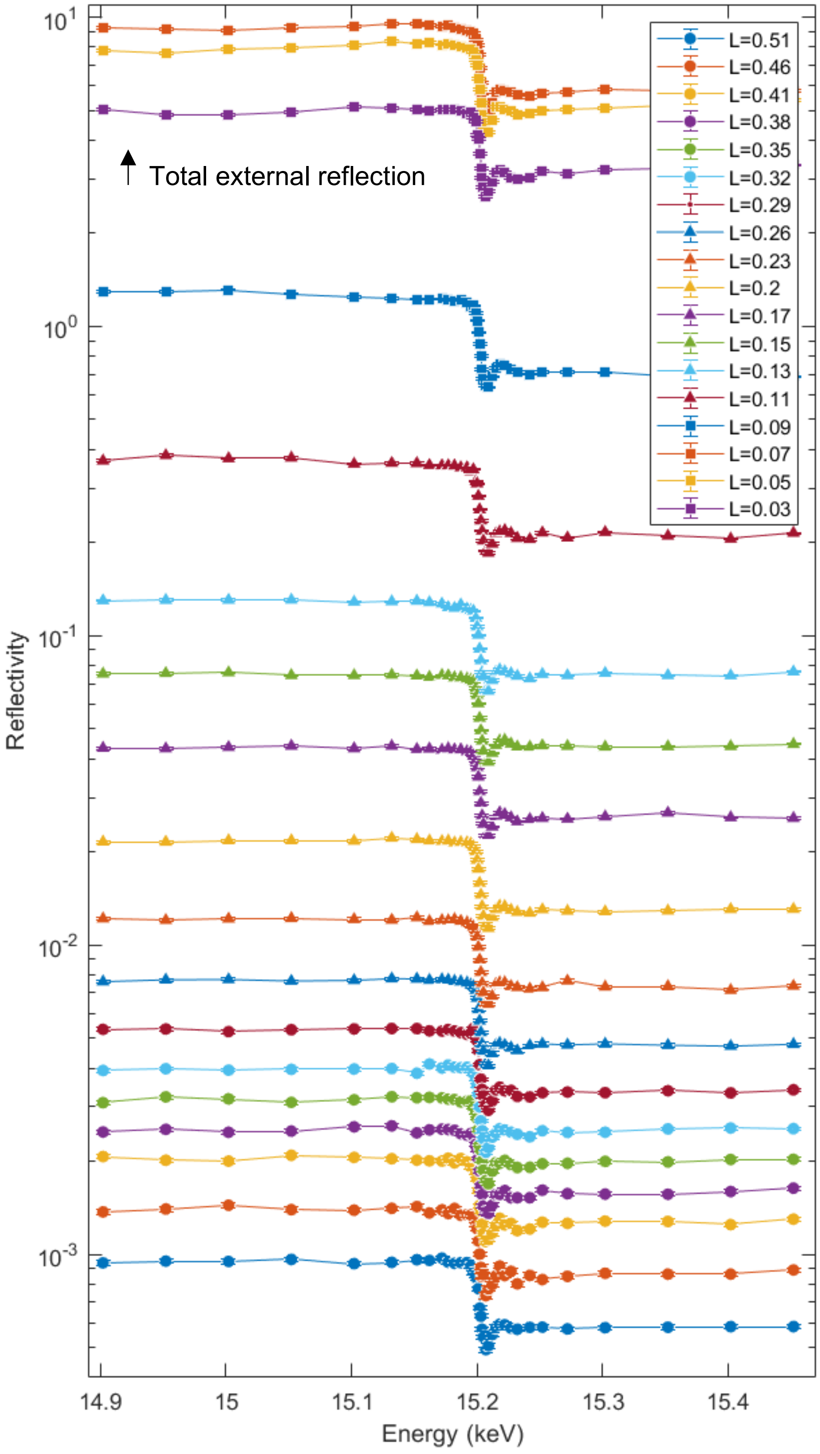

Figure B3. RAXR measurements of 0.1 M RbCl/EG/SiC before linear attenuation correction. All spectra have the same shape and are dominated by the resonance modulation through the bulk electrolyte. Note that the SiC critical angle is $Q = 0.037$ Å^{-1}, or $L = 0.089$ ($Q = 2\pi L/c_{SiC}$). The first three measurements correspond to total external reflection.

EDL, then this method, in principle, does not require any additional measurements. However, the XANES cell and electrochemical cell are not the same thickness, so the measured attenuation through the XANES cell requires a pathlength correction in order to be applied accurately to the electrochemical cell. Such a pathlength correction is nearly impossible to make because the thickness of the XANES cell depends on the amount of solution added during assembly and the pressure the solution exerts on the Kapton film windows. Hence, the thickness is generally unknown. In addition, transmission through the XANES cell is measured before the beamline filters and using ion chambers. The filtering required for the RAXR measurements may lead to beam hardening (lower energy X-rays are filtered more effectively that higher energy X-rays) compared to the XANES attenuation, further complicating the application of this method.

The second approach to perform the linear attenuation correction is by measuring it directly through the electrochemical cell placed on the diffractometer. The sample cell is positioned with all diffractometer angles set to zero such that the X-rays pass through the cell at normal incidence. The electrochemical cell is moved down by 1 mm to ensure the X-rays pass through the bulk electrolyte only. The attenuation is then measured between an ion chamber and the X-ray detector (Figure B4b). This approach requires significant filters to protect the detector from beam damage of the straight through beam (STB). The filter transmission required to protect the detector at the STB condition is ~10^{-9}, which will result in significant beam hardening. Thus, this method suffers from similar complications as the XANES approach.

The third method is to measure the linear attenuation directly through the electrochemical cell but utilizing the reflected intensity, which reduces the flux at the detector. We applied a positive voltage to the EG/SiC electrode in order to repel Rb^+ from the interface so that performing a correction using the measured signal would not artificially reduce the desired EDL resonance contribution (Figure B4c). This method still requires filters, but the same ones as used for RAXR measurements at negative voltage can be used, and therefore any beam hardening effects are directly transferable between +/- V. However, this approach had the same issues as the RAXR measurements with noise in the measured reflectivity (see Chapter 5.4.3 and Figure 5.15). We determined it was not a viable approach. In the end, we measured the linear attenuation through the electrochemical cell placed on the diffractometer and with a pin diode. This obviates concerns about protecting the area detector and beam hardening. We also do not need to worry about path length corrections between the attenuation measurement and the reflectivity measurements.

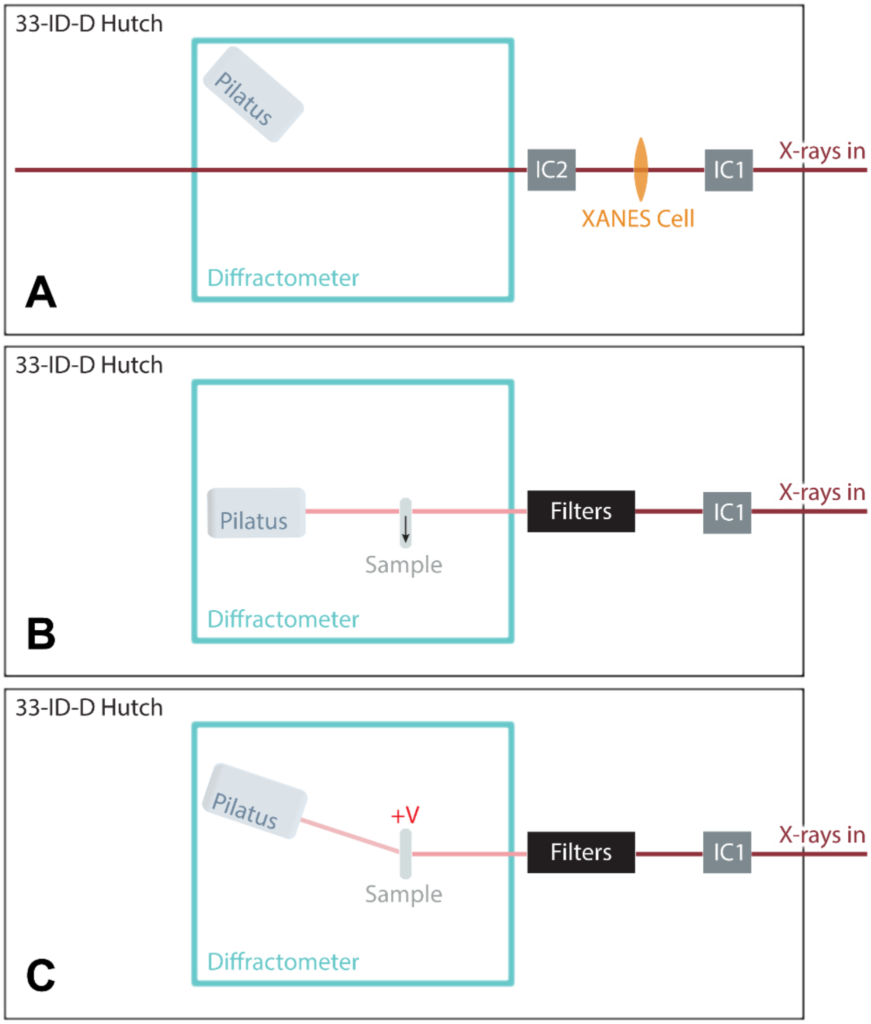

Figure B4. Methods to determine linear attenuation correction at the beamline. (A) The attenuation is measured through a transmission XANES cell at from of beamline using two ion chambers (IC1 and IC2). (B) The attenuation is measured through the bulk solution in the electrochemical cell using the Pilatus area detector, which requires significant filters. (C) The RAXR signal is measured through the cell with a positive voltage applied to the EG/SiC to repel Rb^+ from the interface. Thus, the resonance contribution should only be that of the bulk electrolyte.

B.2: XR Best-Fit Parameter Table for EG/SiC

Table B1. Non-resonant XR best-fit results for EG/6H-SiC in DIW and 0.1 M RbCl with uncertainties on the last significant figures in parentheses. Values without uncertainties were fixed during analysis.

	In DIW			**In 0.1 M RbCl**		
Layer	**z (Å)**	**u (Å)**	**Θ (AUC^{-1})**	**z (Å)**	**u (Å)**	**Θ (AUC^{-1})**
6H-SiC(0001)						
C	−13.236(9)	0.0922	1	-13.242(6)	0.0922	1
Si	−12.603(3)	0.0837	1	-12.606(2)	0.0837	1
C	−10.71(1)	0.0922	1	-10.718(8)	0.0922	1
Si	−10.084(4)	0.0837	1	-10.083(3)	0.0837	1
C	−8.24(2)	0.0922	1	-8.19(1)	0.0922	1
Si	−7.576(6)	0.0837	1	-7.558(6)	0.0837	1
C	−5.68(3)	0.0922	1	-5.67(3)	0.0922	1
Si	−5.05(2)	0.0837	1	-5.04(1)	0.0837	1
C	−3.08(3)	0.0922	1	-3.13(2)	0.0922	1
Si	−2.52(2)	0.0837	0.93(2)	-2.505(6)	0.09(2)	1
C	−0.49(6)	0.0922	1	-0.49(4)	0.0922	1
Si	-0.01(1)	0.14(5)[a]	0.80(2)	-0.004(11)	0.18(3)	.91(6)
Graphene						
S1 (G_0)	2.25(9)	0.32(3)	3.16(7)	2.38(2)	0.24(2)	3.00(6)
S2 (G_0)	2.1(1.5)[a]	0.21	0.80[b]	1.93(1)	0.21	0.91[b]
G_1	5.6(1)	0.16(3)	3.1(3)	5.77(3)	0.11(2)	3.0(3)
G_2	8.9(1)	0.2(1)	1.3(2)	9.05(4)	0.09(9)	1.3(1)
G_3	12.3(1)	0.07(1.18)[a]	0.3(1)	12.51(5)	0.1	0.6(1)
G_4	15.6(3)	0.07(3.55)[a]	0.09[c]	15.9[c]	0.1	0.20(4)
G_5	-	-	-	19.2[c]	0.1	0.05(1)
Liquid						
H_2O	5.7(2)	0.3(2)	0.80(4)[d]	5.7(2)	0.3(2)	0.75(2)[d]
	d_w = 2.94(15)	$\bar{u}$ = 0.75(9)		d_w = 2.76(7)	$\bar{u}$ = 0.53(8)	

[a] These parameters were fixed in the final iterations of the least-squares optimization. [b] Uses model that fixes S2 coverage to that of the terminal Si layer of the SiC substrate. [c] Values were fixed because with them turned on, the position parameters of these layers moved to 1.5-2× the graphene *d*-spacing from the layer below, and the water r.m.s. width became that of a 2D graphene layer at a height consistent with a graphene layer. [d] Calculated from d_w.

References

1. M. L. Schlegel, C. Bataillon, C. Blanc, D. Prêt and E. Foy, *Anodic Activation of Iron Corrosion in Clay Media under Water-Saturated Conditions at 90 °C: Characterization of the Corrosion Interface*, Environ. Sci. Technol. **44**, 1503-1508 (2010).
2. H. Li, H. Yu, T. Zhou, B. Yin, S. Yin and Y. Zhang, *Effect of tin on the corrosion behavior of sea-water corrosion-resisting steel*, Materials & Design **84**, 1-9 (2015).
3. Z. Liu, X. Gao, J. Li, L. Du, C. Yu, P. Li and X. Bai, *Corrosion behaviour of low-alloy martensite steel exposed to vapour-saturated CO_2 and CO_2-saturated brine conditions*, Electrochim. Acta **213**, 842-855 (2016).
4. I. B. Obot, I. B. Onyeachu and S. A. Umoren, *Alternative corrosion inhibitor formulation for carbon steel in CO_2-saturated brine solution under high turbulent flow condition for use in oil and gas transportation pipelines*, Corrosion Science **159**, 108140 (2019).
5. F. T. Wagner and G. A. Somorjai, *Photocatalytic and photoelectrochemical hydrogen production on strontium titanate single crystals*, J. Am. Chem. Soc. **102**, 5494-5502 (1980).
6. E. D. Park, S. H. Choi and J. S. Lee, *Active States of Pd and Cu in Carbon-Supported Wacker-Type Catalysts for Low-Temperature CO Oxidation*, J. Phys. Chem. B **104**, 5586-5594 (2000).
7. V. R. Stamenkovic, B. Fowler, B. S. Mun, G. Wang, P. N. Ross, C. A. Lucas and N. M. Marković, *Improved Oxygen Reduction Activity on $Pt_3Ni(111)$ via Increased Surface Site Availability*, Science **315**, 493-497 (2007).
8. A. Tanaka, K. Nakanishi, R. Hamada, K. Hashimoto and H. Kominami, *Simultaneous and Stoichiometric Water Oxidation and Cr(VI) Reduction in Aqueous Suspensions of Functionalized Plasmonic Photocatalyst Au/TiO_2–Pt under Irradiation of Green Light*, ACS Catalysis **3**, 1886-1891 (2013).
9. B. Dong, J. Cui, T. Liu, Y. Gao, Y. Qi, D. Li, F. Xiong, F. Zhang and C. Li, *Development of Novel Perovskite-Like Oxide Photocatalyst $LiCuTa_3O_9$ with Dual Functions of Water Reduction and Oxidation under Visible Light Irradiation*, Adv. Energy Mater. **8**, 1801660 (2018).
10. S. Kewalramani, G. I. Guerrero-García, L. M. Moreau, J. W. Zwanikken, C. A. Mirkin, M. Olvera de la Cruz and M. J. Bedzyk, *Electrolyte-Mediated Assembly of Charged Nanoparticles*, ACS Central Science **2**, 219-224 (2016).
11. K. Krishnamoorthy, K. Hoffmann, S. Kewalramani, J. D. Brodin, L. M. Moreau, C. A. Mirkin, M. Olvera de la Cruz and M. J. Bedzyk, *Defining the Structure of a Protein–Spherical Nucleic Acid Conjugate and Its Counterionic Cloud*, ACS Central Science **4**, 378-386 (2018).
12. E. Wieland, B. Wehrli and W. Stumm, *The coordination chemistry of weathering: III. A generalization on the dissolution rates of minerals*, Geochim. Cosmochim. Acta **52**, 1969-1981 (1988).
13. C. C. Fuller, J. A. Davis and G. A. Waychunas, *Surface chemistry of ferrihydrite: Part 2. Kinetics of arsenate adsorption and coprecipitation*, Geochim. Cosmochim. Acta **57**, 2271-2282 (1993).

14. J. G. Catalano, T. P. Trainor, P. J. Eng, G. A. Waychunas and G. E. Brown, *CTR diffraction and grazing-incidence EXAFS study of U(VI) adsorption onto α-Al_2O_3 and α-Fe_2O_3 ($1\bar{1}02$) surfaces*, Geochim. Cosmochim. Acta **69**, 3555-3572 (2005).
15. S. S. Lee, P. Fenter, K. L. Nagy and N. C. Sturchio, *Monovalent ion adsorption at the muscovite (001) solution interface: Relationships among ion coverage and speciation, interfacial water structure, and substrate relaxation*, Langmuir **28**, 8637-8650 (2012).
16. A. Fernandez-Martinez, Y. Hu, B. Lee, Y.-S. Jun and G. A. Waychunas, *In Situ Determination of Interfacial Energies between Heterogeneously Nucleated $CaCO_3$ and Quartz Substrates: Thermodynamics of CO_2 Mineral Trapping*, Environ. Sci. Technol. **47**, 102-109 (2013).
17. T. Lindgren, H. Wang, N. Beermann, L. Vayssieres, A. Hagfeldt and S.-E. Lindquist, *Aqueous photoelectrochemistry of hematite nanorod array*, Sol. Energy Mater. Sol. Cells **71**, 231-243 (2002).
18. T. F. Chala, C.-M. Wu, M.-H. Chou and Z.-L. Guo, *Melt Electrospun Reduced Tungsten Oxide /Polylactic Acid Fiber Membranes as a Photothermal Material for Light-Driven Interfacial Water Evaporation*, ACS Appl. Mater. Inter. **10**, 28955-28962 (2018).
19. Y. Yang, S. Niu, D. Han, T. Liu, G. Wang and Y. Li, *Progress in Developing Metal Oxide Nanomaterials for Photoelectrochemical Water Splitting*, Adv. Energy Mater. **7**, 1700555 (2017).
20. C. Morterra, G. Cerrato, L. Ferroni and L. Montanaro, *Surface characterization of yttria-stabilized tetragonal ZrO_2 Part 1. Structural, morphological, and surface hydration features*, Materials Chemistry and Physics **37**, 243-257 (1994).
21. G. Martra, *Lewis acid and base sites at the surface of microcrystalline TiO_2 anatase: relationships between surface morphology and chemical behaviour*, Applied Catalysis A: General **200**, 275-285 (2000).
22. P. Zhang, F. Xu, A. Navrotsky, J. S. Lee, S. Kim and J. Liu, *Surface Enthalpies of Nanophase ZnO with Different Morphologies*, Chemistry of Materials **19**, 5687-5693 (2007).
23. L. Mino, G. Spoto, S. Bordiga and A. Zecchina, *Particles Morphology and Surface Properties As Investigated by HRTEM, FTIR, and Periodic DFT Calculations: From Pyrogenic TiO_2 (P25) to Nanoanatase*, J. Phys. Chem. C **116**, 17008-17018 (2012).
24. Z. Zhang, P. Fenter, L. Cheng, N. C. Sturchio, M. J. Bedzyk, M. Předota, A. Bandura, J. D. Kubicki, S. N. Lvov, P. T. Cummings, et al., *Ion Adsorption at the Rutile−Water Interface: Linking Molecular and Macroscopic Properties*, Langmuir **20**, 4954-4969 (2004).
25. M. Mezger, H. Reichert, S. Schöder, J. Okasinski, H. Schröder, H. Dosch, D. Palms, J. Ralston and V. Honkimäki, *High-resolution in situ x-ray study of the hydrophobic gap at the water–octadecyl-trichlorosilane interface*, Proc. Natl. Acad. Sci. **103**, 18401-18404 (2006).
26. J. G. Catalano, C. Park, Z. Zhang and P. Fenter, *Termination and Water Adsorption at the α-Al_2O_3 (012)−Aqueous Solution Interface*, Langmuir **22**, 4668-4673 (2006).
27. Z. Zhang, P. Fenter, N. C. Sturchio, M. J. Bedzyk, M. L. Machesky and D. J. Wesolowski, *Structure of rutile TiO_2 (110) in water and 1molal Rb+ at pH 12: Inter-relationship among*

surface charge, interfacial hydration structure, and substrate structural displacements, Surf. Sci. **601**, 1129-1143 (2007).
28. M.-P. Gaigeot, M. Sprik and M. Sulpizi, *Oxide/water interfaces: how the surface chemistry modifies interfacial water properties*, J. Phys. Condens. Matter **24**, 124106 (2012).
29. C. A. Fernandez, S. K. Nune, H. V. Annapureddy, L. X. Dang, B. P. McGrail, F. Zheng, E. Polikarpov, D. L. King, C. Freeman and K. P. Brooks, *Hydrophobic and moisture-stable metal-organic frameworks*, Dalton Trans. **44**, 13490-13497 (2015).
30. R. Dash, J. Chmiola, G. Yushin, Y. Gogotsi, G. Laudisio, J. Singer, J. Fischer and S. Kucheyev, *Titanium carbide derived nanoporous carbon for energy-related applications*, Carbon **44**, 2489-2497 (2006).
31. J. Chmiola, C. Largeot, P.-L. Taberna, P. Simon and Y. Gogotsi, *Desolvation of Ions in Subnanometer Pores and Its Effect on Capacitance and Double-Layer Theory*, Angew. Chem. **120**, 3440-3443 (2008).
32. Y. Korenblit, M. Rose, E. Kockrick, L. Borchardt, A. Kvit, S. Kaskel and G. Yushin, *High-Rate Electrochemical Capacitors Based on Ordered Mesoporous Silicon Carbide-Derived Carbon*, ACS Nano **4**, 1337-1344 (2010).
33. A. Kajdos, A. Kvit, F. Jones, J. Jagiello and G. Yushin, *Tailoring the Pore Alignment for Rapid Ion Transport in Microporous Carbons*, J. Am. Chem. Soc. **132**, 3252-3253 (2010).
34. M. C. F. Wander and K. L. Shuford, *Electrolyte Effects in a Model System for Mesoporous Carbon Electrodes*, J. Phys. Chem. C **115**, 4904-4908 (2011).
35. J. N. Israelachvili and R. M. Pashley, *Molecular layering of water at surfaces and origin of repulsive hydration forces*, Nature **306**, 249-250 (1983).
36. M. Luna, J. Colchero, A. Gil, J. Gómez-Herrero and A. M. Baró, *Application of non-contact scanning force microscopy to the study of water adsorption on graphite, gold and mica*, Appl. Surf. Sci. **157**, 393-397 (2000).
37. A. Poynor, L. Hong, I. K. Robinson, S. Granick, Z. Zhang and P. A. Fenter, *How Water Meets a Hydrophobic Surface*, Phys. Rev. Lett. **97**, 266101 (2006).
38. M. Mezger, F. Sedlmeier, D. Horinek, H. Reichert, D. Pontoni and H. Dosch, *On the Origin of the Hydrophobic Water Gap: An X-ray Reflectivity and MD Simulation Study*, J. Am. Chem. Soc. **132**, 6735-6741 (2010).
39. A. Uysal, M. Chu, B. Stripe, A. Timalsina, S. Chattopadhyay, C. M. Schlepütz, T. J. Marks and P. Dutta, *What x rays can tell us about the interfacial profile of water near hydrophobic surfaces*, Phys. Rev. B **88**, 035431 (2013).
40. P. Fenter and S. S. Lee, *Hydration layer structure at solid–water interfaces*, MRS Bull. **39**, 1056-1061 (2014).
41. A. Schlaich, E. W. Knapp and R. R. Netz, *Water Dielectric Effects in Planar Confinement*, Phys. Rev. Lett. **117**, 048001 (2016).
42. G. F. von Rudorff, R. Jakobsen, K. M. Rosso and J. Blumberger, *Fast Interconversion of Hydrogen Bonding at the Hematite (001)–Liquid Water Interface*, J. Phys. Chem. Lett. **7**, 1155-1160 (2016).
43. A. Tuladhar, S. Dewan, J. D. Kubicki and E. Borguet, *Spectroscopy and Ultrafast Vibrational Dynamics of Strongly Hydrogen Bonded OH Species at the* α-$Al_2O_3(11\bar{2}0)/H_2O$ *Interface*, J. Phys. Chem. C **120**, 16153-16161 (2016).

44. C. Zhang, F. Gygi and G. Galli, *Strongly Anisotropic Dielectric Relaxation of Water at the Nanoscale*, J. Phys. Chem. Lett. **4**, 2477-2481 (2013).
45. M. Munz, C. E. Giusca, R. L. Myers-Ward, D. K. Gaskill and O. Kazakova, *Thickness-Dependent Hydrophobicity of Epitaxial Graphene*, ACS Nano **9**, 8401-8411 (2015).
46. L. Fumagalli, A. Esfandiar, R. Fabregas, S. Hu, P. Ares, A. Janardanan, Q. Yang, B. Radha, T. Taniguchi, K. Watanabe, et al., *Anomalously low dielectric constant of confined water*, Science **360**, 1339-1342 (2018).
47. C. Schaaf and S. Gekle, *Dielectric response of the water hydration layer around spherical solutes*, Phys. Rev. E **92**, 032718 (2015).
48. J. G. Catalano, *Relaxations and Interfacial Water Ordering at the Corundum (110) Surface*, J. Phys. Chem. C **114**, 6624-6630 (2010).
49. N. Laanait, E. B. R. Callagon, Z. Zhang, N. C. Sturchio, S. S. Lee and P. Fenter, *X-ray–driven reaction front dynamics at calcite-water interfaces*, Science **349**, 1330-1334 (2015).
50. C. Gao, H. Li, Y. Li, S. Kewalramani, L. C. Palmer, V. P. Dravid, S. I. Stupp, M. Olvera de la Cruz and M. J. Bedzyk, *Electrostatic Control of Polymorphism in Charged Amphiphile Assemblies*, J. Phys. Chem. B **121**, 1623-1628 (2017).
51. J. N. Bracco, S. S. Lee, J. E. Stubbs, P. J. Eng, F. Heberling, P. Fenter and A. G. Stack, *Hydration Structure of the Barite (001)–Water Interface: Comparison of X-ray Reflectivity with Molecular Dynamics Simulations*, J. Phys. Chem. C **121**, 12236-12248 (2017).
52. X. G. Wang, W. Weiss, S. K. Shaikhutdinov, M. Ritter, M. Petersen, F. Wagner, R. Schlögl and M. Scheffler, *The Hematite (α-Fe_2O_3) (0001) Surface: Evidence for Domains of Distinct Chemistry*, Phys. Rev. Lett. **81**, 1038-1041 (1998).
53. A. Tuladhar, S. M. Piontek and E. Borguet, *Insights on Interfacial Structure, Dynamics, and Proton Transfer from Ultrafast Vibrational Sum Frequency Generation Spectroscopy of the Alumina(0001)/Water Interface*, J. Phys. Chem. C **121**, 5168-5177 (2017).
54. Y. R. Shen and V. Ostroverkhov, *Sum-Frequency Vibrational Spectroscopy on Water Interfaces: Polar Orientation of Water Molecules at Interfaces*, Chem. Rev. **106**, 1140-1154 (2006).
55. M. DelloStritto and J. Sofo, *Bond Polarizability Model for Sum Frequency Generation at the Al_2O_3(0001)–H_2O Interface*, J. Phys. Chem. A **121**, 3045-3055 (2017).
56. J. N. Israelachvili and G. E. Adams, *Measurement of forces between two mica surfaces in aqueous electrolyte solutions in the range 0-100 nm*, Journal of the Chemical Society, Faraday Transactions 1: Physical Chemistry in Condensed Phases **74**, 975-1001 (1978).
57. M. Fujihira, *KELVIN PROBE FORCE MICROSCOPY OF MOLECULAR SURFACES*, Annual Review of Materials Science **29**, 353-380 (1999).
58. Y. Gan and G. V. Franks, *High Resolution AFM Images of the Single-Crystal α-Al_2O_3(0001) Surface in Water*, J. Phys. Chem. B **109**, 12474-12479 (2005).
59. T. Fukuma, Y. Ueda, S. Yoshioka and H. Asakawa, *Atomic-Scale Distribution of Water Molecules at the Mica-Water Interface Visualized by Three-Dimensional Scanning Force Microscopy*, Phys. Rev. Lett. **104**, 016101 (2010).
60. A. M. Smith, A. A. Lee and S. Perkin, *The Electrostatic Screening Length in Concentrated Electrolytes Increases with Concentration*, J. Phys. Chem. Lett. **7**, 2157-2163 (2016).

61. D. Martin-Jimenez, E. Chacon, P. Tarazona and R. Garcia, *Atomically resolved three-dimensional structures of electrolyte aqueous solutions near a solid surface*, Nat. Commun. **7**, 12164 (2016).
62. J. W. G. Tyrrell and P. Attard, *Atomic Force Microscope Images of Nanobubbles on a Hydrophobic Surface and Corresponding Force−Separation Data*, Langmuir **18**, 160-167 (2002).
63. J. M. Black, M. Zhu, P. Zhang, R. R. Unocic, D. Guo, M. B. Okatan, S. Dai, P. T. Cummings, S. V. Kalinin, G. Feng, et al., *Fundamental aspects of electric double layer force-distance measurements at liquid-solid interfaces using atomic force microscopy*, Sci. Rep. **6**, 32389 (2016).
64. M. F. Toney, J. N. Howard, J. Richer, G. L. Borges, J. G. Gordon, O. R. Melroy, D. G. Wiesler, D. Yee and L. B. Sorensen, *Distribution of water molecules at Ag(111)/electrolyte interface as studied with surface X-ray scattering*, Surf. Sci. **335**, 326-332 (1995).
65. L. Cheng, P. Fenter, K. L. Nagy, M. L. Schlegel and N. C. Sturchio, *Molecular-Scale Density Oscillations in Water Adjacent to a Mica Surface*, Phys. Rev. Lett. **87**, 156103 (2001).
66. P. Fenter and N. C. Sturchio, *Mineral–water interfacial structures revealed by synchrotron X-ray scattering*, Prog. Surf. Sci. **77**, 171-258 (2004).
67. H. Zhou, P. Ganesh, V. Presser, M. C. F. Wander, P. Fenter, P. R. C. Kent, D.-e. Jiang, A. A. Chialvo, J. McDonough, K. L. Shuford, et al., *Understanding controls on interfacial wetting at epitaxial graphene: Experiment and theory*, Phys. Rev. B **85**, 035406 (2012).
68. M. Gouy, *Sur la constitution de la charge électrique à la surface d'un électrolyte*, J. Phys. Theor. Appl. **9**, 457-468 (1910).
69. D. L. Chapman, *LI. A contribution to the theory of electrocapillarity*, Philosophical Magazine Series 6 **25**, 475-481 (1913).
70. A. J. Bard and L. R. Faulkner, *Electrochemical Methods: Fundamentals and Applications*, (John Wiley & Sons, 2001).
71. O. Stern, *ZUR THEORIE DER ELEKTROLYTISCHEN DOPPELSCHICHT*, Zeitschrift für Elektrochemie und angewandte physikalische Chemie **30**, 508-516 (1924).
72. R. M. Pashley, *DLVO and hydration forces between mica surfaces in Li+, Na+, K+, and Cs+ electrolyte solutions: A correlation of double-layer and hydration forces with surface cation exchange properties*, J. Colloid Interface Sci. **83**, 531-546 (1981).
73. A. A. Kornyshev, *Double-Layer in Ionic Liquids: Paradigm Change?*, J. Phys. Chem. B **111**, 5545-5557 (2007).
74. A. W. C. Lau, D. B. Lukatsky, P. Pincus and S. A. Safran, *Charge fluctuations and counterion condensation*, Phys. Rev. E **65**, 051502 (2002).
75. M. Z. Bazant, B. D. Storey and A. A. Kornyshev, *Double Layer in Ionic Liquids: Overscreening versus Crowding*, Phys. Rev. Lett. **106**, 046102 (2011).
76. J. P. Valleau and G. M. Torrie, *The electrical double layer. III. Modified Gouy−Chapman theory with unequal ion sizes*, J. Chem. Phys. **76**, 4623-4630 (1982).
77. J. J. Howard, J. S. Perkyns and B. M. Pettitt, *The Behavior of Ions near a Charged Wall—Dependence on Ion Size, Concentration, and Surface Charge*, J. Phys. Chem. B **114**, 6074-6083 (2010).

78. D. di Caprio, Z. Borkowska and J. Stafiej, *Simple extension of the Gouy–Chapman theory including hard sphere effects.: Diffuse layer contribution to the differential capacity curves for the electrode/electrolyte interface*, Journal of Electroanalytical Chemistry **540**, 17-23 (2003).
79. L. Lue, *A variational field theory for solutions of charged, rigid particles*, Fluid Phase Equilibria **241**, 236-247 (2006).
80. L. Lue, N. Zoeller and D. Blankschtein, *Incorporation of Nonelectrostatic Interactions in the Poisson−Boltzmann Equation*, Langmuir **15**, 3726-3730 (1999).
81. Y. Burak and D. Andelman, *Hydration interactions: Aqueous solvent effects in electric double layers*, Phys. Rev. E **62**, 5296-5312 (2000).
82. M. N. Tamashiro and H. Schiessel, *Where the linearized Poisson–Boltzmann cell model fails: Spurious phase separation in charged colloidal suspensions*, J. Chem. Phys. **119**, 1855-1865 (2003).
83. J. Pittler, W. Bu, D. Vaknin, A. Travesset, D. J. McGillivray and M. Lösche, *Charge Inversion at Minute Electrolyte Concentrations*, Phys. Rev. Lett. **97**, 046102 (2006).
84. A. A. Lee, C. S. Perez-Martinez, A. M. Smith and S. Perkin, *Underscreening in concentrated electrolytes*, Faraday Discussions **199**, 239-259 (2017).
85. A. A. Lee, C. S. Perez-Martinez, A. M. Smith and S. Perkin, *Scaling Analysis of the Screening Length in Concentrated Electrolytes*, Phys. Rev. Lett. **119**, 026002 (2017).
86. M. J. Bedzyk, G. M. Bommarito, M. Caffrey and T. L. Penner, *Diffuse-Double Layer at a Membrane-Aqueous Interface Measured with X-Ray Standing Waves*, Science **248**, 52-56 (1990).
87. B. E. Conway, *Electrochemical supercapacitors: scientific fundamentals and technological applications*, (Springer Science & Business Media, 2013).
88. P. Simon and Y. Gogotsi, *Materials for electrochemical capacitors*, Nat. Mater. **7**, 845-854 (2008).
89. J. Li, H. Xie, Y. Li, J. Liu and Z. Li, *Electrochemical properties of graphene nanosheets/polyaniline nanofibers composites as electrode for supercapacitors*, Journal of Power Sources **196**, 10775-10781 (2011).
90. S. Biswas and L. T. Drzal, *Multilayered Nano-Architecture of Variable Sized Graphene Nanosheets for Enhanced Supercapacitor Electrode Performance*, ACS Appl. Mater. Inter. **2**, 2293-2300 (2010).
91. D. N. Futaba, K. Hata, T. Yamada, T. Hiraoka, Y. Hayamizu, Y. Kakudate, O. Tanaike, H. Hatori, M. Yumura and S. Iijima, *Shape-engineerable and highly densely packed single-walled carbon nanotubes and their application as super-capacitor electrodes*, Nat. Mater. **5**, 987-994 (2006).
92. J. Huang, B. G. Sumpter and V. Meunier, *A universal model for nanoporous carbon supercapacitors applicable to diverse pore regimes, carbon materials, and electrolytes*, Chemistry-A European Journal **14**, 6614-6626 (2008).
93. D. Weingarth, M. Zeiger, N. Jäckel, M. Aslan, G. Feng and V. Presser, *Graphitization as a Universal Tool to Tailor the Potential-Dependent Capacitance of Carbon Supercapacitors*, Adv. Energy Mater. **4**, 1400316 (2014).
94. M. Armand, F. Endres, D. R. MacFarlane, H. Ohno and B. Scrosati, *Ionic-liquid materials for the electrochemical challenges of the future*, Nat Mater **8**, 621-629 (2009).

95. M. J. Gillan, D. Alfè and A. Michaelides, *Perspective: How good is DFT for water?*, J. Chem. Phys. **144**, 130901 (2016).
96. K. Lejaeghere, G. Bihlmayer, T. Björkman, P. Blaha, S. Blügel, V. Blum, D. Caliste, I. E. Castelli, S. J. Clark, A. Dal Corso, et al., *Reproducibility in density functional theory calculations of solids*, Science **351**, aad3000 (2016).
97. L. Ruiz Pestana, O. Marsalek, T. E. Markland and T. Head-Gordon, *The Quest for Accurate Liquid Water Properties from First Principles*, J. Phys. Chem. Lett. **9**, 5009-5016 (2018).
98. J. G. Brandenburg, T. Maas and S. Grimme, *Benchmarking DFT and semiempirical methods on structures and lattice energies for ten ice polymorphs*, J. Chem. Phys. **142**, 124104 (2015).
99. A. J. Cohen, P. Mori-Sánchez and W. Yang, *Challenges for Density Functional Theory*, Chem. Rev. **112**, 289-320 (2012).
100. S. Grimme, J. Antony, S. Ehrlich and H. Krieg, *A consistent and accurate ab initio parametrization of density functional dispersion correction (DFT-D) for the 94 elements H-Pu*, J. Chem. Phys. **132**, 154104 (2010).
101. V. N. Staroverov, G. E. Scuseria, J. Tao and J. P. Perdew, *Tests of a ladder of density functionals for bulk solids and surfaces*, Phys. Rev. B **69**, (2004).
102. F. Tran, J. Stelzl and P. Blaha, *Rungs 1 to 4 of DFT Jacob's ladder: Extensive test on the lattice constant, bulk modulus, and cohesive energy of solids*, J. Chem. Phys. **144**, 204120 (2016).
103. P. Pernot, B. Civalleri, D. Presti and A. Savin, *Prediction uncertainty of density functional approximations for properties of crystals with cubic symmetry*, J. Phys. Chem. A **119**, 5288-5304 (2015).
104. G. I. Csonka, J. P. Perdew, A. Ruzsinszky, P. H. T. Philipsen, S. Lebègue, J. Paier, O. A. Vydrov and J. G. Ángyán, *Assessing the performance of recent density functionals for bulk solids*, Phys. Rev. B **79**, 155107 (2009).
105. J. Klimeš, D. R. Bowler and A. Michaelides, *Chemical accuracy for the van der Waals density functional*, J. Phys. Condens. Matter **22**, 022201 (2010).
106. B. Santra, J. Klimes, A. Tkatchenko, D. Alfè, B. Slater, A. Michaelides, R. Car and M. Scheffler, *On the accuracy of van der Waals inclusive density-functional theory exchange-correlation functionals for ice at ambient and high pressures*, J. Chem. Phys. **139**, 154702 (2013).
107. J. C. Grossman, E. Schwegler, E. W. Draeger, F. Gygi and G. Galli, *Towards an assessment of the accuracy of density functional theory for first principles simulations of water*, The Journal of Chemical Physics **120**, 300-311 (2004).
108. P. Fenter, S. Kerisit, P. Raiteri and J. D. Gale, *Is the Calcite–Water Interface Understood? Direct Comparisons of Molecular Dynamics Simulations with Specular X-ray Reflectivity Data*, J. Phys. Chem. C **117**, 5028-5042 (2013).
109. M. Předota, Z. Zhang, P. Fenter, D. J. Wesolowski and P. T. Cummings, *Electric Double Layer at the Rutile (110) Surface. 2. Adsorption of Ions from Molecular Dynamics and X-ray Experiments*, J. Phys. Chem. B **108**, 12061-12072 (2004).
110. J. L. Fulton, E. J. Bylaska, S. Bogatko, M. Balasubramanian, E. Cauët, G. K. Schenter and J. H. Weare, *Near-Quantitative Agreement of Model-Free DFT-MD Predictions with XAFS*

Observations of the Hydration Structure of Highly Charged Transition-Metal Ions, J. Phys. Chem. Lett. **3**, 2588-2593 (2012).

111. M. Gerosa, F. Gygi, M. Govoni and G. Galli, *The role of defects and excess surface charges at finite temperature for optimizing oxide photoabsorbers*, Nat. Mater. **17**, 1122-1127 (2018).
112. G. Cicero, J. C. Grossman, E. Schwegler, F. Gygi and G. Galli, *Water Confined in Nanotubes and between Graphene Sheets: A First Principle Study*, J. Am. Chem. Soc. **130**, 1871-1878 (2008).
113. G. Cicero, J. C. Grossman, A. Catellani and G. Galli, *Water at a Hydrophilic Solid Surface Probed by Ab initio Molecular Dynamics: Inhomogeneous Thin Layers of Dense Fluid*, J. Am. Chem. Soc. **127**, 6830-6835 (2005).
114. B. Jönsson, *Monte carlo simulations of liquid water between two rigid walls*, Chem. Phys. Lett. **82**, 520-525 (1981).
115. C. Y. Lee, J. A. McCammon and P. J. Rossky, *The structure of liquid water at an extended hydrophobic surface*, J. Chem. Phys. **80**, 4448-4455 (1984).
116. E. Spohr, *Computer simulation of the water/platinum interface*, J. Phys. Chem. **93**, 6171-6180 (1989).
117. M. C. F. Wander and A. E. Clark, *Structural and Dielectric Properties of Quartz−Water Interfaces*, J. Phys. Chem. C **112**, 19986-19994 (2008).
118. V. N. Koparde and P. T. Cummings, *Molecular Dynamics Study of Water Adsorption on TiO2 Nanoparticles*, J. Phys. Chem. C **111**, 6920-6926 (2007).
119. M. F. Toney, J. N. Howard, J. Richer, G. L. Borges, J. G. Gordon, O. R. Melroy, D. G. Wiesler, D. Yee and L. B. Sorensen, *Voltage-dependent ordering of water molecules at an electrode–electrolyte interface*, Nature **368**, 444-446 (1994).
120. O. M. Magnussen, B. M. Ocko, M. J. Regan, K. Penanen, P. S. Pershan and M. Deutsch, *X-Ray Reflectivity Measurements of Surface Layering in Liquid Mercury*, Phys. Rev. Lett. **74**, 4444-4447 (1995).
121. M. J. Regan, E. H. Kawamoto, S. Lee, P. S. Pershan, N. Maskil, M. Deutsch, O. M. Magnussen, B. M. Ocko and L. E. Berman, *Surface Layering in Liquid Gallium: An X-Ray Reflectivity Study*, Phys. Rev. Lett. **75**, 2498-2501 (1995).
122. W. J. Huisman, J. F. Peters, M. J. Zwanenburg, S. A. de Vries, T. E. Derry, D. Abernathy and J. F. van der Veen, *Layering of a liquid metal in contact with a hard wall*, Nature **390**, 379-381 (1997).
123. C. J. Yu, A. G. Richter, A. Datta, M. K. Durbin and P. Dutta, *Observation of Molecular Layering in Thin Liquid Films Using X-Ray Reflectivity*, Phys. Rev. Lett. **82**, 2326-2329 (1999).
124. S.-H. Park and G. Sposito, *Structure of Water Adsorbed on a Mica Surface*, Phys. Rev. Lett. **89**, 085501 (2002).
125. J. Wang, A. G. Kalinichev, R. J. Kirkpatrick and R. T. Cygan, *Structure, Energetics, and Dynamics of Water Adsorbed on the Muscovite (001) Surface: A Molecular Dynamics Simulation*, J. Phys. Chem. B **109**, 15893-15905 (2005).
126. G. D. Williams, A. K. Soper, N. T. Skipper and M. V. Smalley, *High-Resolution Structural Study of an Electrical Double Layer by Neutron Diffraction*, J. Phys. Chem. B **102**, 8945-8949 (1998).

127. C.-Y. Ruan, V. A. Lobastov, F. Vigliotti, S. Chen and A. H. Zewail, *Ultrafast Electron Crystallography of Interfacial Water*, Science **304**, 80-84 (2004).
128. S. Chattopadhyay, A. Uysal, B. Stripe, Y.-g. Ha, T. J. Marks, E. A. Karapetrova and P. Dutta, *How Water Meets a Very Hydrophobic Surface*, Phys. Rev. Lett. **105**, 037803 (2010).
129. Q. Du, E. Freysz and Y. R. Shen, *Surface Vibrational Spectroscopic Studies of Hydrogen Bonding and Hydrophobicity*, Science **264**, 826-828 (1994).
130. F. Jiménez-Ángeles, K. J. Harmon, T. D. Nguyen, P. Fenter and M. Olvera de la Cruz, *Nonreciprocal interactions induced by water in confinement*, Phys. Rev. Res. **2**, 043244 (2020).
131. D. J. Bonthuis, S. Gekle and R. R. Netz, *Dielectric Profile of Interfacial Water and its Effect on Double-Layer Capacitance*, Phys. Rev. Lett. **107**, 166102 (2011).
132. M. H. Motevaselian and N. R. Aluru, *Universal Reduction in Dielectric Response of Confined Fluids*, ACS Nano **14**, 12761-12770 (2020).
133. A. Boulesbaa and E. Borguet, *Vibrational Dynamics of Interfacial Water by Free Induction Decay Sum Frequency Generation (FID-SFG) at the* $Al_2O_3(1120)/H_2O$ *Interface*, J. Phys. Chem. Lett. **5**, 528-533 (2014).
134. T. Sakamoto, H. Nakamura, H. Uedaira and A. Wada, *High-frequency dielectric relaxation of water bound to hydrophilic silica gels*, J. Phys. Chem. **93**, 357-366 (1989).
135. K. J. Tielrooij, D. Paparo, L. Piatkowski, H. J. Bakker and M. Bonn, *Dielectric Relaxation Dynamics of Water in Model Membranes Probed by Terahertz Spectroscopy*, Biophysical Journal **97**, 2484-2492 (2009).
136. J. D. Jackson, *Classical Electrodynamics*, (Wiley, New York, 1999).
137. O. Teschke, G. Ceotto and E. F. de Souza, *Interfacial aqueous solutions dielectric constant measurements using atomic force microscopy*, Chem. Phys. Lett. **326**, 328-334 (2000).
138. D. Ben-Yaakov, D. Andelman and R. Podgornik, *Dielectric decrement as a source of ion-specific effects*, J. Chem. Phys. **134**, 074705 (2011).
139. D. C. Grahame, *The Electrical Double Layer and the Theory of Electrocapillarity*, Chem. Rev. **41**, 441-501 (1947).
140. R. D. Shannon and C. T. Prewitt, *Effective ionic radii in oxides and fluorides*, Acta Cryst. B **25**, 925-946 (1969).
141. R. Shannon, *Revised effective ionic radii and systematic studies of interatomic distances in halides and chalcogenides*, Acta Cryst. A **32**, 751-767 (1976).
142. Q. Hu, C. Weber, H.-W. Cheng, F. U. Renner and M. Valtiner, *Anion Layering and Steric Hydration Repulsion on Positively Charged Surfaces in Aqueous Electrolytes*, ChemPhysChem **18**, 3056-3065 (2017).
143. D. T. Richens, *The Chemistry of Aqua Ions: Synthesis, Structure and Reactivity: ATour Through the Periodic Table of the Elements*, (Wiley, 1997).
144. S. S. Lee, P. Fenter, C. Park, N. C. Sturchio and K. L. Nagy, *Hydrated Cation Speciation at the Muscovite (001)−Water Interface*, Langmuir **26**, 16647-16651 (2010).
145. L. B. Bhuiyan and C. W. Outhwaite, *Comparison of exclusion volume corrections to the Poisson–Boltzmann equation for inhomogeneous electrolytes*, J. Colloid Interface Sci. **331**, 543-547 (2009).

146. M. M. Hatlo, R. van Roij and L. Lue, *The electric double layer at high surface potentials: The influence of excess ion polarizability*, EPL (Europhysics Letters) **97**, 28010 (2012).
147. D. C. Grahame, *Diffuse Double Layer Theory for Electrolytes of Unsymmetrical Valence Types*, J. Chem. Phys. **21**, 1054-1060 (1953).
148. Y. Lauw, M. D. Horne, T. Rodopoulos, A. Nelson and F. A. M. Leermakers, *Electrical Double-Layer Capacitance in Room Temperature Ionic Liquids: Ion-Size and Specific Adsorption Effects*, J. Phys. Chem. B **114**, 11149-11154 (2010).
149. L. B. Bhuiyan, L. Blum and D. Henderson, *The application of the modified Gouy–Chapman theory to an electrical double layer containing asymmetric ions*, J. Chem. Phys. **78**, 442-445 (1983).
150. C. Schaaf and S. Gekle, *Spatially resolved dielectric constant of confined water and its connection to the non-local nature of bulk water*, J. Chem. Phys. **145**, 084901 (2016).
151. A. Ajdari, *Electro-Osmosis on Inhomogeneously Charged Surfaces*, Phys. Rev. Lett. **75**, 755-758 (1995).
152. M. Mußotter, M. Bier and S. Dietrich, *Heterogeneous surface charge confining an electrolyte solution*, J. Chem. Phys. **152**, 234703 (2020).
153. C. McCallum, S. Pennathur and D. Gillespie, *Two-Dimensional Electric Double Layer Structure with Heterogeneous Surface Charge*, Langmuir **33**, 5642-5651 (2017).
154. W. H. Van Riemsdijk, G. H. Bolt, L. K. Koopal and J. Blaakmeer, *Electrolyte adsorption on heterogeneous surfaces: adsorption models*, J. Colloid Interface Sci. **109**, 219-228 (1986).
155. W. M. de Vos and S. Lindhoud, *Overcharging and charge inversion: Finding the correct explanation(s)*, Advances in Colloid and Interface Science **274**, 102040 (2019).
156. K. Besteman, M. A. G. Zevenbergen, H. A. Heering and S. G. Lemay, *Direct Observation of Charge Inversion by Multivalent Ions as a Universal Electrostatic Phenomenon*, Phys. Rev. Lett. **93**, 170802 (2004).
157. M. L. Jiménez, Á. V. Delgado and J. Lyklema, *Hydrolysis versus Ion Correlation Models in Electrokinetic Charge Inversion: Establishing Application Ranges*, Langmuir **28**, 6786-6793 (2012).
158. A. W. C. Lau, *Fluctuation and correlation effects in a charged surface immersed in an electrolyte solution*, Phys. Rev. E **77**, 011502 (2008).
159. P. A. Fenter, *X-ray Reflectivity as a Probe of Mineral-Fluid Interfaces: A User Guide*, Rev. Mineral. Geochem. **49**, 149-221 (2002).
160. C. J. Yu, A. G. Richter, A. Datta, M. K. Durbin and P. Dutta, *Molecular layering in a liquid on a solid substrate: an X-ray reflectivity study*, Physica B Condens. Matter **283**, 27-31 (2000).
161. J. Wang, B. M. Ocko, A. J. Davenport and H. S. Isaacs, *In situ x-ray-diffraction and -reflectivity studies of the Au(111)/electrolyte interface: Reconstruction and anion adsorption*, Phys. Rev. B **46**, 10321-10338 (1992).
162. J. Als-Nielsen and D. McMorrow, *Elements of modern X-ray physics*, (John Wiley & Sons, 2011).
163. P. J. Brown, A. G. Fox, E. N. Maslen, M. A. O'Keefe and B. T. M. Willis, *Intensity of diffracted intensities,* in *International Tables for Crystallography*, Ed. E. Prince, (International Union of Crystallography, 2006). Vol. C, Ch. 6.1, pp. 554-595.

164. I. Robinson, *X-ray Crystallography of Surfaces and Interfaces*, Acta Cryst. A **54**, 772-778 (1998).
165. A. C. Thompson, J. Kirz, D. T. Attwood, E. M. Gullikson, M. R. Howells, J. B. Kortright, Y. Liu, A. L. Robinson, J. H. Underwood, K.-J. Kim, et al., *X-ray Data Booklet*, Ed. A. C. Thompson, Third edition, (Lawrence Berkeley National Lab, Berkeley, CA, 2009). *https://cxro.lbl.gov/x-ray-data-booklet*.
166. I. K. Robinson, *Crystal truncation rods and surface roughness*, Phys. Rev. B **33**, 3830-3836 (1986).
167. M. J. Bedzyk, G. M. Bommarito and J. S. Schildkraut, *X-ray standing waves at a reflecting mirror surface*, Phys. Rev. Lett. **62**, 1376-1379 (1989).
168. F. Pfeiffer, *X-ray ptychography*, Nature Photonics **12**, 9-17 (2018).
169. A. L. Patterson, *A Fourier Series Method for the Determination of the Components of Interatomic Distances in Crystals*, Physical Review **46**, 372-376 (1934).
170. J. R. Fienup, *Reconstruction of an object from the modulus of its Fourier transform*, Opt. Lett. **3**, 27-29 (1978).
171. S. Kandel, S. Maddali, M. Allain, S. O. Hruszkewycz, C. Jacobsen and Y. S. G. Nashed, *Using automatic differentiation as a general framework for ptychographic reconstruction*, Opt. Express **27**, 18653-18672 (2019).
172. E. D. Specht and F. J. Walker, *Oxidation state of a buried interface: Near-edge x-ray fine structure of a crystal truncation rod*, Phys. Rev. B **47**, 13743-13751 (1993).
173. Y. S. Chu, H. You, J. A. Tanzer, T. E. Lister and Z. Nagy, *Surface Resonance X-Ray Scattering Observation of Core-Electron Binding-Energy Shifts of Pt(111)-Surface Atoms during Electrochemical Oxidation*, Phys. Rev. Lett. **83**, 552-555 (1999).
174. K. Akimoto, K. Hirose and J. Mizuki, *Structure at the Yb/GaAs interface studied by anomalous x-ray scattering*, Phys. Rev. B **44**, 1622-1627 (1991).
175. C. Park, P. A. Fenter, N. C. Sturchio and J. R. Regalbuto, *Probing Outer-Sphere Adsorption of Aqueous Metal Complexes at the Oxide-Water Interface with Resonant Anomalous X-Ray Reflectivity*, Phys. Rev. Lett. **94**, 076104 (2005).
176. C. Park and P. A. Fenter, *Phasing of resonant anomalous X-ray reflectivity spectra and direct Fourier synthesis of element-specific partial structures at buried interfaces*, J. Appl. Crystallogr. **40**, 290-301 (2007).
177. J. G. Catalano, C. Park, P. Fenter and Z. Zhang, *Simultaneous inner- and outer-sphere arsenate adsorption on corundum and hematite*, Geochim. Cosmochim. Acta **72**, 1986-2004 (2008).
178. T. Xu, J. E. Stubbs, P. J. Eng and J. G. Catalano, *Response of interfacial water to arsenate adsorption on corundum (0 0 1) surfaces: Effects of pH and adsorbate surface coverage*, Geochim. Cosmochim. Acta **239**, 198-212 (2018).
179. T. Xu, J. E. Stubbs, P. J. Eng and J. G. Catalano, *Comparative response of interfacial water structure to pH variations and arsenate adsorption on corundum (0 1 2) and (0 0 1) surfaces*, Geochim. Cosmochim. Acta **246**, 406-418 (2019).
180. J. N. Bracco, S. S. Lee, J. E. Stubbs, P. J. Eng, S. Jindra, D. M. Warren, A. Kommu, P. Fenter, J. D. Kubicki and A. G. Stack, *Simultaneous Adsorption and Incorporation of Sr2+ at the Barite (001)–Water Interface*, J. Phys. Chem. C **123**, 1194-1207 (2019).

181. J. N. Bracco, S. S. Lee, I. Braha, A. Dorfman, P. Fenter and A. G. Stack, *Pb Sorption at the Barite (001)–Water Interface*, J. Phys. Chem. C **124**, 22035-22045 (2020).
182. S. S. Lee, F. Heberling, N. C. Sturchio, P. J. Eng and P. Fenter, *Surface Charge of the Calcite (104) Terrace Measured by Rb+ Adsorption in Aqueous Solutions Using Resonant Anomalous X-ray Reflectivity*, J. Phys. Chem. C **120**, 15216-15223 (2016).
183. Y. Gründer and C. A. Lucas, *Probing the charge distribution at the electrochemical interface*, Phys. Chem. Chem. Phys. **19**, 8416-8422 (2017).
184. D. C. Koningsberger and R. Prins, *X-ray absorption : principles, applications, techniques of EXAFS, SEXAFS, and XANES*, (Wiley, New York, 1988).
185. N. Elgrishi, K. J. Rountree, B. D. McCarthy, E. S. Rountree, T. T. Eisenhart and J. L. Dempsey, *A Practical Beginner's Guide to Cyclic Voltammetry*, Journal of Chemical Education **95**, 197-206 (2018).
186. T. S. Mathis, N. Kurra, X. Wang, D. Pinto, P. Simon and Y. Gogotsi, *Energy Storage Data Reporting in Perspective—Guidelines for Interpreting the Performance of Electrochemical Energy Storage Systems*, Adv. Energy Mater. **9**, 1902007 (2019).
187. T. C. Liu, W. G. Pell, B. E. Conway and S. L. Roberson, *Behavior of Molybdenum Nitrides as Materials for Electrochemical Capacitors: Comparison with Ruthenium Oxide*, Journal of The Electrochemical Society **145**, 1882-1888 (1998).
188. B. K. K. Kasem and S. Jones, *Platinum as a reference electrode in electrochemical measurements*, Platinum Metals Review **52**, 100-106 (2008).
189. K. J. Harmon, Y. Chen, E. J. Bylaska, J. G. Catalano, M. J. Bedzyk, J. H. Weare and P. Fenter, *Insights on the Alumina–Water Interface Structure by Direct Comparison of Density Functional Simulations with X-ray Reflectivity*, J. Phys. Chem. C **122**, 26934-26944 (2018).
190. K. J. Harmon, K. Letchworth-Weaver, A. P. Gaiduk, F. Giberti, F. Gygi, M. K. Y. Chan, P. Fenter and G. Galli, *Validating first-principles molecular dynamics calculations of oxide/water interfaces with x-ray reflectivity data*, Phys. Rev. Mater. **4**, 113805 (2020).
191. Y. Morikawa, K. Iwata, J. Nakamura, T. Fujitani and K. Terakura, *Ab initio study of surface structural changes during methanol synthesis over Zn/Cu(111)*, Chem. Phys. Lett. **304**, 91-97 (1999).
192. M. Behrens, F. Studt, I. Kasatkin, S. Kühl, M. Hävecker, F. Abild-Pedersen, S. Zander, F. Girgsdies, P. Kurr, B.-L. Kniep, et al., *The Active Site of Methanol Synthesis over Cu/ZnO/Al_2O_3 Industrial Catalysts*, Science **336**, 893-897 (2012).
193. A. Alkauskas, B. B. Buckley, D. D. Awschalom and C. G. Van de Walle, *First-principles theory of the luminescence lineshape for the triplet transition in diamond NV centres*, New J. Phys. **16**, 073026 (2014).
194. J. Davidsson, V. Ivády, R. Armiento, N. T. Son, A. Gali and I. A. Abrikosov, *First principles predictions of magneto-optical data for semiconductor point defect identification: the case of divacancy defects in 4H–SiC*, New J. Phys. **20**, 023035 (2018).
195. C. Zhang, J. Wu, G. Galli and F. Gygi, *Structural and Vibrational Properties of Liquid Water from van der Waals Density Functionals*, J. Chem. Theory Comput. **7**, 3054-3061 (2011).
196. K. Berland and P. Hyldgaard, *Exchange functional that tests the robustness of the plasmon description of the van der Waals density functional*, Phys. Rev. B **89**, 035412 (2014).

197. F. Muttaqien, Y. Hamamoto, I. Hamada, K. Inagaki, Y. Shiozawa, K. Mukai, T. Koitaya, S. Yoshimoto, J. Yoshinobu and Y. Morikawa, *CO_2 adsorption on the copper surfaces: van der Waals density functional and TPD studies*, J. Chem. Phys. **147**, 094702 (2017).
198. W. Dawson and F. Gygi, *Equilibration and analysis of first-principles molecular dynamics simulations of water*, J. Chem. Phys. **148**, 124501 (2018).
199. F. Ren, L. Ward, T. Williams, K. J. Laws, C. Wolverton, J. Hattrick-Simpers and A. Mehta, *Accelerated discovery of metallic glasses through iteration of machine learning and high-throughput experiments*, Sci. Adv. **4**, eaaq1566 (2018).
200. I. C. Lin, A. P. Seitsonen, I. Tavernelli and U. Rothlisberger, *Structure and Dynamics of Liquid Water from ab Initio Molecular Dynamics—Comparison of BLYP, PBE, and revPBE Density Functionals with and without van der Waals Corrections*, J. Chem. Theory Comput. **8**, 3902-3910 (2012).
201. R. A. DiStasio Jr., B. Santra, Z. Li, X. Wu and R. Car, *The individual and collective effects of exact exchange and dispersion interactions on the ab initio structure of liquid water*, J. Chem. Phys. **141**, 084502 (2014).
202. W. Kohn and L. J. Sham, *Self-Consistent Equations Including Exchange and Correlation Effects*, Physical Review **140**, A1133-A1138 (1965).
203. P. Haas, F. Tran and P. Blaha, *Calculation of the lattice constant of solids with semilocal functionals*, Phys. Rev. B **79**, 085104 (2009).
204. M. Chen, H.-Y. Ko, R. C. Remsing, M. F. Calegari Andrade, B. Santra, Z. Sun, A. Selloni, R. Car, M. L. Klein, J. P. Perdew, et al., *Ab initio theory and modeling of water*, Proc. Natl. Acad. Sci. **114**, 10846-10851 (2017).
205. F. Ambrosio, G. Miceli and A. Pasquarello, *Structural, Dynamical, and Electronic Properties of Liquid Water: A Hybrid Functional Study*, J. Phys. Chem. B **120**, 7456-7470 (2016).
206. J. Wang, J. Polleux, J. Lim and B. Dunn, *Pseudocapacitive Contributions to Electrochemical Energy Storage in TiO2 (Anatase) Nanoparticles*, J. Phys. Chem. C **111**, 14925-14931 (2007).
207. S. J. T. Brugman, P. Raiteri, P. Accordini, F. Megens, J. D. Gale and E. Vlieg, *Calcite (104) Surface–Electrolyte Structure: A 3D Comparison of Surface X-ray Diffraction and Simulations*, J. Phys. Chem. C **124**, 18564-18575 (2020).
208. M. Plaza, X. Huang, J. Y. Ko, M. Shen, B. H. Simpson, J. Rodriguez-Lopez, N. L. Ritzert, K. Letchworth-Weaver, D. Gunceler, D. G. Schlom, et al., *Structure of the Photo-catalytically Active Surface of $SrTiO_3$*, J. Am. Chem. Soc. **138**, 7816-7819 (2016).
209. P. J. Eng, T. P. Trainor, G. E. Brown Jr., G. A. Waychunas, M. Newville, S. R. Sutton and M. L. Rivers, *Structure of the Hydrated α-Al_2O_3 (0001) Surface*, Science **288**, 1029-1033 (2000).
210. J. G. Catalano, *Weak interfacial water ordering on isostructural hematite and corundum (001) surfaces*, Geochim. Cosmochim. Acta **75**, 2062-2071 (2011).
211. B. Braunschweig, S. Eissner and W. Daum, *Molecular Structure of a Mineral/Water Interface: Effects of Surface NanoRoughness of α-Al_2O_3 (0001)*, J. Phys. Chem. C **112**, 1751-1754 (2008).
212. J. W. Elam, C. E. Nelson, M. A. Cameron, M. A. Tolbert and S. M. George, *Adsorption of H_2O on a Single-Crystal α-Al_2O_3(0001) Surface*, J. Phys. Chem. B **102**, 7008-7015 (1998).

213. J. P. Fitts, X. Shang, G. W. Flynn, T. F. Heinz and K. B. Eisenthal, *Electrostatic Surface Charge at Aqueous/α-Al_2O_3 Single-Crystal Interfaces as Probed by Optical Second-Harmonic Generation*, J. Phys. Chem. B **109**, 7981-7986 (2005).
214. L. Zhang, C. Tian, G. A. Waychunas and Y. R. Shen, *Structures and Charging of α-Alumina (0001)/Water Interfaces Studied by Sum-Frequency Vibrational Spectroscopy*, J. Am. Chem. Soc. **130**, 7686-7694 (2008).
215. S. Freier, M. Greenshpan, P. Hillman and H. Shechter, *The antiferromagnetic curie point in α-Fe2O3*, Physics Letters **2**, 191-192 (1962).
216. K. M. Rosso, D. M. A. Smith and M. Dupuis, *An ab initio model of electron transport in hematite (α-Fe2O3) basal planes*, J. Chem. Phys. **118**, 6455-6466 (2003).
217. A. Kirfel and K. Eichhorn, *Accurate structure analysis with synchrotron radiation. The electron density in Al_2O_3 and Cu_2O*, Acta Cryst. A **46**, 271-284 (1990).
218. D. Sholl and J. A. Steckel, *Density functional theory: a practical introduction*, (John Wiley & Sons, 2011).
219. P. Ziesche, S. Kurth and J. P. Perdew, *Density functionals from LDA to GGA*, Computational Materials Science **11**, 122-127 (1998).
220. V. Heine, *The Pseudopotential Concept,* in *Solid State Physics*, Ed. H. Ehrenreich, F. Seitz and D. Turnbull, (Academic Press, 1970). Vol. 24, Ch. 1, pp. 1-36.
221. M. C. Payne, M. P. Teter, D. C. Allan, T. A. Arias and J. D. Joannopoulos, *Iterative minimization techniques for ab initio total-energy calculations: molecular dynamics and conjugate gradients*, Rev. Mod. Phys. **64**, 1045-1097 (1992).
222. D. R. Hamann, M. Schlüter and C. Chiang, *Norm-Conserving Pseudopotentials*, Phys. Rev. Lett. **43**, 1494-1497 (1979).
223. M. Schlipf and F. Gygi, *Optimization algorithm for the generation of ONCV pseudopotentials*, Comput. Phys. Commun. **196**, 36-44 (2015).
224. C. Kittel and P. McEuen, *Introduction to solid state physics*, (Wiley New York, 1976).
225. C. L. Reis, J. M. Pacheco and J. L. Martins, *First-principles norm-conserving pseudopotential with explicit incorporation of semicore states*, Phys. Rev. B **68**, 155111 (2003).
226. P. Liu, T. Kendelewicz, G. E. Brown, E. J. Nelson and S. A. Chambers, *Reaction of water vapor with α-Al_2O_3(0001) and α-Fe_2O_3(0001) surfaces: synchrotron X-ray photoemission studies and thermodynamic calculations*, Surf. Sci. **417**, 53-65 (1998).
227. K. C. Hass, W. F. Schneider, A. Curioni and W. Andreoni, *First-Principles Molecular Dynamics Simulations of H_2O on α-Al_2O_3 (0001)*, J. Phys. Chem. B **104**, 5527-5540 (2000).
228. P. Huang, T. A. Pham, G. Galli and E. Schwegler, *Alumina(0001)/Water Interface: Structural Properties and Infrared Spectra from First-Principles Molecular Dynamics Simulations*, J. Phys. Chem. C **118**, 8944-8951 (2014).
229. S. Plimpton, *Fast Parallel Algorithms for Short-Range Molecular Dynamics*, J. Comput. Phys. **117**, 1-19 (1995).
230. R. T. Cygan, J.-J. Liang and A. G. Kalinichev, *Molecular Models of Hydroxide, Oxyhydroxide, and Clay Phases and the Development of a General Force Field*, J. Phys. Chem. B **108**, 1255-1266 (2004).
231. H. J. C. Berendsen, J. R. Grigera and T. P. Straatsma, *The missing term in effective pair potentials*, J. Phys. Chem. **91**, 6269-6271 (1987).

232. F. Gygi, *Architecture of Qbox: A scalable first-principles molecular dynamics code*, IBM J. Res. Dev. **52**, 137-144 (2008).
233. D. R. Hamann, *Optimized norm-conserving Vanderbilt pseudopotentials*, Phys. Rev. B **88**, 085117 (2013).
234. J. P. Perdew, K. Burke and M. Ernzerhof, *Generalized Gradient Approximation Made Simple*, Phys. Rev. Lett. **77**, 3865-3868 (1996).
235. A. P. Gaiduk, F. Gygi and G. Galli, *Density and Compressibility of Liquid Water and Ice from First-Principles Simulations with Hybrid Functionals*, J. Phys. Chem. Lett. **6**, 2902-2908 (2015).
236. G. Bussi, D. Donadio and M. Parrinello, *Canonical sampling through velocity rescaling*, J. Chem. Phys. **126**, 014101 (2007).
237. Y. Chen, E. Bylaska and J. Weare, *First principles estimation of geochemically important transition metal oxide properties,* in *Molecular Modeling of Geochemical Reactions: An Introduction*, Ed. J. D. Kubicki, (John Wiley & Sons, Ltd., 2016). Vol. Ch. 4, pp. 107-149.
238. J. Schmidt, J. VandeVondele, I. F. W. Kuo, D. Sebastiani, J. I. Siepmann, J. Hutter and C. J. Mundy, *Isobaric−Isothermal Molecular Dynamics Simulations Utilizing Density Functional Theory: An Assessment of the Structure and Density of Water at Near-Ambient Conditions*, J. Phys. Chem. B **113**, 11959-11964 (2009).
239. E. Schwegler, J. C. Grossman, F. Gygi and G. Galli, *Towards an assessment of the accuracy of density functional theory for first principles simulations of water. II*, J. Chem. Phys. **121**, 5400-5409 (2004).
240. M. DelloStritto, S. M. Piontek, M. L. Klein and E. Borguet, *Relating Interfacial Order to Sum Frequency Generation with Ab Initio Simulations of the Aqueous* Al_2O_3*(0001) and (11*$\bar{2}$*0) Interfaces*, J. Phys. Chem. C **122**, 21284-21294 (2018).
241. C. Adamo and V. Barone, *Toward reliable density functional methods without adjustable parameters: The PBE0 model*, J. Chem. Phys. **110**, 6158-6170 (1999).
242. C. Zhang, D. Donadio, F. Gygi and G. Galli, *First Principles Simulations of the Infrared Spectrum of Liquid Water Using Hybrid Density Functionals*, J. Chem. Theory Comput. **7**, 1443-1449 (2011).
243. E. J. Bylaska, *Plane-Wave DFT Methods for Chemistry,* in *Annual Reports in Computational Chemistry*, Ed. D. A. Dixon, (Elsevier, 2017). Vol. 13, Ch. 5, pp. 185-228.
244. E. Bylaska, K. Tsemekhman, N. Govind and M. Valiev, *Large-Scale Plane-Wave-Based Density Functional Theory: Formalism, Parallelization, and Applications,* in *Computational Methods for Large Systems*, Ed. J. R. Reimers, (John Wiley & Sons, Ltd., 2011). Vol. Ch. 3, pp. 77-116.
245. M. Valiev, E. J. Bylaska, N. Govind, K. Kowalski, T. P. Straatsma, H. J. J. Van Dam, D. Wang, J. Nieplocha, E. Apra, T. L. Windus, et al., *NWChem: A comprehensive and scalable open-source solution for large scale molecular simulations*, Comput. Phys. Commun. **181**, 1477-1489 (2010).
246. S. Grimme, *Semiempirical GGA-type density functional constructed with a long-range dispersion correction*, J. Comput. Chem. **27**, 1787-1799 (2006).
247. H. J. Monkhorst and J. D. Pack, *Special points for Brillouin-zone integrations*, Phys. Rev. B **13**, 5188-5192 (1976).

248. D. R. Hamann, *Generalized norm-conserving pseudopotentials*, Phys. Rev. B **40**, 2980-2987 (1989).
249. L. Kleinman and D. M. Bylander, *Efficacious Form for Model Pseudopotentials*, Phys. Rev. Lett. **48**, 1425-1428 (1982).
250. E. J. Bylaska, M. Valiev, J. R. Rustad and J. H. Weare, *Structure and dynamics of the hydration shells of the Al^{3+} ion*, J. Chem. Phys. **126**, 104505 (2007).
251. S. Kondo, K. Tateishi and N. Ishizawa, *Structural Evolution of Corundum at High Temperatures*, Jpn. J. Appl. Phys. **47**, 616-619 (2008).
252. E. Cauët, S. Bogatko, J. H. Weare, J. L. Fulton, G. K. Schenter and E. J. Bylaska, *Structure and dynamics of the hydration shells of the Zn^{2+} ion from ab initio molecular dynamics and combined ab initio and classical molecular dynamics simulations*, J. Chem. Phys. **132**, 194502 (2010).
253. D. Marx and J. Hutter, *Ab initio molecular dynamics: basic theory and advanced methods*, (Cambridge University Press, 2009).
254. R. Car and M. Parrinello, *Unified Approach for Molecular Dynamics and Density-Functional Theory*, Phys. Rev. Lett. **55**, 2471-2474 (1985).
255. S. Nosé, *A unified formulation of the constant temperature molecular dynamics methods*, J. Chem. Phys. **81**, 511-519 (1984).
256. W. G. Hoover, *Canonical dynamics: Equilibrium phase-space distributions*, Physical Review A **31**, 1695-1697 (1985).
257. P. E. Blöchl and M. Parrinello, *Adiabaticity in first-principles molecular dynamics*, Phys. Rev. B **45**, 9413-9416 (1992).
258. F. Herbstein, *How precise are measurements of unit-cell dimensions from single crystals?*, Acta Cryst. B **56**, 547-557 (2000).
259. K. W. Corum, X. Huang, J. W. Bennett and S. E. Mason, *Systematic density functional theory study of the structural and electronic properties of constrained and fully relaxed (0 0 1) surfaces of alumina and hematite*, Mol. Simulat. **43**, 406-419 (2017).
260. A. Sundaresan, R. Bhargavi, N. Rangarajan, U. Siddesh and C. N. R. Rao, *Ferromagnetism as a universal feature of nanoparticles of the otherwise nonmagnetic oxides*, Phys. Rev. B **74**, 161306 (2006).
261. U. Bergmann, A. D. Cicco, P. Wernet, E. Principi, P. Glatzel and A. Nilsson, *Nearest-neighbor oxygen distances in liquid water and ice observed by x-ray Raman based extended x-ray absorption fine structure*, J. Chem. Phys. **127**, 174504 (2007).
262. G. Hura, J. M. Sorenson, R. M. Glaeser and T. Head-Gordon, *A high-quality x-ray scattering experiment on liquid water at ambient conditions*, J. Chem. Phys. **113**, 9140-9148 (2000).
263. K. S. Tanwar, S. C. Petitto, S. K. Ghose, P. J. Eng and T. P. Trainor, *Fe(II) adsorption on hematite (0001)*, Geochim. Cosmochim. Acta **73**, 4346-4365 (2009).
264. M. J. DelloStritto, S. M. Piontek, M. L. Klein and E. Borguet, *Effect of Functional and Electron Correlation on the Structure and Spectroscopy of the $Al_2O_3(001)–H_2O$ Interface*, J. Phys. Chem. Lett. **10**, 2031-2036 (2019).
265. A. G. Stack, S. R. Higgins and C. M. Eggleston, *Point of zero charge of a corundum-water interface probed with optical second harmonic generation (SHG) and atomic force*

microscopy (AFM): New approaches to oxide surface charge, Geochim. Cosmochim. Acta **65**, 3055-3063 (2001).

266. M. Kosmulski, *The pH-Dependent Surface Charging and the Points of Zero Charge*, J. Colloid Interface Sci. **253**, 77-87 (2002).
267. G. V. Franks and L. Meagher, *The isoelectric points of sapphire crystals and alpha-alumina powder*, Colloids Surf. A Physiochem. Eng. Asp. **214**, 99-110 (2003).
268. J. Heyd, G. E. Scuseria and M. Ernzerhof, *Hybrid functionals based on a screened Coulomb potential*, J. Chem. Phys. **118**, 8207-8215 (2003).
269. J. Heyd, G. E. Scuseria and M. Ernzerhof, *Erratum: "Hybrid functionals based on a screened Coulomb potential" [J. Chem. Phys. 118, 8207 (2003)]*, J. Chem. Phys. **124**, 219906 (2006).
270. A. V. Krukau, O. A. Vydrov, A. F. Izmaylov and G. E. Scuseria, *Influence of the exchange screening parameter on the performance of screened hybrid functionals*, J. Chem. Phys. **125**, 224106 (2006).
271. A. P. Gaiduk, J. Gustafson, F. Gygi and G. Galli, *First-Principles Simulations of Liquid Water Using a Dielectric-Dependent Hybrid Functional*, J. Phys. Chem. Lett. **9**, 3068-3073 (2018).
272. H. Zheng, M. Govoni and G. Galli, *Dielectric-dependent hybrid functionals for heterogeneous materials*, Phys. Rev. Mater. **3**, 073803 (2019).
273. J. H. Skone, M. Govoni and G. Galli, *Self-consistent hybrid functional for condensed systems*, Phys. Rev. B **89**, 195112 (2014).
274. J. Sun, A. Ruzsinszky and J. P. Perdew, *Strongly Constrained and Appropriately Normed Semilocal Density Functional*, Phys. Rev. Lett. **115**, 036402 (2015).
275. M. D. LaCount and F. Gygi, *Ensemble first-principles molecular dynamics simulations of water using the SCAN meta-GGA density functional*, J. Chem. Phys. **151**, 164101 (2019).
276. V. Kohli, Z. Zhang, C. Park and P. Fenter, *Rb^+ and Sr^{2+} Adsorption at the TiO_2 (110)−Electrolyte Interface Observed with Resonant Anomalous X-ray Reflectivity*, Langmuir **26**, 950-958 (2010).
277. A. K. Geim and K. S. Novoselov, *The rise of graphene*, Nat Mater **6**, 183-191 (2007).
278. C. Lee, X. Wei, J. W. Kysar and J. Hone, *Measurement of the Elastic Properties and Intrinsic Strength of Monolayer Graphene*, Science **321**, 385-388 (2008).
279. A. A. Balandin, S. Ghosh, W. Bao, I. Calizo, D. Teweldebrhan, F. Miao and C. N. Lau, *Superior Thermal Conductivity of Single-Layer Graphene*, Nano Lett. **8**, 902-907 (2008).
280. K. S. Novoselov, A. K. Geim, S. V. Morozov, D. Jiang, Y. Zhang, S. V. Dubonos, I. V. Grigorieva and A. A. Firsov, *Electric Field Effect in Atomically Thin Carbon Films*, Science **306**, 666-669 (2004).
281. J. J. Yoo, K. Balakrishnan, J. Huang, V. Meunier, B. G. Sumpter, A. Srivastava, M. Conway, A. L. Mohana Reddy, J. Yu, R. Vajtai, et al., *Ultrathin Planar Graphene Supercapacitors*, Nano Lett. **11**, 1423-1427 (2011).
282. Y. Yang, C. Han, B. Jiang, J. Iocozzia, C. He, D. Shi, T. Jiang and Z. Lin, *Graphene-based materials with tailored nanostructures for energy conversion and storage*, Materials Science and Engineering: R: Reports **102**, 1-72 (2016).
283. C. Liu, Z. Yu, D. Neff, A. Zhamu and B. Z. Jang, *Graphene-Based Supercapacitor with an Ultrahigh Energy Density*, Nano Lett. **10**, 4863-4868 (2010).

284. Z. Lin, Y. Liu, Y. Yao, O. J. Hildreth, Z. Li, K. Moon and C.-p. Wong, *Superior Capacitance of Functionalized Graphene*, J. Phys. Chem. C **115**, 7120-7125 (2011).
285. J. Yang and S. Gunasekaran, *Electrochemically reduced graphene oxide sheets for use in high performance supercapacitors*, Carbon **51**, 36-44 (2013).
286. M. D. Stoller, S. Park, Y. Zhu, J. An and R. S. Ruoff, *Graphene-Based Ultracapacitors*, Nano Lett. **8**, 3498-3502 (2008).
287. Y. Wang, Z. Shi, Y. Huang, Y. Ma, C. Wang, M. Chen and Y. Chen, *Supercapacitor Devices Based on Graphene Materials*, J. Phys. Chem. C **113**, 13103-13107 (2009).
288. D. Prasai, J. C. Tuberquia, R. R. Harl, G. K. Jennings, B. R. Rogers and K. I. Bolotin, *Graphene: Corrosion-Inhibiting Coating*, ACS Nano **6**, 1102-1108 (2012).
289. S. Dröscher, P. Roulleau, F. Molitor, P. Studerus, C. Stampfer, K. Ensslin and T. Ihn, *Quantum capacitance and density of states of graphene*, Appl. Phys. Lett. **96**, 152104 (2010).
290. Y.-J. Yu, Y. Zhao, S. Ryu, L. E. Brus, K. S. Kim and P. Kim, *Tuning the Graphene Work Function by Electric Field Effect*, Nano Lett. **9**, 3430-3434 (2009).
291. Y. Zhang, T.-T. Tang, C. Girit, Z. Hao, M. C. Martin, A. Zettl, M. F. Crommie, Y. R. Shen and F. Wang, *Direct observation of a widely tunable bandgap in bilayer graphene*, Nature **459**, 820-823 (2009).
292. W. Lv, Z. Li, Y. Deng, Q.-H. Yang and F. Kang, *Graphene-based materials for electrochemical energy storage devices: Opportunities and challenges*, Energy Storage Materials **2**, 107-138 (2016).
293. X. Li, W. Cai, J. An, S. Kim, J. Nah, D. Yang, R. Piner, A. Velamakanni, I. Jung, E. Tutuc, et al., *Large-Area Synthesis of High-Quality and Uniform Graphene Films on Copper Foils*, Science **324**, 1312-1314 (2009).
294. A. J. Van Bommel, J. E. Crombeen and A. Van Tooren, *LEED and Auger electron observations of the SiC(0001) surface*, Surf. Sci. **48**, 463-472 (1975).
295. I. Forbeaux, J. M. Themlin and J. M. Debever, *Heteroepitaxial graphite on 6H-SiC(0001): Interface formation through conduction-band electronic structure*, Phys. Rev. B **58**, 16396-16406 (1998).
296. A. Charrier, A. Coati, T. Argunova, F. Thibaudau, Y. Garreau, R. Pinchaux, I. Forbeaux, J.-M. Debever, M. Sauvage-Simkin and J.-M. Themlin, *Solid-state decomposition of silicon carbide for growing ultra-thin heteroepitaxial graphite films*, J. Appl. Phys. **92**, 2479-2484 (2002).
297. W. A. de Heer, C. Berger, M. Ruan, M. Sprinkle, X. Li, Y. Hu, B. Zhang, J. Hankinson and E. Conrad, *Large area and structured epitaxial graphene produced by confinement controlled sublimation of silicon carbide*, Proc. Natl. Acad. Sci. **108**, 16900-16905 (2011).
298. Y.-M. Lin, C. Dimitrakopoulos, K. A. Jenkins, D. B. Farmer, H.-Y. Chiu, A. Grill and P. Avouris, *100-GHz Transistors from Wafer-Scale Epitaxial Graphene*, Science **327**, 662-662 (2010).
299. M. S. Fuhrer, C. N. Lau and A. H. MacDonald, *Graphene: Materially Better Carbon*, MRS Bull. **35**, 289-295 (2010).
300. E. V. Castro, K. S. Novoselov, S. V. Morozov, N. M. R. Peres, J. M. B. L. dos Santos, J. Nilsson, F. Guinea, A. K. Geim and A. H. C. Neto, *Biased Bilayer Graphene:*

Semiconductor with a Gap Tunable by the Electric Field Effect, Phys. Rev. Lett. **99**, 216802 (2007).

301. T. Ohta, A. Bostwick, T. Seyller, K. Horn and E. Rotenberg, *Controlling the electronic structure of bilayer graphene*, Science **313**, 951-954 (2006).
302. S. Y. Zhou, G. H. Gweon, A. V. Fedorov, P. N. First, W. A. de Heer, D. H. Lee, F. Guinea, A. H. Castro Neto and A. Lanzara, *Substrate-induced bandgap opening in epitaxial graphene*, Nat. Mater. **6**, 770-775 (2007).
303. F. Varchon, R. Feng, J. Hass, X. Li, B. N. Nguyen, C. Naud, P. Mallet, J. Y. Veuillen, C. Berger, E. H. Conrad, et al., *Electronic Structure of Epitaxial Graphene Layers on SiC: Effect of the Substrate*, Phys. Rev. Lett. **99**, 126805 (2007).
304. C. Faugeras, A. Nerrière, M. Potemski, A. Mahmood, E. Dujardin, C. Berger and W. A. d. Heer, *Few-layer graphene on SiC, pyrolitic graphite, and graphene: A Raman scattering study*, Appl. Phys. Lett. **92**, 011914 (2008).
305. S. Kim, J. Ihm, H. J. Choi and Y.-W. Son, *Origin of Anomalous Electronic Structures of Epitaxial Graphene on Silicon Carbide*, Phys. Rev. Lett. **100**, 176802 (2008).
306. J. Röhrl, M. Hundhausen, K. V. Emtsev, T. Seyller, R. Graupner and L. Ley, *Raman spectra of epitaxial graphene on SiC(0001)*, Appl. Phys. Lett. **92**, 201918 (2008).
307. Y. Baskin and L. Meyer, *Lattice Constants of Graphite at Low Temperatures*, Physical Review **100**, 544-544 (1955).
308. A. Bauer, P. Reischauer, J. Krausslich, N. Schell, W. Matz and K. Goetz, *Structure refinement of the silicon carbide polytypes 4H and 6H: unambiguous determination of the refinement parameters*, Acta Cryst. A **57**, 60-67 (2001).
309. J. Robinson, X. Weng, K. Trumbull, R. Cavalero, M. Wetherington, E. Frantz, M. LaBella, Z. Hughes, M. Fanton and D. Snyder, *Nucleation of Epitaxial Graphene on SiC(0001)*, ACS Nano **4**, 153-158 (2010).
310. S. W. Poon, W. Chen, E. S. Tok and A. T. S. Wee, *Probing epitaxial growth of graphene on silicon carbide by metal decoration*, Appl. Phys. Lett. **92**, 104102 (2008).
311. K. V. Emtsev, F. Speck, T. Seyller, L. Ley and J. D. Riley, *Interaction, growth, and ordering of epitaxial graphene on SiC{0001} surfaces: A comparative photoelectron spectroscopy study*, Phys. Rev. B **77**, 155303 (2008).
312. J. Hass, W. De Heer and E. Conrad, *The growth and morphology of epitaxial multilayer graphene*, J. Phys. Condens. Matter **20**, 323202 (2008).
313. F. Owman and P. Mårtensson, *The SiC(0001)6√3 × 6√3 reconstruction studied with STM and LEED*, Surf. Sci. **369**, 126-136 (1996).
314. S. Tanaka, K. Morita and H. Hibino, *Anisotropic layer-by-layer growth of graphene on vicinal SiC(0001) surfaces*, Phys. Rev. B **81**, 041406 (2010).
315. J. Hass, R. Feng, J. E. Millán-Otoya, X. Li, M. Sprinkle, P. N. First, W. A. de Heer, E. H. Conrad and C. Berger, *Structural properties of the multilayer graphene 4H-SiC(000-1) system as determined by surface x-ray diffraction*, Phys. Rev. B **75**, 214109 (2007).
316. C. Riedl, U. Starke, J. Bernhardt, M. Franke and K. Heinz, *Structural properties of the graphene-SiC(0001) interface as a key for the preparation of homogeneous large-terrace graphene surfaces*, Phys. Rev. B **76**, 245406 (2007).

317. V. Ramachandran, M. F. Brady, A. R. Smith, R. M. Feenstra and D. W. Greve, *Preparation of atomically flat surfaces on silicon carbide using hydrogen etching*, Journal of Electronic Materials **27**, 308-312 (1998).
318. N. P. Guisinger, G. M. Rutter, J. N. Crain, P. N. First and J. A. Stroscio, *Exposure of Epitaxial Graphene on SiC(0001) to Atomic Hydrogen*, Nano Lett. **9**, 1462-1466 (2009).
319. Y. Qi, S. H. Rhim, G. F. Sun, M. Weinert and L. Li, *Epitaxial Graphene on SiC(0001): More than Just Honeycombs*, Phys. Rev. Lett. **105**, 085502 (2010).
320. T. Ohta, F. El Gabaly, A. Bostwick, J. L. McChesney, K. V. Emtsev, A. K. Schmid, T. Seyller, K. Horn and E. Rotenberg, *Morphology of graphene thin film growth on SiC(0001)*, New J. Phys. **10**, 023034 (2008).
321. Z. H. Ni, W. Chen, X. F. Fan, J. L. Kuo, T. Yu, A. T. S. Wee and Z. X. Shen, *Raman spectroscopy of epitaxial graphene on a SiC substrate*, Phys. Rev. B **77**, 115416 (2008).
322. C. Berger, Z. Song, T. Li, X. Li, A. Y. Ogbazghi, R. Feng, Z. Dai, A. N. Marchenkov, E. H. Conrad, P. N. First, et al., *Ultrathin Epitaxial Graphite: 2D Electron Gas Properties and a Route toward Graphene-based Nanoelectronics*, J. Phys. Chem. B **108**, 19912-19916 (2004).
323. J. Xia, F. Chen, J. Li and N. Tao, *Measurement of the quantum capacitance of graphene*, Nat. Nanotechnol. **4**, 505-509 (2009).
324. H. Xu, Z. Zhang, Z. Wang, S. Wang, X. Liang and L.-M. Peng, *Quantum Capacitance Limited Vertical Scaling of Graphene Field-Effect Transistor*, ACS Nano **5**, 2340-2347 (2011).
325. C. Zhan, J. Neal, J. Wu and D.-e. Jiang, *Quantum Effects on the Capacitance of Graphene-Based Electrodes*, J. Phys. Chem. C **119**, 22297-22303 (2015).
326. S. Luryi, *Quantum capacitance devices*, Appl. Phys. Lett. **52**, 501-503 (1988).
327. K. V. Emtsev, A. Bostwick, K. Horn, J. Jobst, G. L. Kellogg, L. Ley, J. L. McChesney, T. Ohta, S. A. Reshanov, J. Röhrl, et al., *Towards wafer-size graphene layers by atmospheric pressure graphitization of silicon carbide*, Nat. Mater. **8**, 203-207 (2009).
328. J. D. Emery. *Synchrotron X-ray Studies of Pristine, Intercalated, and Functionalized Epitaxial Graphene on Silicon Carbide(0001)*, Ph.D. Thesis, Northwestern University, (2013).
329. L. B. Valdes, *Resistivity Measurements on Germanium for Transistors*, Proceedings of the IRE **42**, 420-427 (1954).
330. F. M. Smits, *Measurement of sheet resistivities with the four-point probe*, The Bell System Technical Journal **37**, 711-718 (1958).
331. J. D. Emery, B. Detlefs, H. J. Karmel, L. O. Nyakiti, D. K. Gaskill, M. C. Hersam, J. Zegenhagen and M. J. Bedzyk, *Chemically Resolved Interface Structure of Epitaxial Graphene on SiC(0001)*, Phys. Rev. Lett. **111**, 215501 (2013).
332. J. Hass, J. E. Millán-Otoya, P. N. First and E. H. Conrad, *Interface structure of epitaxial graphene grown on 4H-SiC(0001)*, Phys. Rev. B **78**, 205424 (2008).
333. K. V. Emtsev, T. Seyller, F. Speck, L. Ley, P. Stojanov, J. D. Riley and R. C. G. Leckey, *Initial Stages of the Graphite-SiC(0001) Interface Formation Studied by Photoelectron Spectroscopy*, Materials Science Forum **556-557**, 525-528 (2007).
334. A. Mattausch and O. Pankratov, *Ab Initio Study of Graphene on SiC*, Phys. Rev. Lett. **99**, 076802 (2007).

335. F. Varchon, P. Mallet, J. Y. Veuillen and L. Magaud, *Ripples in epitaxial graphene on the Si-terminated SiC(0001) surface*, Phys. Rev. B **77**, 235412 (2008).
336. G. M. Rutter, N. P. Guisinger, J. N. Crain, E. A. A. Jarvis, M. D. Stiles, T. Li, P. N. First and J. A. Stroscio, *Imaging the interface of epitaxial graphene with silicon carbide via scanning tunneling microscopy*, Phys. Rev. B **76**, 235416 (2007).
337. J. Bernhardt, J. Schardt, U. Starke and K. Heinz, *Epitaxially ideal oxide–semiconductor interfaces: Silicate adlayers on hexagonal (0001) and (000$\bar{1}$) SiC surfaces*, Appl. Phys. Lett. **74**, 1084-1086 (1999).
338. Y. Hoshino, T. Nishimura, T. Yoneda, K. Ogawa, H. Namba and Y. Kido, *Initial oxidation of 6H–SiC(0001)-3×3 surface studied by ion scattering combined with photoemission induced by synchrotron-radiation-light*, Surf. Sci. **505**, 234-242 (2002).
339. F. Amy, H. Enriquez, P. Soukiassian, P. F. Storino, Y. J. Chabal, A. J. Mayne, G. Dujardin, Y. K. Hwu and C. Brylinski, *Atomic Scale Oxidation of a Complex System: O_2/α-SiC(0001)-(3×3)*, Phys. Rev. Lett. **86**, 4342-4345 (2001).
340. F. Amy, P. Soukiassian, Y. K. Hwu and C. Brylinski, *Si-rich 6H- and 4H-SiC(0001) 3×3 surface oxidation and initial SiO_2/SiC interface formation from 25 to 650 °C*, Phys. Rev. B **65**, 165323 (2002).
341. H. Huang, W. Chen, S. Chen and A. T. S. Wee, *Bottom-up Growth of Epitaxial Graphene on 6H-SiC(0001)*, ACS Nano **2**, 2513-2518 (2008).
342. M. N. Nair, I. Palacio, A. Celis, A. Zobelli, A. Gloter, S. Kubsky, J.-P. Turmaud, M. Conrad, C. Berger and W. de Heer, *Band gap opening induced by the structural periodicity in epitaxial graphene buffer layer*, Nano Lett. **17**, 2681-2689 (2017).
343. M. Conrad, F. Wang, M. Nevius, K. Jinkins, A. Celis, M. Narayanan Nair, A. Taleb-Ibrahimi, A. Tejeda, Y. Garreau and A. Vlad, *Wide band gap semiconductor from a hidden 2D incommensurate graphene phase*, Nano Lett. **17**, 341-347 (2016).
344. C. Berger, X. Wu, P. N. First, E. H. Conrad, X. Li, M. Sprinkle, J. Hass, F. Varchon, L. Magaud and M. L. Sadowski, *Dirac particles in epitaxial graphene films grown on SiC,* in *Advances in Solid State Physics*, Ed. (Springer, 2008). Vol. Ch. pp. 145-157.
345. Y. J. Shin, Y. Wang, H. Huang, G. Kalon, A. T. S. Wee, Z. Shen, C. S. Bhatia and H. Yang, *Surface-Energy Engineering of Graphene*, Langmuir **26**, 3798-3802 (2010).
346. J. Rafiee, X. Mi, H. Gullapalli, A. V. Thomas, F. Yavari, Y. Shi, P. M. Ajayan and N. A. Koratkar, *Wetting transparency of graphene*, Nat. Mater. **11**, 217-222 (2012).
347. R. Raj, S. C. Maroo and E. N. Wang, *Wettability of Graphene*, Nano Lett. **13**, 1509-1515 (2013).
348. C.-J. Shih, Q. H. Wang, S. Lin, K.-C. Park, Z. Jin, M. S. Strano and D. Blankschtein, *Breakdown in the Wetting Transparency of Graphene*, Phys. Rev. Lett. **109**, 176101 (2012).
349. T. Seyller, *Electronic properties of SiC surfaces and interfaces: some fundamental and technological aspects*, Applied Physics A **85**, 371-385 (2006).
350. F. Tuinstra and J. L. Koenig, *Raman Spectrum of Graphite*, J. Chem. Phys. **53**, 1126-1130 (1970).
351. A. C. Ferrari and D. M. Basko, *Raman spectroscopy as a versatile tool for studying the properties of graphene*, Nat. Nanotechnol. **8**, 235-246 (2013).

352. C. Casiraghi, A. Hartschuh, H. Qian, S. Piscanec, C. Georgi, A. Fasoli, K. S. Novoselov, D. M. Basko and A. C. Ferrari, *Raman Spectroscopy of Graphene Edges*, Nano Lett. **9**, 1433-1441 (2009).
353. K. F. Rinne, S. Gekle and R. R. Netz, *Ion-Specific Solvation Water Dynamics: Single Water versus Collective Water Effects*, J. Phys. Chem. A **118**, 11667-11677 (2014).
354. C. Jang, S. Adam, J. H. Chen, E. D. Williams, S. Das Sarma and M. S. Fuhrer, *Tuning the Effective Fine Structure Constant in Graphene: Opposing Effects of Dielectric Screening on Short- and Long-Range Potential Scattering*, Phys. Rev. Lett. **101**, 146805 (2008).
355. M. D. Radin, T. Ogitsu, J. Biener, M. Otani and B. C. Wood, *Capacitive charge storage at an electrified interface investigated via direct first-principles simulations*, Phys. Rev. B **91**, 125415 (2015).